

Amorphous Silicon Carbide for Photovoltaic Applications

Dissertation

zur Erlangung des
akademischen Grades
Doktor der Naturwissenschaften
(*Dr. rer. nat.*)

an der Universität Konstanz
Fakultät für Physik

vorgelegt von
Stefan Janz
geb. in Leoben/Stmk.

Fraunhofer Institut für Solare Energiesysteme
Freiburg
2006

Referenten: Prof. Dr. Gerhard Willeke
Prof. Dr. Elke Scheer

Tag der mündl. Prüfung: 8. Dezember 2006

*„Der wahre Zweck des Menschen
ist die höchste und proportionierlichste Bildung
seiner Kräfte zu einem Ganzen.“*

Wilhelm v. Humboldt

AMORPHOUS SILICON CARBIDE FOR PHOTOVOLTAIC APPLICATIONS..... 1

1	AMORPHOUS SILICON CARBIDE	17
1.1	INTRODUCTION.....	17
1.2	AMORPHOUS STRUCTURE OF SiC	18
1.2.1	<i>The tetrahedral network</i>	<i>18</i>
1.2.2	<i>Hydrogenated SiC.....</i>	<i>20</i>
1.2.3	<i>Vibrational spectroscopy (Infrared spectra)</i>	<i>21</i>
1.2.4	<i>Silicon and carbon content</i>	<i>22</i>
1.3	PLASMA ENHANCED CHEMICAL VAPOUR DEPOSITION (PECVD).....	23
1.3.1	<i>Basics of plasma physics</i>	<i>24</i>
1.3.2	<i>Methods of plasma excitation</i>	<i>25</i>
1.3.3	<i>Optical Emission Spectroscopy (OES)</i>	<i>31</i>
1.4	SiC LAYER TYPES – DEPOSITION REGIMES.....	33
1.4.1	<i>SiC layer deposition.....</i>	<i>33</i>
1.4.2	<i>Si_xC_{1-x} layer deposition</i>	<i>35</i>
2	ETCHING AND MECHANICAL BEHAVIOUR	39
2.1	ETCHING SiC.....	39
2.1.1	<i>Plasma etching of SiC.....</i>	<i>39</i>
2.1.2	<i>Plasma etching experiments</i>	<i>40</i>
2.1.3	<i>Wet chemical etching of SiC.....</i>	<i>42</i>
2.2	STRESS BEHAVIOUR	43
2.2.1	<i>Stress measurements</i>	<i>43</i>
2.2.2	<i>Stress development with deposition temperature</i>	<i>44</i>
2.2.3	<i>Stress development with annealing temperature</i>	<i>45</i>
2.3	MECHANICAL STABILITY	46
3	OPTICAL BEHAVIOUR.....	49
3.1	INTRODUCTION.....	49
3.2	REFRACTIVE INDEX.....	50
3.2.1	<i>Experiments and results.....</i>	<i>51</i>
3.3	BAND GAP TUNING	53
3.3.1	<i>Optical transmission measurements</i>	<i>53</i>
3.3.2	<i>Experiments and results.....</i>	<i>55</i>
3.3.3	<i>Photothermal deflection spectroscopy (PDS).....</i>	<i>57</i>

3.3.4	<i>Experimental setup and results</i>	59
4	ELECTRICAL BEHAVIOUR	63
4.1	ELECTRICAL CONDUCTIVITY OF AMORPHOUS SEMICONDUCTORS	63
4.2	DOPING	65
4.3	HIGH TEMPERATURE DEPOSITION	67
4.4	INFLUENCE OF ANNEALING	70
4.5	ACTIVATION ENERGY.....	71
4.6	TEMPERATURE DEPENDENT CONDUCTIVITY MEASUREMENTS.....	75
4.6.1	<i>Experimental setup</i>	75
4.6.2	<i>Metal contact-semiconductor junction (Al-SiC)</i>	75
4.6.3	<i>Results</i>	77
4.7	CONDUCTIVITY OF THE RECRYSTALLISED WAFER EQUIVALENT (REXWE).....	80
4.7.1	<i>First principle measurements</i>	80
4.7.2	<i>Advanced experimental setup: the “contows”</i>	81
4.7.3	<i>Measurements of the “contows”</i>	82
5	ANNEALING OF SIC LAYERS (HIGH-TEMPERATURE BEHAVIOUR)	85
5.1	ANNEALING CONDITIONS	85
5.1.1	<i>Temperature regions</i>	86
5.1.2	<i>Different atmospheres</i>	86
5.1.3	<i>Process time</i>	86
5.2	RE-ORGANISATION AND CRYSTALLISATION.....	87
5.2.1	<i>Layer density and refractive index</i>	87
5.2.2	<i>Network re-organisation (FTIR measurements)</i>	89
5.2.3	<i>X-ray diffraction (XRD) measurements</i>	92
5.2.4	<i>Raman measurements</i>	95
5.3	APPEARANCE OF CRACKS.....	98
5.3.1	<i>Internal stress</i>	98
5.3.2	<i>Unequal thermal expansion coefficients</i>	99
5.3.3	<i>Influence of substrate’s surface roughness</i>	100
5.3.4	<i>Blistering coming from hydrogen</i>	102
5.3.5	<i>Contamination on substrate and in SiC layer</i>	103
6	DIFFUSION IN SIC	107
6.1	BASICS OF DIFFUSION	107

6.1.1	<i>Macroscopic access</i>	107
6.1.2	<i>Diffusion constant</i>	110
6.1.3	<i>Segregation coefficient</i>	111
6.2	DIFFUSION BARRIER PERFORMANCE	111
6.2.1	<i>Experimental setup</i>	112
6.2.2	<i>Simulations</i>	116
6.2.3	<i>Results</i>	117
6.3	OUT-DIFFUSION OF BORON AT HIGH TEMPERATURES	120
6.3.1	<i>SiC on a silicon wafer</i>	121
6.3.2	<i>Characterisation methods</i>	121
6.3.3	<i>SiC as an intermediate layer</i>	122
6.3.4	<i>Simulations</i>	126
6.4	SiC AS A HYDROGEN SOURCE	127
6.4.1	<i>Hydrogen bonds in SiC layers</i>	127
6.4.2	<i>Hydrogen effusion out of Si_xC_{1-x} layers</i>	129
6.4.3	<i>Total hydrogen amount in SiC and Si_xC_{1-x} layers</i>	132
7	RECRYSTALLISED WAFER EQUIVALENT (REXWE)	135
7.1	INTRODUCTION	135
7.2	THE REXWE PROCESS	136
7.2.1	<i>Substrates and pre-treatments</i>	136
7.2.2	<i>Silicon Carbide diffusion barrier layer deposition</i>	138
7.2.3	<i>Si seeding layer deposition</i>	139
7.2.4	<i>SiO₂ capping layer</i>	139
7.2.5	<i>Zone Melting Recrystallisation (ZMR)</i>	140
7.2.6	<i>Capping layer removal</i>	142
7.2.7	<i>Epitaxial silicon layer growth</i>	143
7.2.8	<i>High throughput and large area RexWE</i>	144
7.2.9	<i>Impurities in the solar cell material</i>	146
7.3	SOLAR CELLS	147
7.3.1	<i>Crystalline silicon thin-film solar cells</i>	148
7.3.2	<i>Solar cell results</i>	154
7.4	POTENTIAL FOR THE FUTURE	159
7.4.1	<i>High Temperature Processing</i>	159
7.4.2	<i>“Alternative” Backside</i>	159

7.4.3	<i>N-type bulk</i>	160
7.4.4	<i>Ideas for RexWE modules</i>	160
8	SURFACE PASSIVATION WITH $\text{Si}_x\text{C}_{1-x}$	163
8.1	SURFACE RECOMBINATION IN CRYSTALLINE SILICON	163
8.1.1	<i>Basics</i>	163
8.1.2	<i>Fundamentals of surface passivation</i>	164
8.1.3	<i>State of the art passivation layers for c-Si surfaces</i>	167
8.1.4	<i>In-situ plasma cleaning</i>	168
8.1.5	<i>$\text{Si}_x\text{C}_{1-x}$ deposition conditions</i>	168
8.1.6	<i>Physical mechanism of $\text{Si}_x\text{C}_{1-x}$ passivation</i>	169
8.2	LIFETIME SAMPLES	169
8.2.1	<i>Quasi Steady-State Photo Conductance (QSSPC) method</i>	169
8.2.2	<i>Homogeneity and blistering</i>	171
8.2.3	<i>Thermal annealing of lifetime samples</i>	173
8.3	SOLAR CELL APPLICATION.....	174
8.3.1	<i>First solar cell applications</i>	175
8.3.2	<i>Thermal annealing of cell structures</i>	176
8.3.3	<i>Laser-fired versus lithographic defined contacts</i>	178
8.3.4	<i>Optical performance of the $\text{Si}_x\text{C}_{1-x}$ passivated solar cells</i>	180
8.4	CONCLUSIONS	181
9	FURTHER APPLICATIONS FOR PHOTOVOLTAICS	183
9.1	ETCH-STOP LAYER	183
9.2	EMITTER DIFFUSION BARRIER LAYER.....	185
9.3	ANTI-REFLECTION COATING FOR MODULE GLASSES	186
9.4	TRIBOLOGIC COATINGS WITH GOOD OPTICAL TRANSMISSION.....	186
9.5	QUANTUM DOT SUPER LATTICES.....	186
9.5.1	<i>Theory</i>	187
9.5.2	<i>Preparation of Si quantum dots in a matrix</i>	189
9.5.3	<i>Potentials of the SiC quantum dot layers</i>	190
9.6	LAYER STACKS FOR “MULTI-PERFORMANCE” APPLICATIONS	190
9.6.1	<i>SiC stack systems for solar cell processing</i>	190
9.6.2	<i>Rugate filters</i>	192
10	SUMMARY	135

11 DEUTSCHE ZUSAMMENFASSUNG	200
APPENDIX A..... CHARACTERISATION METHODS	203
A.1 ELLIPSOMETRY.....	203
A.2 FOURIER TRANSFORMED INFRARED SPECTROMETRY (FTIR).....	204
A.3 RAMAN SPECTROSCOPY	205
A.4 SECONDARY ION MASS SPECTROMETRY (SIMS)	206
A.5 QUASI-STEADY-STATE PHOTOCONDUCTANCE TECHNIQUE (QSSPC).....	207
A.6 X-RAY DIFFRACTION (XRD)	208
PUBLICATIONS	203
REFERENCES.....	213
ACKNOWLEDGEMENTS.....	225
CURRICULUM VITAE.....	227

- Figure 1.1: One possible amorphous silicon (white) and carbon (black) network with incorporated hydrogen (small black dots) a-SiC:H. 20
- Figure 1.2: Fourier transformed infrared (FTIR) absorption spectra for a typical stoichiometric SiC layer as deposited at 350°C. 21
- Figure 1.3: Auger electron spectroscopy (AES) spectra for a typical stoichiometric SiC layer as deposited at 350°C. 23
- Figure 1.4: Scheme of the dominating processes in the plasma during deposition and etching. 24
- Figure 1.5: Schematic picture of one microwave antenna used in the AK400M reactor from Roth&Rau and graphs of plasma density (n_e) and plasma temperature (T_e). These graphs have been provided by Roth&Rau. 27
- Figure 1.6: Scheme of the AK400M reactor from Roth&Rau company with the reaction chamber (left) and the load lock (right). 28
- Figure 1.7: Optical Emission Spectroscopy graphs of two deposition processes with different CH₄/SiH₄ gas flow ratios. 32
- Figure 1.8: SiC deposition rate in dependence of CH₄/SiH₄ gas flow ratio in the regime for diffusion barrier layers (SiC). 34
- Figure 1.9: C/Si ratio in dependence of the CH₄/SiH₄ ratio for the regime for diffusion barrier layers (SiC). 35
- Figure 1.10: SiC deposition rate in dependence of the microwave power in the regime of low defect generation (Si_xC_{1-x}). 36
- Figure 2.1: Etching rate on stoichiometric SiC layers in dependence of the NF₃/Ar gas flow ratio. 41
- Figure 2.2: Etching rate on stoichiometric SiC layers in dependence of the bias voltage of the RF plasma source. 42
- Figure 3.1: Refractive index n in the SiC layers in dependence of C/Si ratio (diffusion barrier regime). 52
- Figure 3.2: Refractive index n of Si_xC_{1-x} layers in dependence of microwave power (low defect regime). 53
- Figure 3.3: Bandgap determination from transmission measurement data of a SiC layer after the theory of Tauc *et al.*. 55

- Figure 3.4: Bandgap determined by transmission measurements in dependence of the C/Si content (diffusion barrier regime). 56
- Figure 3.5: Bandgap determined by transmission measurements in dependence of the microwave power (low defect regime). 57
- Figure 3.6: Electronic density of states in the amorphous SiC layer. 58
- Figure 3.7: Photo Thermal Deflection Spectroscopy (PDS) measurement setup. 59
- Figure 3.8: Absorption coefficient α (and $\alpha^{-1/2}$) in dependence of the photon energy of two stoichiometric amorphous SiC layers s3 (solid line) and s4 (open circles) both deposited in the diffusion barrier regime. 60
- Figure 4.1: FTIR data of three SiC layers deposited without additional doping gases (black), with 30 sccm of PH₃ (grey) and with 30 sccm of B₂H₆ (light grey). 66
- Figure 4.2: FTIR graph of a boron doped SiC layer deposited at 350°C (black), 500°C (grey) and 650°C (light grey). 68
- Figure 4.3: SIMS graphs of different boron concentrations in SiC layers deposited at different temperatures but with an unchanged diborane flow. 69
- Figure 4.4: Schematic diagram of the density of states distribution showing the conductivity activation energy E_{σ} , the average conduction energy E_{TR} , with respect to the mobility edges and the Fermi energy. The temperature dependence parameters γ_F , γ_G and γ_T are indicated. 72
- Figure 4.5: Temperature dependent conductivity measurements of undoped stoichiometric SiC layers during heating (black) and cooling (light grey). 76
- Figure 4.6: Temperature dependent conductivity measurements of stoichiometric SiC layers with additional diborane flow during deposition of 0 sccm (black), 20 sccm (grey) and 50 sccm (light grey). 77
- Figure 4.7: Temperature dependent conductivity measurements of stoichiometric SiC layers with no diborane flow (black) and additional diborane flow during deposition of 20 sccm (grey) and 30 sccm (light grey) and a following annealing at 650°C for 2 h. 78
- Figure 4.8: Meyer-Neldel plot of undoped, doped and annealed stoichiometric SiC layers. 79
- Figure 4.9: Schematic view of the conductive towers “contow” in a recrystallised wafer equivalent (RexWE) and the path of the electrical current (grey dart) during the measurements. 81

Figure 5.1: Relative decrease in layer thickness with annealing temperature.	87
Figure 5.2: Increase in refractive index with annealing temperature.	88
Figure 5.3: FTIR measurement of boron doped (dashed) and undoped (solid) SiC layers deposited at 350°C (black) and annealed at 550°C (dark grey), 750°C (grey) and 1050°C (light grey) for 2 h under N ₂ -atmosphere.	89
Figure 5.4: FTIR measurement of phosphorous doped (dashed) and undoped (solid) SiC layers deposited at 350°C and annealed at 550°C (dark grey), 750°C (grey) and 1050°C (light grey) for 2 h under N ₂ atmosphere.	90
Figure 5.5: FTIR measurements of undoped SiC layers deposited at 350°C and annealed at 1050°C (light grey) for 2 h under N ₂ atmosphere.	91
Figure 5.6: XRD graphs of SiC layers as deposited (black) and annealed at 1050°C (grey) and 1350°C (light grey).	93
Figure 5.7: XRD graphs of SiC layers as deposited (black) and annealed at 960°C (grey) and after the very short RexWE recrystallisation process step at >1414°C (light grey).	94
Figure 5.8: XRD graphs of SiC layers annealed under argon atmosphere at 1350°C for 2 h (black) and the RBSiC ceramic substrate (grey). “XRD_annSiC2”	95
Figure 5.9: Raman spectrum for a typical stoichiometric SiC layer as deposited (black), annealed at 600°C (grey) and annealed at 1000C (light grey).	96
Figure 5.10: Crack appearance in a 1000 nm thick SiC layer on a Cz silicon substrate after annealing at 1000°C for 1 h.	99
Figure 5.11: Expansion coefficient for differently deposited c-SiC samples and for silicon in the temperature range between 0 and 1500°C.	100
Figure 5.12: Micrograph of a 500 nm thick SiC layer (top view) deposited on a textured silicon wafer and annealed at 1050°C with no visible cracks at all.	101
Figure 5.13: Micrograph of a SiC layer as deposited on a silicon substrate with occurring hydrogen blisters.	102
Figure 5.14: Micrographs of SiC layers as deposited on different metals such as Al (left), Ti (middle) and Ni (right) and occurring blistering effects (black dots).	103
Figure 5.15: Micrograph of a SiC layer as deposited on a silicon substrate and occurring blistering along tweezers traces.	104
Figure 6.1: Concentration profile before and after annealing for different boundary conditions.	110

-
- Figure 6.2: Setup of the multi layer stack for the diffusion experiments with the implanted iron atoms in the SiC layer. 113
- Figure 6.3: Simulated implantation profile (with SRIM) of Fe in SiC with penetration depth and full width half maximum (FWHM) of the profile for different acceleration energies. 115
- Figure 6.4: Simulated implantation profile of Fe in SiC (with SRIM) and the profile measured with SIMS. 118
- Figure 6.5: SIMS measurements of the iron concentration profiles in the layer stack before (black square) and after annealing at 1200°C for 5 min (dark grey circle), 15 min (grey triangle) and 60 min (light grey triangle). 119
- Figure 6.6: SRP measurements of the Si (left)/SiC (black vertical line)/Si (right) layer stack as deposited (black) and after an annealing procedure at 1350°C for 1 h (grey). 123
- Figure 6.7: SIMS measurements of the Si/SiC/Si layer stack after recrystallisation and an additional annealing procedure at 1250°C for 10 min. "RW202..." 124
- Figure 6.8: SIMS measurements of the Si/SiC/SiC/Si layer stack before (black) and after annealing (grey) at 1250°C for 30 min. 125
- Figure 6.9: FTIR measurement of boron doped (dashed) and undoped (solid) SiC layers deposited at 350°C and annealed at 550°C (dark grey), 750°C (grey) and 1050°C (light grey) for 2 h under N₂-atmosphere. 128
- Figure 6.10: Three different rear side passivation structures A (left), B (middle) and C (right) to compare hydrogen effusion from the passivation layer stack into the multi crystalline silicon bulk. 130
- Figure 6.11: Carrier density imaging (emission mode) for the three different rear side passivation structures A (left), B (middle) and C (right) to compare hydrogen effusion from the passivation layer stack into the multi crystalline silicon bulk. 131
- Figure 7.1: Pre-treatment procedures for the RBSiC ceramic substrate before introducing it into the RexWE process. 138
- Figure 7.2: Principle of zone melting recrystallisation (ZMR) with linear halogen lamp as the heating source. 140
- Figure 7.3: Melting zone (top view) of the silicon seeding layer on a RBSiC ceramic substrate. 141

-
- Figure 7.4: Micrographs of different melting zones and the resulting silicon seeding layers recrystallised at a scan speed of 10, 50 and 100 mm/min. 142
- Figure 7.5: Micrographs of three epitaxial layer surfaces with different pre-cleaning procedures. 143
- Figure 7.6: Large area recrystallised wafer equivalent (RexWE) on RBSiC ceramic substrate with an area of 200x200 mm². 146
- Figure 7.7: Depth resolved Glow Discharge Mass Spectrometry (GDMS) measurements of Fe, V, Co from the Si bulk material through the SiC barrier layer into the RBSiC ceramic substrate. 147
- Figure 7.8: Solar cell processed on a Recrystallised Wafer Equivalent (RexWE) with integrated back surface field (BSF) and diffuse rear-reflector. 148
- Figure 7.9: Necessary process adaptations for solar cell processing on RexWEs with a RBSiC ceramic substrate. 149
- Figure 7.10: Micrograph of a KOH textured (right) and a partly plasma textured (left) solar cell surface on a Recrystallised Wafer Equivalent. 150
- Figure 7.11: Micrograph of a photolithographic (left) and a evaporated (right) front grid on a Recrystallised Wafer Equivalent on RBSiC ceramic substrate. 152
- Figure 7.12: Inhomogeneities of the anti-reflection coating due to layer residuals on two different solar cell surfaces (brighter areas). 153
- Figure 7.13: Simulation data (PC1D) of crystalline silicon thin-film cells showing the efficiency in dependence of the solar cell thickness for different layer qualities (effective diffusion length of the minority carriers). 154
- Figure 7.14: EQE, reflection and IQE in dependence of wavelength for an untextured (left) and a textured (right) solar cell. 156
- Figure 7.15: *EQE* of an untextured solar cell (1 cm²) measured by the spectrally resolved light beam induced current method. 157
- Figure 8.1: Scheme of a simple model for the recombination effect with unpassivated (left) and passivation through saturated defects (right) on the silicon solar cell's rear-side. 165
- Figure 8.2 Scheme of a simple model for the recombination effect with no passivation (left) and passivation through a field effect (right) on the silicon solar cell's rear side. 166

- Figure 8.3: Injection dependent effective lifetime measured by QSSPC of a phosphorus doped $a\text{-Si}_x\text{C}_{1-x}$ passivation layer on a $1\ \Omega\text{cm}$ FZ Si wafer. Especially in the higher injection levels the lifetime is limited by Auger recombination. 170
- Figure 8.4: Histogram of effective lifetime distribution on a $4''$ silicon wafer passivated with $\text{Si}_x\text{C}_{1-x}$ with Gaussian distribution fitted to the data. 172
- Figure 8.5: Two CDI measurements to show the homogeneity of the layer quality and some minor surface problems coming from tweezers prints, surface contamination or blistering effects. 173
- Figure 8.6: Scheme of the so called PERC/LFC structure with a $\text{Si}_x\text{C}_{1-x}$ passivation layer on the rear-side. 175
- Figure 8.7: Schematic sketch of the solar cell test structure (without front-side texturisation and contacts) used for the firing experiments. 176
- Figure 8.8: Rear-side of a PERC solar cell structure with a evaporated contact (left) and a laser fired contact (right). 179
- Figure 9.1: Micrographs of a stoichiometric SiC layer on a FZ silicon before (left) and after (right) exposure to 50% concentrated HF. 184
- Figure 9.2: Schematic sketch of the band structure of crystalline silicon (a) and a silicon quantum dot (b: quantum well and c: direct absorption). 188
- Figure 9.3: Silicon rich $\text{Si}_x\text{C}_{1-x}$ and stoichiometric layer stacks (left) form Si quantum dots in a stoichiometric matrix (right) after thermal annealing. 189
- Figure 9.4: Process chain frequently used for industrial silicon solar cells. 191
- Figure 9.5: Discrete refractive indices characteristic as it was assumed for first simulations. 194
- Figure 9.6: Simulated transmission behaviour of 10 SiC layer stacks with a sinusoidal refractive index. 195

1 AMORPHOUS SILICON CARBIDE

Silicon and Carbon are the basic elements in the evolution of life on this planet. Carbon, which is the basic element for biological life, and silicon which was mainly responsible for the technical evolution in the 20th century through its dominating role in microelectronics (and photovoltaics) are therefore two of the most essential elements. Because of that the creation of a molecule out of these two elements implies a special thrill. In this chapter I will give a short introduction to the physical basics of SiC. After that I will present the method we used for the deposition of our layers, which was plasma enhanced chemical vapour deposition (PECVD). Although this method is widely used in laboratories and production facilities, the special features of our two-source system should be described here. At the end of the chapter some characterisations of the deposited layer and the two principal deposition regimes will be discussed.

1.1 Introduction

Silicon Carbide is the only stable compound in the Si-C equilibrium system at atmospheric pressure [1]. The only occurrence of SiC in nature is found in meteorites. Therefore, SiC cannot be mined but must be manufactured with elaborate furnace techniques. In its polycrystalline forms, SiC has long been a well proven material in high-temperature, high-strength and abrasion resistant applications like ceramics. Silicon Carbide as a semiconductor is a more recent discovery, but interest and demand are rising enormously. The amorphous phase of SiC is a relatively new subject of investigation. Nevertheless, one can already find amorphous SiC layers in silicon hetero structures [2-4], as anti-reflection coatings [5] and in microelectronics [6-8]. Furthermore amorphous SiC appears as protective coatings against corrosion

[9], moisture [10], etching [11] and abrasion [12] or for bio-molecular [13] and medical [14] applications.

1.2 Amorphous Structure of SiC

Amorphous networks still raise numerous questions concerning the physical basic understanding. Especially amorphous tetrahedral alloys seem to be a very complex system. In the case of a compound material, as it is the case for SiC, the situation gets even more complicated. In this section I will give some general information about SiC and will afterwards focus on the SiC layers developed throughout this work.

1.2.1 The tetrahedral network

As far as we know from literature [15-17] the deposition method, the precursor gases, the hydrogen content and the C/Si fraction have a very strong influence on the network of an amorphous material. To make things a little easier I will focus my explanations in this basic chapter on stoichiometric amorphous SiC layers which were deposited by plasma enhanced chemical vapour deposition from silane (SiH_4) and methane (CH_4).

Table 1.1: SiC relevant bonds and bond lengths.

bond	length [10^{-1} nm]	bond	length [10^{-1} nm]
C–C	1.54	C=C	1.33
C–H (sp^3)	1.09	C=C (graphite)	1.42
C–Si	1.87	C≡C	1.21
Si–Si (in c-Si)	2.35	Si–H	1.48

First of all it can be stated that amorphous tetrahedral alloys will be more disordered than e.g. amorphous silicon since chemical disorder is added to the inherent structural

disorder. These structural disorders will be even more pronounced if the coordination geometries of the two atoms are different. This is especially the case for increasing difference in bond length (see Table 1.1).

From the ratio of the covalent radii $r_C/r_{Si}=0.66$ (see Table 1.2) we can conclude that the network models, which have been developed for amorphous silicon, are not suitable to describe amorphous SiC networks. They are expected to be much more disordered. Silicon cannot form homo nuclear $p\pi$ -bonds. If carbon atoms form homo or hetero nuclear $p\pi$ -bonds in the alloy (isolated double or triple bonds or resonant π -bonding systems) structural disorder will increase considerably [17].

Table 1.2: Covalent radii and electronegativity of the atoms appearing in the SiC network [15].

atom	radius [10⁻¹ nm]	electronegativity
C	0.77	2.50
Si	1.17	1.74
H	0.28	2.20

For a statistical distribution of atoms in the alloy, there will always be some homo nuclear bonding between majority atoms. Since C-C bonds are thermodynamically more stable than Si-Si and Si-C bonds, it is probable to find C-C bonds already in a material with a C/Si fraction slightly higher than 1. At higher carbon concentrations clusters may be formed which are expected to contain graphitic configurations. Raman measurements in chapter 5 will show the C-C bonds and their development (although at a very low amount) with annealing temperature in our stoichiometric SiC layers.

If we consider a continuous random network, there must be a maximum disorder somewhere between pure amorphous silicon and a pure amorphous carbon network. Since the Si-Si and the C-C bonds stability are different this maximum is not to be expected at a ratio C/Si of 1.

During film deposition, the amorphous network relaxes, especially at higher temperatures, in order to minimise the free energy. Nevertheless, a residual distortion of coordination geometry always remains in an amorphous network. This residual

distortion will be different for carbon and silicon atoms since the coordination behaviour of carbon is much more flexible.

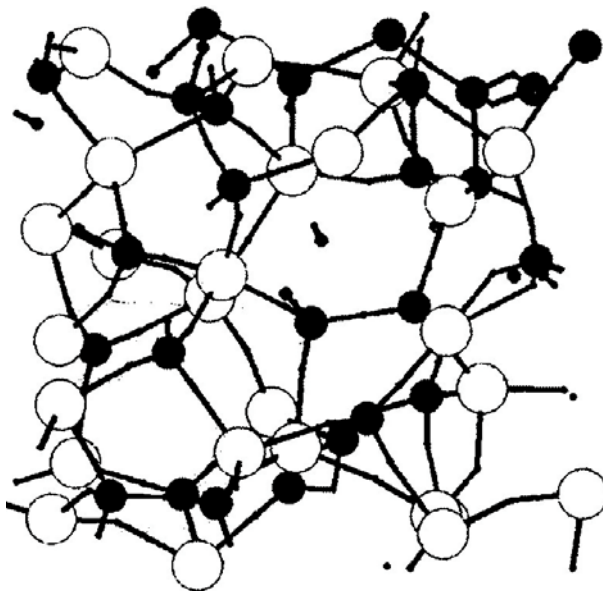


Figure 1.1: One possible amorphous silicon (white) and carbon (black) network with incorporated hydrogen (small black dots) a-SiC:H.

In Figure 1.1 one can see a ball and stick model of a $C_{26}Si_{26}H_{12}$ sample with silicon (white), carbon (black) and hydrogen (grey) atoms [17]. The atom sizes are scaled according to the covalent radii. This sketch shows impressively the complexity of a SiC network.

1.2.2 Hydrogenated SiC

When we grow SiC layers from methane and silane at temperatures below 600°C , a significant amount of hydrogen will be found in the amorphous network. The C-H bonds are much more stable than the Si-H bonds which should have consequences for the thermal stability of the films with respect to hydrogen effusion (see chapter 5). Furthermore carbon atoms are expected to be more hydrogenated than silicon atoms. Due to the different electronegativities of silicon and carbon (see Table 1.3), Si-H bonds are strengthened if the silicon atom is bonded to a carbon atom (on the other hand the C-H bond is weakened).

Table 1.3: Bond energies in kJ/mol at 25°C [15].

	H	C	Si
H	436	416	323
C		356	301
Si			226

1.2.3 Vibrational spectroscopy (Infrared spectra)

A very powerful method of quantification and identification of bonds in amorphous layers is the fourier transformed infrared spectroscopy (FTIR), which will be described in Appendix A. Characterization data of amorphous SiC layers with FTIR can be found in numerous publications [15,18-20].

As the silicon-carbon bond is partly ionic, strong infrared absorption lines are expected from the SiC vibrations. Bullo *et al.* [15] published a comprehensive list for possible absorption frequencies in SiC layers.

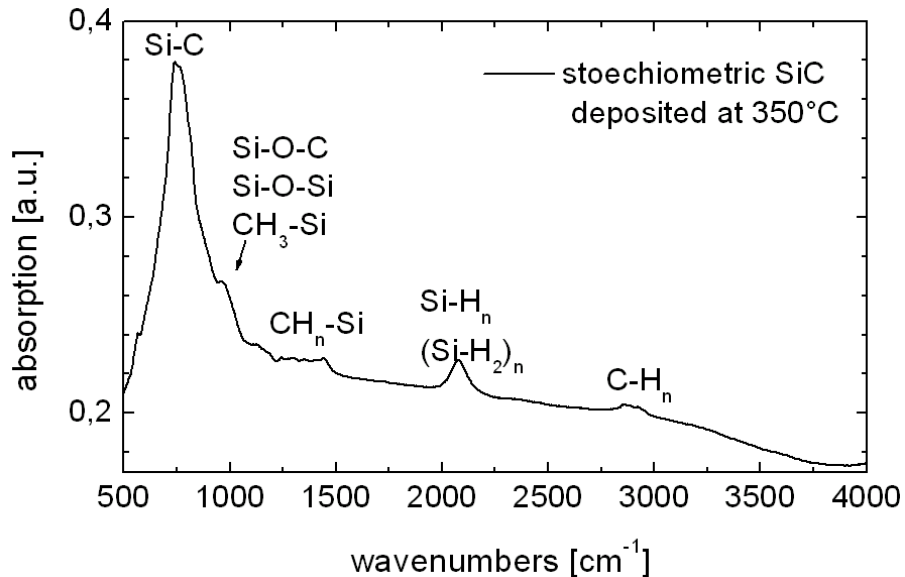


Figure 1.2: Fourier transformed infrared (FTIR) absorption spectra for a typical stoichiometric SiC layer as deposited at 350°C.

Figure 1.2 shows a characteristic FTIR absorption spectrum of a SiC layer deposited at 350°C in our plasma reactor at Fraunhofer ISE. The FTIR spectra were recorded with a Bruker IFS113V spectrometer (resolution 6 cm⁻¹). The focus of our interest is

the existing network in SiC layers as deposited. In the wavelength region from 2850 to 2960 cm^{-1} several C-H_n absorption peaks can be found. The vibration modes result from stretching movements (symmetric or anti-symmetric) of the molecules. In the wavenumber region from 2000 to 2140 cm^{-1} Si-H related absorption bands can be observed. Here again stretching modes are activated. From 1250 to 1470 cm^{-1} absorption bands related to Si-CH_n vibrations are visible though not very pronounced. If we go more into detail a very small but nevertheless visible signal can be found at 1300 cm^{-1} . This is an evidence for a small amount of C-C bonds in our SiC layers. For a more detailed discussion about this C-C bond see chapter 5. Some oxygen related vibration modes in the region of 960 cm^{-1} are possibly present but cannot be separated from the Si-CH₃ signal. The dominant absorption band can be found between 740 and 770 cm^{-1} and is doubtlessly a SiC absorption peak. The form of the peak indicates different overlapping signals. It is almost impossible to find out more about the kind of SiC bonds with this method. However we can learn from the data that there are still CH₄ and SiH₄ related molecules in the network of the layer as deposited which probably could not be broken up in the plasma process. This could be due to a too low energy coupled into the plasma or to a too high growth rate which does not leave the molecules enough time for a sufficiently high amount of collisions. The FTIR spectra presented in Figure 1.2 were measured at an undoped and stoichiometric SiC layer with a thickness of ≈ 200 nm. In chapter 5 I will present more absorption spectra recorded with FTIR and discuss their development with temperature into detail.

1.2.4 Silicon and carbon content

One of the most effective and accurate ways to get information about relative silicon and carbon content in SiC layers is auger electron spectroscopy (AES) [21].

The measurement in Figure 1.3 was done at a ≈ 500 nm thick, undoped SiC layer deposited at 350°C. One can see that the silicon and the carbon contents are both identical (50%) throughout the whole layer thickness. Simultaneously to the silicon and the carbon content oxygen and nitrogen are also detected, but are not plotted in this graph. The signals are both below an intensity of 1%. Only the interface between SiC layer and Si substrate shows a slightly increased oxygen signal due to the native

oxide (≈ 3 nm) which can be found on every silicon substrate after a short exposure to atmosphere.

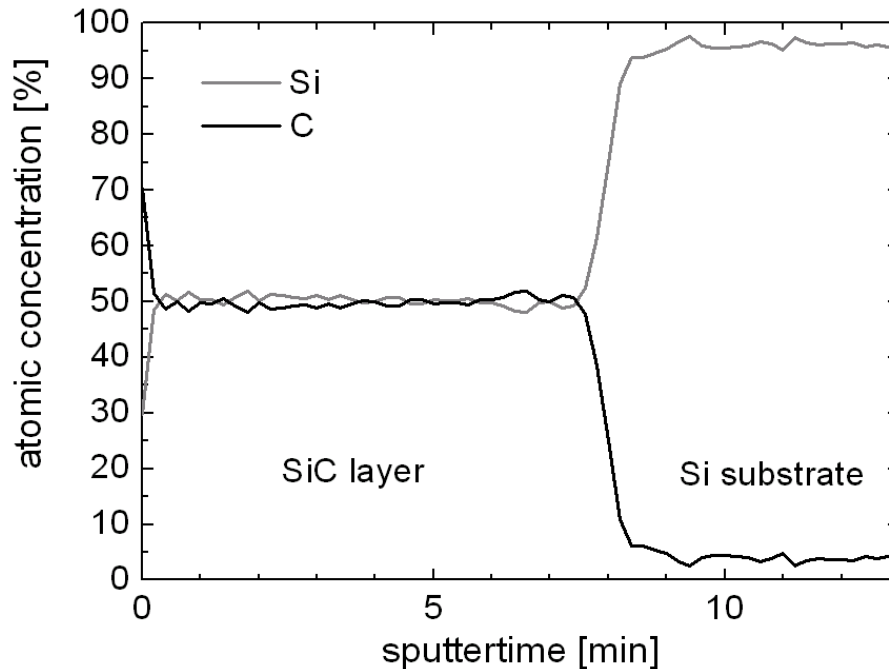


Figure 1.3: Auger electron spectroscopy (AES) spectra for a typical stoichiometric SiC layer as deposited at 350°C.

1.3 Plasma Enhanced Chemical Vapour Deposition (PECVD)

To deposit layers with atoms from different precursor gases one has to break the molecular bonds to rearrange them again. Basically there are two methods of doing that. The first one supplies the necessary energy by heat as it is used in thermal chemical vapour deposition. Although this is a powerful and very frequently used method the high temperature involved and several other peculiarities (e.g. whisker growth) can cause problems [22]. The second possible deposition method is to use energy which does not result from heat to break the precursor bonds. Several of these deposition methods for SiC can be found in literature [23-30]. Plasma enhanced chemical vapour deposition (PECVD) uses electrical power to enable lower deposition temperatures. In microelectronics and photovoltaics PECVD has been for many years now a standard procedure to deposit amorphous SiO₂ or SiN_x layers.

Plasma basics, different excitation sources and the reactor used for this work (AK400M from Roth&Rau) will be discussed in the following chapter.

1.3.1 Basics of plasma physics

All basic information about plasma physics in this chapter is mainly taken from Lieberman *et al.* [31]. A plasma is a collection of free charged particles moving in random directions that is, on the average, electrically neutral. In this present project we did work with weakly ionised plasma discharges, which are plasmas having the following features: (1) they are driven electrically, (2) charged particle collisions with neutral gas molecules are important, (3) there are boundaries at which surface losses are important, (4) ionisation of neutrals sustains the plasma in the steady state and (5) the electrons are not in thermal equilibrium with the ions. These quasineutral plasmas are joined to wall surfaces across thin positively charged layers called sheaths.

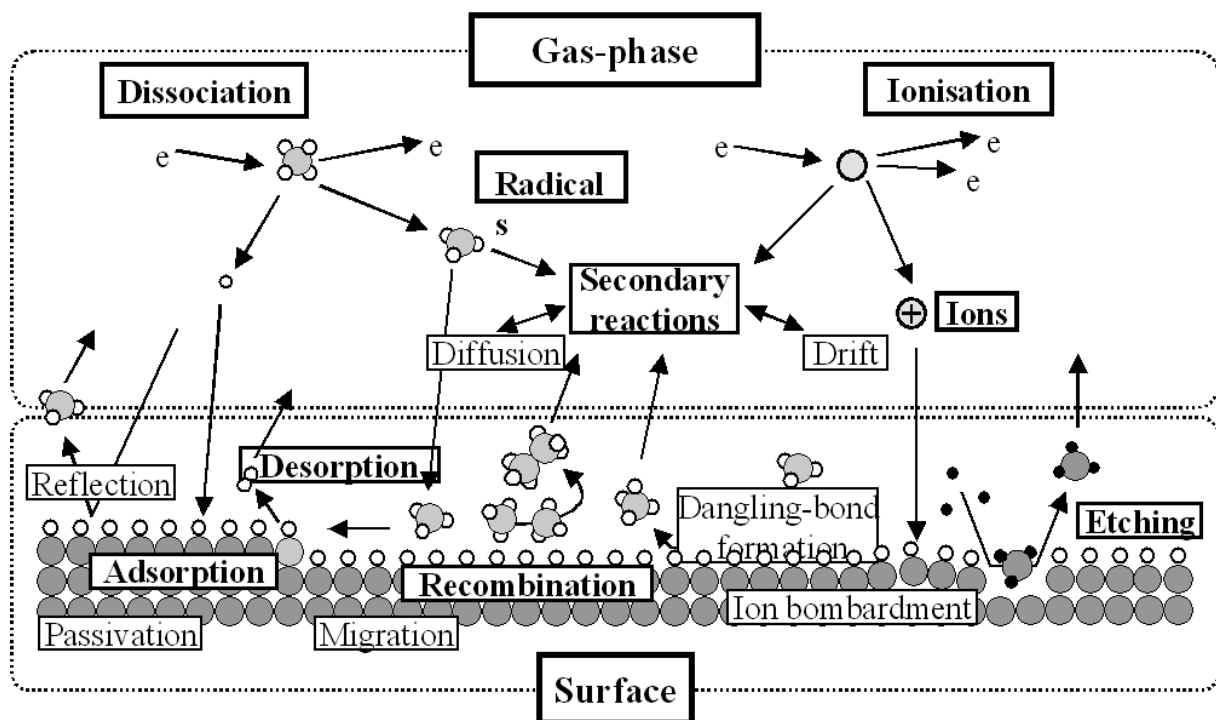


Figure 1.4: Scheme of the dominating processes in the plasma during deposition and etching.

Plasmas are often called the fourth state of matter. As we know, a solid substance in thermal equilibrium generally passes into a liquid state as the temperature is

increased at a fixed pressure. The liquid changes into gas as the temperature is further increased. At a sufficiently high temperature, the molecules in the gas decompose to form a gas of atoms that move freely in random directions, except for infrequent collisions between atoms. If the temperature is further increased, the atoms decompose into freely moving charged particles (electrons and positive ions) and the substance enters the plasma state. This state can be characterised by a common charged particle density $n_{electron} \approx n_{ion} \approx n$ in particles/m³ and, in equilibrium, a temperature $T_{electron} = T_{ion} = T$.

In Figure 1.4 one can find an overview of the processes in a plasma during deposition and etching. The two important regions, the gas-phase and the surface, are encircled. Even this simplified sketch shows the complexity of reaction mechanisms in the plasma. Beside ionisation and dissociation secondary reactions are dominating the reactions in the gas-phase. In the surface region many possible reactions are competing. These reactions are in some kind of equilibrium with one dominating process. Just a small change in process parameters can therefore change a deposition to an etching process.

1.3.2 Methods of plasma excitation

In this chapter I will go into two different methods of plasma excitation and their characteristics. In principle they differ in excitation sources which work at different frequencies and can achieve different plasma states (see Table 1.4).

Table 1.4: Classification of discharges by excitation-frequency [Roth&Rau].

	frequency [kHz]	pressure [Pa]	ionisation [%]	electron density [cm ⁻³]	electron energy [eV]	dissocia- tion	sheaths potential [V]
MW Discharge	2.45 GHz	1 - 10000	0.1 - 1	10 ¹⁰ - 10 ¹²	1 - 10	high	< 50
RF Discharge	13.56 MHz	0.1 - 1000	0.1 - 1	10 ¹⁰ - 10 ¹²	1 - 5	moderate to high	100 - 1000

1.3.2.1 Radio-frequency plasma

Capacitive driven radio-frequency (RF) discharges are commonly used for material processing. The discharge consists of two electrodes separated by a spacing l and is driven by a RF power source. In the AK400M reactor used in this work one electrode is the substrate plate made out of graphite and the second electrode is the reactor's vessel itself. To make comparison with other plasma reactors easier all RF (13.56 kHz) power densities stated in this work and will be given in mW/cm^2 as it is common in plasma physics. They are calculated from the supplied power divided by the plate's area ($20 \times 30 \text{ cm}^2$).

The operation of capacitive driven discharges is reasonably well understood. The mobile plasma electrons, responding to the instantaneous electric fields produced by the RF driving voltage, oscillate back and forth within the positive space charge cloud of ions. The massive ions respond only to the time-averaged electric fields. Oscillation of the electron cloud creates a sheath region near the graphite plate electrode that contains positive charge when averaged over an oscillating period, i.e., the positive charge exceeds the negative charge system, with the excess appearing within the sheaths. This excess produces a strong time-averaged electric field within each sheath directed from the plasma to the electrode. Ions flowing out of the bulk plasma near the centre of the discharge can be accelerated by the sheath fields to high energies as they flow to the substrate, leading to energetic-ion enhanced processes.

1.3.2.2 Microwave plasma

The limitations of RF diodes and their magnetically enhanced variants have led to the development of a new generation of low-pressure, high-density plasma sources. An additionally common feature of these sources is the coupling of the microwave power to the plasma across a dielectric window, rather than direct connection through an electrode in the plasma. In our case the energy was coupled to the plasma by electromagnetic waves generated by two copper antennae inside two quartz tubes. This non capacitive power transfer is the key to achieve low voltages across all plasma sheaths at electrode and wall surface. When operating in the Giga-Hertz (GHz) range (see Table 1.4) the ions can be, because of their mass inertia, considered as resting. The electrons absorb energy through electromagnetic waves which lead, in subsequent collisions with the reactive gases, to ionisation and excitation processes.

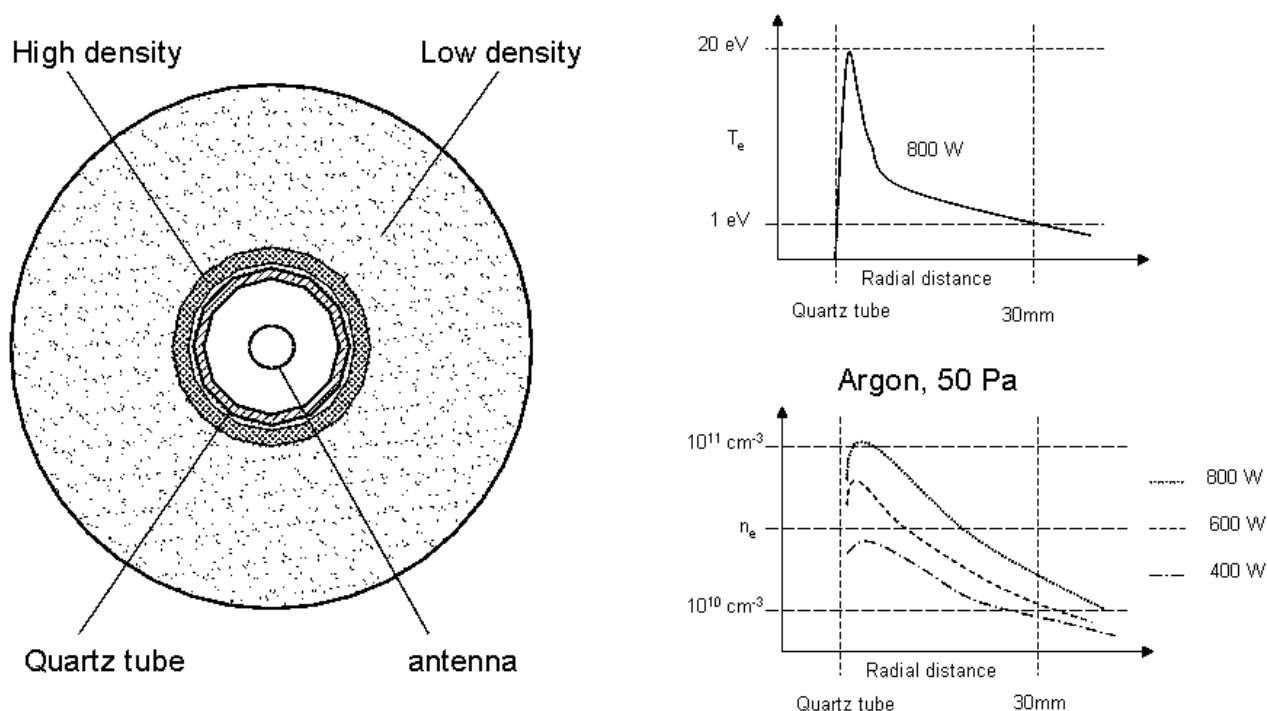


Figure 1.5: Schematic picture of one microwave antenna used in the AK400M reactor from Roth&Rau and graphs of plasma density (n_e) and plasma temperature (T_e). These graphs have been provided by Roth&Rau.

The microwave antenna used in our plasma reactor and corresponding technical data are shown in Figure 1.5. The plasma density is extremely high in the nearest neighbourhood of the quartz tube and decreases very fast with the distance. To enlarge the deposition area two of these sources were used in our reactor.

1.3.2.3 AK400M reactor

The AK400M reactor was developed to investigate deposition and plasma etching on a laboratory scale. The maximum deposition area of $200 \times 300 \text{ mm}^2$ and the reactor's close relation to industrially used reactors enables to work on most photovoltaic applications (standard silicon cell size $156 \times 156 \text{ mm}^2$). In connection with this PhD thesis additional features have been developed in cooperation between Roth&Rau company (Germany), which built the reactor, and our group at Fraunhofer ISE. Especially adaptations for high temperature deposition (up to 800°C), which is quite unusual for a PECVD reactor, like radiation shields had to be developed and several occurring problems, like e.g. a RF contact able to withstand 1000°C , had to be solved. The reason why we wanted to do our depositions at high temperatures was to

enhance hydrogen effusion and make the layer as deposited sufficiently conductive. For details concerning this subject see chapter 4.

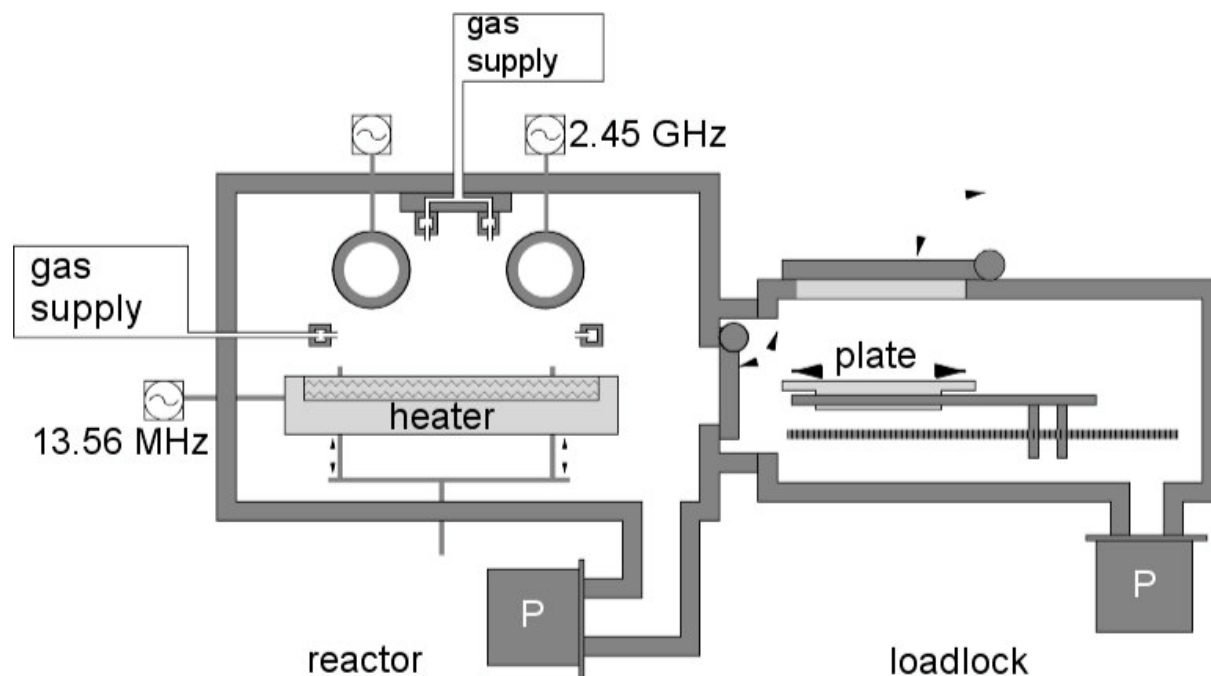


Figure 1.6: Scheme of the AK400M reactor from Roth&Rau company with the reaction chamber (left) and the load lock (right).

As shown in Figure 1.6 the AK400M reactor had a load lock flanged on the reactor chamber. That helped to achieve good vacuum conditions ($\approx 10^{-2}$ Pa) inside the reactor chamber. After having the chamber opened for means of mechanical cleaning or other maintenance work it took us 24 h to remove most of the humidity which was adsorbed inside the chamber. This observation shows the importance of a load lock system. To avoid external contamination a flow box was constructed above the load lock door.

Excitation with two sources

One exceedingly important advantage of this reactor are the two plasma sources. Thus, the deposition parameters concerning the plasma, like for example the splitting up of gas-molecules or the deposition rate, can be influenced almost independently. Different from e.g. a parallel plate RF reactor the amount of radicals from gases with a different binding energy can be tuned without increasing surface damage. In the following chapters the influence of the two generators on the layer performance will

be discussed into detail. To complement the information about our plasma sources it has to be mentioned, that the maximum power density is 1000 mW/cm^2 for the RF source. For the MW generator it is difficult to specify a power density which could be compared to other reactors. The two copper antennae with a length of 0.5 m can be supplied with maximum power of $2 \times 2000 \text{ W}$.

Deposition

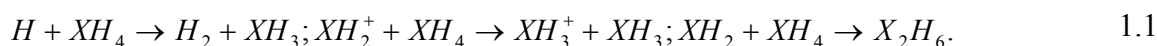
The main problem that has to be solved when using more than one precursor gas are the mostly differing binding energies of the gas molecules. In our project, where we used methane (CH_4) and silane (SiH_4) as precursor gases, the difference in stability was quite pronounced.

Table 1.5: Ionisation values in eV and appearance potentials for radicals and molecules from SiH_4 , CH_4 and H_2 [32].

parent neutral	CH_4^+	CH_3^+	CH_2^+	CH	C^+
CH_4	12.6	14.3	15.1	22.2	25
CH_3		9.8	15.1	17.7	25
CH_2			10.3	17.4	20.2
CH				13.0	20.3
C					16.8
parent neutral	SiH_3^+	SiH_2^+	SiH	Si^+	
SiH_4	12.0	11.5	13.7	12.5	
SiH_3	8.0	12.1	9.7	13.0	
SiH_2		9.0	11.2	9.9	
SiH			7.9	11.2	
Si				8.15	
parental neutral	H_2^+	H^+			
H_2	15.43	18.1			
H		13.6			

In Table 1.5 the ionisation values which are needed to generate the different gas radicals from silane, methane and hydrogen can be found. It is quite obvious that the CH_4 related species are much harder to break than the SiH_4 related ones. Although

the pure SiH₄ and CH₄ plasma chemistries are well known there is still little information on the ion and radical flux composition in gas-mixture discharges by in situ plasma diagnostics. In chapter 1.3.3 the need for such an investigation will be pointed out briefly in one example. Nevertheless, Perrin *et al.* [33] drew some general conclusions from their experiences with XH₄ (CH₄, GeH₄ and SiH₄) species: (1) The dominant neutral (respective ionic) fragments of XH₄ molecules by electron impact are H (resp. H⁺) and XH₃ and XH₂ (resp. XH₃⁺ and XH₂⁺). (2) The relative concentration of XH₃ and XH₃⁺ increases with the pressure due to fast secondary reactions such as



No primary decomposition of CH₄ by electron impact in low power SiH₄-CH₄ discharges takes place. Methyl radicals CH₃ or SiH_nCH₃ species are generated by secondary reactions of SiH₄ primary fragments. (3) The relative XH₃ concentration is however limited in high power discharge by bi-radical recombination



(4) The gas phase polymerization of positive and negative ions and radicals eventually leads to powder formation at high pressure. (5) The ion to radical fraction decreases as the pressure increases, which explains why ion bombardment (surface damage) is mostly effective in low pressure discharges.

As SiC is a wide bandgap semiconductor and a thermally activated electrical conductivity of such an intrinsic layer would be difficult, we doped our SiC layers. For this reason phosphine (PH₃) and diborane (B₂H₆) highly diluted in H₂ (<1%) were added to the precursor gases. As these doping gases were quite difficult to handle in respect to their toxicity an alternative doping with nitrogen (N₂) diluted in hydrogen was tested. To increase the collision rate and to stabilise plasma argon (Ar) was also added to the deposition gases. Although reported from Pham *et al.* [34] no influence of doping gas concentration on deposition rate could be observed during my investigations.

Etching

For cleaning the reactor walls and the graphite plate, reactive etch gases such as nitrogen trifluoride (NF_3), oxygen (O_2) and dinitrogen oxide (N_2O) were also connected to the plasma reactor. As the etching of SiC layers on samples was not our initial aim we tried to optimise the etching rate at the microwave quartz tubes and the surrounding reactor parts. This reactor cleaning was necessary to extend the deposition periods and made the necessity of mechanical cleaning very seldom. To concentrate the etching process to the quartz tubes and the radiation shield above and to increase the etching rate we worked at pressures between 10 and 30 Pa. In general it can be reported that etching of amorphous stoichiometric SiC seems to be very difficult. Details concerning etching of stoichiometric SiC layers in general and in the AK400M reactor in particular will be discussed in chapter 2.

Another etching method developed in our reactor was an iron sputtering like process. Therefore we used the non-reactive gases Ar and H_2 and kind of sputtered very carefully the substrate's surface. This cleaning process was e.g. used very successfully for in situ surface cleaning before depositing the surface passivation layers (see chapter 9).

Different gas inlets

Another feature of the AK400M reactor was the possibility to choose the gas inlet position in the reactor. Some process gases like CH_4 could be introduced through a gas pipe which was positioned between the microwave quartz tubes. The other position was a ring gas pipe inlet around the deposition area (graphite plate). This additional process parameter had of course strong influence on the plasma reactions and in consequence on layer composition and assembly. The re-etching (cleaning) of the quartz tubes for example could be significantly enhanced by introducing NF_3 through the gas inlets between the tubes.

1.3.3 Optical Emission Spectroscopy (OES)

One possibility to get direct access to the complex processes in the plasma is optical emission spectroscopy (OES). One main advantage of this and all the other optical methods is that they do not disturb the process itself. Especially OES uses emitted electromagnetic waves which are radiated by the plasma [31]. The basic processes are absorption and emission of photons. The transition from one excitation level to the

other can occur spontaneously or can be induced from outside. In both cases the energy difference E_{kl} between two levels is radiated.

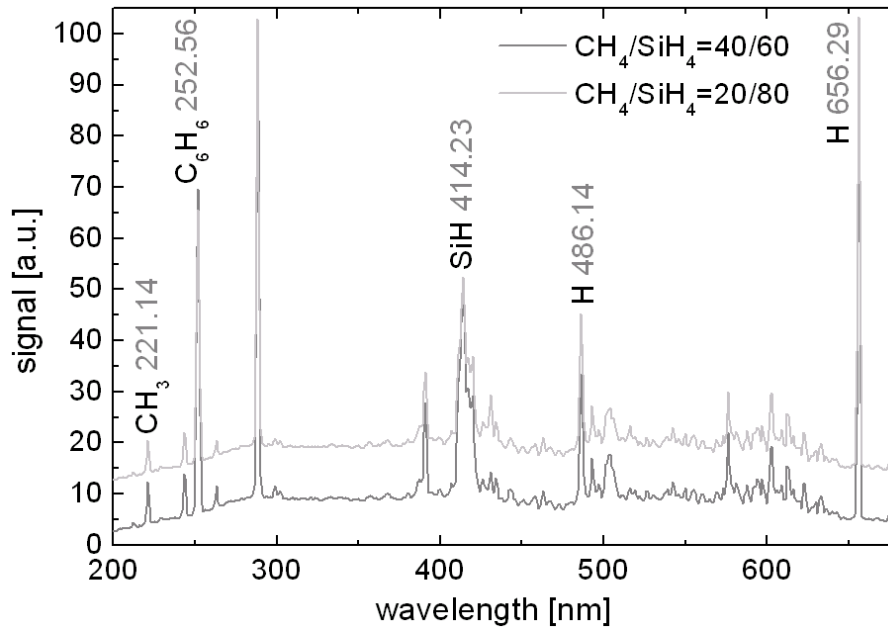


Figure 1.7: Optical Emission Spectroscopy graphs of two deposition processes with different CH_4/SiH_4 gas flow ratios.

To demonstrate the numerous advantages of an OES tool two spectra recorded during SiC deposition in our plasma reactor are presented in Figure 1.7. The difference between the two processes was the SiH_4/CH_4 gas ratio in the reaction chamber. What we can learn from the emission measurements of the plasma is, that the process with the higher CH_4 ratio (grey) has a much higher peak at 252.56 nm (C_6H_6) and an insignificantly higher one at 221.14 nm (CH_3). These results do not seem to be surprising and could have been guessed without any spectroscopic analysis. The process with the higher SiH_4 ratio (light grey) on the other hand side has even a smaller peak at 414.23 nm which is correlated to SiH. The whole graph has been shifted to avoid overlapping of the data. A significant increase in height of the signal can also be found at 656.29 nm which is correlated to a higher H content. This is rather surprising and shows that, although pressure (5 Pa), total gas flow (130 sccm) and temperature (350°C) during deposition are the same, it is quite difficult to establish a correlation between precursor gas ratios and the amount of radicals in the plasma.

1.4 SiC Layer Types – Deposition Regimes

The motivation to start with amorphous SiC at Fraunhofer ISE was to develop an electrically conductive diffusion barrier layer. We could find a suitable set of parameters for this purpose which resulted in a stoichiometric SiC layer (all the already presented measurements in this chapter have been deposited in this regime). Throughout this work I will display this stoichiometry through non-existing indices (as many silicon as carbon atoms). This deposition regime is characterised by high growth rate and homogeneity which is an important premise because achieving high throughput is always a most important cost factor. The initially found “standard” SiC for diffusion barrier applications is deposited achieving the following performance: a growth rate of more than 1 nm/s and a layer thickness variation of $\pm 1\%$ on an area of 200x300 mm².

In a second development layers for surface passivation applications on silicon wafers have been developed. The set of parameters here is optimised on low surface damage and lattice match with crystalline silicon. This layer will be labelled in this thesis as Si_xC_{1-x} because the C content was generally far below 50%.

Throughout this whole thesis, as far as it is not explicitly mentioned, I will write about one of these two standard layers. I will show in this work, that not the C/Si ratio alone is responsible for layer performance and that one cannot speak of the “Silicon Carbide” layer. The labelling with indices is one attempt to distinguish deposition regimes in a not too confusing way.

1.4.1 SiC layer deposition

The SiC layer deposition for diffusion barriers has a very high growth rate and a good homogeneity. To achieve such results in a plasma deposition process the pressure has to be relatively low (≈ 5 Pa). In such pressure regions the free path length is high and the atoms and radicals can reach high impulses between two collisions. This widens the reaction cross sections and reduces the local dependence of processes. That means for example that the locally differing power densities of the microwave plasma sources smear and do not lead to inhomogeneous deposition conditions. The power of the RF source is in the region of 250 mW/cm², which enables the high deposition rate and the high amount of cracking of the precursor gases. The power for the microwave source is in the region of 2x1000 W. An increasing of the MW power leads to an

increasing reflected power. In the fine tuned adjustment this is a clear signal that more power cannot be coupled into the plasma through the microwave source and would therefore have no effect on the plasma reaction processes.

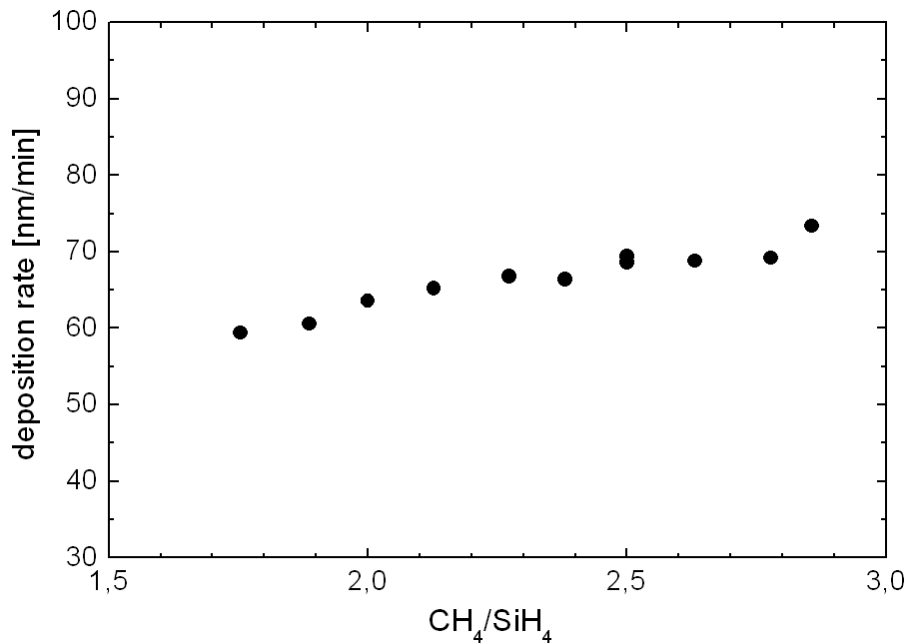


Figure 1.8: SiC deposition rate in dependence of CH₄/SiH₄ gas flow ratio in the regime for diffusion barrier layers (SiC).

Although the standard layer is deposited at a gas flow ratio of CH₄/SiH₄=1.5 several other ratios have been tested. As can be seen in Figure 1.8 the deposition rate does not depend very strongly on the changing of gas flows which is another advantage of this deposition regime (see chapter 3). The deposition takes place at a temperature of 350°C. Higher temperatures would be possible (see chapter 4) but due to an aspired industrial implementation of the process we want to keep the temperature in regions normally used in an industrial reactor.

In the following chapters we will see how strongly layer composition, and here especially C/Si ratio is related to layer performance. Therefore we measured with secondary ion mass spectroscopy (SIMS, see Appendix A) the C/Si ratio for different CH₄/SiH₄ gas flow ratios for the diffusion barrier application (see Figure 1.9). The graph shows a linear dependence of gas flow ratios and layer composition. Over the whole parameter range a factor 1.6 more CH₄ is necessary to get the same C as Si

content. This is an effect obviously caused by the higher stability of the CH_4 molecule.

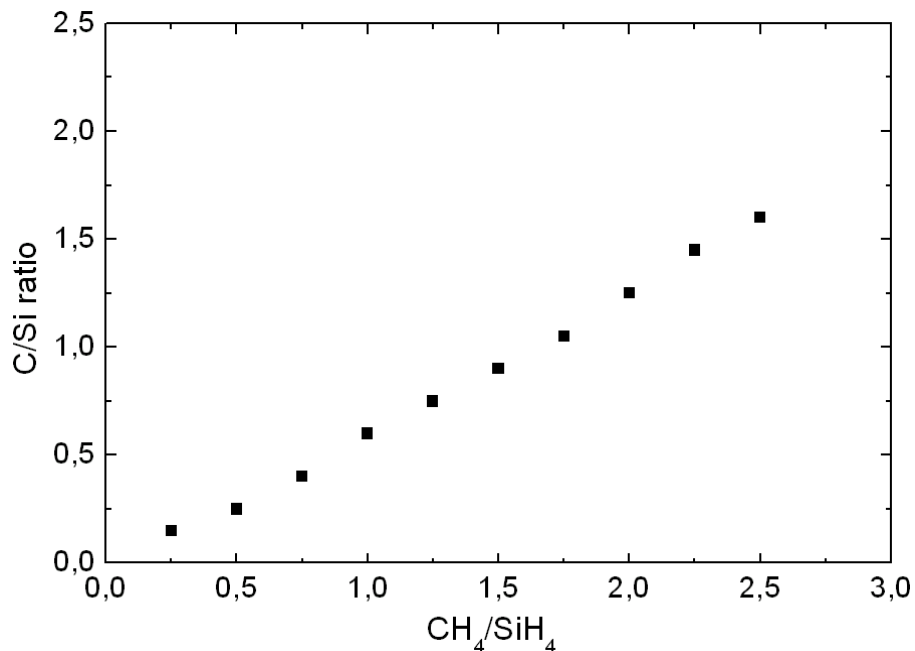


Figure 1.9: C/Si ratio in dependence of the CH_4/SiH_4 ratio for the regime for diffusion barrier layers (SiC).

It has to be mentioned that this deposition regime has a significant disadvantage. That is the high ion bombardment of the overgrown surfaces (substrate or underlying SiC layer). This is no problem for many applications but some of them, like surface passivation, are extremely sensitive to surface damage. Therefore we had to find another deposition regime for this and related applications.

1.4.2 $\text{Si}_x\text{C}_{1-x}$ layer deposition

With increasing knowledge about the performance of our SiC and the need for a temperature stable $\text{Si}_x\text{C}_{1-x}$ surface passivation layer we started to expand our investigations into this field. The new focus was to establish a process with less surface damage. Again we were able to find a deposition regime which was suitable for our applications.

In Figure 1.10 one can see the dependence of deposition rate on the microwave power. As the thickness measurements have a high accuracy the strong variations in

the graph should be realistic. The unexpected dependence points out that the deposition regime is extremely sensitive to variation of process parameters. The deposition pressure was increased to 30 Pa which minimises the damage but makes a homogeneous deposition much harder. The deposition temperature is fixed at 350°C. Due to lack of time a variation of this parameter has not been realised yet. For some applications deposition temperature should be as low as possible. But for our aim to realise best temperature stable layers, a higher deposition temperature is assumed to lead to still better results. The power of the RF source is in the region of 30 mW/cm². Together with the also very low microwave power ($\approx 2 \times 150$ W) the defect generation on the substrate's surface can be minimised.

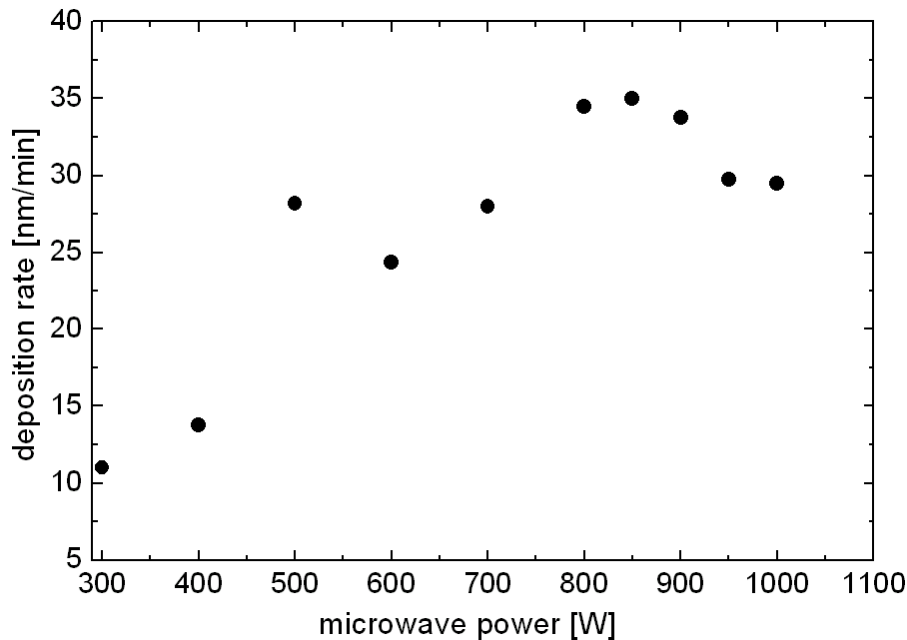


Figure 1.10: SiC deposition rate in dependence of the microwave power in the regime of low defect generation ($\text{Si}_x\text{C}_{1-x}$).

The disadvantages of this deposition regime are the low deposition rate (≈ 1 Å/s) and the much lower homogeneity achieved (thickness variation 5% on 100x200 mm²). It has to be mentioned that the $\text{Si}_x\text{C}_{1-x}$ deposition regime has been far less investigated (due to lack of time) than the SiC regime and that there should be still a lot of room for optimisation.

2 ETCHING AND MECHANICAL BEHAVIOUR

For many applications of a thin solid film a controlled etching process is necessary. I will present some wet chemical and plasma methods which can be used for this purpose. Especially plasma etching processes carried out in our plasma deposition reactor will be discussed. The second part of this chapter will focus on the stress behaviour and the stability of SiC layers. Additionally, I will present several stress measurements in dependence of deposition temperature and show relatively low stress values (in comparison with SiO₂ and Si₃N₄). Furthermore, the good mechanical stability of this material will be discussed at the end of this chapter.

2.1 Etching SiC

At the beginning of this project the etching of SiC was first of all focused on a suitable cleaning procedure for our plasma reactor (see chapter 1). Later on we tried to evaluate the maximum etching rates on our SiC layers which will be subject of this section. As the SiC diffusion barrier layers were partly recrystallised after the wafer equivalent process (see chapter 7), we looked for defect selective etching procedures to find out about the crystalline structure of the annealed layers. When introducing SiC into the solar cell processes, the excellent etch resistivity to several wet chemical etches became our interest which will be subject of our discussion in chapter 9.

2.1.1 Plasma etching of SiC

We know from literature [35] that etching of organic materials with oxygen and fluorine atoms is the most promising way to achieve high etching rates. One possible reaction equation appearing when etching organic materials could be



In literature different etching procedures using SF₆/O₂ [36], NF₃/O₂ [37] and other fluoride containing gases [38] can be found. Unfortunately all these publications worked with crystalline SiC and the reported etching rates should therefore not be valid for amorphous SiC. Only Schmid *et al.* [39] used NF₃/O₂ mixtures to etch crystalline and amorphous SiC. The published results will be presented briefly: NF₃ is a stable gas at room temperature and the binding energies of N-F bonds are D(F₂N-F)=239 kJ/mol, D(FN-F)=297 kJ/mol and D(N-F)=297 kJ/mol, respectively. NF₃ easily generates F and NF₂ radicals at 300°C. The same dependence of the substrate temperature on the etching rate on a-SiC and 3C-SiC could be observed. The optimum temperature seemed to be 300°C while higher temperatures led to enhanced oxidation on the surface which acted as an etch stop. A similar dependence of varying parameters like gas pressure as well as RF power for all SiC materials was also approved through further etching experiments. Nevertheless, all investigations showed a higher etching rate for a-SiC than for 3C-SiC. One explanation could be an average binding energy which should be lower in a-SiC mainly due to hydrogen incorporation. The maximum etching rate achieved at a-SiC was 135 nm/min (at $p=20$ Pa and $T=300^\circ\text{C}$).

According to these results we decided to equip our AK400M plasma reactor also with NF₃ as a gas for reactor cleaning.

2.1.2 Plasma etching experiments

Despite varying parameters intensive etching experiments with a NF₃/N₂O gas mixture first led to very small etching rates. Many process parameters even led to a deposition in spite of an etching procedure. Thereby the carbon, oxygen and fluorine atoms most probably formed long organic chains which grew on the stoichiometric SiC layers. Attempts to substitute N₂O with pure O₂ did not enhance the etching processes.

Subsequently we changed to NF₃/Ar gas mixtures and achieved encouraging results. For testing the etching rates in dependence of the NF₃/Ar gas flow ratio (see Figure 2.1) we worked at a pressure of 5 Pa, a $T=300^\circ\text{C}$ and used microwave powers of 2x1000 W (RF source out of action).

No direct dependencies of gas flows and etching rate can be found. It seems that, although the total gas flow is fixed to 120 sccm, the etching rate reacts very sensitive to smallest changes in the gas flow ratios. Especially in the regions with a low NF_3 content the results are confusing. Between 0.7 and 2.0 an almost linear dependence can be achieved. When the NF_3 flows ($\text{NF}_3/\text{Ar}=5$) are increased further the polymer growth started again.

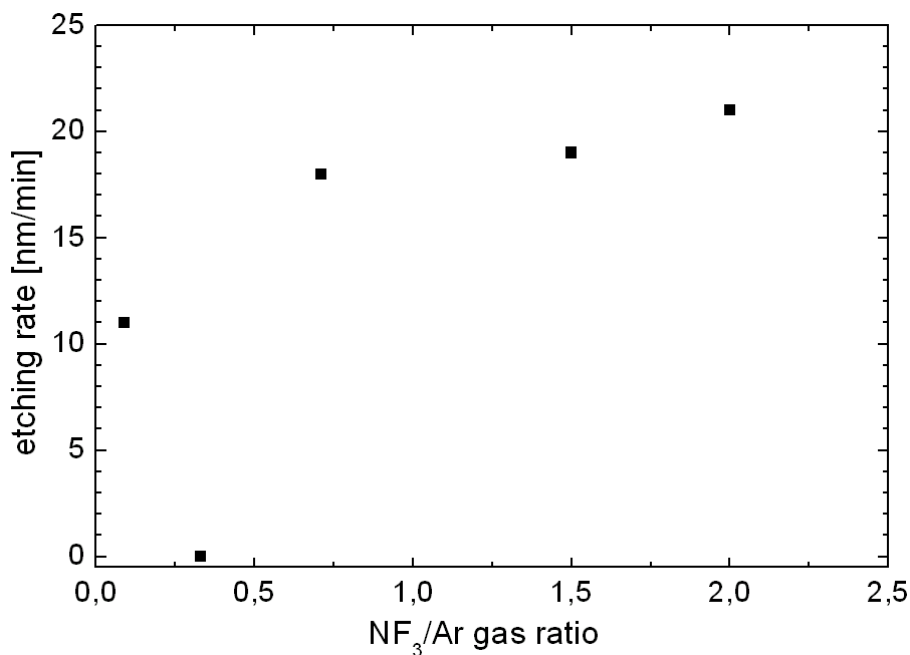


Figure 2.1: Etching rate on stoichiometric SiC layers in dependence of the NF_3/Ar gas flow ratio.

The second parameter scan focuses on the influence of RF bias voltage on the etching rate. For this purpose we work at a pressure of 5 Pa, $T=300^\circ\text{C}$, microwave powers of 2×1000 W and a NF_3/Ar ratio of 2.0. The dependencies can be found in Figure 2.2. These results show that the influence of bias voltage does not seem to be very strong. A small increase of etching rate with bias voltage at the above mentioned set of parameters can be observed.

The conclusion of our investigations is, that etching of stoichiometric SiC layers with a NF_3/Ar mixture seems to be possible. A maximum etching rate of 30 nm/min, which is half the deposition rate can be achieved. The processes are very sensitive to smallest changes in the gas flows and in worst cases even deposition of organic layers can be observed.

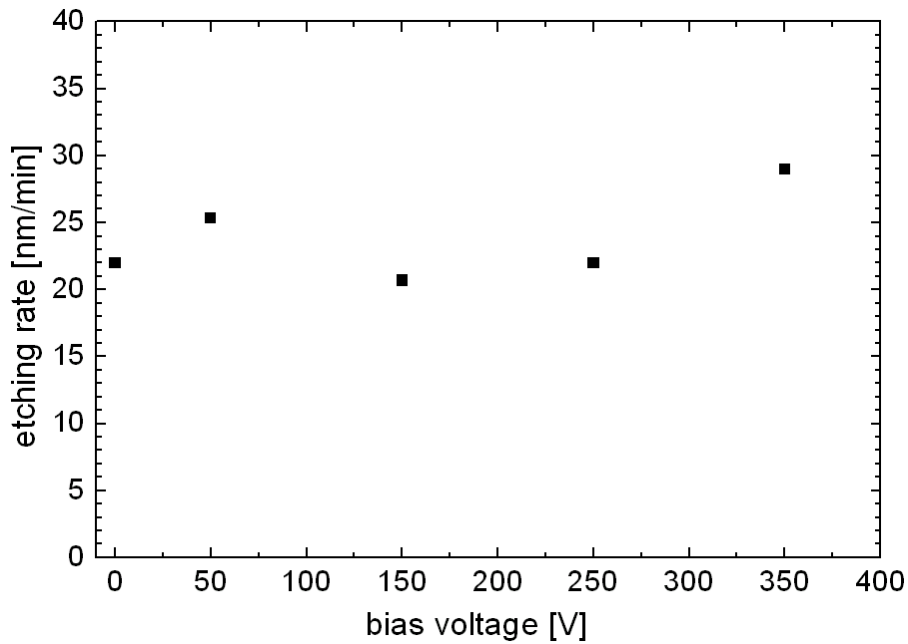


Figure 2.2: Etching rate on stoichiometric SiC layers in dependence of the bias voltage of the RF plasma source.

2.1.3 Wet chemical etching of SiC

Due to its excellent chemical inertness, single crystalline and partly also stoichiometric amorphous SiC is stable in many known aqueous etching solutions. Exceptions are phosphoric acid at 215°C and alkaline solution of $K_3Fe(CN)_6$ at temperatures higher than 100°C. Etching in phosphoric acid, however, is impractical since the reaction is slow and leaves a layer of silicon dioxide on the surface that causes etching to stop [40]. Some other authors reported [39] that amorphous SiC could be etched in a boiling HF:HNO₃ solution (1:1) at rates of about 100 nm/min. In doing so no significant deterioration could be observed and the surface roughness decreased.

Electrochemical etching of SiC occurs through holes provided by the etching process which are involved in oxidation. The resulting reaction products, SiO_x and CO_x, are removed by electrolyte and gas phase nucleation, respectively. The electrolytes studied and reported by Zhuang *et al.* [40] included HF, KOH, NaOH, H₂SO₄, HCl and H₂O₂. In particular, HCl was not effective in dissolving SiO₂ and therefore oxidation instead of etching occurs when using HCl as an electrolyte.

Because our stoichiometric SiC layers started to crystallise after the intensive thermal treatment during the wafer equivalent process (see chapter 5 and 7), we started to look for defect selective etches to find out about the crystalline phases occurring. One possibility would be etching with molten KOH and its mixtures with other salts at temperatures of around 300-600°C. Molten salt etching requires the presence of oxygen. The oxygen is provided either by decomposition of the molten salts or by surrounding atmosphere. As melting of KOH is very complicated and the necessary equipment was not available at our institute we did not try to realise this defect selective etching solution. Up until now we have not found any wet chemical etching process for SiC which would be suitable for our requirements.

2.2 Stress Behaviour

For many SiC layer applications, like e.g. as a membrane, a detailed knowledge of the film stress σ is of great importance. It is known from literature that especially SiC has a very widely tuneable stress parameter range. The deposition parameters pressure and SiH₄ flow rate seem to be the most influent ones [34]. For the application of SiC as a diffusion barrier layer the influence of annealing on layer stress had to be observed closely. The high temperature stability of Si_xC_{1-x} passivation layer depends also on relatively low stress dependence of temperature to withstand the firing during solar cell processing.

2.2.1 Stress measurements

In order to evaluate stress in the SiC films they are deposited on one side of a wafer. To get information about film stress the wafers are measured before and after deposition with a curvature monitor [41]. This tool measures with a laser beam scanner the changes in the radius of curvature of the silicon substrate caused by the deposition of the stressed SiC layer (see Table 2.1). The stress σ can be calculated using

$$\sigma = \frac{Eh^2}{(1-\nu)6Rt}, \quad 2.2$$

where E and ν are Young's modulus and Poisson's ratio of the substrate, respectively ($[E/(1-\nu)]$ is 1.805×10^{11} Pa for a 4" silicon wafer). h and t are the thicknesses of substrate and film. R is the radius of curvature determined from

$$\frac{1}{R} = \frac{1}{R_2} - \frac{1}{R_1}, \quad 2.3$$

where R_1 is the average radius of the bare substrate. The substrate is deformed to a new radius R_2 after the film deposition. A very homogeneous curvature over the whole wafer is a good evidence for a homogeneous stress distribution. In conclusion the network should be homogeneous too.

2.2.2 Stress development with deposition temperature

The layers were deposited on the polished sides of 525 μm thick $\langle 111 \rangle$ Cz silicon wafers, at both high (550°C) and low (350°C) deposition temperatures. The other process parameters were in the standard settings which ended up in a stoichiometric SiC layer with a thickness of ≈ 600 nm. In Table 2.1 the stress data for stoichiometric SiC layers are listed.

Table 2.1: Stress measurements of SiC layers deposited at 350°C and 550°C.

	radius	height	stress
	[m]	[μm]	[MPa]
wafer	-308	-4	
wafer&SiC 350°C	-76	-16	-266
wafer	81	16	
wafer&SiC 550°C	35	35	+162

The SiC layer deposited at 350°C shows compressive stress (-266 MPa) which is quite weak compared to other authors [34,39,41]. The SiC layer deposited at 550°C shows tensile stress (162 MPa). When we compare the stress values with that of other

PECVD deposited layers like SiO_2 (300 MPa) and SiN_x (500 MPa) it is evident that our SiC layers achieve relatively low stress values [42].

For the $\text{Si}_x\text{C}_{1-x}$ passivation layer no stress measurements were done. Khakani *et al.* [6] showed in their work, that the highest stress values were achieved with stoichiometric layers. The lower the carbon content became the more the layer stress decreased. As the carbon content in our $\text{Si}_x\text{C}_{1-x}$ surface passivation layers is pretty low the resulting stress values should be low though. Unfortunately no comprehensive stress measurements investigating the other deposition parameters could be realised during this work.

2.2.3 Stress development with annealing temperature

Schmid *et al.* [39] explained the compressive stress of SiC layers as deposited with ion bombardment during growth, as it results in the implantation of argon ions and/or the breaking of hydrogen bonds in the SiC layers. These defects are more effectively annihilated at higher temperatures (see chapter 5).

Table 2.2: Stress measurements of SiC layers deposited at 350°C and 550°C and annealed at 950°C for 15 min under argon atmosphere.

	radius [m]	height [μm]	stress [MPa]
wafer	192	6.5	
wafer&SiC 350°C + anneal	18	70	+523
wafer	219	6	
wafer&SiC 550°C + anneal	25	50	+742

To find out about annealing behaviour of the stress of our SiC layers we took the layers deposited at different temperatures and applied several annealing procedures. Unfortunately at temperatures above 1000°C the layers cracked and further characterization was no longer possible [43]. This layer cracking at high temperatures (>1000°C) is no principle problem. Detailed information about the dependence of

cracking to layer thickness, surface roughness and other parameters can be found in chapter 5.

After annealing the samples at 950°C under argon atmosphere for 15 min the stress values change significantly. Especially the SiC films deposited at 350°C achieve now tensile stress values of 523 MPa. The SiC layer deposited at 550°C increases its stress to 742 MPa. This shows very clearly that the tensile stress increases with temperature. As the annealing lasted only 15 min the difference in stress values between the two layers can be explained [39]. Therefore our conclusion is, that no matter at which temperature the films are deposited, the stress behaviour with annealing temperature is almost the same. Similar results concerning activation of dopants with temperature can be found in chapter 4.

When interpreting these stress values of high temperature annealed SiC layers another aspect has to be considered. The expansion coefficient α of silicon and amorphous SiC changes with temperature. Although no values for amorphous SiC can be found in literature the values for crystalline SiC point to a stronger dependence of α_{SiC} (see chapter 5) on temperature. But as long as the deformation of the substrate is elastic this has no influence on the measurement. Therefore we made a curvature measurement of a silicon wafer before and after annealing (without any layer on it). The result shows no change in curvature. This proves that the wafer is not deformed plastically after our annealing procedure.

2.3 Mechanical Stability

The mechanical hardness of SiC layers is also strongly dependent on the layer composition. Khakani *et al.* [6] showed that the hardness H increased with carbon content from 10.8 GPa (33% C) to 19.5 GPa (60% C). Still higher carbon contents seemed to have no further effect on the hardness development. Furthermore the hydrogen content seemed to play an important role for this layer parameter. The lower the hydrogen content was the higher became the hardness.

As stoichiometric SiC layers have an excellent mechanical stability many applications in tribology as wear-resist coatings can be found in literature [12,14]. In chapter 9.4 I will present an experiment where we used SiC as a wear-resist layer for an aluminium mirror.

3 OPTICAL BEHAVIOUR

A thin film with a bandgap and a refractive index which can be tuned over a wide range, would be desirable for numerous applications in photovoltaics. In this chapter I will give a short introduction into the theories behind optical performance of amorphous layers and here especially SiC. Furthermore I will discuss different characterization methods which provide information about refractive index, bandgap and defect density of the SiC layers. The experiments presented will show how to realise SiC layers with bandgaps from 1.8 to 2.4 eV and refractive indices from 2.3 to 3.4 by changing just one deposition parameter. At the end of this chapter the low defect densities in a doped SiC standard layer will be proved.

3.1 Introduction

Optical properties of solids are directly related to their electronic structure and their electronic properties. Optical measurements have, however, a significant advantage over electrical measurements: they are practically independent of the Fermi level position, trapping processes, minority carriers, impurities and bending at interfaces, which strongly affect electrical transport measurements [15] as we will see in chapter 4. Optical transitions between the valence and conduction band are responsible for the main absorption band and are the primary measure of the band gap energy [44]. The optical data are also used to extract information about the band tail density of states. However, the absorption coefficient depends on both conduction and valence band density of states and the transition matrix elements and cannot be separated by optical absorption measurements alone.

There are several differences between the absorption of amorphous and crystalline SiC: (1) Crystalline materials exhibit sharp absorption behaviour which corresponds to transitions at the band extremities and where two bands have parallel dispersion

curves, and hence a large joint density of states. The lack of k -conservation and the disorder of the amorphous phase remove these sharp features. (2) The distinction between a direct and an indirect gap is absent in amorphous SiC because the momentum is not conserved in the transition. (3) Some of the transitions near the band gap energy of the amorphous material involve localised states. The transition probability for localised-to-extended transitions is the same as for extended-to-extended transitions, but between two localised states separated by a large distance compared to the localization radius, the probability is reduced. (4) Crystals exhibit excitonic effects near the band edges in which the Coulomb interaction between an electron and a valence band hole results in absorption which does not follow the one particle joint density of states. Excitons produce an absorption peak just below the band gap energy and modify the absorption at higher energies. There is no exciton absorption peak observable in any amorphous semiconductor, because it is broadened out by the disorder. The Coulomb interaction is present in amorphous SiC but its significance in the optical absorption is unclear.

The most significant optical parameters in amorphous semiconductors are the optical band gap E_g , the steepness parameter of the exponential absorption edge the Urbach energy E_0 and the refractive index n . It is well known that in amorphous SiC alloys the optical gap and the refractive index strongly depend on film composition [45-48]. For all applications of SiC investigated in this work the optical performance of the different layers was of enormous importance. No matter if they were used as a back reflector in the wafer equivalent (chapter 7), as a passivation layer on the rear side of a high efficiency solar cell (chapter 8) or as a Rugate filter (chapter 9), the optical performance was of highest interest.

3.2 Refractive Index

Measuring the refractive index n of a material can be realised with several methods. As will be explained below the measurement of the optical transmission can be one way which additionally leads to information about layer thickness and optical bandgap. For a simple determination of refractive index and layer thickness we used ellipsometry (see Appendix A). To apply this method several conditions have to be fulfilled: (1) a smooth substrate with a much higher refractive index than the investigated layer and (2) an approximate value for the refractive index or the layer

thickness. In our case we unexceptionally used polished mono crystalline silicon substrates (float zone or Czochralski) for this purpose. To measure an approximate thickness value independently we created structures (step between layer surface and substrate surface) on the samples on which we could measure the layer thickness with a mechanical profiler from TENCOR.

3.2.1 Experiments and results

In chapter 1 I already described the two most frequently used deposition regimes. In principle one was for the deposition of the diffusion barrier layers (SiC) and the second for layers which were deposited in a regime with low defect generation in the substrate ($\text{Si}_x\text{C}_{1-x}$).

For the first type of SiC layer we had a process window where the refractive index could be tuned without having too much influence on the growth rate and thickness homogeneity as I will show below. This was a desirable feature because many applications demand refractive indices which are easily tuneable. And the high throughput (high rate and good homogeneity) is always desirable because of economical reasons. Therefore the change of the refractive index by just tuning the CH_4 gas flow was investigated. The corresponding carbon and silicon contents were measured with time-of-flight Secondary Ion Mass Spectroscopy (ToF-SIMS). Details to the measurement setup can be found in Appendix A.

In Figure 3.1 one can see that the refractive index n in this process window can be changed from 2.3 to 3.4. The deposition rate for all the layers is between 52 and 62 nm/min. One data point in the region with high silicon content probably is an outlier. A possible explanation for that is the too low difference in refractive index to the substrate (Si with $n=3.8$) or that this thickness/refractive index pair is difficult to measure with an one-wavelength ellipsometer (which can be the case). This means that still higher refractive indices could presumably be realised (still more silane flow possible) but an accurate measurement with our ellipsometer is not the appropriate tool to measure it. The region with the higher C/Si ratios (higher amount of methane) seems to go into saturation and a still higher carbon content could not be realised with just increasing the methane flow. Applications where this continuous optical tuning can be used will be discussed in chapter 9.

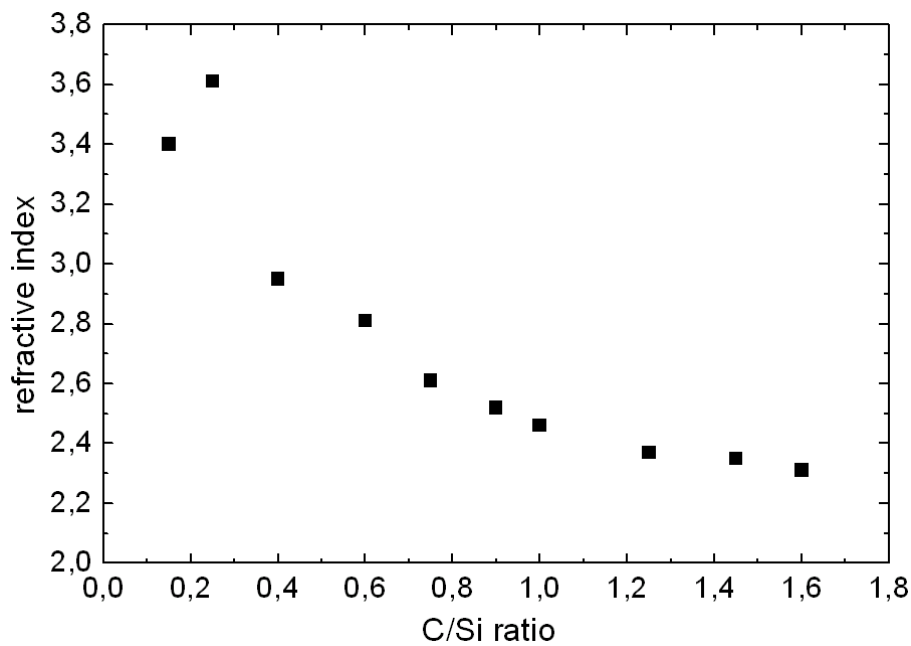


Figure 3.1: Refractive index n in the SiC layers in dependence of C/Si ratio (diffusion barrier regime).

To go below the value of $n=2$ (still higher carbon content) we would have to find another process window with a probably higher microwave power and an increased total gas flow. Nevertheless a transition from a carbon rich amorphous SiC layer to an amorphous carbon layer could cause several problems (network defects, radical change in refractive index) [49,50] and was not investigated in our reactor yet.

For the deposition regime with a low defect generation on the substrate surface (very important for passivation layers) it is much more difficult to find a process window where we can change the refractive index over a wide range without influencing the deposition rate. Due to the relatively high pressure the homogeneity is in principle not as good as for the other process. However this high pressure is necessary to minimise the defect generation. Starting with the deposition regime described in chapter 1 we changed the power of the microwave source to change n (see Figure 3.2). The deposition rate changes with increasing microwave power from 10 to 35 nm/min (determined with TENCOR measurements) and has a maximum at 2x800 W. On the other hand side the refractive index never decreases below 3.1 though the total methane flow is much higher than the silane flow. There seems to be a limitation of carbon incorporation into the layers. One explanation could be a too low free wavelength (very high pressure) that results in a too low amount of cracked

methane specimen. This means that, although ellipsometry is not very accurate in this refractive index region, in the low defect regime a limit of carbon incorporation takes place and directly connected to that the variation of refractive index n is limited.

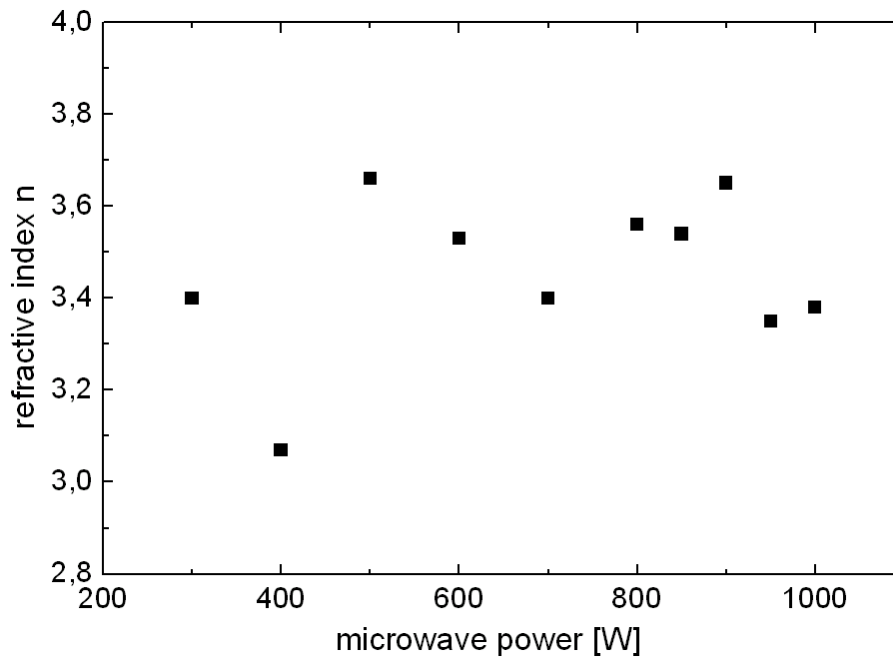


Figure 3.2: Refractive index n of $\text{Si}_x\text{C}_{1-x}$ layers in dependence of microwave power (low defect regime).

3.3 Band Gap Tuning

The optical absorption of thin layers determines in many cases its field of application. A front side passivation layer for example has to have a high transmittance to allow as much light transmission as possible. It is therefore very important to know more about the correlation between changes in the SiC layer network and the optical bandgap.

3.3.1 Optical transmission measurements

Typical transmission spectra are characterised by interference minima and maxima that are dependent on film thickness and refractive index n . They can be used for optical characterization of such materials. Swanepol *et al.* [51] presented a theory for

amorphous silicon how to calculate the refractive index n and the optical absorption α [46]:

$$n = \sqrt{N_0 + \sqrt{N_0^2 - n_s^2}}, \quad 3.1$$

where n_s is the substrates refractive index, and

$$N_0 = \frac{1+n_s^2}{2} + 2n_s \left(\frac{1}{T_{\min}} - \frac{1}{T_{\max}} \right), \quad 3.2$$

where T_{\max} and T_{\min} are the envelopes of the transmission spectra in the low absorption region. It is possible to calculate the reflection coefficients

$$R_{12} \cong \left(\frac{1-n}{1+n} \right)^2, \quad 3.3$$

$$R_{23} \cong \left(\frac{n-n_s}{n+n_s} \right)^2 \quad 3.4$$

and the film thickness d may be written as

$$d = \frac{1}{2n} \left(\frac{1}{\frac{1}{\lambda_1} - \frac{1}{\lambda_2}} \right), \quad 3.5$$

where λ_1 and λ_2 are the wavelengths of the interference maxima and minima. The resulting absorption coefficient can be calculated with

$$\alpha(\hbar\omega) = \frac{1}{d} \ln \frac{(1-R_{12})(1-R_{23})}{T(\hbar\omega)}. \quad 3.6$$

For amorphous semiconductors exhibiting an exponential absorption edge the optical band gap energy E_g can be obtained from the Tauc plot [52]

$$\sqrt{\alpha\hbar\omega} = B(\hbar\omega - E_g), \quad 3.7$$

where α again is the absorption coefficient and B is a constant.

In Figure 3.3 one can find a typical transmission measurement analysis. According to Equation 3.7 the bandgap E_g can be extracted from the slope of the function. Where the line of best fit (in the linear region of the function) meets the x-axis the bandgap can be extracted [53]. As this fitting is afflicted with a high error the bandgap values

have also a low accuracy. Besides, the theory of Tauc was developed for amorphous silicon and several adaptations would be necessary for amorphous SiC (especially for layers with a high carbon content). Nevertheless, although the values are maybe afflicted with a systematic error, this method can be used to investigate correlations between optical bandgap (relative changes) and the layer network.

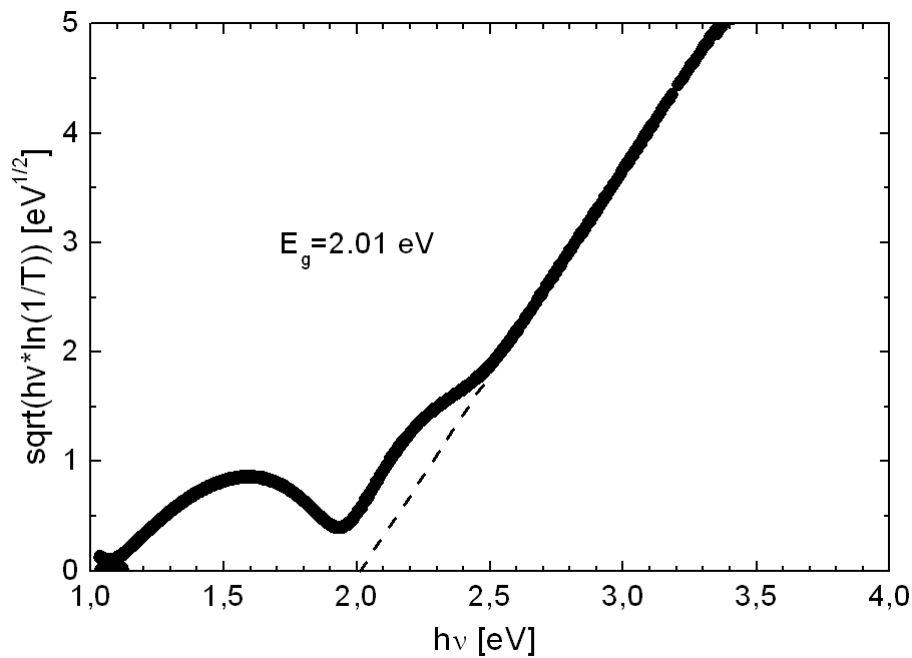


Figure 3.3: Bandgap determination from transmission measurement data of a SiC layer after the theory of Tauc *et al.*

3.3.2 Experiments and results

For transmission measurements we deposited the different SiC layers on quartz glass substrates of 1 mm thickness. The measurements were made in a Spectrophotometer Cary 500i scanning from 250 to 1200 nm wavelength. Afterwards the measurements were corrected by the transmission data measured at the quartz substrate alone. The data were analyzed according to the theory in chapter 3.3.1, subsequently. Again the two deposition regimes were compared and the influence of C/Si ratio and microwave source power on the optical bandgap could be extracted.

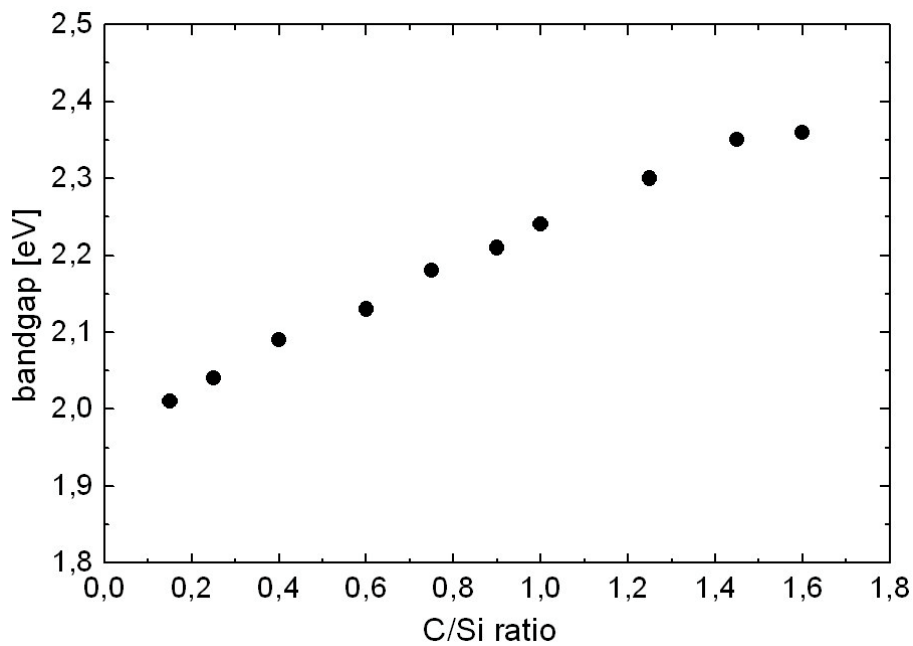


Figure 3.4: Bandgap determined by transmission measurements in dependence of the C/Si content (diffusion barrier regime).

The bandgap variation with silicon and carbon content in the layer is again (in accordance to the refractive index) very high in the regime for diffusion barrier. With an increasing carbon content the bandgap can be varied from 2.01 to 2.36 eV (see Figure 3.4). These results are in good accordance with values published by Demichelis *et al.* [47]. Systematic errors coming from the analysis method therefore seem to be unlikely. The bandgap for our stoichiometric standard diffusion barrier layer is determined with 2.21 eV. Considering errors coming from theory and analysis the estimated accuracy should be in the region of ± 0.02 eV.

In the deposition regime with a low defect generation in the overgrown layer the bandgap variation is between 1.77 and 1.88 eV (see Figure 3.5). The same consideration concerning accuracy has to be made as for the results in the diffusion barrier regime. These results were in no correlation with the refractive indices from ellipsometry measurements for the same samples (see chapter 3.2.1). Several explanations are possible: (1) the ellipsometry measurements in the regions of $n \approx 3.4$ have a very high error due to the low difference of refractive indices compared to silicon, (2) the layer growth rate on silicon (ellipsometry) and quartz (transmission) is differing and (3) the refractive index reacts much more sensitive to the microwave source power than the bandgap does.

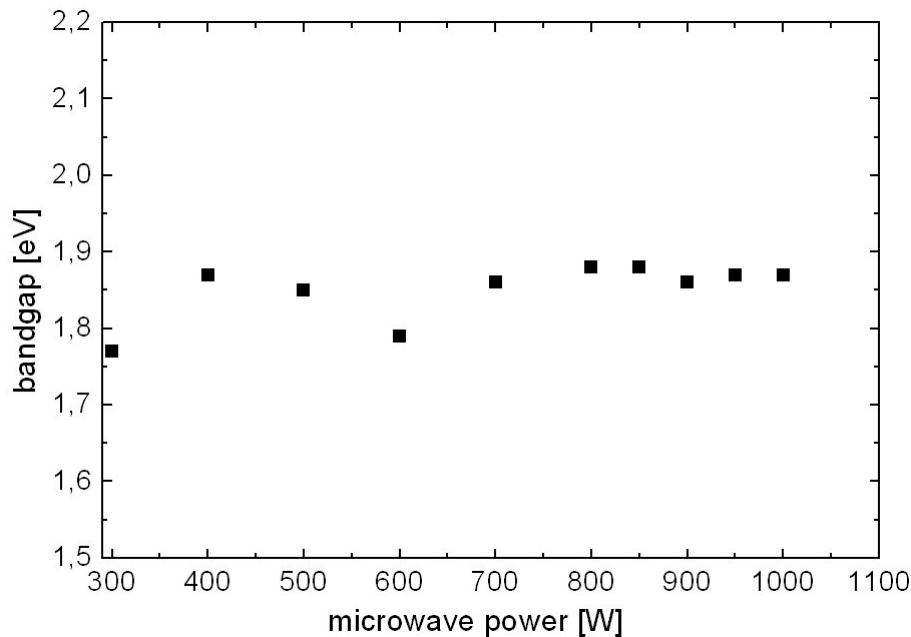


Figure 3.5: Bandgap determined by transmission measurements in dependence of the microwave power (low defect regime).

3.3.3 Photothermal deflection spectroscopy (PDS)

The optical absorption arising from the defect transitions is weak because of the low defect densities and cannot be measured therefore in thin layers by optical transmission [44]. However, the Photo Decay Spectroscopy (PDS) technique (see chapter 3.3.4) has sufficient sensitivity. It measures the heat absorbed in the sample and detects all of the possible optical transitions (see Figure 3.6, [47]). At room temperature virtually all the recombination is non-radiative and generates heat by phonon emission.

From the absorption spectra (see Figure 3.8) of the amorphous SiC layer [45] the bandgap values E_g are again estimated after equation 1.7.

The optical absorption shows an exponential energy dependence in the vicinity of the band gap energy

$$\alpha(h\nu) = \alpha_0 \exp\left(\frac{h\nu}{E_0}\right). \quad 3.8$$

This form of the absorption typically occurs in amorphous layers with a low defect density. The exponential tail is called the Urbach energy and can be found in all amorphous semiconductors. The theoretical ideas of its origin have gone through a complete transformation over the years. The most successful of the various models proposed is that of an exciton transition broadened by random internal electric fields arising from the disorder. This model is able to account for the exponential slope with internal fields which are reasonably consistent with the disorder of the amorphous semiconductors. Considering this theory the integral of the absorption coefficient in the low energy range, as obtained after subtraction of the extrapolated Urbach tail contribution, is directly related to the density of states associated with dangling bonds or similar defects,

$$\alpha_D(h\nu) = \alpha_{\text{exp}} - \alpha_0 \exp\left(\frac{h\nu}{E_0}\right). \quad 3.9$$

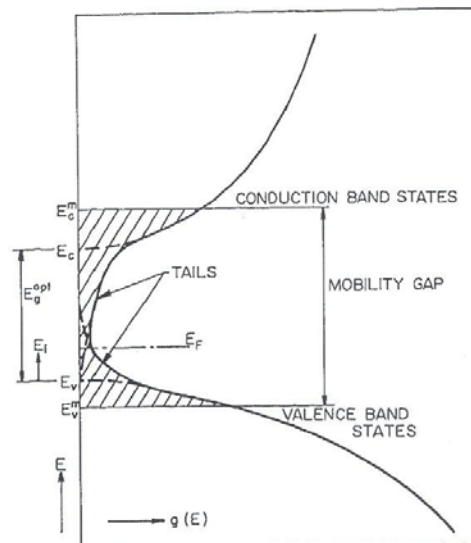


Figure 3.6: Electronic density of states in the amorphous SiC layer.

Rejeb *et al.* [45] reported an increase of E_0 with carbon content in the layers which should be due to an alloying process. The optical absorption in the low energy region also increased considerably with carbon content.

The transitions are likely to be involved as the final states of the extended conduction levels. The density of defects N_D can be calculated using the Jackson and Amer model [54]

$$N_D = 7.9 \times 10^{15} \int \alpha_D(h\nu) d(h\nu). \quad 3.10$$

Rejeb *et al.* [45] furthermore reported, that dilution in hydrogen favours the incorporation of carbon atoms shown by higher gap values in the diluted samples. Illumination by white light for several hours increased the absorption in the low energy range due to the creation of induced defects. The Urbach energy E_0 was to the contrary unchanged and the disorder was not influenced by illumination.

3.3.4 Experimental setup and results

A schematic sketch of the photo thermal deflection spectroscopy (PDS) setup used for this investigation can be found in Figure 3.7.

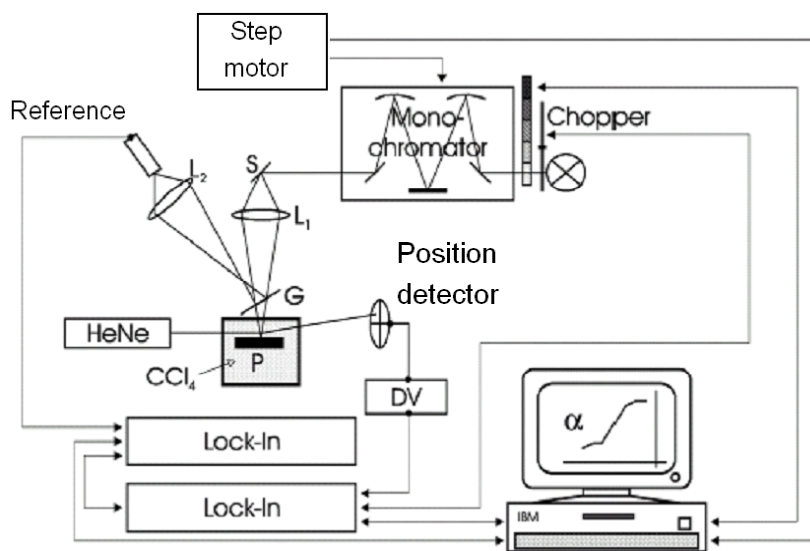


Figure 3.7: Photo Thermal Deflection Spectroscopy (PDS) measurement setup.

The sample is fixed in a small and transparent container and surrounded by a CCl_4 solution. A helium neon laser beam passes the sample very closely to the layers surface. While a monochromator scans through a wide wavelength range of the irradiated light a position detector measures the deflection of the laser beam. This deflection is caused by the change of the refractive index in the CCl_4 solution which itself comes from the warming of the solution. Wavelengths which are absorbed by the layer lead to a stationary warming, others do not. Using this experimental setup

the absorption of the layer in dependence of the irradiated lights' wavelength can be determined. For these measurements the SiC layers were deposited on quartz glass. To get a signal with sufficient intensity we deposited 1800 nm thick layers. The standard deposition process for the stoichiometric diffusion barrier layers was used. The layer was doped with boron (20 sccm diborane flow, see chapter 4). The PDS measurements were done at the Universitat Politecnica de Catalunya (Spain) in the group of M. Vetter. Due to the effort this method causes, we could not carry out as comprehensive measurements as with the transmission or ellipsometry method.

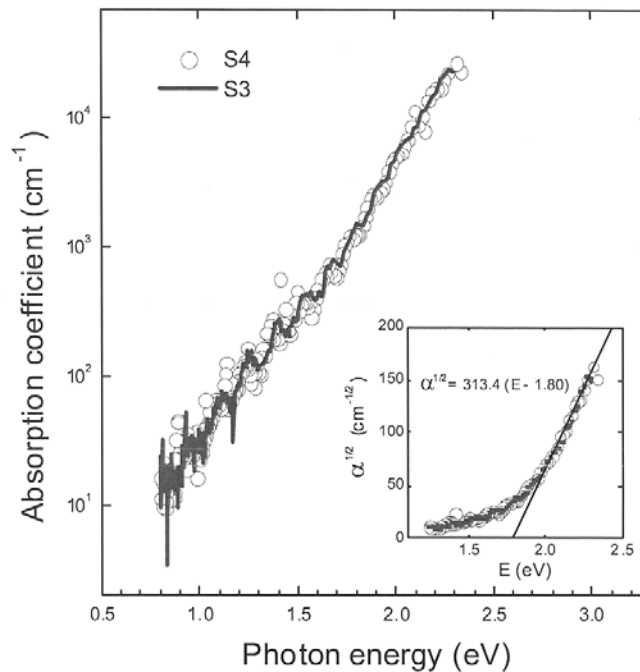


Figure 3.8: Absorption coefficient α (and $\alpha^{1/2}$) in dependence of the photon energy of two stoichiometric amorphous SiC layers s3 (solid line) and s4 (open circles) both deposited in the diffusion barrier regime.

The measurements show a linear dependence between α and the photon energy in the SiC layers. This means that α_0 is not dependent on the photon energy. This fact assumes a low amount of defects in the layer. Although the amount of hydrogen in the SiC layers is expected to be raised (dopant gas highly diluted in H_2) this seems to have no influence on the defect density. From the gradient of the curves' function (see Formula 3.7) a band gap of 1.80 eV could be extracted. A second sample, which

was prepared in a completely equivalent procedure, leads to exactly the same results. This proves the good reproducibility of the measurements. The difference in absolute bandgap values between the PDS measurement (1.80 eV) and the value calculated from the transmission data (2.21 eV) cannot be explained yet. From literature [47] bandgap values for stoichiometric SiC layers were expected to be in the region of 2.2 eV. Unfortunately, for reasons explained above, a comprehensive study to compare the two methods could not be realised yet.

4 ELECTRICAL BEHAVIOUR

In this chapter I will present investigations focusing on doping of the SiC layers with boron, phosphine and nitrogen. After an introduction into the physical theories of conductivity in amorphous layers, I will present results focusing on the impact of doping on the SiC layer network. The activation of dopants by increased deposition temperature and subsequent annealing will also be discussed. The benefits of temperature dependent conductivity measurements and such measurements of our SiC layers will follow afterwards. At the end of the chapter measurements of the SiC diffusion barrier layer's conductivities inside the wafer equivalent layer stack with the "contow" method will be presented.

4.1 Electrical Conductivity of Amorphous Semiconductors

The distinction between localised and extended electronic states is one of the fundamental concepts in the study of amorphous semiconductors [44]. At zero temperature, carriers in extended states are conducting, but localised states are not. Most of the experimental measurements of the localised state distribution rely on this property. The conductivity is a complex macroscopic quantity which represents an average property of the carriers as they move from site to site. The calculation of the conductivity therefore involves the transfer rate, scattering and trapping processes, as well as the appropriate average over the distribution of states. The averaging due to the disorder is most difficult and leads to many interesting effects. In general it has to be mentioned, that the theory of conductivity near a mobility edge in disordered systems has been debated for many years now and a consensus could not be reached yet [55].

The conductivity σ is the product of the carrier density n and the carrier mobility μ

$$\sigma = ne\mu. \quad 4.1$$

The contributions to σ are summed over the density of states

$$\sigma = \int N(E)e\mu(E)f(E,T)dE, \quad 4.2$$

where $f(E,T)$ is the Fermi function. The integral contains contributions from electron transport above the Fermi energy E_F and hole transport below E_F . When conductivity takes place far from E_F by a single type of carrier, non-degenerate statistics can be applied

$$\sigma = \int N(E)e\mu(E)\exp\left[-\frac{(E-E_F)}{kT}\right]dE. \quad 4.3$$

This equation is more conveniently written as

$$\sigma = \frac{1}{kT} \int \sigma(E)\exp\left[-\frac{(E-E_F)}{kT}\right]dE, \quad 4.4$$

where

$$\sigma(E) = N(E)e\mu(E)kT \quad 4.5$$

is the conductivity when $E=E_F$.

The dominant conduction path is determined by the density of states, the carrier mobility and the Boltzmann factor k . When a very high defect density appears in the middle of the bandgap, conduction takes place by hopping at the Fermi energy. A much lower amount of defects prevents this mechanism from contributing significantly and instead conduction takes place by electrons or holes at the band edges, where both the density of states and the mobility increase with energy. Thus $\sigma(E)$ is increasing monotonically with energy. For the particular case in which $\sigma(E)$ increases abruptly from zero to a finite value σ_{min} at the mobility edge energy E_C , the evaluation of equation 4.4 leads to

$$\sigma = \sigma_{min} \exp\left[-\frac{E_C - E_F}{kT}\right]. \quad 4.6$$

σ_{min} is referred to as the minimum metallic conductivity and is given by

$$\sigma_{\min} = N(E_C)e\mu_0kT, \quad 4.7$$

where μ_0 is the free carrier mobility at E_C . The early theories predicted that the conductivity does increase abruptly at E_C , but there is considerable doubt now about the sharpness or even the existence of a mobility edge. Nevertheless, virtually all the conductivity experiments are analysed in terms of equation 4.6. This remains a reasonable approximation even if $\sigma(E)$ changes abruptly, provided that it increases rapidly over a limited energy range. The experiments inevitably measure an average of $\sigma(E)$ over an energy range of at least kT .

The central problem studying the conductivity is to find the energy and temperature dependence of $\sigma(E)$ and the related $\mu(E)$ and to understand the physical processes involved in the transport. The motion of carriers at temperatures above zero may be either in extended states or by hopping in localised states. The magnitude of the conductivity is determined by elastic and inelastic scattering mechanisms. In addition, when there is any local inhomogeneity of the materials, the measured conductivity is an average value over the distribution of local values of σ .

4.2 Doping

To enhance the electrical conductance of our intrinsic SiC layers we started to dope them with boron [56] or phosphorus. Several methods like ion implantation [57] would have been possible. In our case we simply added doping gases to the standard precursors methane (CH_4) and silane (SiH_4). Actually the doping gases diborane (B_2H_6) and phosphine (PH_3) are highly diluted ($\ll 1\%$) in hydrogen. This is for safety reasons because diborane and phosphine are highly toxic gases and the handling in diluted form is less critical. To find out how the layer composition changes when adding additional gases we deposited three SiC standard layers which were undoped (black), doped with PH_3 (grey) and doped with B_2H_6 (light grey). The process pressure was in the region of 5 Pa and the total gas flow changed from 130 sccm (without doping gas) to 160 sccm. The Fourier Transformed Infrared Spectroscopy (FTIR) data can be found in Figure 4.1. As the FTIR data are not corrected concerning interference, the transmission signals have a typical wavelike form. The almost perfect superposition of this signal delivers the additional information, that the

growth rate (see chapter 1) is also unaffected by the adding of doping gases (as the deposition time is equivalent). The slight shifting of the peak maxima results from minimal layer thickness differences (<5 nm). These differences are within the normal homogeneity fluctuations of the deposition process.

Looking at the important peaks (see chapter 1) for SiC, Si-H and C-H_n, the absorption signals have exactly the same intensity. This indicates that the networks of the SiC layers as deposited seem to be unchanged with or without any doping. Yet, it could not be found out if the amount of free hydrogen is also unchanged (much higher H₂ concentration in process gases due to dilution of dopant gases).

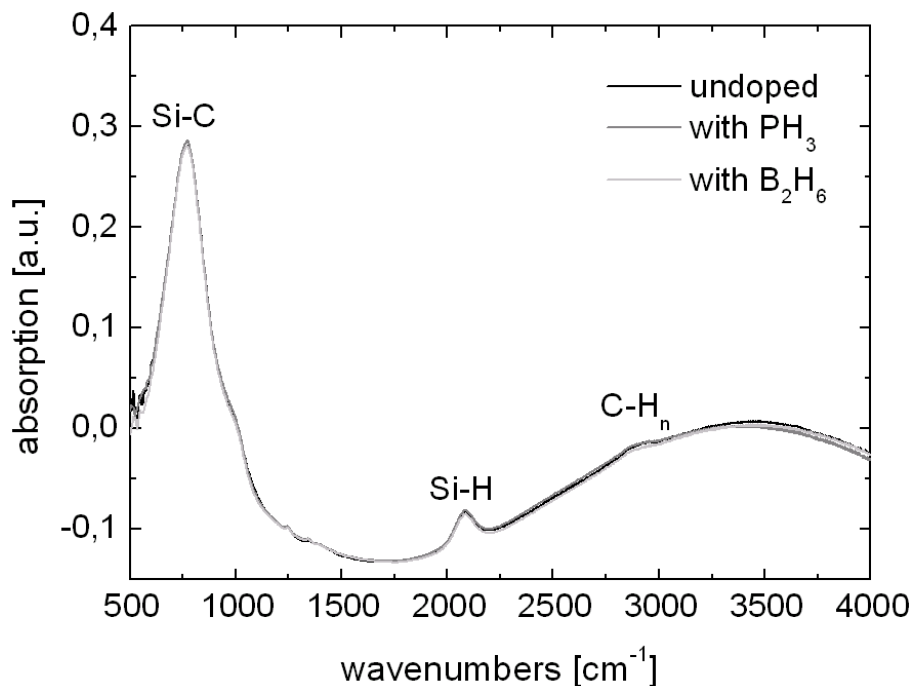


Figure 4.1: FTIR data of three SiC layers deposited without additional doping gases (black), with 30 sccm of PH₃ (grey) and with 30 sccm of B₂H₆ (light grey).

From PDS measurements presented in chapter 3 we just know that the amount of defect densities, which should be related to the hydrogen content in the layer, is still very low after doping. In general one can summarise that adding of doping gases such as diboran and phosphine to the standard gases for SiC layer deposition seems to leave the deposition process and the layer network unchanged. However, from other authors we know that this is not necessarily the case [58].

Table 4.1: Correlation between doping gas flows and dopant concentrations measured by secondary ion mass spectroscopy (SIMS).

gas flow	boron concentration [cm ⁻³]	gas flow	phosphorus concentration [cm ⁻³]
10 sccm B ₂ H ₆	4*10 ¹⁹		
20 sccm B ₂ H ₆	6*10 ¹⁹		
30 sccm B ₂ H ₆	7*10 ¹⁹	30 sccm PH ₃	2*10 ²⁰
60 sccm B ₂ H ₆	1*10 ²⁰		
70 sccm B ₂ H ₆	2*10 ²⁰		

For the Secondary Ion Mass Spectroscopy (SIMS) measurements (see Appendix A) presented in Table 4.1 the SiC depositions were done with different doping gas flows. One can clearly see that by means of increasing the amount of doping gases the dopant concentrations can be enhanced. That alone is not surprising but there seems to be no linear dependence between these two parameters. One explanation for this effect can be a complicated incorporation process. Nevertheless the SIMS data prove, that a high amount of boron and phosphorus can be integrated into the stoichiometric SiC layer. Furthermore, at these process parameters, the incorporation of dopants seems to take place homogeneously, because the SIMS signal is constant over the whole SiC layer thickness. The lateral homogeneity should be, due to the relatively low process pressure during the deposition, no problem either.

Because phosphine is difficult to handle, first attempts of substituting it with nitrogen were started [59,60]. Therefore we highly diluted N₂ gas in H₂. From optical measurements we learn that some layers have the properties of stoichiometric phosphorus doped layers (see chapter 4.4). But it was not clear until the end of this work, if the incorporated nitrogen causes an enhancement of the electrical conductivity or not.

4.3 High Temperature Deposition

The amount of dopants such as boron and phosphorus are high in our layers, as we could learn from SIMS measurements. But not every doping atom automatically

releases electrons or holes which could enhance electrical conductivity (see chapter 4.6). Therefore we tried to “activate” as many atoms as possible. This means on the physical level to crack all hydrogen related bonds, create dangling bonds through hydrogen effusion and connect the doping atoms to them.

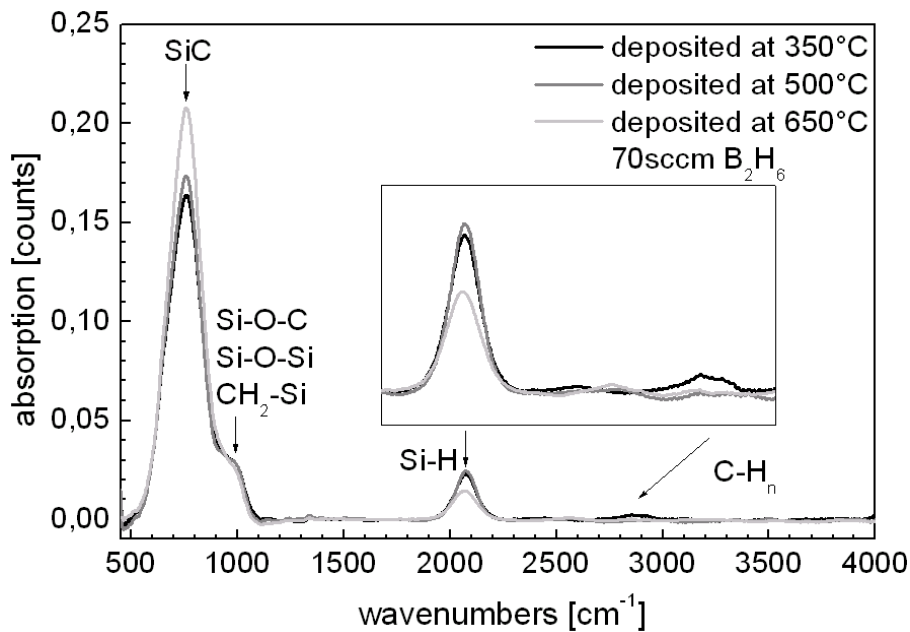


Figure 4.2: FTIR graph of a boron doped SiC layer deposited at 350°C (black), 500°C (grey) and 650°C (light grey).

We started first attempts by increasing the deposition temperature. From parallel investigations (see chapter 6) we knew, that hydrogen effusion takes place until a temperature of around 600°C. Therefore we wanted to know what impact an increase in deposition temperature would have on the layer composition and its network. In Figure 4.2 one can find FTIR data of three boron doped SiC layers deposited at 350°C (black), 500°C (grey) and 650°C (light grey). It is obvious that the deposition at 500°C does not change the amount of bonded hydrogen and the layer’s network significantly. But at a deposition temperature of 650°C the hydrogen related bonds diminish and the Si-C absorption peak at around 700 cm⁻¹ increases in return. That is a clear sign for either hydrogen effusion during deposition or an already lower amount of incorporated hydrogen at this deposition temperature. The same explanation can be given for the Si-C peak. The conclusion of these experiments is,

that the deposition temperature has a significant influence on the network of the SiC layer.

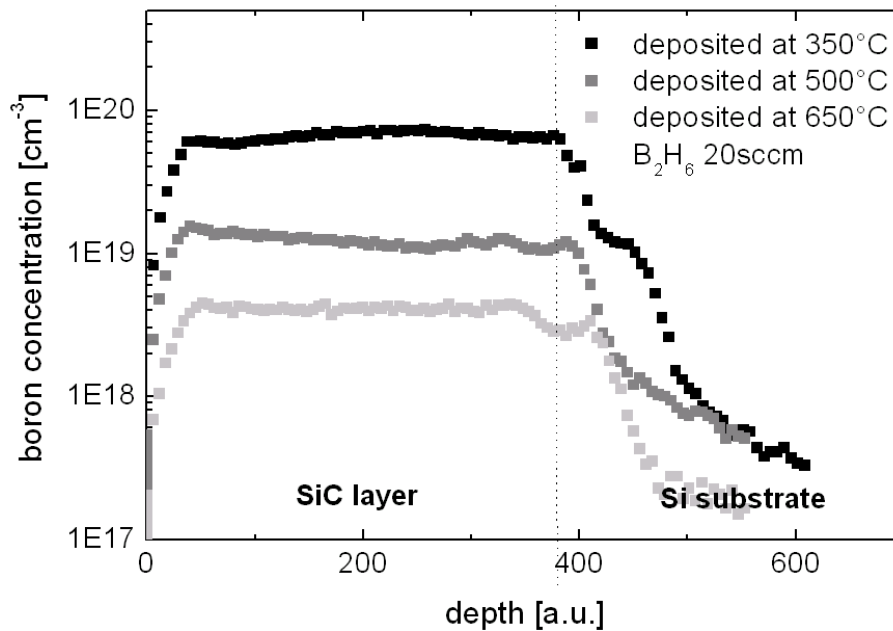


Figure 4.3: SIMS graphs of different boron concentrations in SiC layers deposited at different temperatures but with an unchanged diborane flow.

The second question concerning the activation of dopants by means of high temperature deposition was the influence of the deposition temperature on the amount of incorporated doping atoms. Through SIMS measurements (see Figure 4.3) we found out, that the amount of boron in the layers decreases with deposition temperature. At a deposition temperature of 650°C the amount decreases by around one order of magnitude. The temperature dependent effects presented in this section on electrical conductivity will be discussed in chapter 4.6.3.

In general it has to be mentioned that the deposition at high temperatures batters the AK400M reactor. Although radiation shields and other adaptations have been developed the gasket areas become much warmer and an extended operation at high temperatures is therefore problematical.

4.4 Influence of Annealing

As far as we could learn from the foregoing chapters adding doping gas and working at higher deposition temperatures could have an influence on the network of our stoichiometric SiC layers. In chapter 5 I will discuss into detail the annealing behaviour of the SiC layers when working with temperatures beyond the plasma reactor's maximum temperature. In this chapter I will give an answer to the question what influence annealing temperatures, which can be achieved in the plasma reactor, have on the activation of dopant atoms. Because some authors [61] reported a decrease of the bandgap with the amount of doping atoms we tried to investigate a possible correlation between these two parameters.

Table 4.2: Bandgap energies measured and calculated from optical transmission measurements, with annealing temperature of two differently doped SiC samples.

temperature [°C]	20 sccm B ₂ H ₆	30 sccm B ₂ H ₆
350 as deposited	2.1	2.1
500	2.0	2.0
650	1.7	1.6

In order to determine the band gap of our doped layers we used the optical transmission method described in detail in chapter 3. The layers were deposited at 350°C and annealed (1 h) in situ after deposition in the plasma reactor. The results for two stoichiometric SiC layers doped with 20 sccm and 30 sccm of diborane can be found in Table 4.2. Already at annealing temperatures of 500°C the band gap slightly starts to become narrower. But after an annealing at 650°C it decreases significantly [62]. The difference between doping with 20 sccm and 30 sccm diborane is small. This effect can be explained by generation of an intermediate band state by the boron atoms. The activation of the boron atoms leads to a broadening of the density of state distribution. A similar effect was reported for the ionization of phosphorus emitters by Altermatt *et al.* [63]. The conclusion of these optical transmission measurements of the boron doped SiC layers is that already annealing temperatures of 650°C

significantly activate the boron in the layer and new intermediate band states are created. The temperature dependent conductivity measurements of these layers will be presented in chapter 4.6. For more information about boron diffusion through and from the SiC layer see chapter 6.

Table 4.3: Bandgap development, measured and calculated from optical transmission measurements, after annealing at 650°C of phosphorus and nitrogen doped SiC samples.

temperature [°C]	40 sccm PH ₃	N ₂ /H ₂ =0.03	N ₂ /H ₂ =0.04
350 as deposited	2.1	2.1	2.1
650	1.7	1.5	1.7

In order to compare p-type (boron) and n-type (phosphorus, nitrogen) doping we realised transmission samples as described above but doped them with PH₃ and a N₂/H₂ gas mixtures. These SiC layers as deposited show the same bandgap as the boron doped samples. After annealing at 650°C, which has an significant influence on the boron doped samples, the phosphorus and the nitrogen doped samples behave equally. For the nitrogen doped samples a N-N clustering with annealing would be an alternative explanation (beside the intermediate band state creation) for the band gap narrowing. This bonding would also have an absorption energy of 1.7 eV. But due to the extremely small amount of nitrogen in the reaction gases and due to a second bandgap value at 1.5 eV a real doping of the stoichiometric SiC layers with nitrogen seems to be most probable [64].

Unfortunately no conductivity measurements of neither phosphorus doped nor nitrogen doped samples could be realised until the end of this work.

4.5 Activation Energy

The conductivity of amorphous SiC [44] is usually thermally activated (at least over a limited temperature range) and can be described by

$$\sigma(T) = \sigma_0 \exp\left(\frac{-E_\sigma}{kT}\right) = \sigma_0 \exp\left[-\frac{(E_{TR} - E_F)}{kT}\right], \quad 4.8$$

where E_{TR} is defined as the average energy of the conduction electrons and σ_0 is the conductivity pre-factor. E_{TR} coincides with E_c for the model of conductivity above an abrupt mobility edge, but other transport mechanisms are possible for which $E_{TR} \neq E_c$, such as band tail hopping. The energies E_σ and E_{TR} are illustrated in Figure 4.4 [44] in relation to the density of states and the electron distribution. One might imagine that a measurement of $\sigma(T)$ immediately gives the location of the mobility edge ($E_c - E_F$), and that the pre-factor gives the conductivity at the mobility edge.

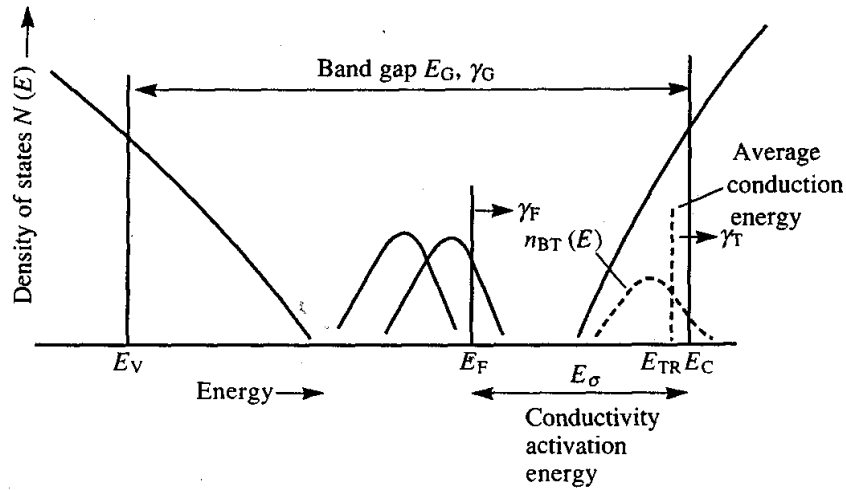


Figure 4.4: Schematic diagram of the density of states distribution showing the conductivity activation energy E_σ , the average conduction energy E_{TR} , with respect to the mobility edges and the Fermi energy. The temperature dependence parameters γ_F , γ_G and γ_T are indicated.

However the measurements can be unhelpful in this respect as there is a huge variation in the values of σ_0 . The correlation between σ_0 and the activation energy E_σ is referred to as the Meyer-Neldel relation and is described by

$$\ln \sigma_0 = \ln \sigma_{00} + \frac{E_\sigma}{kT_m}, \quad 4.9$$

where σ_{00} is a constant with a value of about $0.1 \Omega^{-1} \text{cm}^{-1}$ and $kT_m \approx 50 \text{ meV}$. The Meyer-Neldel relation is only approximately obeyed. The combination of equation 4.1 and 4.2 leads to

$$\ln \sigma(T) = \ln \sigma_{00} + \frac{E_{\sigma}}{kT_m} - \frac{E_{\sigma}}{kT}, \quad 4.10$$

so that

$$\sigma(T_m) = \sigma_{00}. \quad 4.11$$

The Meyer-Neldel relation is a statement that the temperature dependence data for different samples all intersect at the same value of conductivity, σ_{00} . There is still no satisfactory explanation for why this occurs.

The most obvious mechanism by which the pre-factor becomes different from the expected value is when the activation energy is temperature dependent:

$$E_{TR} - E_F = (E_{TR} - E_F)_0 - \gamma T, \quad 4.12$$

where a constant value of γ represents the first order approximation to the temperature dependence and $(E_{TR} - E_F)_0$ is the value extrapolated to zero temperature. Inserting equation 4.5 into 4.1 leads to

$$\sigma = \sigma_0 \exp\left(\frac{\gamma}{k}\right) \exp\left[-\frac{(E_{TR} - E_F)_0}{kT}\right]. \quad 4.13$$

Therefore within the linear approximation, the conductivity activation energy E_{σ} is a measure for the value of $(E_{TR} - E_F)_0$ and the pre-factor contains the additional factor $\exp(\gamma/k)$. The temperature dependence of the energies accounts for the Meyer-Neldel relation provided that

$$\frac{\gamma}{k} = \ln\left(\frac{\sigma_{00}}{\sigma_0}\right) + \frac{E_{\sigma}}{kT_m}. \quad 4.14$$

There are three easily identifiable contributions to the temperature dependence factor γ . The locations of E_{TR} and E_F may change with respect to the density of states distribution. In addition, the band gap is temperature dependent, so that the different gap states move with respect to each other as the temperature is varied. The three contributions to the temperature dependence combine to give

$$(E_{TR} - E_F) = (E_{TR} - E_F)_0 - (\gamma_F + \gamma_G + \gamma_T)T. \quad 4.15$$

The temperature dependence of E_F is referred to as the statistical shift and is present whenever the Fermi energy lies within an asymmetrical density of states distribution. The position of E_F is determined by the electron concentration n_e with

$$n_e = \int N(E)f(E, E_F T)dE. \quad 4.16$$

At zero temperature all the states are filled up to E_F , but at an elevated temperature there are empty states below E_F and filled ones above. $E_F(T)$ moves in the direction of lower $N(E)$ as the temperature is raised, when E_F lies in a monotonically varying density of states.

The second component, γ_G , results from the temperature dependence of the energy levels with respect to each other. Optical absorption data (see section above) find that the bandgap E_G decreases with increasing temperature. The Fermi energy is never further than half the bandgap energy from the main conduction path and consequently γ_G is at most $1/2\gamma_{G0}$. There is no detailed information about the temperature dependence of the defect levels and it is usually assumed that γ_G is proportional to $(E_{TR}-E_F)$:

$$\gamma_G = \gamma_{G0} \frac{E_{TR} - E_F}{E_G}. \quad 4.17$$

E_F is in the middle of the gap in undoped samples and $\gamma_G \sim 1/2\gamma_{G0}$. In doped samples, when E_F is in the band tail, this scaling does not apply as the band tails are broader at high temperature rather than steeper, but in any event γ_G is small.

The temperature dependence of E_{TR} is more difficult to evaluate. The Boltzmann factor in equation 4.4 increases the contribution to the conduction from higher energy states as the temperature increases. This results in a negative value for γ_T , with a magnitude which depends on how rapidly $\sigma(E)$ increases with energy. There is another contribution γ_T if the shape of $\sigma(E)$ is temperature dependent.

A more detailed analysis of conductivity data is needed to explain the pre-factor and to understand the Meyer-Neldel relation but would exceed these work. However, the magnitudes of γ_T and γ_G depend on the location of the Fermi energy, the density of states distribution and the thermal state of the material.

4.6 Temperature Dependent Conductivity Measurements

The theory part of this chapter showed clearly that the knowledge of conductivity in dependence of the temperature would lead to important information about activation behaviour of the amorphous SiC layers [65]. Therefore we will in this chapter present measurements hitting this subject.

4.6.1 Experimental setup

Measurements of temperature dependent electrical conductivity had to be done on electrical insulating substrates which could stand some temperature treatment. For this purpose we used quartz glass samples with an area of around 20x20 mm². Some of the samples were annealed after deposition. Due to the different thermal expansion coefficients of quartz glass and SiC cracking of the layers appeared at too high temperatures and made lateral measurements impossible. Therefore we were limited to an annealing temperature of 650°C. After layer deposition (and annealing) we used 1 µm thick evaporated aluminium contacts which were sintered at 350°C after deposition to enhance the contacts. The contact structure consisted of 4 pads with 10 mm in length and 2 mm in width.

The measurements were done at the Universitat Politecnica de Catalunya (Spain) in the group of M. Vetter. In a vacuum chamber (no illumination) the samples are slowly heated from room temperature up to 260°C. At the same time the layer's conductivity is measured. An impressed voltage of 10 V causes currents which are, for the intrinsic layers, extremely small (10⁻⁹ A). With the contact area, the distance between the contacts and the layer thickness the specific conductivities can be determined.

4.6.2 Metal contact-semiconductor junction (Al-SiC)

For typical conductivity measurements made in coplanar structures it is well known that adsorbates at the free surface and trapped charges at the substrate-semiconductor interface can produce space charge layers. Since the space charge layer can be more conductive than the bulk of the film, the bulk conductivity cannot be determined easily. Bullot *et al.* [15] reported that with an increasing carbon content this surface effects might be unimportant. Furthermore the conductivity of a-Si:H is drastically

changed after exposure to intense gap light. This effect has also been observed in SiC alloys and could influence the measurements drastically. But the higher the deposition temperature gets and especially after a thermal annealing step this effect can be neglected.

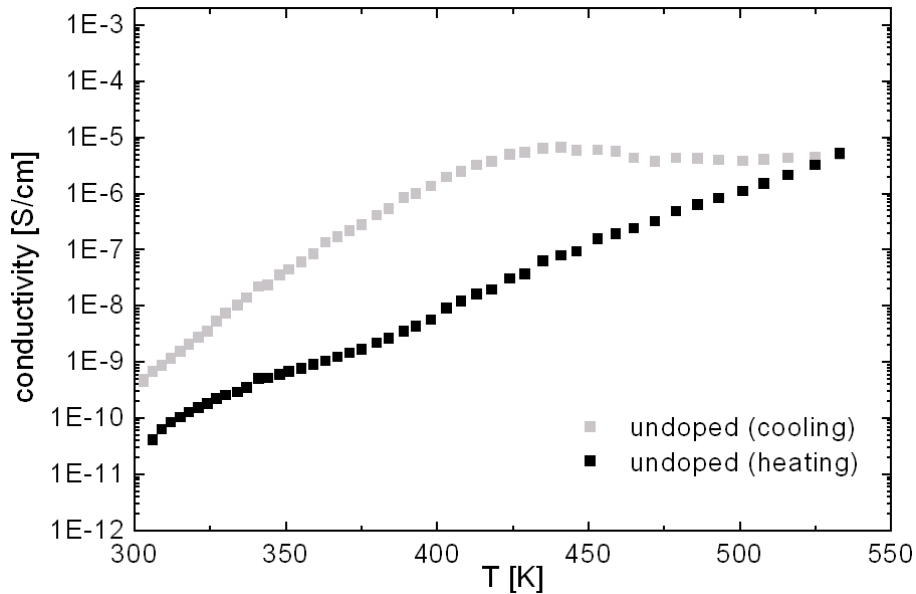


Figure 4.5: Temperature dependent conductivity measurements of undoped stoichiometric SiC layers during heating (black) and cooling (light grey).

When heating and cooling the samples very slowly (0.5 K/min) some kind of hysteresis effect can be observed (see Figure 4.5). Since one measurement took many hours we could not repeat them several times and see how this effect develops with repetitions. Nevertheless, when starting a second heating up some kind of memory effect can be observed. Several explanations are possible: (1) As especially the “undoped” layers show a significant enhancement after one cycle some kind of unwanted doping coming from the reactor walls from preceding depositions could be possible. Although the aluminium contact sintering was already done at 350°C a time span of sintering that long (around 12 h for one heating ramp) could furthermore activate the dopants inside the SiC layer. (2) The second possible explanation is also connected to the slow ramping and a sintering effect. The aluminium/SiC contact could change chemically with temperature [66].

4.6.3 Results

Considering that possible uncertainties of the temperature dependent conductivity measurements have another origin, we will just focus on the data measured during heating of the samples. To achieve higher accuracies other contact grids and other contact materials and an advanced measurement setup would be necessary. Nevertheless, the measurements presented here in this work should be correct concerning the order of magnitude (or better) and should give most interesting information about the dependence of process parameters and electrical conductivity.

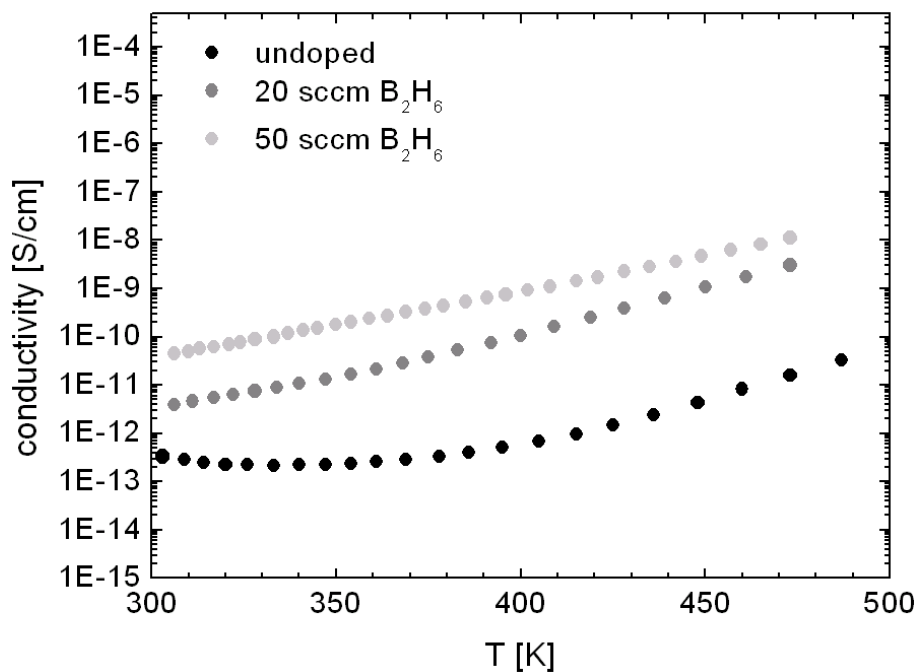


Figure 4.6: Temperature dependent conductivity measurements of stoichiometric SiC layers with additional diborane flow during deposition of 0 sccm (black), 20 sccm (grey) and 50 sccm (light grey).

In Figure 4.6 the intrinsic SiC layer shows a conductivity in the order of 10^{-13} S/cm. This is also the lower limit for the measurement setup. The difference in boron content in the SiC layers is below the factor 2 (see SIMS measurements). In contrast, the conductivity data show a difference of one order of magnitude. Although the accuracy of the conductivity measurements is doubtful there seems to be another effect which enhances the conductivity at higher boron concentrations. Nevertheless a

sufficiently high conductivity cannot be achieved with a high boron concentration in the layers alone.

The next step consisted in increasing the deposition temperature from 350°C to the reasonable maximum temperature of 650°C. The enhancement of the conductivities is neglectable (below one order of magnitude). This is surprising in the first moment, but considering the still relatively low temperatures and the short deposition times (<10 min) the results become understandable.

The process times for the annealing were therefore extended to 2 h. It was obvious, that in reality annealing times in that region would be much too long, but considering the much higher temperatures achieved in our wafer equivalent process (>1400°C) the procedures were not comparable anyway.

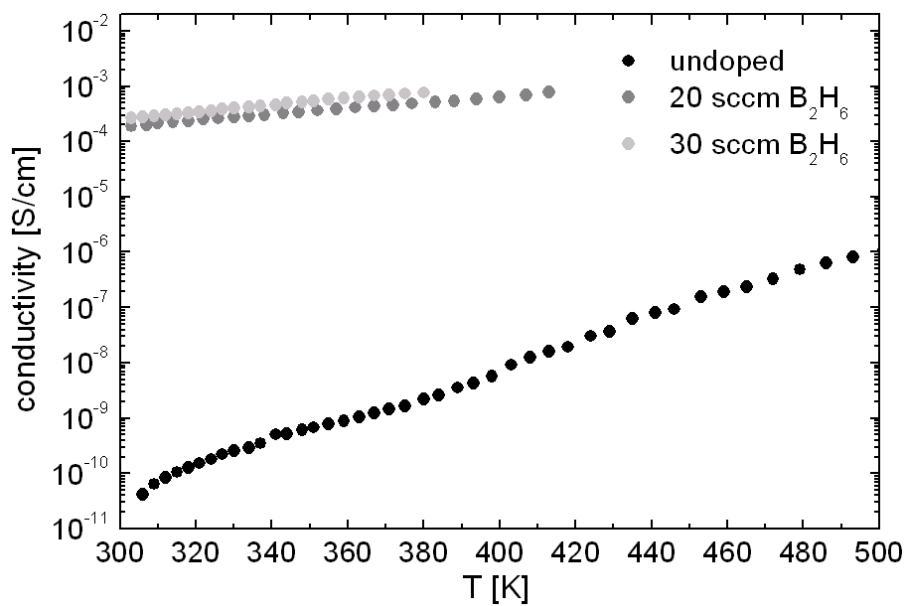


Figure 4.7: Temperature dependent conductivity measurements of stoichiometric SiC layers with no diborane flow (black) and additional diborane flow during deposition of 20 sccm (grey) and 30 sccm (light grey) and a following annealing at 650°C for 2 h.

The measured data for three different SiC layers, one undoped and two doped with 20 sccm and 30 sccm of diborane (around 6×10^{19} to 1×10^{20} cm⁻³ of boron) can be seen in Figure 4.7. Even the intrinsic layer improves its conductivity by two orders of magnitude. This is another argument for a quite small dopant concentration also present in the “intrinsic” layers. Maybe the hydrogen effusion, which should be

advanced after this procedure, additionally enhances this effect. The two doped layers show a significantly enhanced conductivity after this procedure, e.g. the conductivity of the still lowly doped layer (4 times more diborane gas flow achievable) improved by 8 orders of magnitude after the annealing procedure. The best conductivity value measured at room temperature on a boron doped SiC sample is 10^{-3} S/cm. As mentioned above the standard treatment, during the wafer equivalent procedure, includes several high temperature steps with much higher temperatures. We can therefore expect a conductivity performance of the SiC layer which is comparably good or better.

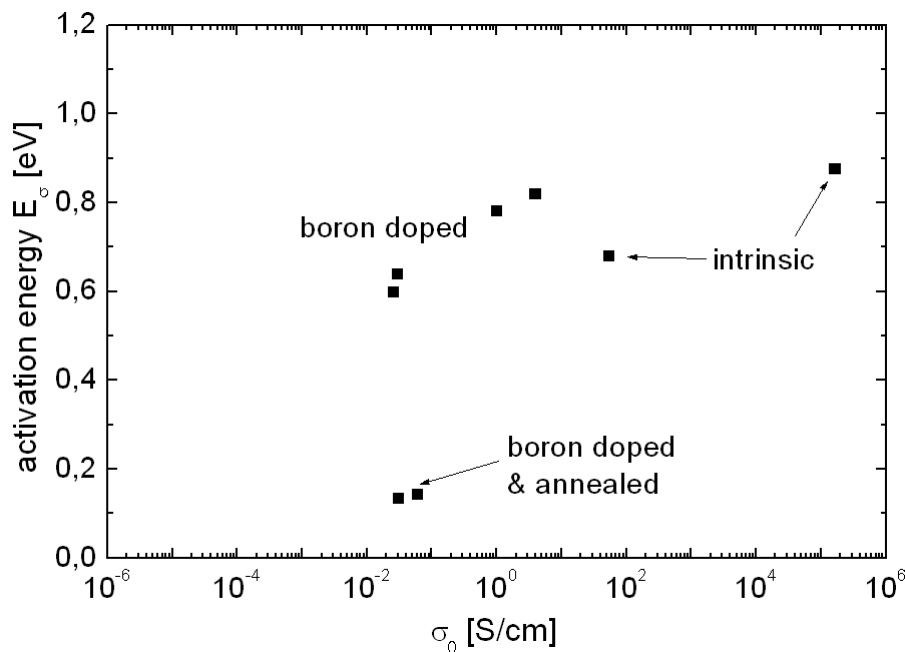


Figure 4.8: Meyer-Neldel plot of undoped, doped and annealed stoichiometric SiC layers.

After calculating the activation energies as described above, the Meyer-Neldel plot (see Figure 4.8) could be drawn [46]. Values for intrinsic layers published by Bulot *et al.* [15] are comparable to our measurements. For the boron doped layers as deposited Pereyra *et al.* [67] presented also data which appeared in the same region as our boron doped layers do. The doped and subsequently annealed layers show of course much lower activation energies E_σ at same σ_0 values. Unfortunately we could not gather enough data to find out the pre-factor σ_{00} , which was our initial aim. Therefore more measurements would be necessary. Especially additional data for n-

doped SiC layers would be a completion. Measurements of appropriate samples with phosphorus and nitrogen doping are already in progress.

4.7 Conductivity of the Recrystallised Wafer Equivalent (RexWE)

To find out about the electrical conductivity of our SiC diffusion barrier layers after all thermal treatments in the RexWE process we could not apply any standard measurement method. First of all, an annealing of a SiC layer on a quartz substrate could not be simulated that easily (completely different absorption conditions due to other furnaces and substrates) and would furthermore lead to a cracking of the SiC layers because of the difference in expansion coefficient with SiO₂. Therefore we developed an alternative method (see 4.7.2).

4.7.1 First principle measurements

In order to measure the resistivity of the complete recrystallised wafer equivalent (RexWE) layer stack (see chapter 7) we deposited aluminium contacts on the front- and rear-side of our samples followed by sintering at 400°C. The RBSiC ceramic substrate alone was contacted similarly in a parallel investigation. After assuring a good contact between the ohmmeter and the aluminium contacts we measured the resistivity and calculated a specific value of 0.1 Ωcm at the RBSiC ceramic sample alone. The resistivity for exactly the same kind of RBSiC ceramics was published to be 0.4 Ωcm by Kunz *et al.* [22]. The higher conductivity values measured here could be due to an error of our characterization method or an increased amount of metallic contaminations in our ceramic material.

For calculating the resistivity of the whole ReWE layer stack the resistivities of the 10 μm thin silicon seeding layer (boron content $2 \times 10^{18} \text{ cm}^{-3}$) and the 30 μm thin epitaxial layer (boron content $4 \times 10^{16} \text{ cm}^{-3}$) were neglected. This leads to a specific resistivity of the SiC layer of $\approx 10^2 \text{ Ωcm}$. The measured values vary a lot from contact point to contact point. We explain this with oxide layers on the ceramic rear side surface (which would be electrically insulating). Another reason for the differing measurements could be possible cracks in the SiC intermediate layer. To get more

detailed information a new concept for a more accurate measurement was developed which will be described in the following.

4.7.2 Advanced experimental setup: the “contows”

For detailed investigation we developed a new measuring concept [68] called “conductive towers” or “contows”. The idea of the set up designed to measure the intermediate layer’s (IL) conductivity consisted in trying to isolate the undesirable SiC layer cracking effects by means of cutting columns into the layer stacks. This cutting into the substrate had the benefit of getting locally resolved data of the conductivities. The stack towers had to be cut deep enough (into the ceramic substrate) to ensure a electrical current flow through the whole layer stack from the epitaxial silicon layer to the ceramic substrate (without any shortcuts).

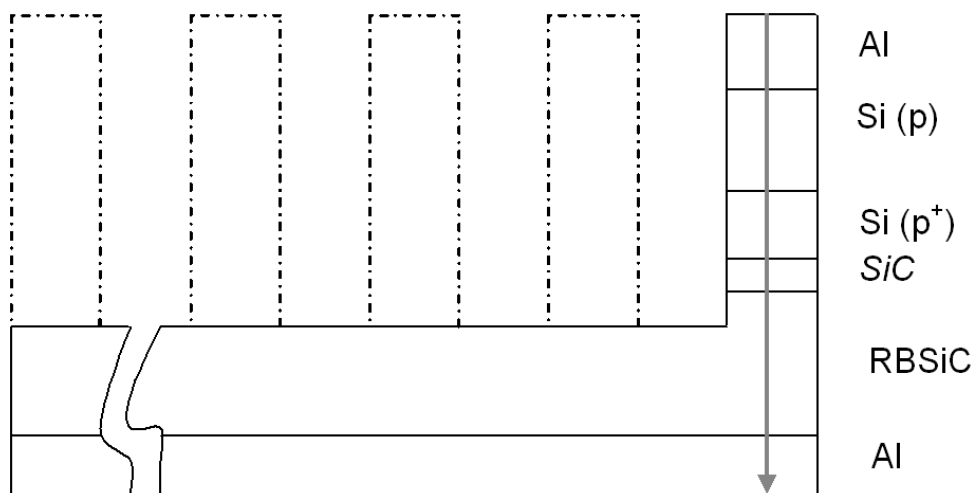


Figure 4.9: Schematic view of the conductive towers “contow” in a recrystallised wafer equivalent (RexWE) and the path of the electrical current (grey dart) during the measurements.

We started with the deposition of 2 μm of aluminium on the front-side. The subsequent cutting of the columns was done with a dicing saw. It would have been easier to use a laser, but that would have molten the layers around the edge of the cut, which is not desirable. The cutting by dicing saw also presented some problems, since the ceramic substrate was too hard for the standard blade. Therefore a new one especially designed for ceramic cutting had to be purchased.

The substrates were cut in columns with an area of around 1 mm². Because a smearing during cutting could not be ruled out a subsequent etching step, to remove all cutting remains from the grooves, was necessary. We used a plasma etching process at a temperature of -15°C with SF₆ which is normally used for silicon etching.

Finally, an aluminium layer was deposited on the rear-side (2 µm), in order to enhance the contact between ceramic and measurement setup. A sintering process was necessary to establish a good contact between front- and rear-side materials (Si and RBSiC ceramic) and the aluminium contacts. During the sintering step, the native SiO₂ layer was etched by Al, and the contacts improved. The sintering was done at 400°C for 45 min.

4.7.3 Measurements of the “contows”

In Table 4.4 one can find the well known values for specific resistance of the different layers and materials which can be found in the RexWE stack. Additionally the thicknesses of these layers are listed.

Table 4.4: Specific ohmic resistance and thickness of the different layers in the recrystallised wafer equivalent (RexWE) stack.

	ρ [Ωcm]	layer thickness [cm]
Al	3×10^{-6}	2×10^{-4}
Si (p)	0.5	30×10^{-4}
Si (p ⁺)	0.01	10×10^{-4}
SiC	?	0.6×10^{-4}
RBSiC	0.1	0.1
Al	3×10^{-6}	2×10^{-4}

With these material parameters we can calculate the resistivity of the SiC layer with

$$R_{tower} = \sum \rho_i \left(\frac{l_i}{A_i} \right), \quad 4.18$$

where ρ_l was the specific resistance of the layer, l_i the thickness of the layer and A_i the area which is perpendicular to the path of the current. With this equation the specific resistance of SiC can easily be solved to

$$\rho_{SiC} = \frac{R_{lower} - 0.20252}{6 \cdot 10^{-3}}. \quad 4.19$$

After measuring the electrical resistivities of several columns on different samples and eliminating statistical outliers a mean value of 0.313Ω can be determined. When putting this value into equation 4.19 we get a mean specific ohmic resistance for SiC of $\rho_{SiC}=18.4 \Omega\text{cm}$. The theory, that the activation through the thermal treatments occurring in the wafer equivalent process is higher, compared to that applied for the measurements on quartz substrates, seems to be confirmed. Furthermore we find this result in good correlation with first solar cell results which will be presented in chapter 7.

5 ANNEALING OF SiC LAYERS (HIGH-TEMPERATURE BEHAVIOUR)

The initial motivation to investigate SiC layers was to find out about their applicability as low-stress, conductive diffusion barrier layers in our Recrystallised Wafer Equivalent. A layer for such an application has to resist temperatures up to the melting point of silicon which is 1414°C. Therefore the high-temperature behaviour, where temperatures above the maximum deposition temperature of our plasma reactor are considered, was a most important point of interest. I will present FTIR measurements showing the structural changes of the layer's network during these high temperature steps. Furthermore, measurements with XRD and Raman, aiming at the crystallisation of our initially amorphous layers at high temperatures, will be discussed. Possible explanations for sometimes occurring layer cracking will conclude this chapter.

5.1 Annealing Conditions

In the earlier chapters we already discussed temperature behaviour of our SiC layers. For example, an activation of dopants in the layers or the changes in stress from compressive to tensile could be observed, when heating them up to temperatures around 600°C. In all these investigations we focused on the maximum temperature of our plasma reactor which was reasonably limited to 650°C. All annealing procedures there were performed under vacuum conditions ($\approx 10^{-4}$ Pa). In this chapter annealing in high temperature ($\approx 1400^\circ\text{C}$) furnaces under several atmospheres (N₂, Ar, vacuum) will be discussed in detail.

5.1.1 Temperature regions

When we started to investigate the high temperature annealing behaviour of SiC we had to choose the interesting temperature regions. Orientated towards the diffusion barrier application three temperatures, having their origin in our wafer equivalent processing, were the starting points: (1) the silicon seeding deposition at 960°C, (2) the epitaxial silicon growth at 1160°C and (3) the recrystallisation at more than 1414°C. Unfortunately many substrates used for characterisation (e.g. quartz glass) could not withstand the high temperatures. Furthermore, many substrates had a completely different expansion coefficient and the layers cracked and could not be characterised any more (e.g. by electrical conductivity measurements). Other restrictions were the maximum temperatures of the furnaces for annealing tests under different atmospheres. The annealing tube with a connected vacuum system for example could not be heated to temperatures above 1000°C. The quartz tube which builds the reaction chamber already started to deform at this temperatures. All these circumstances made it almost impossible to investigate all layer behaviours of interest from room temperature to the melting point of silicon at 1414°C.

5.1.2 Different atmospheres

In literature several authors [69-71] point out, that the atmospheres in which the layers were sintered had a strong influence on the sintering results. Therefore we also annealed under argon, nitrogen and vacuum conditions to find similar effects. As we had to use different furnaces, as mentioned above, the procedures could not be compared directly due to furnace specific, distinctive features like e.g. the temperature profiles.

5.1.3 Process time

The times chosen for the annealing procedures were again determined by the process times of the wafer equivalent which are: (1) ≈ 10 min for seeding deposition, (2) 15 min for epitaxial silicon growth and (3) ≈ 10 min for recrystallisation. To find out if the annealing effects inside the layers went into saturation after some time, we extended some experiments to 2 h. This should have been long enough to bring most of the temperature enhanced processes in the SiC layers into an advanced stadium.

5.2 Re-organisation and Crystallisation

In order to learn more about the microscopic changes in the SiC network several methods were applied to learn more about the crystallisation behaviour of our layers. This knowledge is of big importance when fitting the barrier layer to the ceramic substrate and when the complex diffusion through the layers has to be explained

5.2.1 Layer density and refractive index

To find out about thickness changes due to layer density changes with temperature, we measured the undoped stoichiometric SiC layers before and after annealing with an ellipsometer (see Appendix A).

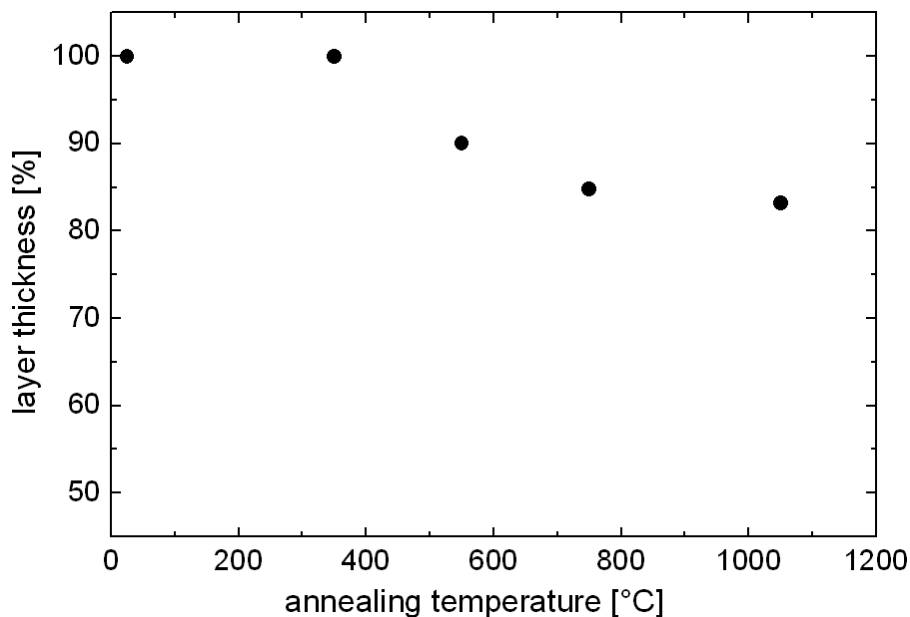


Figure 5.1: Relative decrease in layer thickness with annealing temperature.

The samples were heated for 1 h at 550°C, 750°C and 1050°C under vacuum conditions. Since thickness and refractive index could not be measured independently with the ellipsometer, the layer thickness was additionally determined with a mechanical profile-meter from TENCOR. For these measurements we lithographically created steps in the layer. By doing that we could independently measure the thickness and had no problems even when appearing cracks made the optical measurement difficult [68].

In Figure 5.1 one can see, that the layer thickness decreases from 100% (corresponds to 655 nm) at room temperature (layer deposited at 350°C) to 83% after an annealing at 1050°C. It is not impossible that some of this thickness decrease comes from some kind of evaporation (especially under vacuum conditions) but the predominant part should be an effect of the increasing density of the layer. In correlation with that behaviour the refractive index n of the same layers increases with the annealing temperature and time.

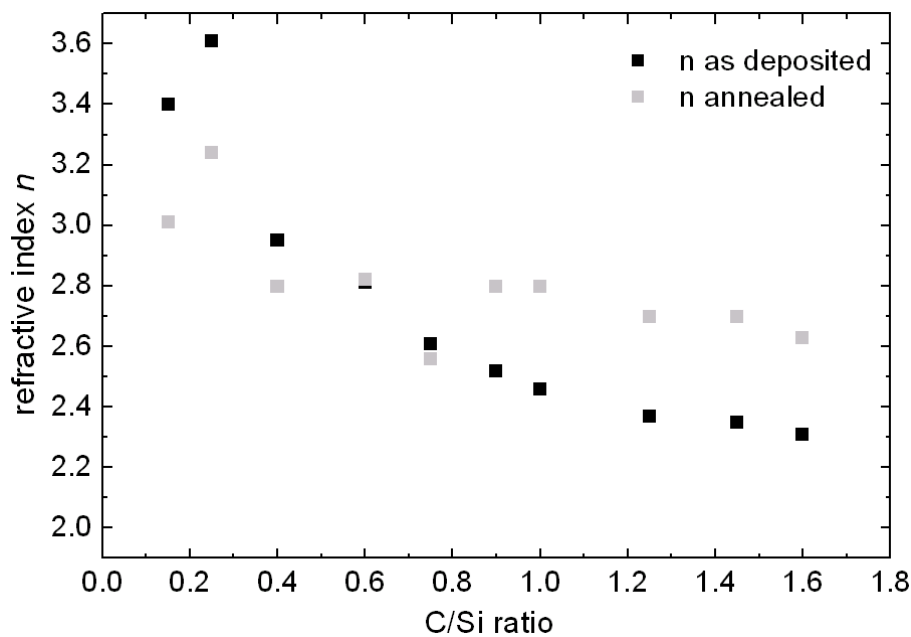


Figure 5.2: Increase in refractive index with annealing temperature.

The annealing process applied to the SiC layers in Figure 5.2 was done at 1100°C under argon atmosphere for 30 min. As the change of the refractive index of the deposited layer was expected to depend strongly on the C/Si ratio we tried to find a dependence of these two layer parameters. The stoichiometric standard SiC layer (C/Si ratio=1) behave completely similar compared to the same layer annealed under vacuum conditions. It is surprising to see, that an increase of the silicon amount in the layers above 50% seems to change the optical annealing behaviour of the layers. The higher the silicon content becomes the more the refractive index decreases after annealing. The parallel thickness measurements show a change of layer thickness of around 80% for all layers independent of the C/Si ratio. Although the refractive indices measured at very high silicon contents are afflicted with a relatively high

error (for explanation see chapter 1) the change in trend is significant. Possible explanations for this effect can be differences in hydrogen effusion, network re-organisation and possibly starting temperature for crystallisation (see subsequent chapters).

5.2.2 Network re-organisation (FTIR measurements)

As already described in chapter 1, Fourier Transformed Infrared Spectroscopy (FTIR, see Appendix A) is especially capable to provide information about the amount of Si-C and hydrogen related bonds [18,72-77]. In this chapter we will focus on the bonds not hydrogen related (which will be discussed in chapter 6). All the samples measured for section 5.2.2 were deposited on polished float zone (FZ) silicon substrates and were annealed afterwards in a resistance heated quartz tube furnace in different atmospheres.

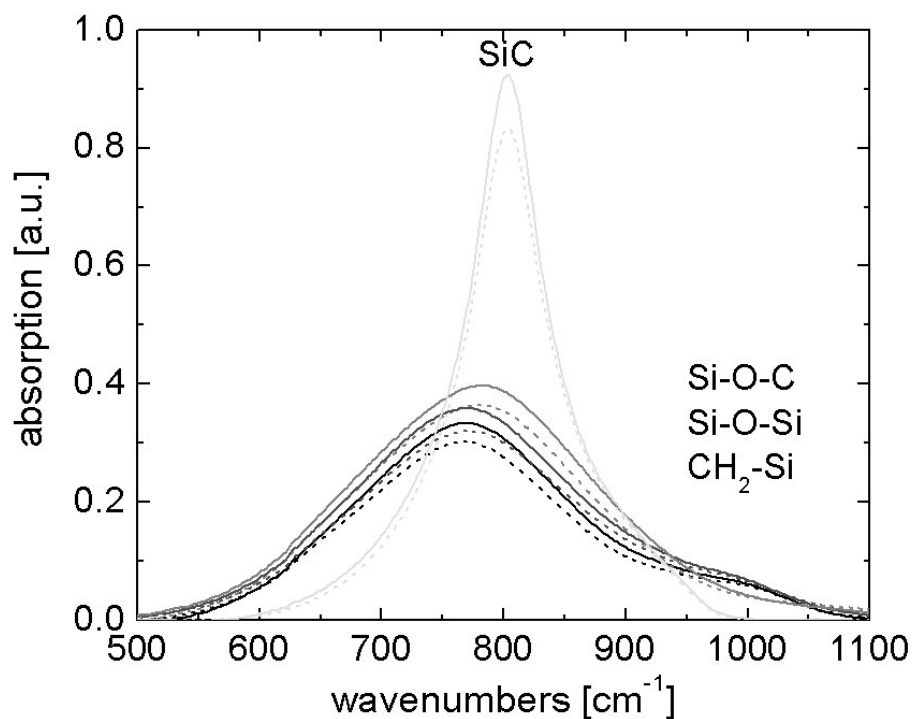


Figure 5.3: FTIR measurement of boron doped (dashed) and undoped (solid) SiC layers deposited at 350°C (black) and annealed at 550°C (dark grey), 750°C (grey) and 1050°C (light grey) for 2 h under N₂-atmosphere.

The SiC related peak of the layers as deposited was detected at 770 cm⁻¹ (see Figure 5.3, Figure 5.4). The different types of stoichiometric SiC layers were doped with

boron (see Figure 5.3) or phosphorous (see Figure 5.4) (dashed lines) and undoped (solid lines). The two SiC peaks are slightly different in height due to the slightly differing layer thicknesses coming from the deposition time. After an annealing at 550°C (2 h) the signal intensity increases a little bit but does not shift to other wavenumbers. This means that new Si-C bonds are built but the crystalline amount of SiC does not change.

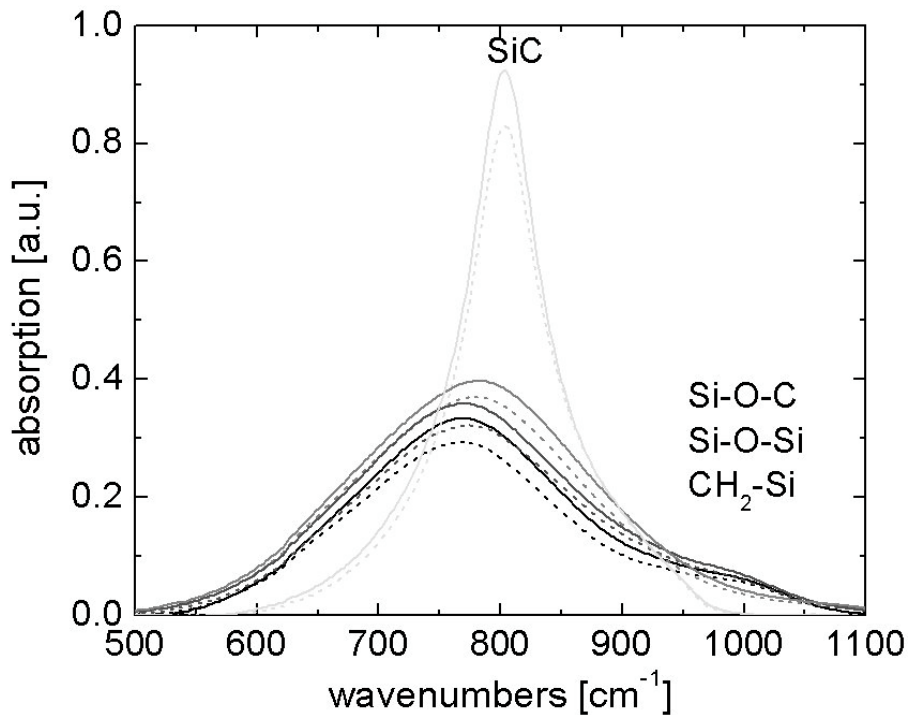


Figure 5.4: FTIR measurement of phosphorous doped (dashed) and undoped (solid) SiC layers deposited at 350°C and annealed at 550°C (dark grey), 750°C (grey) and 1050°C (light grey) for 2 h under N₂ atmosphere.

Increasing the annealing temperature to 750°C (2 h) leads to a further increase in peak height and a small shift to higher wavenumbers (783 cm⁻¹), lower wavelengths, starts. After an annealing process for 2 h at 1050°C the peak already shifts to 804 cm⁻¹ and increases significantly. Additionally the peak width becomes narrower. These are clear evidences that the crystalline SiC amount in the layers increases. The enormous peak height increase comes from newly build Si-C bonds having its origin in temperature cracked other bonds (see also chapter 6). The additional dopants (around 10¹⁹ cm⁻³ of boron) seem to have no influence on the sintering and crystallisation behaviour of the SiC layer.

In the absorption region around 1000 cm^{-1} two oxygen related (Si-O-Si, Si-O-C) and one methane (CH_2 -Si) related peak can be observed. Beginning at 750°C annealing temperature these three signals begin to decrease and vanish completely at 1050°C . Many of these temperature cracked molecules probably form the new Si-C bonds and make the enormous absorption signal growth possible.

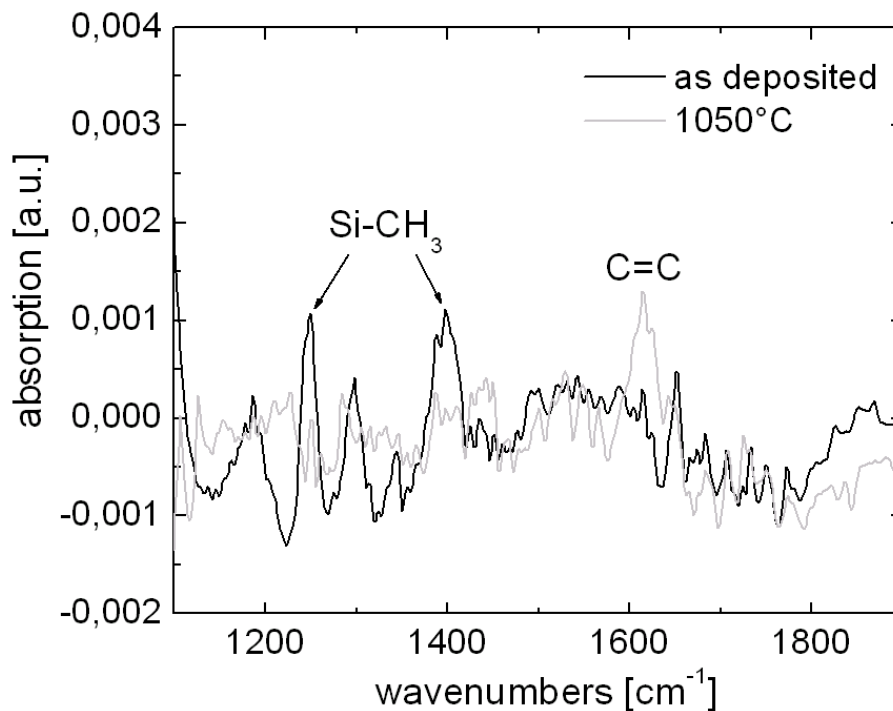


Figure 5.5: FTIR measurements of undoped SiC layers deposited at 350°C and annealed at 1050°C (light grey) for 2 h under N_2 atmosphere.

Another interesting detail which we could extract from the FTIR data can be found in the region between 1100 and 1900 cm^{-1} (see Figure 5.5). At 1250 and 1400 cm^{-1} two clear absorption signals corresponding to Si-CH₃ vibrations appear in the SiC layer as deposited. They almost vanish after the annealing procedure at 1050°C for 2 h (N_2 atmosphere). In contrast a clear signal at 1620 cm^{-1} appears. This is an evidence for the formation of carbon clusters (C=C) in the layers at high temperatures. Nevertheless, this signal is very weak and the predominant part of carbon atoms, originating from C-H_x, cracking form new Si-C bonds.

5.2.3 X-ray diffraction (XRD) measurements

In order to get more structural information about our annealed SiC films, and here especially about the crystalline phases [78], we used the X-ray Diffraction (XRD) method (see Appendix A). The basis of XRD is the constructive interference of x-ray reflections from regularly spaced atomic planes. Elastically scattered X-ray waves can only propagate in directions for which there is constructive interference. Thus, an X-ray elastically scattered by a single plane of waves must have an exit angle equal to the entry angle (relative to the plane). The path length difference between reflections from adjacent planes must have a path length difference (PLD) equal to an integer number of wavelengths in order to obtain constructive interference.

Table 5.1: Significant XRD peaks for SiC layer and RBSiC ceramic substrate [79].

crystal	plane	2 theta [°]
3C-SiC	111	35.67
3C-SiC	200	41.43
3C-SiC	220	60.03
3C-SiC	311	71.82
3C-SiC	222	75.56
4H-SiC	101	34.88
4H-SiC	102	38.27
4H-SiC	103	43.43
6H-SiC	101	34.22
6H-SiC	103	38.27
6H-SiC	105	45.46

3C is normally regarded as the most likely polytype obtained, when SiC films are annealed at $<1600^{\circ}\text{C}$ [80]. However, the hexagonal polytypes have peaks near all 3C peaks due to the lower symmetry. All the allowed peaks for 3C are shown in Table 5.1, along with the 3 strongest peaks of the two most common hexagonal polytypes which do not appear near a 3C peak. 3C-SiC can thus only be identified by the absence of all hexagonal-only peaks. The difference in polytypic structure relates to the relative location (3 locations possible, A, B, and C) of successive layers of

hexagonally close-packed (HCP) layers in the stacking sequence along the c-axis. The number refers to the number of layers stacked along the c-axis before a repetition in structure occurs, e.g. 3C is ABC-ABC, 4H is ABAC-ABAC etc. All the polytypes still retain the basic building block of a tetrahedrally (4-fold) co-ordinated Si-C network [1].

Since it was difficult to record diffraction patterns from thin films, a very thick $\approx 2 \mu\text{m}$ (standard layers are $<600 \text{ nm}$) SiC layer was prepared in order to have higher diffracted intensities when gaining experience with this technique. We deposited the SiC layers on Cz silicon samples $<100>$ and annealed them for two hours at 1050°C (grey line) and 1350°C (light grey line).

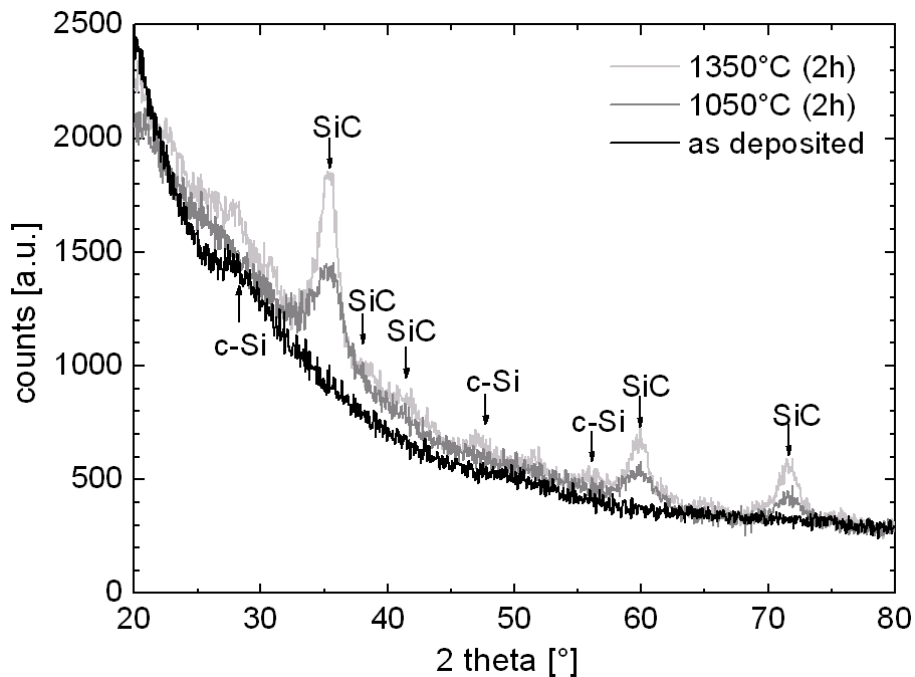


Figure 5.6: XRD graphs of SiC layers as deposited (black) and annealed at 1050°C (grey) and 1350°C (light grey).

The corresponding XRD data are presented in Figure 5.6. The atmosphere was argon with possible residues of air due to gas density problems in the annealing furnace. It is obvious that the film contains a significant proportion of both, c-Si and c-SiC. The differences between the two annealed layers are mostly small. But some SiC peaks are significantly increased in size upon going to 1350°C (111, 220, 222, 442, 333, 511), and many Si peaks are a little bit increased (111, 220, 311, 400). Thus it can be

concluded that the film contains a significant fraction of c-SiC and some c-Si clusters after annealing at 1350°C in argon atmosphere.

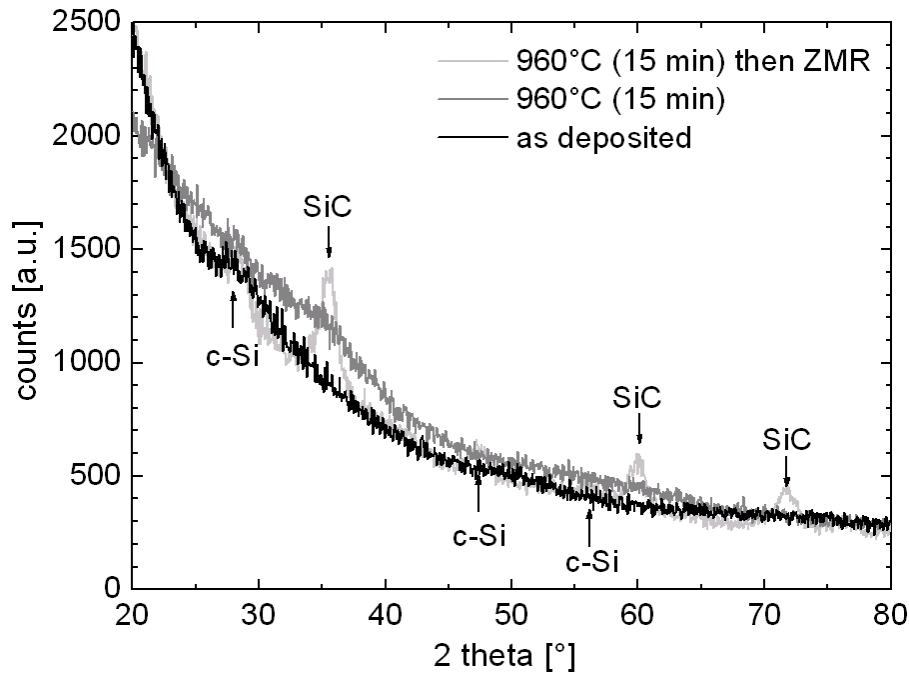


Figure 5.7: XRD graphs of SiC layers as deposited (black) and annealed at 960°C (grey) and after the very short RexWE recrystallisation process step at >1414°C (light grey).

To simulate the thermal treatment for our diffusion barrier SiC layers closer to reality, we followed the annealing times of our RexWE process as discussed at the beginning of this chapter. In Figure 5.7 one can see that even after short annealing procedures such as 15 min at 960°C (equal to silicon seeding layer deposition, grey line) and after 10 min at 1250°C and some seconds at >1414°C (equal to recrystallisation process, light grey line) one can find clear signals for crystalline fractions of c-SiC and c-Si. A third annealing procedure (equal to the epitaxial silicon growth) should lead to a further increase of the already pronounced peaks but was left out for these investigations.

The SiC ceramic substrates (supplied by H.C. Starck ceramics) used for the RexWE application (see chapter 7) were also examined. Since they can be considered as semi-infinite, they pose no thickness related problems and can be measured in the standard goniometric geometry ($\omega=\theta$). In Figure 5.8 one can see the comparison of the annealed SiC layer (black) and the signal which comes from the ceramic substrate

(light grey). About 73% of the peaks can definitely be attributed to c-SiC, with 13.5% from other phases and 13.5% are uncertain. Clear peaks are the hexagonal-only at 34.1° (6H-101), 38° (6H-103, or 4H-102), 45.2° (6H-105), and thus the sample contains significant proportions of 6H-SiC, although possibly with 3C-SiC as well. The good accordance of the recrystallised SiC layer and the RBSiC ceramic substrates explains why these two materials are that adapted for an application in our wafer equivalents.

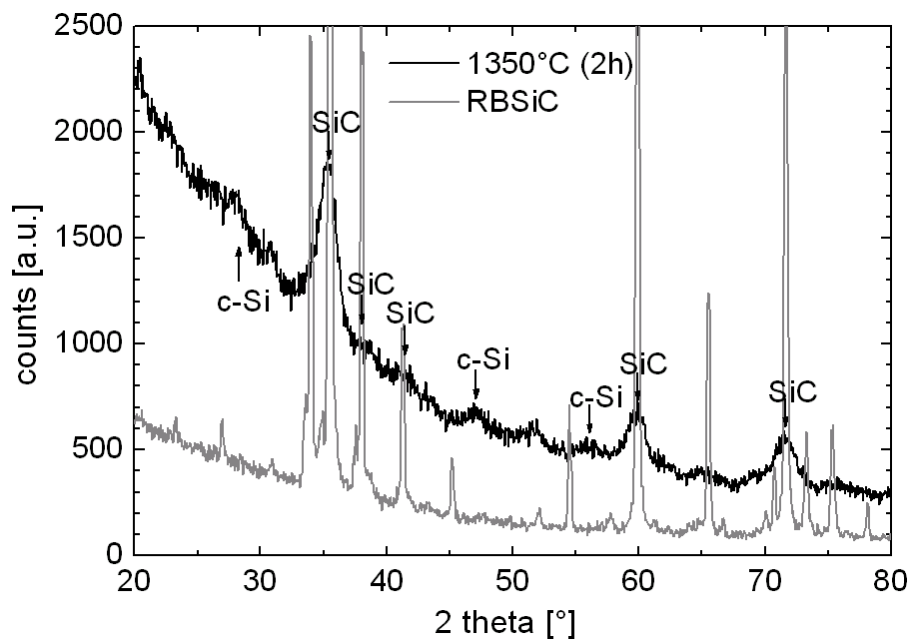


Figure 5.8: XRD graphs of SiC layers annealed under argon atmosphere at 1350°C for 2 h (black) and the RBSiC ceramic substrate (grey). “XRD_annSiC2”

5.2.4 Raman measurements

In order to learn more about the re-organisation of the amorphous SiC layer network we used Raman spectroscopy. This method (see Appendix A) should help us to answer two important questions: (1) what clusters are crystallised by annealing the various alloy films and (2) how the segregation proceeds by annealing before crystallisation. Raman spectroscopy should therefore be capable to determine the presence of amorphous homo-nuclear phases such as a-C and a-Si, or μc -graphite in the annealed SiC layers [81-83].

For a clear signal again relatively thick layers ($>1\ \mu\text{m}$) on polished Cz silicon substrates were necessary. Due to internal tensions in the layers it was impossible to recrystallise layers of this thickness without any generation of cracks. But as far as we could find out, the cracks had no influence on the raman measurements (this was also valid for XRD measurements). The optical excitation was realised using an argon laser at 514.5 nm. After deposition at 350°C in our plasma reactor, the layers were annealed under argon atmosphere in an optically heated quartz tube for 1 h in each case (same furnace used for XRD samples).

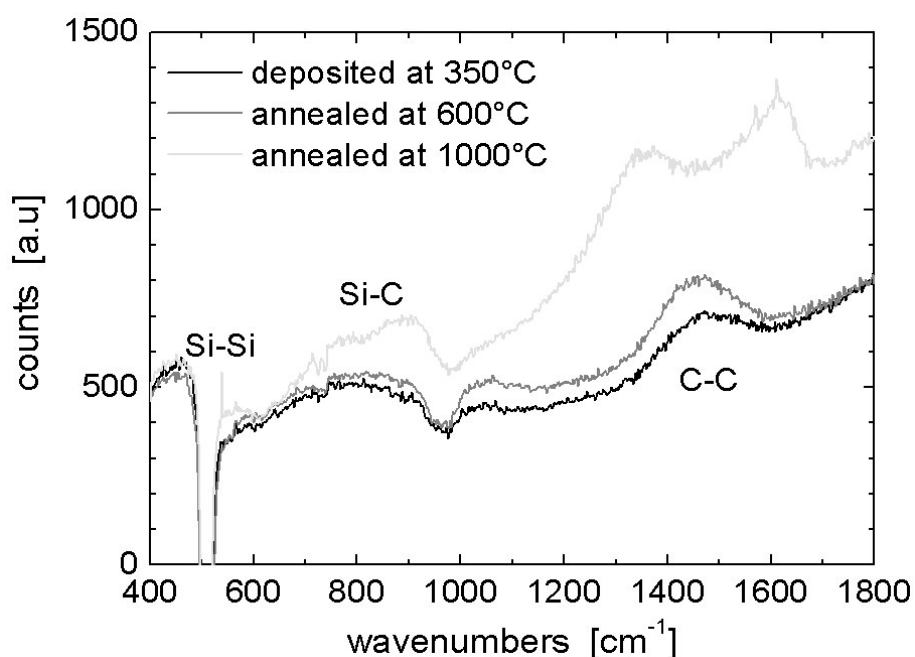


Figure 5.9: Raman spectrum for a typical stoichiometric SiC layer as deposited (black), annealed at 600°C (grey) and annealed at 1000°C (light grey).

Figure 5.9 shows the Raman spectra for SiC films as deposited (black line), annealed at 600°C (grey line) and annealed at 1000°C (light grey line). The data are corrected by subtracting the signal measured at an uncoated silicon substrate. Strictly speaking, it is inappropriate to use the terms “transverse acoustic (TA)”, “longitudinal acoustic (LA)”, “longitudinal optical (LO)” and “transverse optical (TA)” for binary amorphous materials. For convenience the vibrational modes in these binary amorphous films corresponding to those in amorphous silicon are called TA-, LA-, LO- and TO-like modes. Furthermore the degenerated sharp line observed in a

crystalline film at $k=0$ which consisted of the TO and LO modes is for convenience also considered as a TO-like mode.

The sharp feature at 520 cm^{-1} is the overcompensated c-Si TO/LO peak. This notch clearly comes from the substrate because the layer as deposited still shows a very sharp c-Si peak. If all the probe beam was absorbed in the layer as deposited, one would not expect a sharp peak from this film (only a very broad one corresponding to a-Si). At 490 cm^{-1} an a-Si hump surrounding the main peak would be expected. As they do not change shape with annealing, the silicon should be crystallising at 1000°C , there seems to be no crystalline silicon present. On the other side a clear peak at 539 cm^{-1} appearing after annealing at 1000°C could be corresponding to the TO-like band of c-Si.

A clear Si-C bond double feature appears at the 1000°C sample at 780 and 960 cm^{-1} . This double shoulder feature can be observed in many of the SiC layers. The as-deposited and the 600°C annealed samples show the double feature before it starts to split, with a broad peak at 840 cm^{-1} . The crystalline 3C-SiC has sharp peaks at 780 cm^{-1} (TO phonon) and 960 cm^{-1} (LO phonon). Hexagonal SiC has peaks very close to 3C. It is well known that the SiC peaks are expected to be weak compared to the homo-nuclear Si-Si/C-C peaks because of a lower (determined by quantum mechanics) raman scattering probability.

The notch at 980 cm^{-1} comes from the silicon reference and is just the 2nd order TO phonon scattering from the silicon substrate. It is very clear on the reference sample, because the full beam power penetrates the substrate (also overcompensated). They are broader than the main peak (and downshifted from $2 \times 520\text{ cm}^{-1} = 1040\text{ cm}^{-1}$), because 2 phonons are involved. One could have phonons with opposite k involved ($k+k=0$) and still conserve momentum. This broadened and lowered the energy (considering the shape of the optical phonon branch, as the magnitude of k increases, the energy is slightly lowered) of the phonons which are available for raman scattering.

The 1450 cm^{-1} peak for the film as deposited and the film annealed at 600°C is the C-C sp^2 bonding. It is not split up into the well known D (1350 cm^{-1}) and G (1580 cm^{-1}) graphite bands, and hence shows, that the carbon is amorphous, without graphite crystals. At 1000°C the bands separates and thus indicates the onset of graphitisation. Actually the D band is forbidden for a perfect graphite crystal. Its presence shows small grain sizes.

It can thus be proposed, that if these samples start out stoichiometric, they are already segregated into a-Si, a-SiC, a-C at 600°C. Further heating increases the C-C fraction thus these films are maintaining its segregation.

The comparison of undoped, phosphorous- and boron-doped amorphous SiC layers shows no obvious difference between the crystallisation behaviour. This is surprising because many authors reported strong effects of dopant concentration on crystallisation of SiC [84-86].

5.3 Appearance of Cracks

Especially in our stoichiometric SiC layers sometime cracks appear when annealing the layers above 600°C. To handle this problem we tried to find out the origins of this behaviour. In this chapter I will present investigations hitting this subject and will show that with appropriate adaptations even the stoichiometric SiC layers can be annealed above 1400°C without any crack formation at all.

5.3.1 Internal stress

We learned in chapter 5.2 that, due to the re-organisation of the amorphous network, the beginning crystallisation and segregation, the density of our SiC layers increases with temperature. As long as this process appears homogeneously throughout the whole layer this probably just leads to increasing internal stress (which does not affect the layers integrity). But temperature gradients cannot be avoided (optical heated from one side, substrate below,) and concentrations of atoms and clusters may not be homogeneously allocated.

These arguments apply especially for layers with increasing thicknesses. Therefore a critical layer thickness can be found where, depending on layer composition and substrate, cracking of the layers can be observed. The micrograph in Figure 5.10 shows the SiC layer's surface (thickness \approx 1000 nm) deposited on a Cz silicon substrate after an annealing at 1000°C for 1 h.

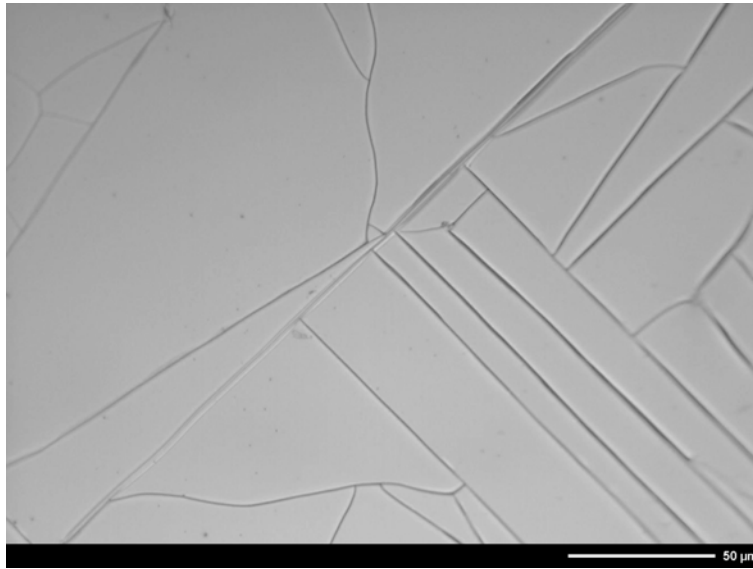


Figure 5.10: Crack appearance in a 1000 nm thick SiC layer on a Cz silicon substrate after annealing at 1000°C for 1 h.

5.3.2 Unequal thermal expansion coefficients

For characterisation reasons it was essential to deposit the SiC layers on different substrate materials, depending on the characterisation method. It is obvious, that problems can occur when trying to anneal these two material systems. Different expansion coefficients can lead to tensions between the different materials and, in our case, the SiC layers can start to crack or even flake from the substrates [87]. This is especially true for SiC layers on quartz substrates (used for optical and electrical characterisation).

For many other characterisation methods already described in this chapter and for the application on wafer equivalents silicon substrates were used. In Figure 5.11 one can see the thermal expansion coefficients α of two differently deposited silicon carbides (both crystalline) [88,89] and crystalline silicon [90]. Unfortunately we could not find data for amorphous SiC so the conclusions have to be regarded carefully. Nevertheless, there seems to be a good correlation between the expansion coefficients, though, especially in the higher temperature range, the discrepancy increases. This can lead to the conclusion, that at temperatures above 600°C this discrepancy in expansion coefficient can lead to layer cracking or worse.

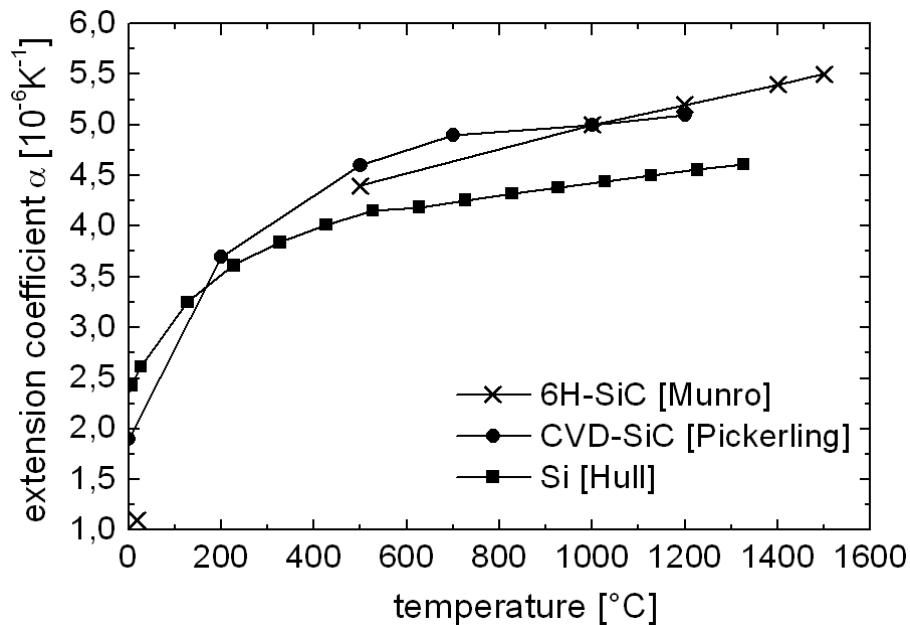


Figure 5.11: Expansion coefficient for differently deposited c-SiC samples and for silicon in the temperature range between 0 and 1500°C.

5.3.3 Influence of substrate's surface roughness

Several silicon substrates with different surface roughnesses were used as substrates for the SiC layer characterisation. These investigations were done in connection with the development of Bragg reflectors for the wafer equivalent application (rear-side reflector, see chapter 7). The SiC layers were deposited on the rough side of the wafer and annealed afterwards under vacuum conditions. The temperature ramping was very slow (5 K/min) to provide enough time for rearrangement of the layers. In 1 h the samples were heated up to 1050°C and this temperature was maintained for 2 h.

Although it is sometimes hardly possible to scan the surface with the optical microscope, we can find a clear dependence between crack amount and surface smoothness. The rougher the substrates becomes the less cracks can be observed. In Figure 5.12 one can observe a micrograph of a 500 nm thick SiC layer on a KOH textured silicon wafer after annealing at 1000°C for 1 h.

For an advanced investigation we tried to find the optimum SiC layer thickness for our recrystallised wafer equivalent (see chapter 7) when using silicon as a substrate. Therefore we again prepared silicon wafers with different surface roughnesses. After depositing SiC layers of different thicknesses, a 10 μm thin silicon layer was grown

at 960°C. Afterwards we recrystallised this thin silicon layer and prepared cross sections of the samples. The results show, that on a polished silicon wafer the SiC had no cracks up to a thickness of 300 to 400 nm. Thicker layers start to crack intensively. This explained the problems we had with our diffusion experiments in chapter 6. The rougher the substrate becomes the thicker SiC layers without cracks can be found after intensive temperature treatment. As the surface's roughness is not homogeneous over the whole samples we cannot determine exact values for the dependences. Nevertheless SiC layers with thicknesses up to 1000 nm without any cracks at all can be found amongst the samples.

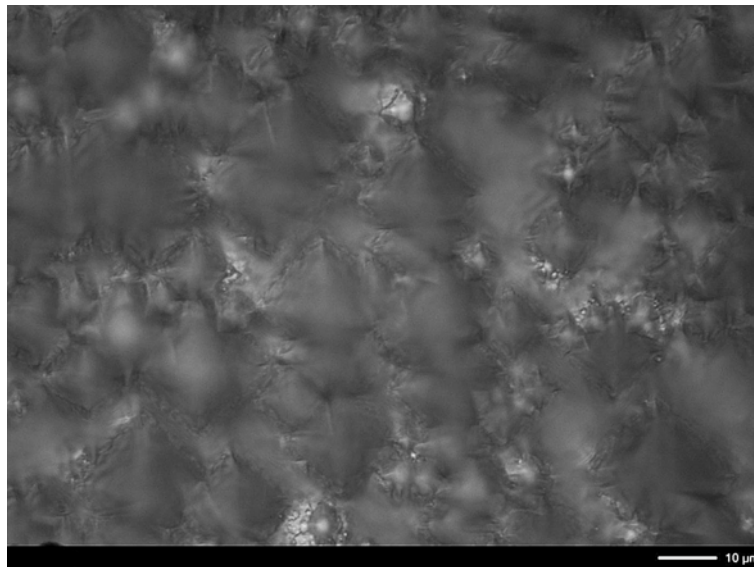


Figure 5.12: Micrograph of a 500 nm thick SiC layer (top view) deposited on a textured silicon wafer and annealed at 1050°C with no visible cracks at all.

These experiments show a clear cracking behaviour dependence of surface roughness and layer thickness. The thicker the layers become the higher the surface roughness has to be. One possible explanation would be an enhanced interlocking of layer and substrate with increasing substrate roughness. The second one could be a smaller influence of discrepancies in thermal expansion coefficient due to more effective degrees of freedom for the expansion (three-dimensional).

5.3.4 Blistering coming from hydrogen

Another reason for crack formation at high temperatures could be blistering coming from hydrogen bubbles. This problem is well known in photovoltaics. It appears quite frequently when surface passivation layers like a-Si or SiN_x are annealed. The theory behind this phenomenon is [91,92], that hydrogen, which resides in the layers in bonded (see chapter 5.2.2) or free form, diffuses to the interface with the substrate. There, the atomic hydrogen forms molecules and, when a sufficiently high amount is available, bubbles. These bubbles can even detach the layers from the substrate. They can also be origins for crack formation because the layers are much thinner at the positions where bubbles occur [93-95].



Figure 5.13: Micrograph of a SiC layer as deposited on a silicon substrate with occurring hydrogen blisters.

Although hydrogen diffuses very fast in almost every solid material, an interface between two materials (e.g. SiC layer and Si wafer surface) can be a region with a higher concentration of hydrogen [96]. This can happen due to a difference in segregation coefficients between these two materials. The interface acts as a drain for the hydrogen atoms and molecules. We tried to verify this theory by depositing SiO₂ on top of the Si/SiC system. This should create a second interface which is also capable of “soaking” hydrogen out of the SiC layer. The results show that the blistering effect on the Si/SiC interface is significantly reduced when a SiO₂ layer

covers the SiC. To further advance this investigations different transparent layers with differing hydrogen solubilities would be needed.

We also tried to find out if other materials at the interface to the SiC layer would have a catalytic effect on the hydrogen blistering. Therefore aluminium, nickel and titanium fingers were deposited on a FZ silicon sample. Subsequently the SiC layer was deposited on it. In Figure 5.14 one can see three micrographs of the surfaces (interfaces) in a top view. The Al/SiC interface (left) shows large blisters over the whole aluminium surface. At the other two metals the blisters seemed to occur significantly smaller. Especially the Ni/SiC interface (right) shows almost no blistering effects at all. This is in good agreement with the prediction, that Ni would have the strongest catalytic effect of this three metals. It is true that other factors like the electrical conductivity of the underlying samples also could cause deposition effects. But in this case, in connection with previous results in this chapter, we can be almost sure to observe a catalytic hydrogen formation caused by different SiC/metal interfaces [97].

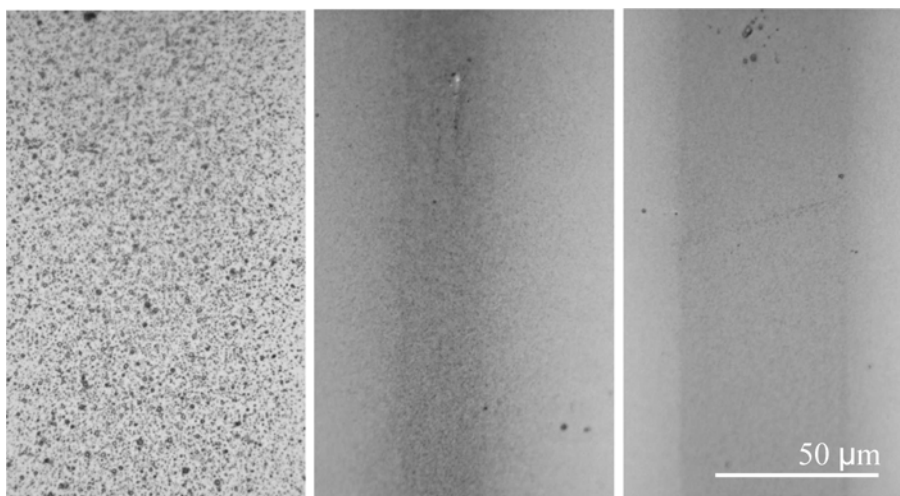


Figure 5.14: Micrographs of SiC layers as deposited on different metals such as Al (left), Ti (middle) and Ni (right) and occurring blistering effects (black dots).

5.3.5 Contamination on substrate and in SiC layer

Contamination of the substrate surface have a detrimental influence on layer quality and, as a consequence, on cracking behaviour. Markings and prints coming from

tweezers (see Figure 5.15) or wet chemical processing can be observed after the deposition and are pronounced after thermal treatment.

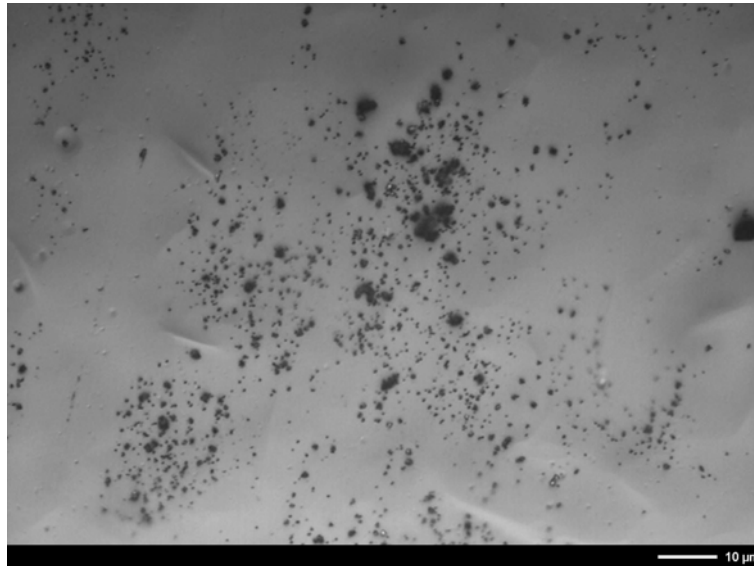


Figure 5.15: Micrograph of a SiC layer as deposited on a silicon substrate and occurring blistering along tweezers traces.

Another most important factor for a good layer quality is the avoidance of inclusions in the layer during deposition. After very long deposition periods without any mechanical cleaning, the reactor gets heavily coated with parasitic depositions. Thereby, small flakes fall on the substrate during SiC deposition and are incorporated into the layer. These inclusions act as starting points for cracks when heating up the samples subsequently.

6 DIFFUSION IN SiC

There are several possible diffusion related applications for a thin film in photovoltaics. In this work we focus on SiC as a diffusion barrier layer. Another application which will be discussed is the use of SiC layers as a donor to provide dopants or hydrogen. This can be useful to generate doping profiles or to passivate dangling bonds in the silicon bulk material during high-temperature processes. After a brief introduction into the matter of diffusion I will present measurements which show the good diffusion barrier performance of SiC against iron, which is as good as that of SiN_x. Furthermore, the out-diffusion of boron and the effusion of hydrogen during high-temperature processes will be discussed. At the end of this chapter I will present estimations about the hydrogen contents of the different SiC/Si_xC_{1-x} layers.

6.1 Basics of Diffusion

The oriented transport of matter where particles move from one region with a high concentration to another region with a low concentration is called diffusion. This transport takes place as long as a concentration gradient exists and ends when an equilibrium state is reached. The dynamics of diffusion can be derived either in a microscopic way by using statistical methods, or in a macroscopic way. Since only the latter approach was used in this work it will be introduced in the following. More detailed information about this topic can be found in [98].

6.1.1 Macroscopic access

For a species of particles which is distributed in a solid medium the First Fickian law

$$\vec{j} = -D \cdot \vec{\nabla} c \quad 6.1$$

is valid, where \vec{j} is the particle flux, i.e. the number of particles which penetrate the unit area during time unit, and c is the (spatially varying) concentration of particles in the medium. The proportional factor D is called diffusion coefficient and is usually quoted in cm^2/s . D contains all information about the microscopic structure of the medium as well as the specific diffusion mechanism.

By combining the First Fickian law with the continuity equation

$$\frac{\partial c}{\partial t} = -\nabla \cdot \vec{j}, \quad 6.2$$

we get the Second Fickian law

$$\frac{\partial c}{\partial t} = -\nabla \cdot (D \cdot \vec{\nabla} c). \quad 6.3$$

If the diffusion constant D is spatially invariant the equation simplifies to

$$\frac{\partial c}{\partial t} = D \cdot \Delta c, \quad 6.4$$

where Δ is the Laplace operator. For most cases this simplification is a good approximation. However, there are two cases in which D cannot be treated as spatially invariant: (1) if the medium is not isotropic in all dimensions or (2) if the diffusion coefficient depends on the concentration. Since in all realistic cases of diffusion concentration gradients are present, this is equivalent to a spatial dependence of $D = D(c(\vec{r}))$. Due to limited knowledge about impurity diffusion in amorphous layers, D was regarded as not concentration dependent in most of the investigations and analysis carried out in this work.

For diffusion problems which are not too complex concerning geometrical structure and boundary conditions, the Fickian equations can be solved analytically. Two simple cases which were either important for this work or are important for solar cell processing will be presented here. The formula given here were calculated only for one dimension, but can easily be extended to the three dimensional case.

If a finite amount Q of a substance is present in an infinite medium at the time $t=0$ with negligible extension at the place $x=x_0$ the starting conditions and boundary conditions

$$\begin{aligned} c(x_0, t = 0) &= Q \cdot \delta(x - x_0) \\ c(x \rightarrow \pm\infty, t) &= 0 \end{aligned} \quad 6.5$$

are valid and the concentration profile after a diffusion step of the time t is given by

$$c(x, t) = \frac{Q}{2\sqrt{\pi Dt}} e^{-\frac{(x-x_0)^2}{4Dt}}. \quad 6.6$$

As can be easily found this solution has the form of a Gaussian curve. Due to its generality it is possible to calculate the diffusion of any concentration profile in an infinite medium by simply superimposing solutions of this first simple problem. If for example the initial profile has a Gaussian shape like

$$c(x, 0) = c_0 \cdot e^{-\frac{x^2}{2\sigma^2}} \quad 6.7$$

the diffusion problem is described by

$$c(x, t) = c_0 \cdot \sqrt{\frac{2\sigma^2}{4Dt + 2\sigma^2}} \cdot e^{-\frac{x^2}{2Dt + \sigma^2}} \quad 6.8$$

which also has a Gaussian shape. This equation was used for the analysis of diffusion profiles of implanted metallic impurities (Fe).

A second important case for diffusion problems is an infinite amount of substance of concentration c_0 placed on the surface of a semi-finite medium. Here the boundary conditions are

$$\begin{aligned} c(x = 0, t > 0) &= c_0 \\ c(x \rightarrow \infty) &= 0 \\ c(x > 0, t = 0) &= 0. \end{aligned} \quad 6.9$$

With these boundary conditions the Fickian law can be solved to

$$c(x, t) = c_0 \cdot \operatorname{erfc}\left(\frac{x}{2\sqrt{Dt}}\right) \quad 6.10$$

with the inverse error function

$$\operatorname{erfc}(z) = 1 - \operatorname{erf}(z) = 1 - \frac{2}{\sqrt{\pi}} \int_0^z e^{-x^2} dx. \quad 6.11$$

Equation 6.10 gives an excellent description e.g. for diffusion of a dopant (like boron) out of a SiC layer into the silicon bulk to create a back surface field. The SiC

layer in first order approximation can act as an infinite source with constant boron concentration.

However, many diffusion problems cannot be solved analytically due to their complexity in boundary conditions. The Fickian equations then have to be solved numerically. Two examples for different boundary conditions can be found in Figure 6.1. In the left graph an amount of substance Q concentrated at $x_0(t_0)$ (black) changes its Gaussian profile with diffusion time (grey and light grey). The maximum concentration x_0 decreases. The right graph shows a constant concentration c_0 at a surface x_0 (black). With increasing diffusion time more and more atoms diffuse into the solid (grey and light grey). The software we used for our simulations will be presented in the following sections.

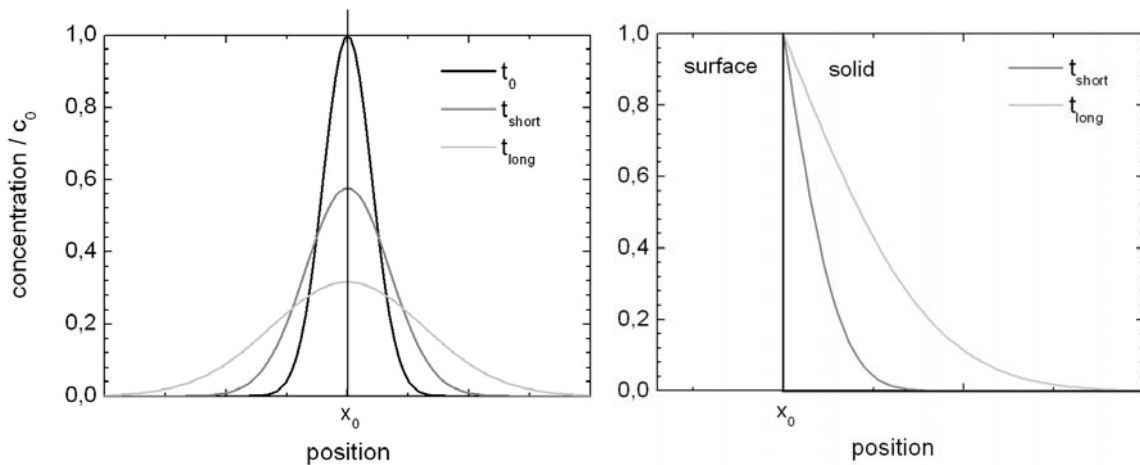


Figure 6.1: Concentration profile before and after annealing for different boundary conditions.

6.1.2 Diffusion constant

It was shown above that the diffusion constant D is the most important parameter for a macroscopic access to diffusion. In real systems, D can depend on the concentration but is always dependent on the temperature. Since diffusion is a thermally activated effect, in most cases the temperature dependence of the diffusion coefficient can be described by

$$D(T) = D_0 \cdot e^{-\frac{E_a}{k_B T}}, \quad 6.12$$

were D_0 is the diffusion constant at infinite temperature, E_a is the activation energy, k_B is the Boltzmann constant and T is the diffusion temperature, respectively. The diffusion constant D_0 can vary by several orders of magnitude, depending on the diffusing species and the composition of the medium, whereas E_a usually is in the magnitude of 1 eV.

6.1.3 Segregation coefficient

In thermodynamic equilibrium the concentrations of foreign atoms in different phases of the same material are often unequal. E.g. the concentration in the liquid phase is typically much higher than that in the solid state phase. The ratio of the concentrations on two sides of a phase transition is called segregation coefficient m . This effect is e.g. used in our zone melting process (see chapter 7) where we enlarge the silicon grains and, with the same procedure, perform a physical cleaning of the seeding layer [99]. The liquid melting zone which is moving over the substrate gathers the foreign atoms and reassembles a much lower concentration of it into the recrystallised silicon crystal due to the lowering of melting point with contamination.

A segregation coefficient cannot only occur between different phases but also between different materials in the same phase (e.g. between Si and the SiC barrier layer). The segregation coefficient can be written as

$$m = \frac{c_{SiC}}{c_{Si}}. \quad 6.13$$

6.2 Diffusion Barrier Performance

We started our SiC layer development with the presumption [22], that stoichiometric SiC layers would show the best diffusion barrier performance. Beside that (because of economical aspects) two more requirements considered were thickness homogeneity over the whole deposition area and a high growth rate. The major work of this chapter was done in connection with the diploma thesis of Holger Habenicht [100] realised under my supervision.

Diffusion through the barrier layer is dependent on the condition of the SiC layer (as it can be found in the RexWE, see chapter 7) and the foreign atom which diffuses through the layer. Due to lack of time we could not investigate all possible

contamination appearing in the ceramic substrate. So we focused on metallic impurities which: (1) have a high diffusion constant in silicon and can therefore spread in the silicon cell bulk very easily and (2) have a detrimental influence on the solar cell performance through enhanced recombination of minority carriers because of their ability to generate new trap levels. Bounassisi *et al.* [101] could show that not only the concentration but also the appearance of the metallic impurities is of enormous importance.

Table 6.1: Diffusion constants, D and D_0 , and activation energy, E_A , of iron in different matrices [100].

foreign atom	matrix	D_0 [cm ² /s]	E_A [eV]	D at 1200°C [cm ² /s]
Fe	PECVD-SiO ₂	6.9×10^{-10}	0.88	6.77×10^{-13}
Fe	PECVD SiN _x	4×10^{-12}	0.62	3.04×10^{-14}
Fe	c-Si	1.3×10^{-3}	0.68	6.16×10^{-6}

Following these criteria we focused on iron as a foreign atom (see Table 6.1). We know that the typical concentration of iron in a contaminated substrate is around 1%. The solar cell efficiency is degraded with 40% when 0.1 ppma of iron contaminate the cell bulk [102]. Therefore it is obvious that SiC has to prevent this transition metal from diffusing into the silicon cell bulk to avoid this detrimental silicon degradation effect.

6.2.1 Experimental setup

A testing setup for the diffusion behaviour of a thin layer and the diffusion constant of a foreign atom in it can be realised by following different ways. They have all in common, that the diffusion is enhanced by thermal annealing. The change in the concentration profile before and after annealing is measured. Reber [98] tested in his work several setups to find out about diffusion behaviour of iron, chromium and vanadium in SiO₂ and SiN_x. His conclusion was that the implantation of foreign atoms in the analysed film is the best method to do that.

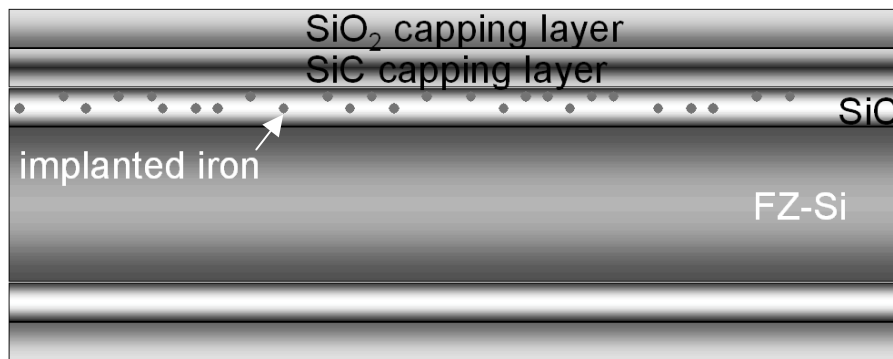


Figure 6.2: Setup of the multi layer stack for the diffusion experiments with the implanted iron atoms in the SiC layer.

Therefore the SiC layer was deposited on a silicon FZ wafer. To achieve a more realistic layer network the temperature treatments appearing during the RexWE process (see chapter 7) were simulated by one pre-annealing step. In this annealed layer iron was implanted afterwards. Before depositing a SiO₂ layer on both sides of the wafer to enclose the layer stack during the diffusion annealing and to prevent iron from contaminating the furnace, a SiC layer was deposited on the front-side. During the second annealing the iron concentration profile changed and could be determined afterwards with a Secondary Ion Mass Spectroscopy (SIMS) measurement (see Appendix A). By comparison of the SIMS measurements before and after annealing and the simulated data the diffusion constant of iron in SiC can be extracted.

6.2.1.1 Substrate, SiC-layer, pre-annealing,

To have a pure substrate we used float zone (FZ) silicon wafers with a polished surface. The wafer was doped with boron (10^{13} cm^{-3}) and had a thickness of 300 μm . Before depositing the SiC layer we cleaned the wafer with a so called RCA cleaning (standard cleaning procedure in high efficiency silicon solar cell processing) which removed all organic and metallic impurities from the surface. For the deposition of the 470 nm thick SiC barrier layer we used the process for stoichiometric layers (see chapter 1). The pre-annealing procedure should change the SiC layer network as it is done during the silicon seeding layer deposition. It has to be confessed that this pre-annealing leads to a non-realistic situation compared to the much more complicated layer reorganisation and diffusion process during silicon seeding layer deposition. And also the recrystallisation process, where liquid silicon is in direct contact with the SiC diffusion barrier layer, is not simulated with this pre-annealing. Nevertheless

the pre-annealing can provide the hydrogen effusion and the SiC network reorganisation.

We just imitated the temperature profile ($\approx 1000^\circ\text{C}$ for 5 min) of the silicon deposition furnace in a similar furnace and used an argon atmosphere. After this pre-annealing the SiC layers showed several cracks (see chapter 5) which caused problems for the further processing. Along the cracks a faster diffusion process had to be expected. From investigations which were finished after the diffusion experiments we learned that the SiC layers on smooth silicon wafers can have a maximum thickness of ≈ 300 nm. As these thicknesses would have been too thin to measure a reasonable broadening of the iron contamination profile the cracking was a problem we had to cope with.

6.2.1.2 Implantation

In order to get a high concentration of iron atoms with a Gaussian concentration profile in the SiC layer we used an ion implanter. With the freeware software SRIM [98] we simulated the desired implantation parameters. The depth of implantation could be provided by the ion acceleration energy. But the higher this energy is chosen the broader the profile gets and the more defects are introduced into the layer network [103]. To have a maximum broadening effect a very narrow profile is preferable but the maximum resolution of the SIMS measurements is around 10 nm. Furthermore there was no information available about implantation in amorphous SiC layers of our kind. All these aspects had to be considered when choosing the right ion acceleration energy.

In Figure 6.3 one can find the penetration depths and the full width half maximum (FWHM) values in dependence of the implantation energy. We used 100 keV because we found it a good compromise with a simulated mean penetration depth of ≈ 80 nm and a FWHM value of ≈ 60 nm.

The dose of implanted iron atoms should be as high as possible for the SIMS measurements. As the detection limit is 10^{15} cm^{-3} as many concentration values as possible should be above this level. On the other side a too high amount of iron in the layer's network can lead to precipitates which can form iron-complexes. Therefore we chose a maximum iron concentration (through time of implantation) of $7 \times 10^{18} \text{ cm}^{-3}$.

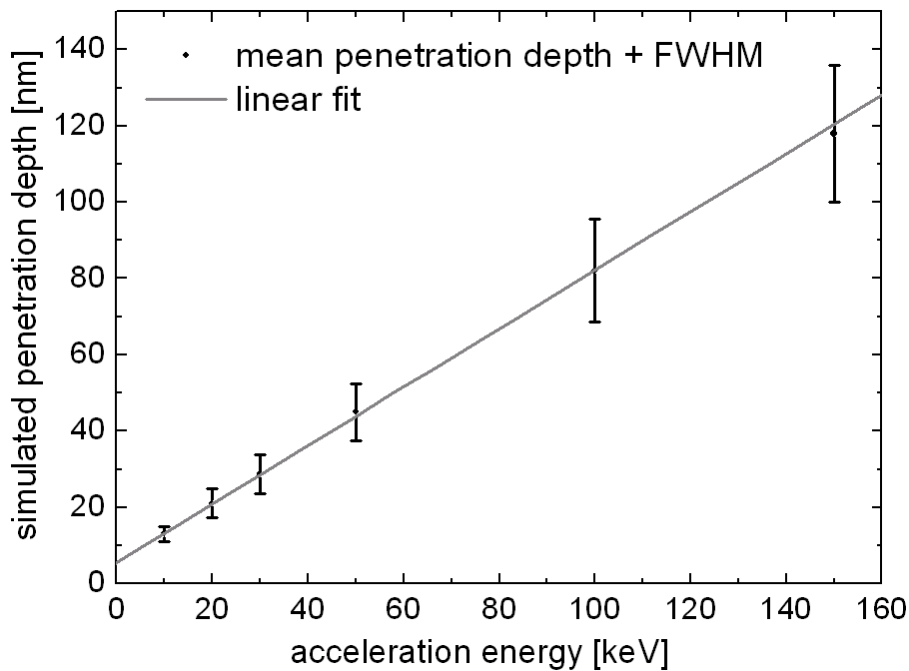


Figure 6.3: Simulated implantation profile (with SRIM) of Fe in SiC with penetration depth and full width half maximum (FWHM) of the profile for different acceleration energies.

6.2.1.3 Diffusion annealing

The SiC diffusion barrier has to withstand several temperature treatments in the recrystallised wafer equivalent (RexWE) process (see Table 6.2). Throughout all these procedures it should prevent as much iron as possible (and other impurities) from diffusing into the silicon bulk material. As mentioned above the silicon seeding deposition was simulated with a pre-annealing step to transform the SiC layer network. The temperature here was relatively low compared to the other steps. The second high temperature procedure is the recrystallisation of this seeding layer. Thereby a liquid silicon ($>1400^{\circ}\text{C}$) zone is moving over the layer. This process, as already mentioned above, cannot be simulated with an annealing because the silicon wafer in the diffusion setup would also melt. Furthermore, the situation is much more complicated because a dissolving procedure between SiC layer and liquid silicon takes place which changes diffusion and segregation conditions completely. Additionally the iron in the liquid phase is accumulating there because the more iron is in the silicon the lower the melting point of silicon gets. The third high-temperature procedure is the epitaxial growth of silicon at 1200°C .

Table 6.2: Process temperatures and times occurring in the ReWE process.

process temperatures [°C]	RexWE process	process time [min]
960	Si seeding deposition	5
>1400	recrystallisation	0.5
1200	Si epitaxy	8

We focused our investigations on an annealing temperature of 1200°C. The starting diffusion parameters (E_A and D_0) were assumed to be in the range of the parameters for SiN_x. The calculated time of 60 min should lead to an optimum broadening of the concentration profile (with the SiN_x parameters). With annealing times of 5, 15 and 120 min an analysis should be possible as well if the diffusion constant was 2 orders of magnitude higher or one order of magnitude lower. With these parameters just a few samples lead to a maximum amount of information.

6.2.2 Simulations

The used samples had an iron concentration which was laterally homogeneous. This reduced the diffusion to a one-dimensional problem (diffusion perpendicular to the SiC layer).

The calculation of the diffusion was performed by a software that solved the First Fickian law numerically. The total diffusion time t was therefore divided into intervals dt and the total layer thickness was divided into very small cell units. From the difference in concentration between two of these cells, the stream of particles in the time period dt was calculated. This sequence increased, respectively decreased, the concentration in the unit cells. These calculations were computed for all cells and repeated iteratively.

As a starting point both, a constant concentration level and a concentration profile can be used. In our case the measured profile of the as-implanted sample was used as the starting condition. The variable parameters were the segregation coefficient between the materials, the diffusion constant and the thickness of the layers. By a

change of the diffusion constant in the SiC layer, the simulated profile had to be fitted to the profile measured with SIMS.

6.2.3 Results

When interpreting the SIMS measurements one has to consider that the standard SIMS setup can only measure the e/m -ratio. That means a decrease in resolution when the analysed element has the same or a multiple atomic mass as the substrate material. Iron (^{56}Fe) has almost exactly double the mass of the silicon (^{28}Si) atom. At different grades of ionisation we get therefore the same e/m -ratio. To avoid this situation we used the ^{54}Fe isotope. For other details concerning the SIMS analyses see Appendix A. The electrical isolating SiO_2 capping layer had to be removed with hydrofluoric acid (HF) before the SIMS measurement to avoid a charging of the sample's surface.

Table 6.3: Diffusion temperatures and times for the 4 samples measured with SIMS.

sample	diffusion temperature [°C]	diffusion time [min]
Ref		
1	1200	5
2	1200	15
3	1200	60

The reference was the first sample to measure. In Figure 6.4 one can see the comparison of the simulated and the measured Fe concentration profile. Two differences have to be noticed. The measured FWHM value of the implanted curve is surpassing the simulated one by 12%. On the other side the maximum concentration of the implanted curve ($1 \times 10^{19} \text{ cm}^{-3}$) is significantly higher than that of the simulated one ($7 \times 10^{18} \text{ cm}^{-3}$). The integration over the whole areas below the two curves leads to the result, that the implanted dose surpasses the simulated one by around 50%.

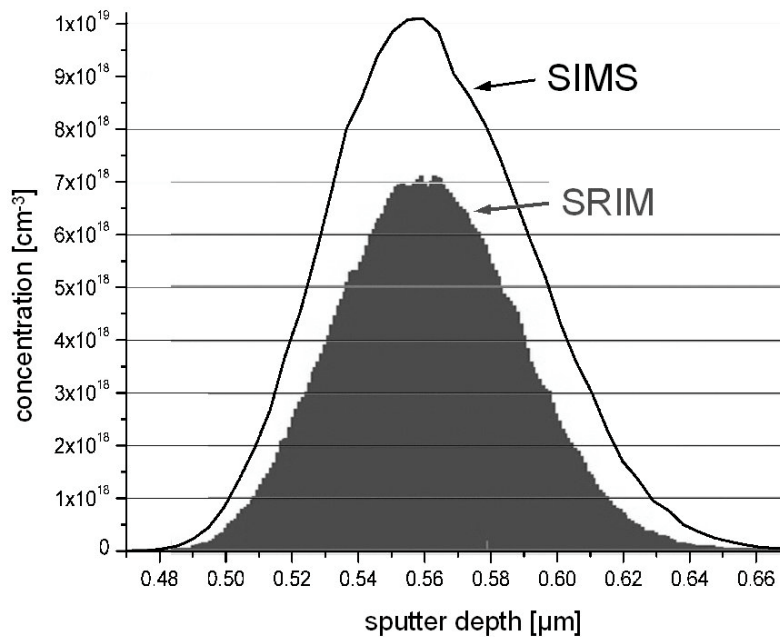


Figure 6.4: Simulated implantation profile of Fe in SiC (with SRIM) and the profile measured with SIMS.

As the layer thickness of the different samples was not exactly the same, the curves had to be shifted into the right position. As an indicator a carbon measurement (monitor signal) parallel to the iron measurement was used. Between the two SiC layers a small carbon peak can be found. This can be explained by a possible damage of the layer during implantation. In Figure 6.5 one can find all SIMS measurements of the different iron concentration profiles.

One significant feature of all measurements is the sharp bend between the two SiC layers. No simulation supposing a two layer system with two identical layers could approximate this trend. We came to the conclusion that network defects caused by iron implantation are the best explanation for this behaviour.

As it was quite difficult to simulate the whole curve from silicon substrate into the SiC capping layer we divided the total profile into different regions. They can also be found in Figure 6.5 and were as follows: (1) plateau in the implanted SiC layer, (2) transition between the two SiC layers and (3) slope in the SiC capping layer.

After many simulations for the different regions in the different layers we had to accept, that the data could not be conciliated. The layers have significantly differing diffusion behaviour which, from our point of view, can only be explained by cracks in the layers. Depending of the measured position on the sample it is not guaranteed

that the measured area is crack free. When hitting a crack the diffusion constant is extremely increased because of the enormous diffusion velocity of metallic impurities along these cracks.

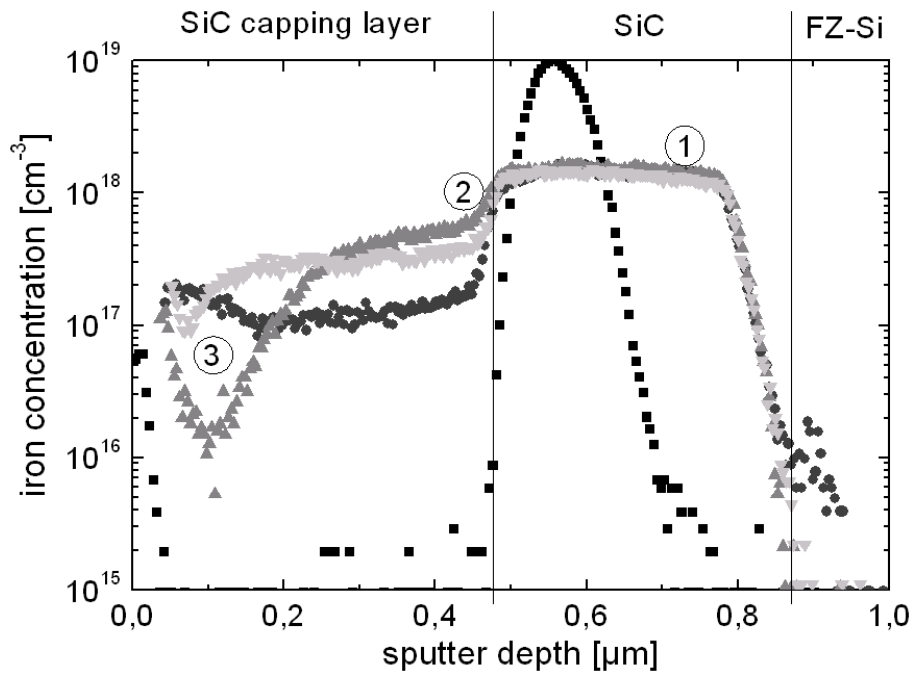


Figure 6.5: SIMS measurements of the iron concentration profiles in the layer stack before (black square) and after annealing at 1200°C for 5 min (dark grey circle), 15 min (grey triangle) and 60 min (light grey triangle).

Nevertheless the following conclusions of all these results can be made:

- The diffusion in region 1 is very fast and leads to diffusion constants in the range of 10^{-12} cm²/s. That could be explained by an already cracked SiC layer during implantation and a damage of the layers network during the implantation.
- In region 2 the diffusion constants for the experiments for 15 min and 60 min differ by one order of magnitude. This can be explained by more cracks inside the measured area of the 15 min sample.
- In region 3 the diffusion constants differ again (but at a lower level) by one order of magnitude. Here the different damage generation or again cracks can be a possible explanation.

Table 6.4: Overview of all results concerning the diffusion constant of iron in SiC for the different regions in the layer stack.

region	diffusion time [min]	diffusion constant D [cm²/s]
overall diffusion	15	1×10^{-13}
1	5, 15, 60	$\geq 1 \times 10^{-12}$
2	15	3×10^{-14}
	60	3×10^{-15}
3	5	5×10^{-15}
	15	2×10^{-15}
	60	4×10^{-16}

Nevertheless, the diffusion constant for crack free regions is most probably in the range of 10^{-15} to 10^{-16} cm²/s. This is an excellent value when comparing it to other amorphous layers (see Table 6.4) like SiN_x (3×10^{-14} cm²/s) and SiO₂ (7×10^{-13} cm²/s). It is true that the diffusion experiments did not run as well as expected but after understanding the cracking behaviour of the SiC layer at high temperature (see chapter 5) we are able to use the SiC layer for its original application in the recrystallised wafer equivalent (see chapter 7). Just by reducing the SiC thickness below 400 nm, cracking of the layers can be prevented (on polished surfaces). On rough substrates like our RBSiC ceramic substrates the SiC layer can even be processed (without cracking) with thicknesses up to 1000 nm. This thickness should be highly sufficient to avoid transition metal diffusion from the contaminated substrate into the silicon cell bulk material.

6.3 Out-diffusion of Boron at High Temperatures

In chapter 4 we measured (with SIMS) very high amounts of boron and phosphorous (10^{20} cm⁻³) in our SiC layers. There the enhancement of the electrical conductivity was our aim. In connection with this topic we already discussed activation of the dopant atoms with temperature. Another process which is extremely

dependent on temperature is diffusion, as presented above. Not only diffusion inside SiC, but also effusion of dopant atoms into surrounding layers can be very interesting for possible applications of SiC (e.g. in-situ BSF). Therefore, in this chapter the application of SiC as a source for boron will be discussed in detail. The major work of this chapter was done in connection with the diploma thesis of Dominik Suwito [104] realised under my supervision.

6.3.1 SiC on a silicon wafer

First diffusion experiments were done on a model system, where we used a silicon Czochralsky wafer ($3 \times 10^{15} \text{ cm}^{-3}$ of boron) as a substrate and deposited a boron doped SiC layer on it. The boron concentration in the 300 nm thin layer as deposited was $6 \times 10^{19} \text{ cm}^{-3}$ (SIMS data). The further processing of this test system was closely related to the recrystallisation process (ZMR) used for the Recrystallised Wafer Equivalent (RexWE, see chapter 7). We varied scan speed and subsequent annealing time. The other parameters used in the ZMR furnaces (power of large area heater- and melting lamp-power) were the same as we usually used for standard recrystallisation processes.

When liquid silicon got in direct contact with the doped SiC layer a certain amount of boron (dependent on scan speed/contact time) was dissolved in the silicon. Due to the very high diffusion constant a homogeneous distribution took place almost immediately. The higher the scan speed was adjusted the less deep was the melting into the wafer. With 10 mm/min 130 μm and with 100 mm/min just 10 μm could be molten. According to this fact the concentration of boron was increasing. By integration of the boron concentration over the molten silicon volume just a minor dependence of contact time (liquid Si/SiC) and the amount of solved boron could be found.

6.3.2 Characterisation methods

For the characterisation of the doping profiles two different analysis methods were used: (1) spreading resistance profiling (SRP) [105], a frequently used method at Fraunhofer ISE to measure boron concentration in high temperature deposited silicon layers and (2) secondary ion mass spectroscopy (SIMS) as a reliable standard method for highly resolved measurements.

Several experiments with SRP on thin layer systems and on layer systems consisting of different materials showed the limitations of this method. As the method is based on a conductivity measurement the change of material within one measurement (difference in specific resistance), thin layer stacks (undefined current paths) and surfaces (charging and undefined current paths) cause several problems. Besides that, the direct comparison between SIMS and SRP data must be handled carefully, because SIMS measures the boron concentration and SRP calculates the free carriers (all electrical active dopants and impurities) in the material.

6.3.3 SiC as an intermediate layer

6.3.3.1 SRP on annealed layer stacks

The second step was to look at SiC as an intermediate layer in a silicon stack system as it is normally used in the RexWE process. The silicon substrate was again a Cz wafer with a boron concentration of $9 \times 10^{14} \text{ cm}^{-3}$. The 300 nm thick SiC layer contained boron with a concentration of about $1 \times 10^{19} \text{ cm}^{-3}$. The 8 μm thick so called silicon seeding layer was deposited at 960°C ($1 \times 10^{14} \text{ cm}^{-3}$). After sample preparation we annealed the layer stack at 1350°C for 1 h.

In Figure 6.6 one can see the SRP measurement of the layer stack as deposited (black) and after annealing it at 1350°C (grey). Starting with the interpretation of the data in the seeding layer (left) one can find boron concentrations of $3 \times 10^{13} \text{ cm}^{-3}$ in the as-deposited and $4 \times 10^{15} \text{ cm}^{-3}$ in the annealed one. The decreasing concentration, when coming closer to the SiC layer, most probably is a method connected measuring artefact. The SRP analysis is based on the assumption of an infinite layer thickness. When coming closer to another material (bevelled section) with different transition resistivities and a differing specific resistivity the electric current paths are strongly influenced.

Especially in our case (large difference in electrical resistance) the current flows most probably mainly in the silicon layer and therefore the measured resistivity increases when approaching the SiC layer. The measured boron concentrations in the SiC layer itself cannot be measured. In the silicon substrate the measured boron concentration in the as-deposited case of $9 \times 10^{14} \text{ cm}^{-3}$ fits well to the manufacturer data. The annealed sample shows a boron concentration starting from $9 \times 10^{16} \text{ cm}^{-3}$ and decreasing to $9 \times 10^{14} \text{ cm}^{-3}$. Although we do not know exactly the boron concentrations

in the SiC layers a difference in concentration and therefore a segregation coefficient of $m_{\text{SiC/Si}} = c_{\text{SiC}}/c_{\text{Si}} \geq 10$ can be extracted from this data.

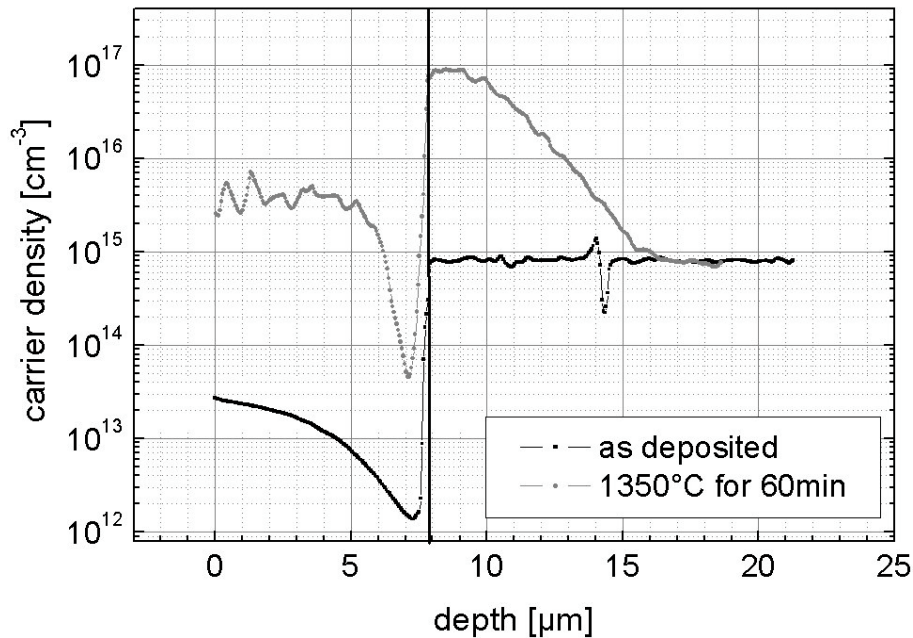


Figure 6.6: SRP measurements of the Si (left)/SiC (black vertical line)/Si (right) layer stack as deposited (black) and after an annealing procedure at 1350°C for 1 h (grey).

6.3.3.2 SRP on recrystallised layer stacks

The layer stack for the recrystallisation analysis was realised quite similar to the layer stack used above just completed by a 2 μm thick SiO_2 capping layer deposited with plasma enhanced chemical vapour deposition. Additional differences were the boron concentrations of the SiC layer ($6 \times 10^{19} \text{ cm}^{-3}$) and the Cz substrate ($2 \times 10^{15} \text{ cm}^{-3}$).

The interpretation of the SRP measurements proves to be very difficult because of the sensibility of the recrystallisation process. The bevelled section shows clearly, that the complete seeding layer is recrystallised. The substrate, on the other side, was just locally molten and therefore the boron concentration is also strongly differing depending on the position of measurement. Nevertheless the concentration in the recrystallised seeding layer increases to $7 \times 10^{17} \text{ cm}^{-3}$. The boron concentration in the substrate jumps from $2 \times 10^{15} \text{ cm}^{-3}$ (not molten) to $1 \times 10^{19} \text{ cm}^{-3}$ (molten).

6.3.3.3 SIMS on recrystallised layer stacks

When characterising similar stack systems with SIMS we could not use exactly the same samples due to a relatively rough surface. When sputtering the samples from top to bottom a rough surface meant measuring the concentration in different depths (blurred signal). Therefore we had to prepare new layer stacks on a polished Cz substrate. The initial boron concentrations before recrystallisation were as follows: Cz silicon ($2 \times 10^{15} \text{ cm}^{-3}$), 300 nm SiC layer ($6 \times 10^{19} \text{ cm}^{-3}$) and 15 μm silicon seeding layer ($1 \times 10^{14} \text{ cm}^{-3}$).

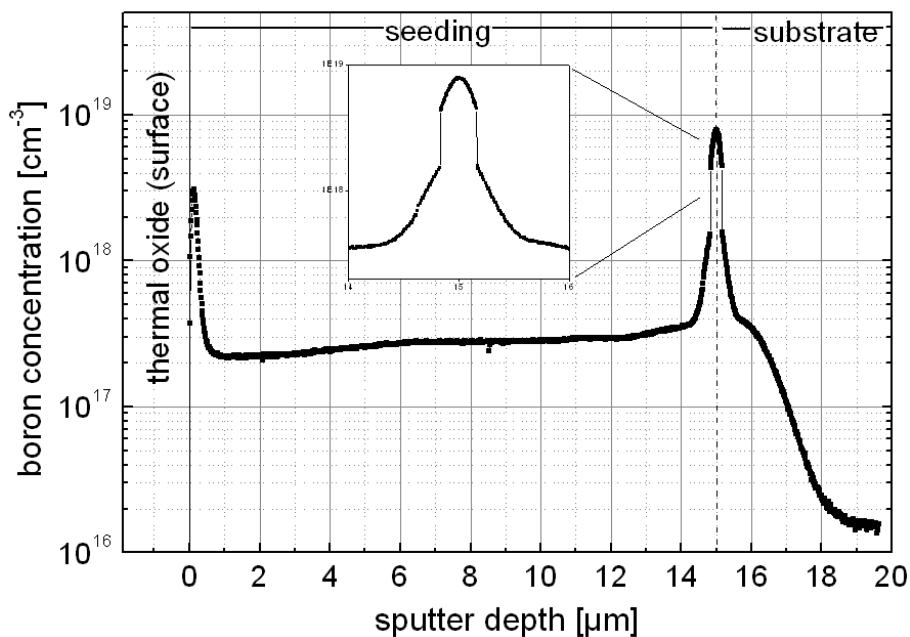


Figure 6.7: SIMS measurements of the Si/SiC/Si layer stack after recrystallisation and an additional annealing procedure at 1250°C for 10 min.

In Figure 6.7 one can see the SIMS data of the recrystallised layer stack. After recrystallisation an annealing procedure (1250°C for 10 min) was attached to get additional information about solid state diffusion. On the left side of the graph a significant boron concentration peak between seeding layer and oxide capping can be observed. This seems to be a segregation effect. The boron concentration in the recrystallised seeding layer keeps almost constant at $3 \times 10^{17} \text{ cm}^{-3}$. The boron concentration in the SiC layer is determined at $8 \times 10^{18} \text{ cm}^{-3}$. The step in the data above and below the SiC layer comes from a difference due to calibration (different ionisation rate dependent on surrounding network). The different sputter rates

influencing the thickness measurements have been corrected. The boron profile in the Cz substrate starts at the same boron level as the seeding layer and decreases to around $1 \times 10^{16} \text{ cm}^{-3}$. This effect can only be explained by a melting of the substrate during recrystallisation (in a depth of around $100 \mu\text{m}$) and a subsequent solid state diffusion afterwards. The segregation coefficient between SiC and Si calculated from this data is in the region of 20.

6.3.3.4 SIMS on annealed layer stacks with SiC double layers

The boron concentrations in recrystallised silicon seeding layers seem to be dominated by the contact between liquid silicon with the highly doped SiC layer. Almost independently from scan speed the SiC layer acts as an infinite boron source and boron is solved and spread immediately in the liquid phase.

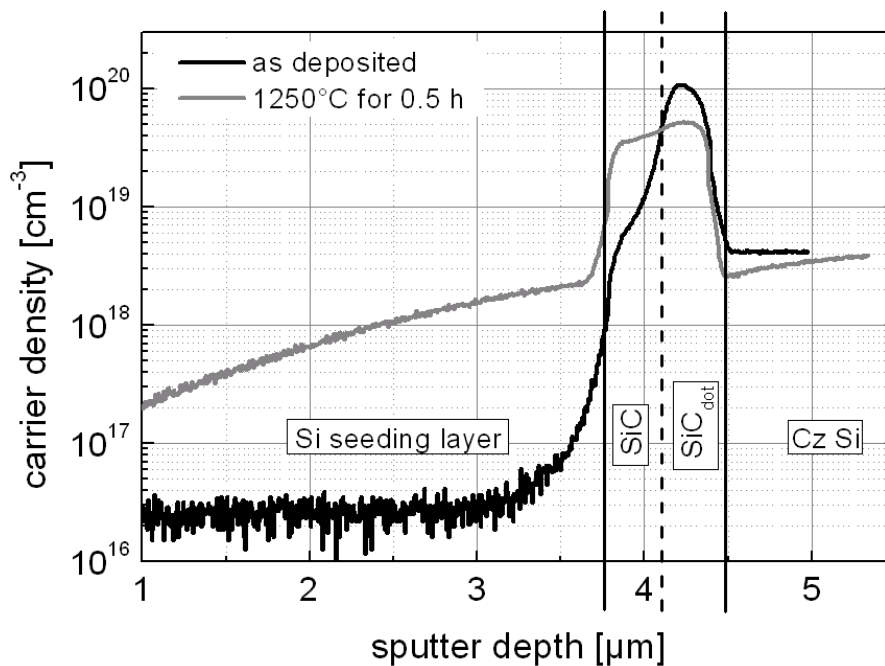


Figure 6.8: SIMS measurements of the Si/SiC/SiC/Si layer stack before (black) and after annealing (grey) at 1250°C for 30 min.

To avoid this direct contact an undoped SiC layer (300 nm) was deposited on top of the doped one (300 nm). During recrystallisation a direct contact between liquid silicon seeding layer and the highly doped SiC layers should thereby be intercepted. Unfortunately the undoped SiC layer was already partly doped during seeding layer deposition (950°C for 10 min) by the adjacent highly doped SiC layer.

This doping effect can be observed in Figure 6.8. The doped SiC layer in the as-deposited case (right) shows a boron concentration of around 10^{20} cm^{-3} . Although the boron concentration in the initially undoped SiC layer (left) is significantly lower, a level of around 10^{18} cm^{-3} can be assumed. The relatively high boron concentration in the silicon seeding layer has another origin. As previous silicon depositions in the RTCVD furnace used high diborane (B_2H_6) flows an unwanted auto-doping is most probable.

After annealing the layer stack at 1250°C for 30 min the seeding layer has a gradient in concentration profile. In the SiC stack itself the initially doped layer impoverishes and the initially undoped layer is “filled” with boron ($4 \times 10^{19} \text{ cm}^{-3}$). The segregation coefficient between silicon and SiC extracted from these data is again in the region of 20.

6.3.4 Simulations

A more detailed analysis of the SIMS measurements, and here especially the diffusion constant and the segregation coefficient in SiC, were made with the diffusion simulation program already introduced in chapter 6.2.2. All simulations done concentrated on the SIMS measurement presented in chapter 6.3.3.4.

The broadening of the boron concentration profile had to be separated in two simulation steps: (1) boron diffusion during the silicon seeding deposition and (2) annealing at 1250°C .

The effective diffusion time of the first step was assumed as 13.5 min because heating and cooling had to be considered. Through an adequate free parameter assumption the SIMS profile should be simulated as good as possible. The diffusion constant of boron in silicon is known from literature. For the two SiC layers equal diffusion constants were assumed. This implies a concentration independent diffusion constant for the SiC layers. The segregation coefficients between SiC and the two silicon layers were assumed to be different. Considering the micro crystallinity of the seeding layer and the mono crystallinity of the Cz substrate this seemed to be arguable. The best fit was still not perfectly congruent with the measured SIMS profile. Nevertheless the diffusion constant of boron in SiC (at 950°C) calculated from these data is $1 \times 10^{-13} \text{ cm}^2/\text{s}$.

The simulation of the annealing process data show comparable problems. Assuming a temperature of 1250°C and a diffusion time of 30 min the simulated data cannot be fitted perfectly to the simulated ones. Nevertheless, the diffusion constant of boron in SiC at 1250°C of $8 \times 10^{-13} \text{ cm}^2/\text{s}$ is calculated.

The diffusion in SiC seems to be relatively fast. Unfortunately no data for amorphous and partly crystalline SiC layers could be found in literature. The data for crystalline SiC show a wide range of values from 10^{-14} to $10^{-24} \text{ cm}^2/\text{s}$ [104]. Possible explanations of the problems with our SIMS data would be a cracking of the SiC layer and a concentration dependent diffusion constant. Although no cracks can be found in cross sections, the relatively thick SiC layer stack (600 nm) and the polished substrate surface together let this explanation be the most probable one. The concentration dependent diffusion constant can be explained by boron cluster formation at too high concentrations and therefore different diffusion mechanisms as assumed.

6.4 SiC as a Hydrogen Source

Hydrogen plays an important role for several applications in photovoltaics. Especially bulk and interface defects in silicon can be effectively passivated with it. Due to its very small atomic size, very high diffusion velocities are possible. In amorphous SiC layers significant amount of free hydrogen and bonded hydrogen is expected in the layers deposited below 550°C. In this chapter the hydrogen effusion of bonded and free hydrogen will be discussed.

6.4.1 Hydrogen bonds in SiC layers

In chapter 5 we already described the annealing behaviour of the SiC layers. Especially the FTIR measurements brought a lot of information about the temperature driven molecule cracking and the new formation of Si-C bonds. In this section we want to focus on the hydrogen related bonds to Si and C [106]. Not only Si-H_x and C-H_x bonds but also more complex molecule chains are expected to be present in the SiC network. The formation processes of these complex chains are not known in detail. It is expected that not only reaction products of the precursor gases SiH₄ and

CH₄ are connected to new chains but that much more complicated processes play also an important role.

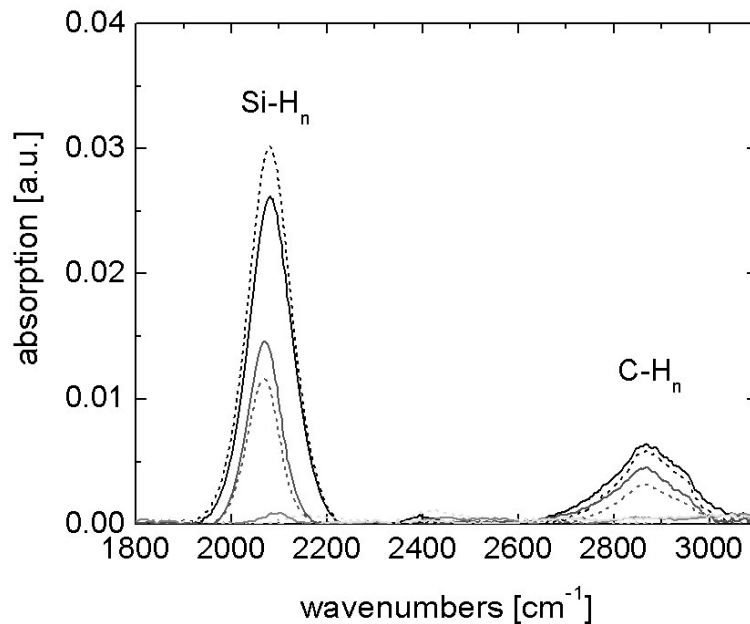


Figure 6.9: FTIR measurement of boron doped (dashed) and undoped (solid) SiC layers deposited at 350°C and annealed at 550°C (dark grey), 750°C (grey) and 1050°C (light grey) for 2 h under N₂-atmosphere.

In Figure 6.9 the two important hydrogen related peaks corresponding to the C-H_n stretching mode at 2870 cm⁻¹ and the Si-H_n stretching mode at 2080 cm⁻¹ can be observed. The two different SiC layers are undoped (solid) and doped with boron (dashed). Surprisingly the Si-H signal of the doped layer is relatively higher though the layer thickness is a little bit below that of the undoped one. This is the only evidence that adding doping gases (B₂H₆, PH₃) might influence the layer growth process. Comparing the layers as deposited with annealed ones, the beginning hydrogen effusion can be detected. The Si-H bond has a much lower activation energy (0.44 eV) and shows a much higher signal decrease after the annealing at 550°C than the C-H_n bond (1.3 eV) [107]. This means in numbers that already 73% of the Si-H bonds (area under the curve) are cracked after the 550°C annealing for 2 h and in comparison only 39% of the C-H_n ones (undoped layers) are so too. It is most interesting to see that the Si-H peak of the doped layer decreases much more than that of the comparable undoped SiC layer. This effect could not be explained yet. After the annealing at 750°C the hydrogen related absorption peaks vanishes completely.

Table 6.5: Hydrogen related FTIR absorption peaks of an undoped layer and its relative decrease with annealing time.

layer status	Si-H	C-H _n
as deposited	100%	100%
550°C for 1 h	36%	67%
550°C for 4 h	25%	47%
550°C for 24 h	17%	41%

The next step in our investigation was to increase the annealing time (see Table 6.5). Extending the annealing time from 4 h to 24 h still leads to a difference in hydrogen related absorption peaks. This points out that SiC layers can be seen as source for hydrogen for several hours at temperatures around 550°C or for some minutes in higher temperature regions.

6.4.2 Hydrogen effusion out of Si_xC_{1-x} layers

The absolute content of hydrogen in materials cannot be determined without greater effort [108-110]. Because of its high mobility hydrogen atoms are hard to detect and therefore deuterium is e.g. often used for several characterisation methods. But especially for our surface passivation layers (Si_xC_{1-x}), this hydrogen content is of enormous importance. Due to lack of time we used a qualitative method to find out about the hydrogen content of our Si_xC_{1-x} layers. The idea was to compare the bulk passivating effect of hydrogen coming out of SiN_x (which is well known) with the bulk passivation effect of Si_xC_{1-x}. Therefore we deposited layers which were used for excellent surface passivation (see chapter 8) and compared them, in a test structure, with highly hydrogen containing SiN_x passivation layers. The differences in minority carrier lifetimes in these multi crystalline silicon wafer should then give us an idea of the bulk passivation performance of our passivation layers.

6.4.2.1 Test structure

The three different test structures used for this investigation can be seen in Figure 6.10. Multicrystalline silicon wafers (125x125 mm²) cut from the same ingot were passivated on the front-side with thick thermal oxide (100 nm).

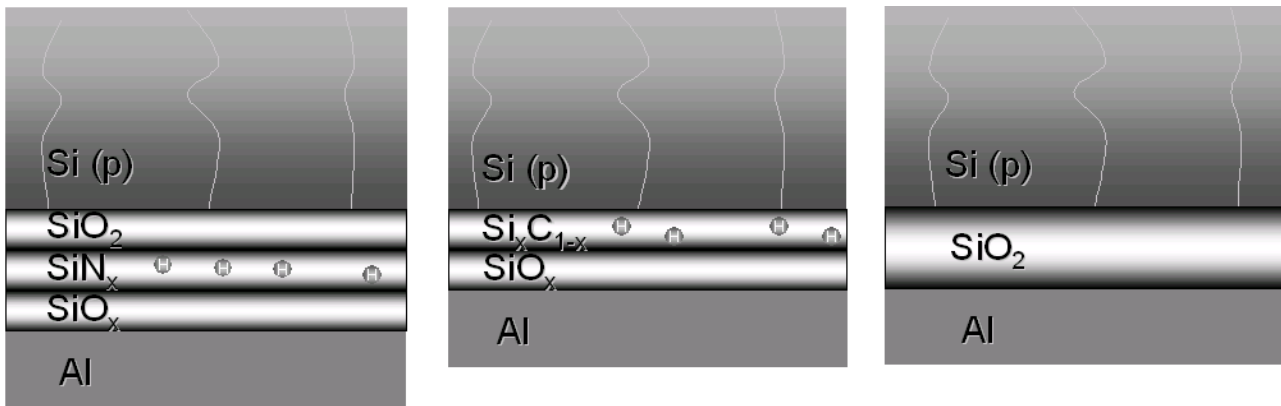


Figure 6.10: Three different rear side passivation structures A (left), B (middle) and C (right) to compare hydrogen effusion from the passivation layer stack into the multi crystalline silicon bulk.

After removing the thick oxide from the rear-side of concept A (left picture) a thin wet oxide (10 nm) was grown on all wafers. This guaranteed the same thermal budget for all wafers (detrimental for minority carrier lifetimes in the bulk material). After this thin oxide a 50 nm thick SiN_x with high hydrogen content and subsequently a 100 nm thick SiO_x layer were deposited with plasma enhanced chemical vapour deposition (PECVD). The rear-side passivation of concept A was now finished. From the wafers of concept B (middle picture) the thermal oxide was removed from the rear-side. After an in situ plasma cleaning procedure, which will be introduced in chapter 8, a 100 nm thick Si_xC_{1-x} passivation layer and a 500 nm thick SiO_x layer were deposited. The wafers of concept C had a thermal oxide layer with a thickness of ≈100 nm on front- and rear-side and acted as references for the characterisation methods. An effusion of hydrogen out of these layers could not be expected.

6.4.2.2 Experiments

After finishing the rear-sides the firing procedure was applied. This process should simulate the firing step of screen printed contacts, which is frequently used in solar cell fabrication. Therefore the samples were transported through an 800°C hot firing furnace (≈3 s). After depositing 2 μm of aluminium (with an e-gun process) on the rear-side another sintering at 350°C for some minutes was done to enhance the passivation performance of the thermal oxide.

With emission CDI [111] we could measure now (spatially resolved) the minority carrier lifetimes in the samples.

6.4.2.3 Results

The parallel processed lifetime samples on FZ material which should act as references show for all three concepts sufficient surface passivation in the region of some 100 nm. Therefore we can be sure that the measured lifetimes on our multi crystalline wafers are limited by the bulk recombination. In Figure 6.11 one can see the lifetime measurements for the three best wafers from each concept.

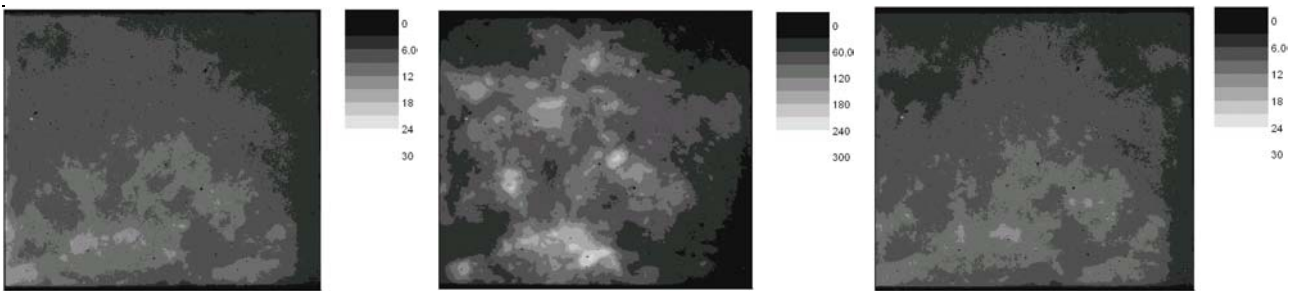


Figure 6.11: Carrier density imaging (emission mode) for the three different rear side passivation structures A (left), B (middle) and C (right) to compare hydrogen effusion from the passivation layer stack into the multi crystalline silicon bulk.

When comparing concept C (thermal oxide) and concept A (SiN_x stack) one can find increased lifetime values in the SiN_x passivated samples. This is an expected behaviour because the oxide should provide no hydrogen for silicon bulk passivation. The increased lifetimes in concept A therefore proves that out of the SiN_x , hydrogen diffuses into the silicon bulk. Surprisingly the difference in lifetimes between concept A and C is quite small.

When comparing the lifetime measurements of concept A and B the map for concept B shows a completely white wafer. Therefore the maximum range of values had to be changed from 30 μs to 300 μs for concept B. Within the measurement's error ($\approx 10\%$) the maps show significantly increased lifetime values for the wafer passivated with $\text{Si}_x\text{C}_{1-x}$ layer compared to the SiN_x stack.

It is surprising that the thin oxide layer (10 nm) which should stabilise the surface passivation performance of the SiN_x stack, obviously acts as a that good diffusion barrier for hydrogen. Otherwise the enormous discrepancy in bulk passivation between $\text{Si}_x\text{C}_{1-x}$ and SiN_x cannot be explained. Nevertheless, the $\text{Si}_x\text{C}_{1-x}$ passivation layer proves impressively that it can be used as an excellent hydrogen source during firing steps.

6.4.3 Total hydrogen amount in SiC and Si_xC_{1-x} layers

The comparison of relative hydrogen amounts (total amounts) in the different SiC layers could be realised by measuring with time-of-flight (ToF) SIMS (see Appendix A). For this we deposited the different silicon carbide layers on FZ silicon substrates. The comparison of SiC and Si_xC_{1-x} layers shows 23% less total hydrogen content in surface passivation (Si_xC_{1-x}) layers. The different deposition regimes themselves show no significant changes in hydrogen contents though the deposition parameters, CH₄-flows for SiC and microwave power for Si_xC_{1-x}, were changed during deposition.

7 RECRYSTALLISED WAFER EQUIVALENT (REXWE)

The initial aim of this work was to establish SiC as a conductive diffusion barrier layer in our Recrystallised Wafer Equivalent (RexWE) concept. The previous chapters described in detail the different physical behaviours which made me optimistic that SiC is an appropriate layer. In this chapter I will present comprehensive results concerning the realisation of Recrystallised Wafer Equivalents on low-cost substrates. Furthermore solar cell results processed on these RexWEs will be discussed. At the end of this chapter the potential of our concept for future photovoltaic applications will be discussed.

7.1 Introduction

The primary idea of the Recrystallised Wafer Equivalent (see Figure 7.8) is to reduce wafer costs by a radical reduction of the used silicon amount. This wafer equivalent should be, as one could conclude from its name, as closely related to a crystalline silicon wafer referring to its suitability to be processed to a solar cell. This means that the “active” layer has to be multi-crystalline silicon. The necessary assumptions to realise such a wafer equivalent are a temperature stable substrate, a conductive diffusion barrier layer, an appropriate silicon deposition technique and a grain-enlargement method. All these processes and materials, except the conductive diffusion barrier layer, have been tested and/or developed for the last 10 years at the crystalline thin-film group at Fraunhofer ISE.

In the following sections I will briefly explain the materials and the process steps used. I will afterwards focus on my contributions to these developments which mainly consisted in the RBSiC ceramic substrate pre-treatment, the conductive SiC barrier layer, the adaptations to the zone melting recrystallisation (ZMR) and the first solar cell processes with our RexWEs.

7.2 The RexWE Process

The transition from the production of the wafer equivalent to the solar cell processing can hardly be defined. Starting with the deposition of the SiC layer we work on the optical confinement of the thin-film cell and by depositing the highly doped seeding layer we create a back surface field (BSF) layer. Nevertheless I will focus in the beginning of this chapter on the way to create a Recrystallised Wafer Equivalent and will report about solar cell processing later on in this chapter.

7.2.1 Substrates and pre-treatments

A suitable substrate for the silicon high-temperature path has to meet the following requirements: (1) temperature stability above 1400°C, (2) thermal expansion coefficient close to that of silicon and (3) sufficiently low electrical resistivity (<0.1 Ωcm). The availability and the cost-efficiency are of course as important as the preceding points but will be brought up for discussion not until the end of this chapter.

7.2.1.1 Silicon wafer as a substrate

Silicon based substrates will always play an important role for process optimisation because they are from many points of view the perfect model substrates. But it is also still a promising option to use e.g. metallurgical grade silicon wafers as “real” substrates. In my work, investigations in the field of in-situ back surface field, rear-reflector and high speed zone melting recrystallisation have been carried out on solar grade silicon wafers. The achieved results will be discussed in chapter 7.3.

Before depositing the diffusion barrier layer on the silicon wafer, a CP133 etching process was the standard cleaning procedure. By this procedure the thin native and insulating oxide and possible organic or metallurgic impurities should be removed. Except for the rear-reflector tests we started with very smooth (shiny etched or even mechanically polished) surfaces.

7.2.1.2 Reaction bonded SiC (RBSiC) ceramic as a substrate

In the last 10 years several ceramic materials such as Si₃N₄, Al₂O₃, SiC in pressed, casted or infiltrated form have been under investigation in several thin-film groups [112]. On almost all of these ceramic type wafer equivalents high quality silicon

layers could be realised. Nevertheless, the demand for electrical conductivity and high-throughput production led us to tape-casted (reaction bonded) SiC (RBSiC) ceramic substrates. Since we concentrated all efforts on this substrate type we could, in cooperation with our project partners, the University of Erlangen (Germany) and H.C. Starck ceramics in Selb (Germany), achieve significant progress concerning the following topics.

Porosity reduction (slurry mixture)

The porosity is, as we will learn in chapter 7.3, one of the main problems one has to deal with during solar cell processing. It is important to control the substrate's surface roughness to realise a good rear-reflector. Especially by simulation and following optimisation of the slurry and the casting process, amount and diameter of pores could be reduced significantly.

High throughput and large area production (tape-casting)

The tape-casting apparatus at H.C. Starck ceramics (Selb, Germany) can cast green tapes with a throughput of more than 15 m²/h. The tape width is 400 mm. Because such areas cannot be handled in the following RexWE and solar cell processes we limited the maximum substrate size to 207x207 mm². After the drying chamber the green tape is, because of the organic components, still very soft and can be cut very easily to the suitable size. To get the organic components out of the tapes again a pyrolysis at 800°C has to be done.

Sintering procedure (reaction bonding)

The standard sintering procedure started with heating up the green tapes very slowly from room temperature to 1500°C. After some hours the free silicon reacts with the carbon to new SiC grains. To minimise subsequent out-gassing during the RexWE process where it would be detrimental for the furnaces we varied the sintering atmospheres. As the substrate's mechanical stability was directly dependent on the sintering process, we also investigated different sintering temperatures (up to 2000°C) for some of the samples. As presumed, the reaction bonding process leads to a denser and therefore more stable SiC matrix compared to samples sintered at the standard temperature of 1600°C.

Optimised pre-treatment procedure

Before the ceramic could be used for the RexWE process (first step: barrier layer deposition) some pre-treatments to clean the samples had to be done. A schematic sketch can be found in Figure 7.1.

First of all, dipping in isopropanol and acetone, and subsequent rinsing in distilled water was applied. The idea was to remove organic impurities and small particles like dust. To minimise out-gassing an annealing step at 1350°C for 30 min under argon atmosphere was the next pre-treatment step. This annealing should additionally reduce possible out-gassing during the following high-temperature steps (prevent parasitic depositions in the furnaces). Finally a dry cleaning in the RTCVD furnaces (see chapter 7.2.2) under HCl atmosphere at 1200°C, with the aim to remove metallic impurities from the surface, was applied.

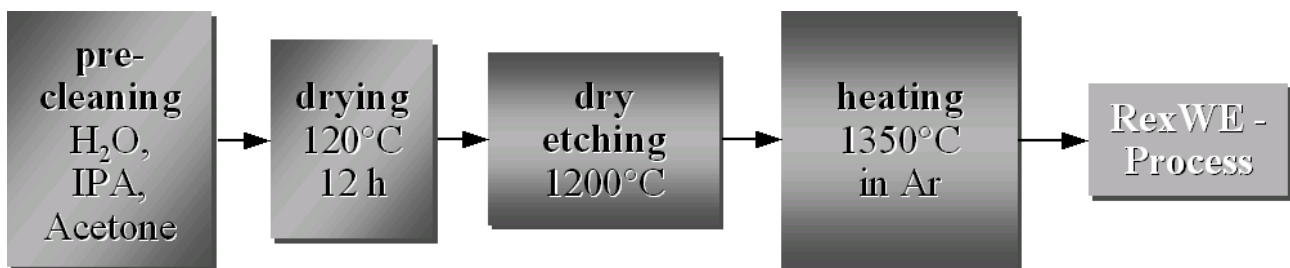


Figure 7.1: Pre-treatment procedures for the RBSiC ceramic substrate before introducing it into the RexWE process.

7.2.2 Silicon Carbide diffusion barrier layer deposition

Silicon carbide diffusion barrier layers especially developed for this application were deposited in the AK400M plasma reactor from Roth&Rau (Wüstenbrand, Germany). For details concerning deposition conditions see chapter 1. For the two different substrates (RBSiC ceramic and silicon wafer), different layer thicknesses due to different expansion coefficients and surface roughness had to be deposited (see chapter 6). For smooth silicon wafers a maximum layer thickness of 400 nm was used. With thicker layers the recrystallisation process could not be realised successfully. The situation on the RBSiC ceramic substrates appeared to be different. Due to the good agreement in expansion coefficients layer thicknesses up to 1000 nm were reasonable. Here the coverage of the pores was the problem. Although too large

open pores could not be covered completely, coverage of the grains' surfaces seemed to be sufficient. To avoid contamination of the reactors for silicon deposition and recrystallisation, the rear-side of the substrate was also capped with a SiC diffusion barrier layer.

During the end of this work the final decision for the optimum layer thickness was not made. But all investigations and the economical consideration point to an optimum thickness of around 300 nm (on both substrate types).

7.2.3 Si seeding layer deposition

At Fraunhofer ISE research activities on silicon deposition with atmospheric pressure chemical vapour deposition (APCVD) have been a major subject for years [105]. This silicon CVD is based on the deposition from process gases composed of a silicon precursor (e.g. SiHCl₃) and hydrogen gas.

We know from simulation, that with the minority carrier lifetimes achieved in our silicon grains a highly doped back surface field layer of around 5 µm would be desirable. The deposition at 960°C on our SiC layers led to very homogeneous and whisker free silicon layers. Especially on the highly contaminated RBSiC ceramic substrate this was an encouraging result. The good silicon layer quality proved that the SiC layer prevented metallic impurities from diffusing to the SiC/Si interface. Otherwise these impurities would act as seeds for whisker growth [113].

Unfortunately 5 µm of silicon seeding could not be recrystallised on the RBSiC substrates. Due to the high open porosity and the substrate's roughness we had to deposit layers with a thickness of 15 µm. After recrystallisation the thickness reduced to 5 to 10 µm because some of the silicon was soaked by the substrate. These thicknesses were again in an acceptable range regarding their back surface field effect.

7.2.4 SiO₂ capping layer

In order to prevent the liquid Si from forming drops during recrystallisation, an oxide capping layer had to be deposited on it. This thin films had a good transparency ($n=1.46$) and became relatively soft at the silicon melting point, which minimised the risk of crack formation. The standard capping layer was deposited with nitrous oxide

(N₂O) and silane (SiH₄) in a parallel plate plasma reactor. The deposited thickness was 2 μm at a deposition rate of 200 nm/min.

Taking up previous investigations regarding thin capping oxides we tried to establish a thermal oxide capping. This could be grown directly before recrystallisation inside the zone melting furnace. Assuming a homogeneous and smooth silicon seeding layer the results were promising concerning crystal size and quality. One essential advantage of a SiC barrier layer seems to be the better wetting effect of liquid silicon on it. This effect made it possible to reduce thermal oxide capping layers to a thickness of close to 100 nm. After 15 min process time at 1250°C in the zone melting recrystallisation (ZMR) reactor with a pure O₂ atmosphere this thickness could be achieved. As mentioned above this capping procedure could be done in-situ, directly before the recrystallisation itself.

7.2.5 Zone Melting Recrystallisation (ZMR)

By liquid phase recrystallisation, grain size can be increased by several orders of magnitude. During this work, this effect was used in the zone melting recrystallisation (ZMR) which was employed for grain enlargement.

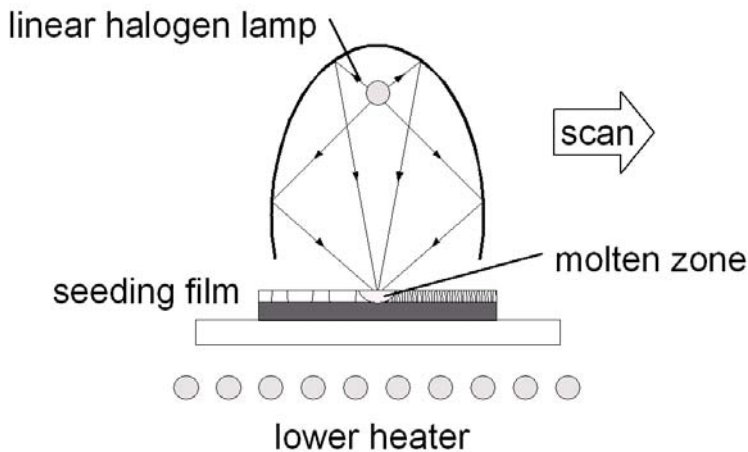


Figure 7.2: Principle of zone melting recrystallisation (ZMR) with linear halogen lamp as the heating source.

The principle of this technique is shown in Figure 7.2, where halogen lamps are used as heat sources [99]. These lamps are fixed in the focal line of an elliptical reflector and create a small molten line which is moved across the thin film. Behind the molten area the melt cools down below the melting point and heterogeneous nucleation starts. Stable crystallites develop and act as seeds for further growth. Due to

anisotropic crystal growth speed, grains with a particular crystal direction soon prevail. Grains grown by ZMR reach up to several millimetres in width and up to the substrates length (several centimetres) [99].

In connection with the very good wetting effect of the liquid silicon on the SiC layers, thermal capping led to encouraging results. As the optical absorption changed completely with the rough ceramic substrates, different process parameters for silicon and RBSiC substrates had to be chosen. In principle lower radiation intensity from the rear side was sufficient to melt the Si-layer on the ceramic substrates.

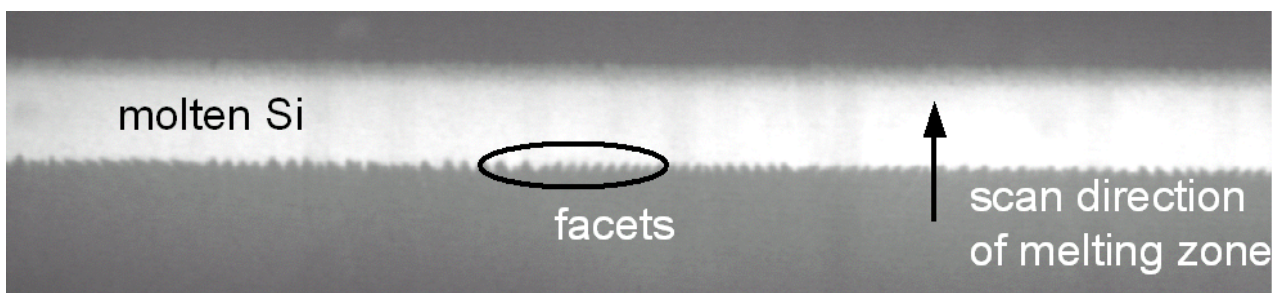


Figure 7.3: Melting zone (top view) of the silicon seeding layer on a RBSiC ceramic substrate.

Another speciality of ZMR on RBSiC ceramics was a sometimes occurring curvature of the RexWE after the recrystallisation. This curvature seemed to be scan speed dependent. Simulations of the ZMR procedure on ceramics realised by the University of Erlangen pointed to a possible cooling effect of the ceramic edges coming from the process gases. As these gases are not pre-heated before being introduced into the furnace this cooling effect could possibly lead to the substrate curvature. Another important point in connection with the temperature gradients was the radiation equilibrium in the furnace. To prevent a cooling of the substrate's edges, stripes of the same material were placed around the sample to avoid radiation losses, and thereby cooling down, of the samples.

Investigations in connection with scan speed led to the pleasant result, that higher scan speed ended up in larger silicon grains. In Figure 7.4 one can see three micrographs of recrystallised silicon layers on silicon substrates with SiC diffusion barrier layers. After ZMR a HF dip and a defect etch was done to make the grains visible. The scan speed during ZMR was 10 (left), 50 (middle) and 100 mm/min (right). The increasing crystal grain size with scanning speed is obvious. Additionally

these three layers were capped with a thermal oxide which was grown in-situ. The combination of these two results means an enormous step forward in the RexWE process chain. As capping layer deposition and scan speed are most important cost factors, this means a significant potential for cut down production cost.

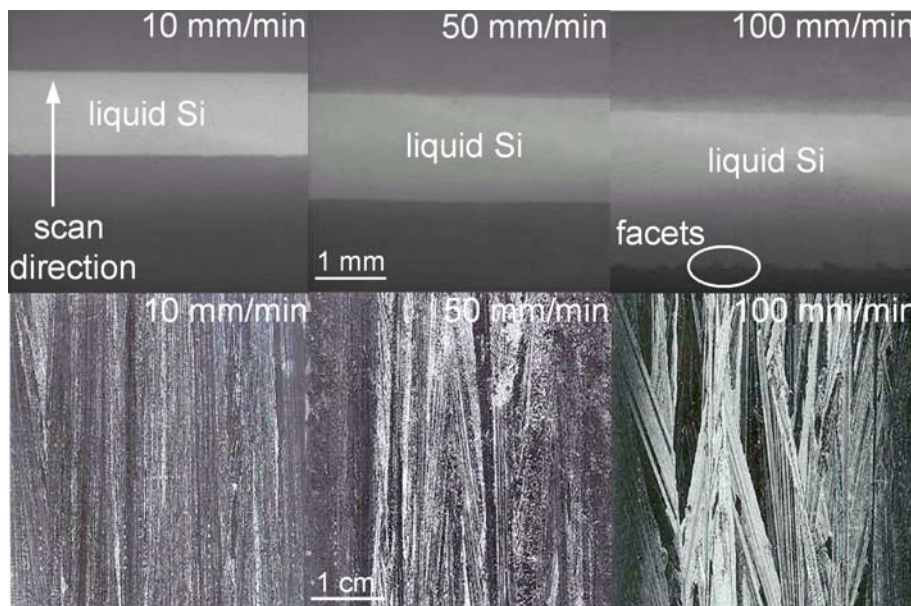


Figure 7.4: Micrographs of different melting zones and the resulting silicon seeding layers recrystallised at a scan speed of 10, 50 and 100 mm/min.

7.2.6 Capping layer removal

In order to remove the SiO_2 capping layer we used highly concentrated hydrofluoric acid HF (50%). On the samples with PECVD oxide we tested two wet chemical etching solutions for their influence on epitaxial layer growth and quality (see chapter 7.2.7). The standard procedure consisted in etching in 50% KOH for one minute. This should remove oxygen clusters and impurities in the upper microns of the silicon layers. The epitaxially grown silicon layer had a relatively rough surface after this treatment which led to problems during solar cell processing. As an alternative we tried to etch in CP73 for several minutes. This wet chemical etch removes silicon relatively slowly ($0.5 \mu\text{m}/\text{min}$) and led to smoother surfaces. Surprisingly the best results concerning surface roughness could be achieved when the samples were not additionally etched after capping layer removal with HF. However, growth of sporadic large whiskers show that the surface cleanness is not

sufficient in this case. The conclusion of these investigations is, that the removal of some hundreds of nanometers of silicon is necessary to achieve good epitaxial layer qualities.

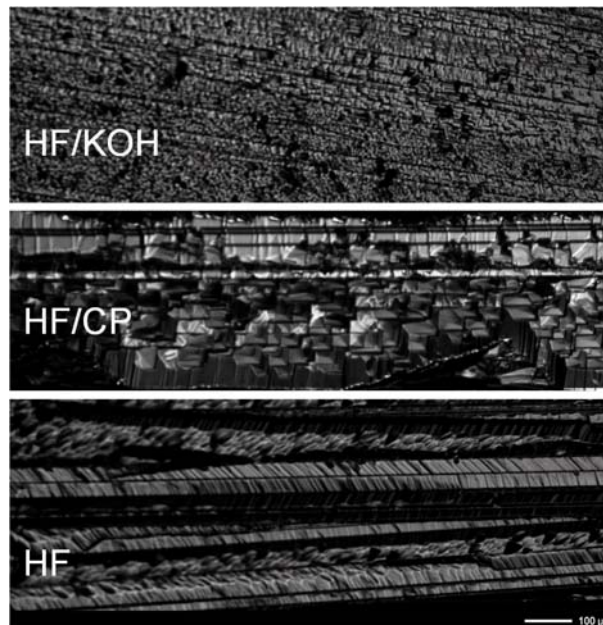


Figure 7.5: Micrographs of three epitaxial layer surfaces with different pre-cleaning procedures.

One major difference between thermally grown and plasma deposited oxide emerged when we tried to etch the capping layers. The two oxide layers seemed to be different concerning the interface of Si and SiO₂ after ZMR. Whereas the thermal oxide, maybe due to dissolving effects in the liquid silicon, had a floating transition the plasma deposited oxide was still clearly separated from the recrystallised seeding layer. The samples with a thermally grown capping oxide therefore had to be etched in KOH (50%) to remove the SiO_x in the transition zone between silicon seeding and SiO₂ layer. Otherwise an epitaxial silicon layer growth without a high amount of whiskers was impossible.

7.2.7 Epitaxial silicon layer growth

To enhance optical absorption we grew an epitaxial silicon layer on our thin recrystallised seeding layer. At a temperature of 1160°C around 15 μm of silicon were deposited. Two different doping profiles for this Si bulk layer were under

investigation. The standard layer had a constant boron doping level of $3 \times 10^{17} \text{ cm}^{-3}$. As the minority carrier lifetime in the epitaxial layers was expected to be not too high ($< 30 \mu\text{s}$), we tried to affect the carrier diffusion direction with a doping gradient profile. There, the doping level started at $1 \times 10^{17} \text{ cm}^{-3}$ and uniformly decreased to $1 \times 10^{16} \text{ cm}^{-3}$.

All silicon depositions in the RTCVD furnaces showed a significant difference in growth rate depending on the type of substrate. This could be explained with different absorption coefficients which lead to temperature differences of several degrees on the sample surfaces. The substrates were optically heated from the backside. The relatively rough and highly absorbing RBSiC ceramic could therefore reach a higher maximum temperature. Especially during the epitaxial deposition this led to a 30-50% higher layer growth rate.

7.2.8 High throughput and large area RexWE

In this chapter the maximum areas of our wafer equivalents, which could be produced with already existing furnaces, will be discussed. As wafer size enlargement is a main topic in solar cell industry, the potential of area enlargement of the RexWE is also most important for future applications and will be discussed.

RBSiC ceramic substrate

The tape-casting apparatus at H.C. Starck ceramics was able to produce tapes with a length of several meters. This would be too large for silicon solar cell processing of the nearest future. But the idea of integrating (interdigitated connected) many large cells (e.g. $20 \times 20 \text{ cm}^2$) on one ceramic substrate which is one or two meters long (corresponding to 10-20 solar cells) could be an interesting idea for low-cost module productions of the future. The ceramics substrate would thereby not only act as a substrate for the solar cells but provide the whole module with mechanical stability.

SiC deposition

The maximum area which could be coated with SiC (AK400M reactor) was $30 \times 20 \text{ cm}^2$. The transfer of the process to plasma reactors with deposition areas of $100 \times 100 \text{ cm}^2$ was already in progress but could not be concluded until the end of this work. As this transfer could be successfully realised for SiO_2 and SiN_x processes, no major problems during the SiC transfer are expected.

Si deposition and etching in the ConCVD reactor

The newest stage of RTCVD reactors development at ISE is represented by a continuous system with high throughput, the so called ConCVD. This machine enables us to deposit (at around 1000°C) a silicon layer of 10 µm thickness on an area of 5 m² in one hour time. The silicon layers deposited on SiC coated RBSiC showed no whisker growth at all which was a clear indicator for high layer quality. The HCl cleaning step of the ceramics could also be realised in the ConCVD reactor and showed as high throughput as the seeding deposition.

Recrystallisation in ZMR400con

The maximum melting width of in the ZMR400con reactor also developed at ISE is 40 cm. The length is limited by the quartz carriers needed for the sample transport (also 40 cm). The radiation losses at the edges of the samples are more serious in this apparatus than in the laboratory furnace (ZMR100) due to cold walls of the reactor. On the other hand side the large area heater has a crossed lamp field (with independent zones) which enables us to adjust the temperature gradient much more precisely. This offers additional possibilities for the process tuning. With a scan speed of 100 mm/min on RBSiC substrates a throughput of 2.4 m²/h can be achieved. Recrystallisation on large area RBSiC ceramics in the ZMR400con led to promising results (see Figure 7.6).

Current capacities at ISE

Using all the reactors described above we were able to realise a recrystallised wafer equivalent on RBSiC ceramic substrate with an area of 200x200 mm². In Figure 7.6 one can see a top view of the recrystallised silicon layer with grains as long as the substrate and up to one centimetre in width. This is an excellent result which has never been realised on such an area so far.

Calculating a 24 h day and considering all maximum throughputs of our already existing machines we would be able to produce 1.5 m²/d of RexWEs. This value is limited by the SiC deposition in the AK400M laboratory scale reactor. All the other machines are able to produce around 50 m²/d. For still laboratory scale equipment this is a high throughput and shows that a pilot production of our RexWEs with already existing reactors can be possible in the nearest future (≈2.5 MW/a already possible).

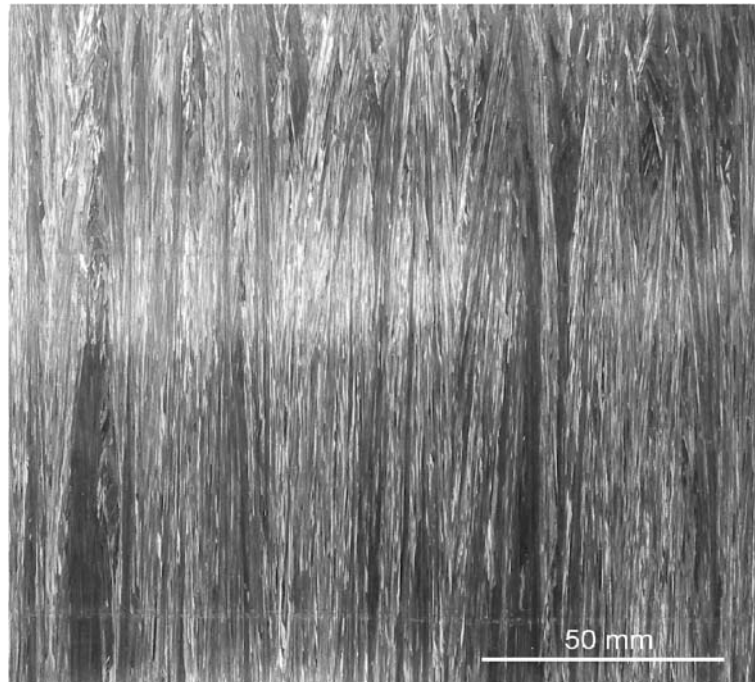


Figure 7.6: Large area recrystallised wafer equivalent (RexWE) on RBSiC ceramic substrate with an area of 200x200 mm².

7.2.9 Impurities in the solar cell material

The raw materials (Si and SiC powders) for cost efficient RBSiC ceramic substrates contain high amounts of transition metals. To avoid solid and liquid phase diffusion of these metals from substrate into the cell bulk (especially during the high temperature process steps) the SiC diffusion barrier layer covers the ceramic's surface. For the Glow Discharge Mass Spectrometry (GDMS) measurements a 1 μm thick layer was deposited in our plasma reactor (see chapter 1) with the precursor gases CH_4 (methane), SiH_4 (silane) and the doping gas B_2H_6 (diborane) to achieve sufficient electrical conductivity (see chapter 4).

In order to check the effectiveness of the barrier layer the impurity profile of the processed RexWE was determined with GDMS by sputtering from the surface of the cell bulk into the ceramic substrate [100]. We focused on Fe, V and Co concentration because these metals have the most detrimental influence on minority carrier lifetime and, because of that, on solar cell performance. The GDMS measurements (see Figure 7.7) show a decrease in concentration from substrate into silicon cell bulk of 3

to 4 orders of magnitude. A cross-check of the absolute impurity concentration in the substrate with the data provided with the raw powders show a good correlation with the measured data. Nevertheless, the differences in matrix (sputtering behaviour) of ceramic and silicon layer can have a strong effect on accuracy of the measurement. Especially the measured iron concentration in the silicon bulk is relatively high. Cross sections of comparable samples show some very large pores on the RBSiC ceramic's surface which could not be covered completely by the SiC layer. The GDMS measurement was most likely done near such a pore. This explains the still relatively high metal concentrations. For more details concerning diffusion through SiC see chapter 6.

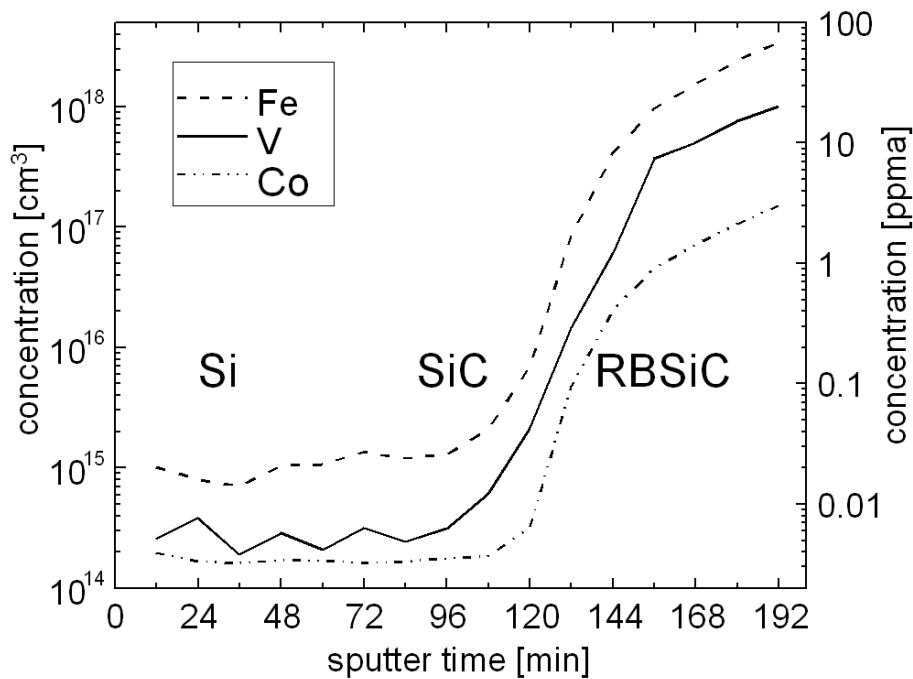


Figure 7.7: Depth resolved Glow Discharge Mass Spectrometry (GDMS) measurements of Fe, V, Co from the Si bulk material through the SiC barrier layer into the RBSiC ceramic substrate.

7.3 Solar Cells

We started solar cell processing with RexWEs only towards the end of this work. This can be explained by the effort to find the optimised RBSiC ceramic

substrate and the optimised SiC diffusion barrier. Nevertheless, some experience concerning cell processing with this wafer equivalent could be gathered and will be helpful for future works.

7.3.1 Crystalline silicon thin-film solar cells

Although the RexWEs are crystalline silicon wafer equivalents, not all standard solar cell processes applied on silicon wafers can be transferred directly. In this chapter we will give an overview on tested solar cell processes, will discuss occurring challenges and show the progress already achieved.

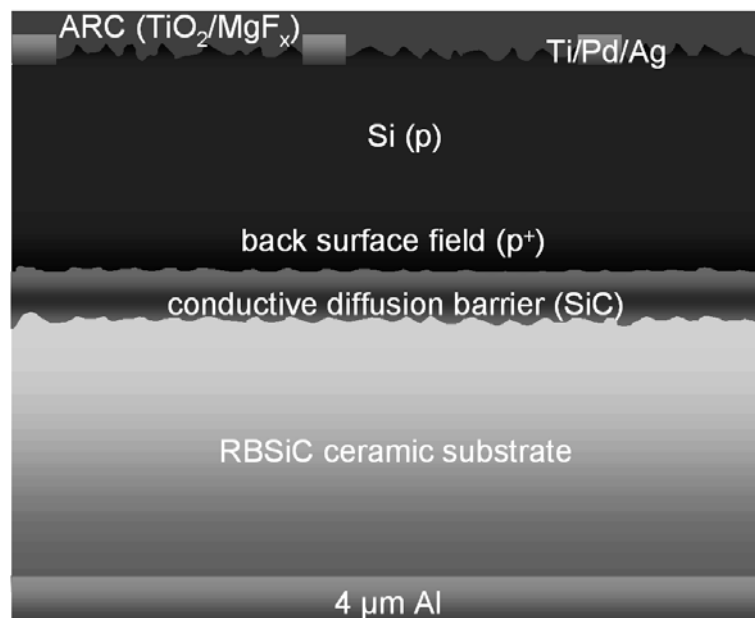


Figure 7.8: Solar cell processed on a Recrystallised Wafer Equivalent (RexWE) with integrated back surface field (BSF) and diffuse rear-reflector.

In Figure 7.8 one can see a typical solar cell processed on a RexWE using RBSiC ceramic as substrate. The front-side of the cell is textured and covered by a $\text{TiO}_2/\text{MgF}_x$ anti-reflection coating which both enhance the couple in of irradiated light into the device. The cell bulk has a gradient doping profile to increase the yield of minority carriers reaching the p-n-junction. On the rear-side of the cell bulk there is the highly doped back surface field layer. The SiC layer and the rough ceramic surface act as a rear-reflector and enhance total reflection. On the ceramic's rear-side the back contact of the wafer equivalent solar cell is deposited.

7.3.1.1 Process adaptations

To process the wafer equivalents on ceramic substrates we had to solve some specific problems: (1) open porosity of the ceramic's rear-side, (2) curvature of the wafer equivalent and (3) silicon surface roughness. Especially the open porosity caused several problems due to soaking of wet chemical etches. Therefore some additional process steps had to be introduced.

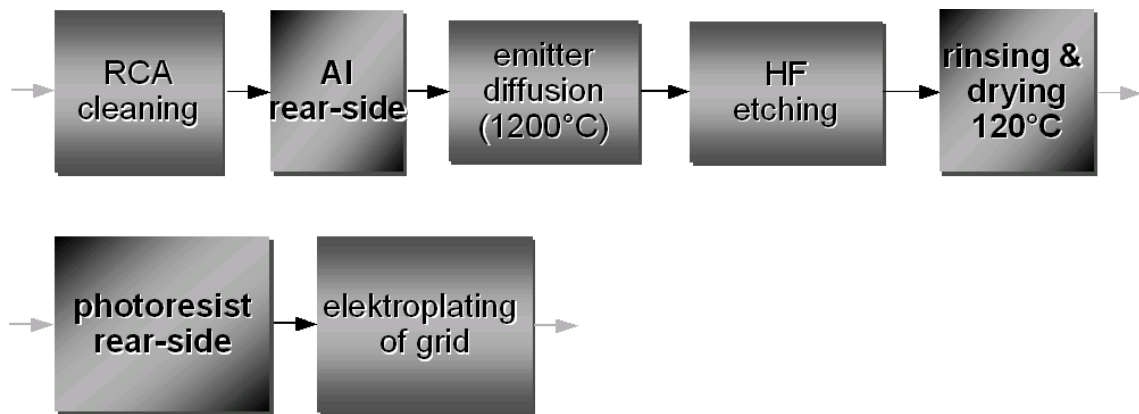


Figure 7.9: Necessary process adaptations for solar cell processing on RexWEs with a RBSiC ceramic substrate.

In principle the porous substrate structure is in favour of “dry” processes, but wet chemical processing is also possible when applying intense rinsing or when working with one side etching processes. The suitable one-side-etching-equipment for high throughput applications is already available and is becoming more and more important in industrial silicon solar cell processing. Our way was to cap the ceramic's rear-side as early as possible in the process chain. For this purpose an aluminium layer was deposited before emitter formation and a photoresist coated the rear-side during electroplating (see Figure 7.9)

7.3.1.2 Optical confinement

As the absorbing silicon layer in a thin-film cell is just some μm thick, the optical confinement of the cell is of enormous importance. This includes, beside an anti-reflection coating, a texturised front side and a diffuse reflector at the cell's rear-side. Different texturisation processes were tested in application to the RexWE. Two texturised surfaces are shown in Figure 7.10. On the left side a partly plasma etched one, with very small pyramids can be found. To point out the difference between a

texturised and an untexturised surface, half of the sample was capped with a protection layer during etching with SF_6 . It can be clearly seen, that all grains are homogeneously textured (reflection $\approx 20\%$). The removed amount of silicon was around $4\ \mu\text{m}$. The right micrograph shows the textured surface which was wet chemically processed with 85°C hot KOH/IPA for several minutes. Due to the anisotropic etching behaviour of KOH the random “pyramids” look different from grain to grain. Only grains with $\langle 100 \rangle$ surface have random pyramids. The silicon surfaces of the sample in Figure 7.10 were obviously tilted relative to $\langle 100 \rangle$. Therefore the random pyramids were etched diagonally out of the silicon.

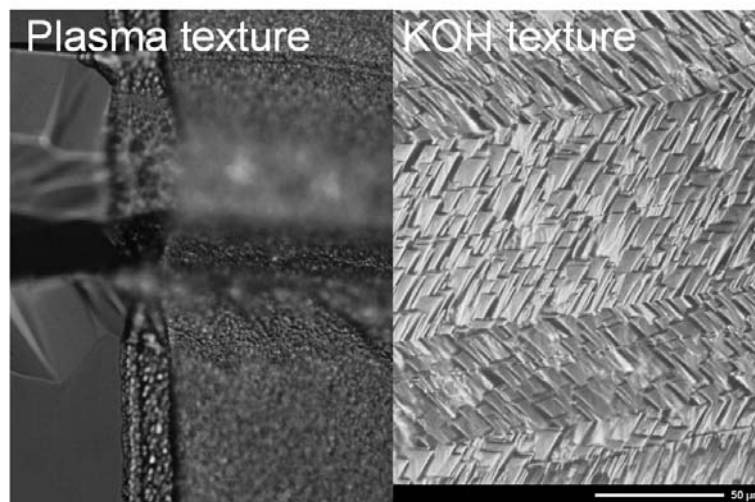


Figure 7.10: Micrograph of a KOH textured (right) and a partly plasma textured (left) solar cell surface on a Recrystallised Wafer Equivalent.

At the rear-side of the cell bulk the SiC diffusion barrier layer should have an as low refractive index as possible. This should lead, in combination with the rough surface structure of the ceramic substrate, to a diffuse reflector on the rear-side of the solar cell. All SiC layers used so far had a refractive index of ≈ 2.5 . For this refractive index a minimum angle of incident of around 40° leads to total reflection. A lower n would only be possible by increasing the carbon amount of the layer (down to ≈ 1.9). It has not been investigated yet how an increasing carbon content would influence diffusion barrier and electrical performance of the layer. Together with possible $\text{SiC}/\text{Si}_x\text{C}_{1-x}/\text{Si}_{1-x}\text{C}_x$ layer stack solutions this will be subject of investigations in the nearest future.

Furthermore the surface roughness of the RBSiC ceramic substrate can also be tuned over a wide range by changing the grain sizes of ingredients and sintering procedures. This optimisation processes is already under investigation.

7.3.1.3 Emitter formation

In order to compare different grid structures we tested emitters between 80 and 120 Ω/sq . For contacts fully evaporated through shadow masks, 80 Ω/sq . emitters were used. As this process does not allow a passivation of the surface, a higher doping level to lower the effective surface recombination velocity was chosen. The photolithographic front grids were applied on 120 Ω/sq . emitters. Here the emitter surface was passivated with a 10 nm thin oxide. This thin oxide did not just ensure a good surface passivation but furthermore avoided problems during electroplating. Without the thin oxide layer, parasitic depositions of Ag on silicon tips of the rough surface could appear. The emitters were diffused in a tube furnace with POCl_3 . Measurements with emission sheet resistance imaging (SRI) [114] on the silicon references showed good homogeneities of all emitters. Unfortunately no measurements, not even with a 4-point-probe, were possible on the RexWEs. Crystallinity (lateral conductivity dependent on grain boundaries) and surface roughness strongly influenced the measurements and made an interpretation almost impossible. Measurements of the doping profile with secondary ion mass spectroscopy (SIMS) did not seem promising either, because the always rough surface would make a good depth resolution impossible. As the emitter furnace was heated with a resistance heater optical absorption should have just a minor influence on the temperature on the sample's substrate. Therefore we concluded that the emitters should not be that different on silicon wafer and wafer equivalent.

The most challenging problem during solar cell processing was the phosphorus glass removal after emitter formation. Depending on the etch solution, a more or less pronounced colouring of the surface could be observed. Nevertheless, the parasitic layer, though invisible below around 10 nm thickness, could never be completely removed. All attempts trying to identify the composition or the origin of this layer have not been successful yet. Due to excellent solar cell results on the silicon references (one at the beginning and one at the end of the tube) a cross contamination during emitter diffusion could be excluded. Cross contamination during wet chemical processing or drying could be excluded with the same argumentation. Further

characterisations could just find SiO_x components in this residual layer. But annealing in oxygen atmosphere could not change the etching behaviour (HF) of the layer.

7.3.1.4 Front contacts

As already mentioned above we tested different grid designs and deposition methods on our RexWEs. Figure 7.11 (left) shows the grid which was deposited with photolithographic processing frequently used for high efficiency solar cells. Due to surface roughness and curvature of the substrate the too small grid fingers were often intercepted. On solar cell areas of 21 cm^2 several cells with these interceptions could be found. Although the substrate curvature could be reduced significantly throughout our experiments this was still one of our major challenges.



Figure 7.11: Micrograph of a photolithographic (left) and a evaporated (right) front grid on a Recrystallised Wafer Equivalent on RBSiC ceramic substrate.

The evaporated grid (30/30/5000 nm of Ti/Pd/Ag) had very broad fingers which adhered quite well to the cell surface. Of course the shadowing effect of this grid was very high (see Figure 7.11, right micrograph). One solar cell with an evaporated grid was additionally thickened with electroplating. No differences in the cell performance could be observed. Therefore we conclude that the evaporated grid finger's series resistance did not limit the electrical current of the solar cell.

7.3.1.5 Hydrogen bulk passivation

As the recrystallised silicon layers have relatively high defect concentrations (especially in the epitaxial layer), a bulk passivation with remote plasma hydrogen passivation (RPHP) is necessary. The process parameters for multi crystalline silicon cells are 30 min at 350°C with a gas flow ratio of $H_2/Ar=7/4$. This standard parameters led to a V_{oc} enhancement of about 10 to 20 mV. Compared to earlier results on other ceramic substrates, this enhancement is only one third of the “usual” value. Due to the very frequent changes in RexWE and solar cell processing an optimisation of the passivation process was not possible yet.

7.3.1.6 Anti-reflection coating

The effect of layer residuals after phosphorus glass removal had detrimental impact on the TiO_2/MgF_x anti-reflection coating (ARC). As both RexWE solar cell types had undefined layer residuals the ARC thickness could not be adjusted. The cell performance therefore was even worse after ARC deposition for some solar cells (see Table 7.2). Figure 7.12 shows a micrograph of the solar cell surface after ARC with the unidentified layer residuals.

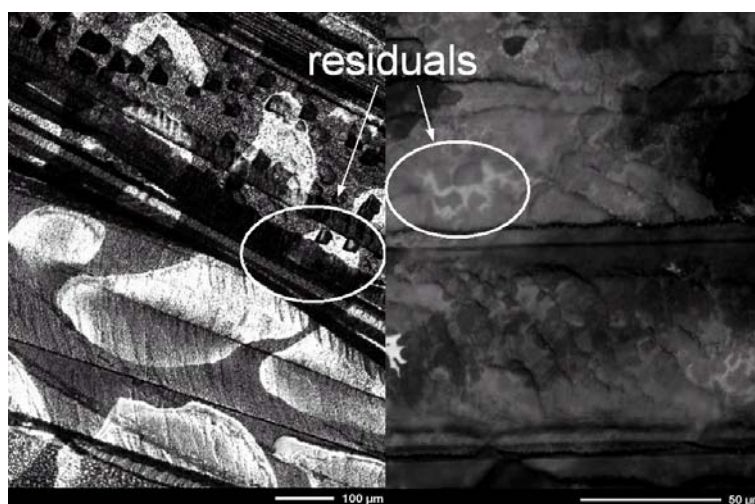


Figure 7.12: Inhomogeneities of the anti-reflection coating due to layer residuals on two different solar cell surfaces (brighter areas).

7.3.2 Solar cell results

In this chapter I will present simulations which show the efficiency potential of crystalline silicon thin-film solar cells. Furthermore, first solar cell results with the new RBSiC/SiC Recrystallised Wafer Equivalents will be presented. These results will be discussed in order to check the proof of concept.

7.3.2.1 Diffusion length and efficiency

Reber [unpublished] made simulations to check the efficiency potentials of our thin-film concept. As the efficiency is one of the most important cost factors of a photovoltaic system, knowledge about the theoretical efficiency limit is of enormous importance.

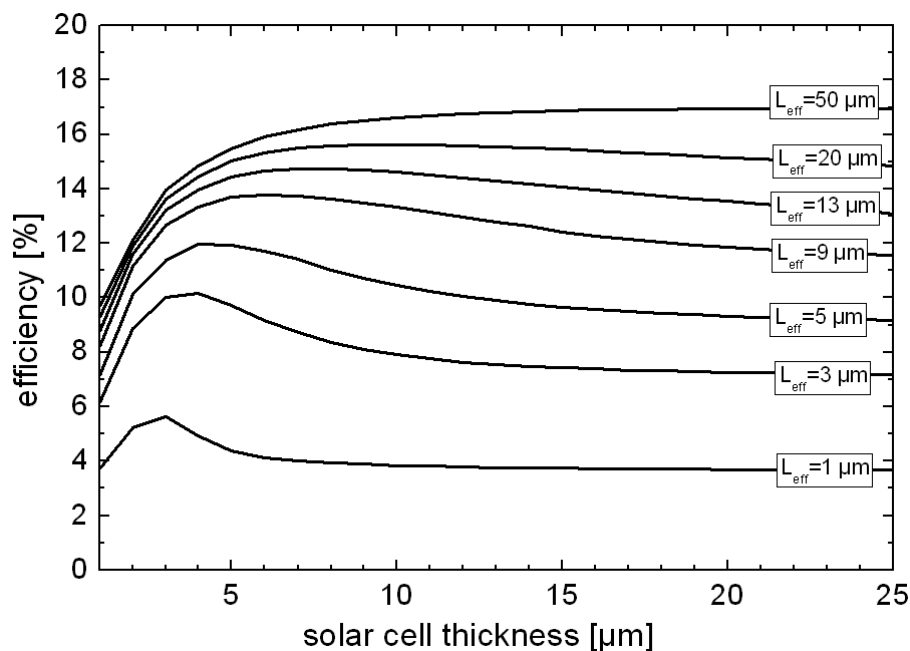


Figure 7.13: Simulation data (PC1D) of crystalline silicon thin-film cells showing the efficiency in dependence of the solar cell thickness for different layer qualities (effective diffusion length of the minority carriers).

The simulations were all realised with PC1D [115] tool, most frequently used for solar cell simulations. The simulation results presented in Figure 7.13 were done under the following assumptions: the back surface field had a boron concentration of 10^{19} cm^{-3} and a thickness of $1 \mu\text{m}$, the recombination velocity on the front-side $S_{front}=100 \text{ cm/s}$, internal front/back reflection 92% (diffuse), front texture $1 \mu\text{m}$,

$R_p=1000 \Omega$, $R_s=0.3 \Omega$, emitter $107 \Omega/\text{sq}$. The results clearly show that no matter how good the crystal quality of the layer is, around $10 \mu\text{m}$ thickness of the absorbing layer is sufficient to exploit the layer's potential. With effective diffusion lengths for minority carriers of $50 \mu\text{m}$ efficiencies up to 17% are possible. The simulations show that with a good optical confinement some μm of silicon can be sufficient to realise high conversion efficiencies.

7.3.2.2 Proof of concept: conductivity (1 cm^2 cells)

First solar cells with a standard contact structure (rear- and front-side) on Recrystallised Wafer Equivalents could be realised. Both-side contacted cells are only possible with SiC diffusion barrier layers which are sufficiently electrical conductive. Conductivity measurements of the wafer equivalent layer stack with a SiC diffusion barrier layer on a RBSiC ceramic substrate showed a specific resistivity for the boron doped SiC layer of $\rho_{\text{SiC}}=18 \Omega\text{cm}$ after RexWE processing (see chapter 4). To check the influence of both resistivities (SiC layer and RBSiC substrate) on series resistance we realised solar cells with base contacts on rear-side (1) and front-side (2) of the wafer equivalent. Furthermore, textured (plasma texture) and untextured solar cells were realised. The solar cells had a POCl_3 emitter ($120 \Omega/\text{sq}$), photolithographic grid fingers and a $\text{TiO}_2/\text{MgF}_x$ anti-reflection coating. A comparison of solar cell results on 1 cm^2 proves (see Table 7.1), that the series resistance of diffusion barrier layer and ceramic substrate do not limit the cell performance at this level of J_{sc} .

Table 7.1: Solar cell results (1 cm^2) on RexWE with RBSiC substrate and conductive SiC diffusion barrier layer.

contact scheme	V_{oc} [mV]	J_{sc} [mA/cm ²]	FF [%]	η [%]
1 (untextured)	524	20.5	67.3	7.1
2 (untextured)	525	20.6	67.0	7.2
1 (textured)	551	24.5	26.9	3.6

The fill factors and the values for short circuit density J_{sc} are almost identical. The solar cell with a textured front-side shows a still higher J_{sc} . Unfortunately both solar cells suffer on the bad contact adhesion coming from the phosphorus glass residuals. Especially the textured cell has therefore an extremely poor fill factor. During further characterisation some of the contact grid fingers even detached completely.

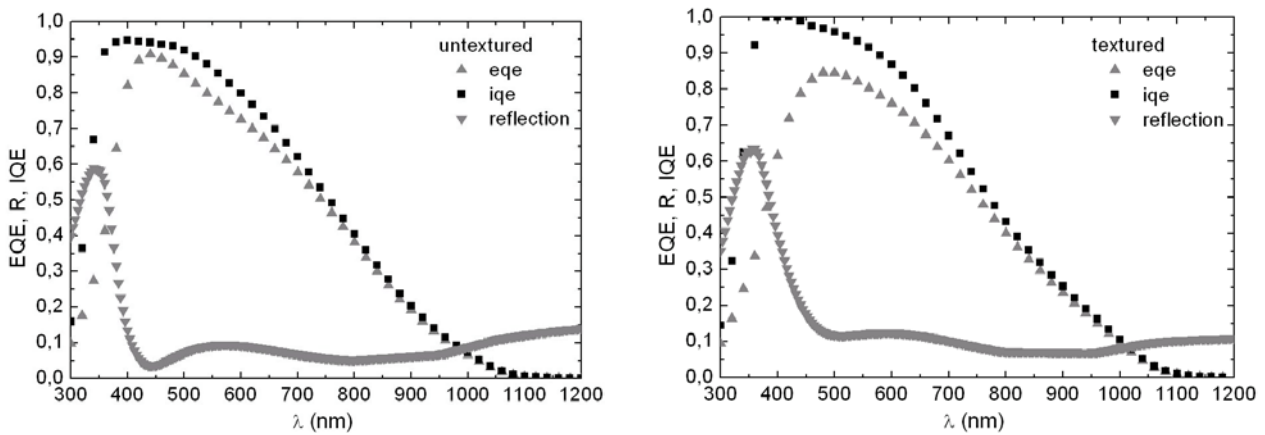


Figure 7.14: EQE, reflection and IQE in dependence of wavelength for an untextured (left) and a textured (right) solar cell.

Further characterisation included measurement of spectral response, reflectance and quantum efficiency of the solar cells [116]. As light absorption in a semiconductor is a function of wavelength, the measurement of short circuit current density in dependence of wavelength allows to extract depth dependent device properties. The spectral response (SR) is defined as the ratio of short circuit density J_{sc} to irradiance of monochromatic light $E(\lambda)$. The external quantum efficiency $EQE(\lambda)$ is obtained if the short circuit current density is not related to the incident energy but to the number of incident photons. If additional information about the wavelength dependent reflection $R(\lambda)$ is available the internal quantum efficiency $IQE(\lambda)$ can be calculated as $EQE(\lambda)/1-R(\lambda)$. In Figure 7.14 all these data for the two solar cells already described above can be seen.

Taking into consideration the contacting problems and position dependent changes in reflection (due to the residuals) we can draw the following conclusions: In the short wavelength range both curves show a relatively good EQE characteristic. The untextured cell has an even better one which can be a result of differing emitter profiles (possible inhomogeneities of the emitter formation process). In the long

wavelength region the textured cell has a better response characteristic which results from the enhanced optical confinement. Nevertheless, both cells show too low values which. This can be an indicator, that the optical confinement is still far from optimised. As the series resistance of the solar cell is very high the poor cell's response in the long wavelength region can also have other reasons which cannot be identified. The reflection characteristics is good for both cells, but surprisingly the untextured cell has a better light absorption then the textured one. Possible explanations for this strange behaviour could be significant differences in the anti-reflection coating. As the reflection data are questionable the *IQE* characteristic is also burdened with a high error.

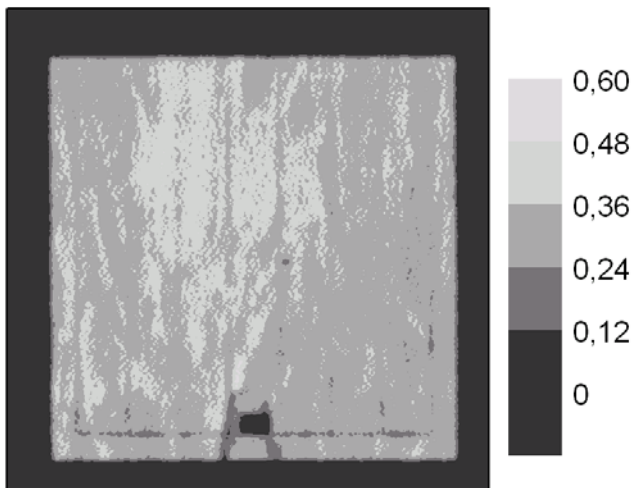


Figure 7.15: *EQE* of an untextured solar cell (1 cm^2) measured by the spectrally resolved light beam induced current method.

With the spatially resolved light beam induced current (SR-LBIC) method [116,117] we measured the *EQE* for the untextured solar cell. This method measures the J_{sc} at different wavelengths using laserdiodes working at up to 950 nm. As the penetration depth of light with a wavelength 950 nm is above $60 \mu\text{m}$, one important assumption for the analysis method is an infinite solar cell bulk thickness. This assumption cannot be satisfied for the thin-film solar cell. Therefore we used only diodes with a maximum wavelength of 830 nm which on the other side lowered our statistic accuracy. The *EQE* plot shows a relatively good homogeneity over the whole cell area. When looking very closely, the grain boundaries generated by the recrystallisation process can be seen. The contact pad (bottom) and some grid fingers can also be observed.

7.3.2.3 Proof of concept: diffusion barrier (21 cm²)

As the fabrication of large area wafer equivalents up to 200x200 mm² could already be demonstrated and the diffusion barrier performance of SiC (on large areas) had to be investigated, we also enlarged the solar cell area. The most important difference to the processing of 1 cm² solar cells was, as already mentioned above, the curvature of the substrates. Due to grid interceptions and the residual layers on the surface, the best cell with a photolithographic grid, a plasma front texture and an 80 Ω/sq. emitter achieves only an efficiency of 1.9% with a V_{oc} =470 mV and a J_{sc} =14 mA/cm² (FF =29%). The reference cell on float zone silicon processed in the same batch (η =16.9%, V_{oc} =640 mV, J_{sc} =34 mA/cm², FF =78%) shows, that the process itself is capable of high conversion efficiencies. As the references were processed together with the wafer equivalents, the good efficiency of these cells prove that cross contamination does not seem to be an issue.

Table 7.2: Solar cell results (21 cm²) on RexWE with RBSiC substrate and conductive SiC diffusion barrier layer.

process status	V_{oc} [mV]	J_{sc} [mA/cm²]	FF [%]	η [%]
contacts	532	18.4	55.2	5.4
RPHP	545	18.8	57.9	5.9
ARC	543	18.9	56.2	5.8

The results for the best solar cell with an evaporated grid design can be found in Table 7.2. Considering all occurring problems, like the unsuccessful ARC, during cell processing and the uniqueness of the cell (first cell on such an area) the efficiency of 5.9% is encouraging. The low fill factor (FF) reflects the series resistance problems most probably caused by the residual layer on the cell surface. Relatively high V_{oc} values were another proof (see chapter 6) for the good diffusion barrier performance of the SiC layer on large areas. The best float zone silicon reference cell with an efficiency η =9.8%, V_{oc} =608 mV and J_{sc} =22.3 mA/cm², (FF =72%) before ARC shows the high shadowing effect of the evaporated grid and the need for an enhanced texturisation process.

7.4 Potential for the Future

When thinking about an alternative to the standard silicon wafer additional benefits beside the saving of enormous silicon amounts have to be taken into consideration. In this chapter I will point out some of these additional benefits and potentials.

7.4.1 High Temperature Processing

Several solar cell processes which are well known from high efficiency processing on mono-crystalline solar cells are not suitable for multi-crystalline substrates. The main problem is the ‘contamination’ of the substrate with metallic impurities during solidification of the Si block (ingot casting). As far as it is known these impurities are embedded in clusters which are electrically relatively inactive. But as soon as the material is heated up again to temperatures in the region of 800°C and higher the clusters dissolve and decrease minority carrier lifetime in the material significantly.

As the silicon bulk material of the RexWE is fabricated in a completely different way than a block casted silicon wafer, impurity clusters should not be present as far as the diffusion barrier layer is working well. Therefore high temperature processes do not change the Si material performance. One example for a process which could not be applied on multi crystalline wafers would be a thermally grown oxide layer for excellent emitter passivation as it is used for high efficiency solar cells.

7.4.2 “Alternative” Backside

Metallic contacts on the rear-side of Si standard solar cells are in most cases made out of purified aluminium. Not just that the production of such a material is relatively expensive, additionally the electrical conductivity of aluminium is much worse than that of e.g. copper.

On our RexWE the application of copper or low-cost aluminium contacts on the rear-side would cause no contamination of the silicon cell bulk. The diffusion barrier here as well prevents a diffusion of all impurities coming from the substrate into the bulk. Not only a significant reduction of processing cost is possible, especially when thinking of the increased demand in the future, it could moreover lead to a much lower series resistance of the whole solar cell.

7.4.3 N-type bulk

Many solar cell groups around the world are working on silicon solar cell concepts which start with a n-type silicon wafer. This material has the advantage that the so-called "silicon-boron-complex" is not active and that metallic impurities have a much less negative impact on minority-carrier lifetimes. The doping of our Recrystallised Wafer Equivalent can easily be changed just by replacing the doping gases during layer depositions. Full advantage of a n-type bulk could be taken of without any higher processing effort.

7.4.4 Ideas for RexWE modules

In our opinion it is not enough to stop working on an equivalent for silicon wafers after the solar cell process. As one can learn from other thin-film concepts, the feasibility has to be proved for the module or even the whole system. Amorphous Si solar cells e.g. generate a big part of their attractiveness from the very cost-effective solar module manufacturing. Therefore I will briefly present possible advantages of our concepts compared to today's and future silicon wafer modules.

It is a widespread consensus that silicon wafer cells will become much thinner than they are today (maybe $\approx 100 \mu\text{m}$). With the wafer's thinness the mechanical stability and in connection with that handling could become a serious problem. Not only in the solar cell but also in the module production a high breakage rate could be the result. The RexWE solar cell will never have a problem like this because no matter how thin the solar cell will become there will always be mechanical support provided by the substrate.

There has been no decision yet in the silicon solar community which maximum cell area is a good compromise between low production costs (high throughput) and therewith upcoming problems (high current, breakage, etc.). As we could show before, the production of large area RexWEs is already possible ($207 \times 207 \text{ mm}^2$). With our actual machines 207 mm in height and up to 1 m in length are the limit. Although it is maybe not reasonable to process such a large solar cell one could imagine a process to realise many cells in a row on one substrate. This could open new ways of module manufacturing. Maybe an alternative interconnection (conductive SiC layer, contact wrap through) on these really large ceramic substrates could be an additional benefit.

8 SURFACE PASSIVATION WITH $\text{Si}_x\text{C}_{1-x}$

The surface passivation of silicon is a well studied subject in solar cell and semiconductor technology. Thermally grown oxide layers were, for a long time, an unbeatable layer for this purpose. Later on, due to necessity of high throughput and low temperature, alternative layers like plasma enhanced chemical vapour deposited (PECVD) amorphous silicon, oxide and nitride layers became more and more important. In this chapter I will describe $\text{Si}_x\text{C}_{1-x}$ as an excellent surface passivation layer. Beginning with the characterisation of lifetime samples I will especially focus on the excellent temperature stability of this layer which is unique for a low-temperature deposited passivation layer. High efficiency solar cells using $\text{Si}_x\text{C}_{1-x}$ will proof its applicability as a rear-side passivation layer.

8.1 Surface Recombination in Crystalline Silicon

In this chapter I will give an overview on physics of surface recombination and surface passivation. I will discuss properties of different passivation layers and will introduce plasma cleaning of the passivated surface and deposition of the $\text{Si}_x\text{C}_{1-x}$ passivation layers. At the end of this section the passivation mechanisms of $\text{Si}_x\text{C}_{1-x}$ will be discussed.

8.1.1 Basics

The surface of a silicon [118] wafer can be considered as a massive dislocation of the lattice. Therefore a high density of defects within the forbidden energy gap of the semiconductor is expected. The main mechanism of recombination results from the very high amount of unsaturated bonds. This recombination at defects is described by the Shockley-Read-Hall theory [119,120]. The special case of the net recombination rate per unit area U_s for a single defect placed at an energy level E_t is

$$U_s = \frac{v_{th} N_{st} (n_s p_s - n_i^2)}{\frac{n_s + n_1}{\sigma_p} + \frac{p_s + p_1}{\sigma_n}} \quad 8.1$$

When we insert the fundamental recombination velocities for electrons $S_{n0} \equiv v_{th} N_{st} \sigma_n$ and holes $S_{p0} \equiv v_{th} N_{st} \sigma_p$ the equation can be written as

$$U_s = \frac{\frac{n_s p_s - n_i^2}{S_{p0}}}{\frac{n_s + n_1}{S_{p0}} + \frac{p_s + p_1}{S_{n0}}} \quad 8.2$$

where N_{st} is the density of defects per unit area, n_s (p_s) is the density of electrons (holes) at the surface and v_{th} is the thermal velocity of charge carriers (10^7 cms⁻¹ in crystalline silicon at 300 K). Therefore the surface recombination can be characterised by a surface recombination velocity, S , defined as,

$$U_s = S \cdot \Delta n_s, \quad 8.3$$

where Δn_s is the excess minority carrier density at the surface. In contrast to bulk recombination via defects an electric field is usually found at the semiconductor's surface. This leads to a situation where n_s is far away from p_s since this field creates significant differences between n_s and p_s , respectively. Therefore it is useful to define an effective surface recombination velocity S_{eff} as

$$U_s = S_{eff} \cdot \Delta n, \quad 8.4$$

where $\Delta n = \Delta p$ is the minority carrier density at the border of the space charge region created at the surface. In contrast to Δn_s , Δn can be easily measured and controlled by changing the illumination level.

With the presence of the above mentioned electric field at the silicon surface, the dependence of U_s on the other physical parameters of the surface (S_{n0} , S_{p0} , Δn) is quite complex. Nevertheless, based on the gathered knowledge about surface recombination, we will analyse strategies to reduce U_s in the following chapter.

8.1.2 Fundamentals of surface passivation

In this section I present a simple model for the recombination effect at the rear side of a solar cell (see Figure 8.1, Figure 8.2). The charged carriers migrate through the

silicon bulk and pass along some defects in the substrate itself. When they come to the surface of the solar cell many active defects (thick horizontal lines) result in a high recombination rate U_s . At top and bottom of the sketches the conduction band (CB) and the valence band (VB) are illustrated. The dashed line shall state the surface of the silicon crystal.

From what we know about recombination mechanisms in silicon two different strategies facing surface recombination are possible:

Reduction of S_{n0} and S_{p0} :

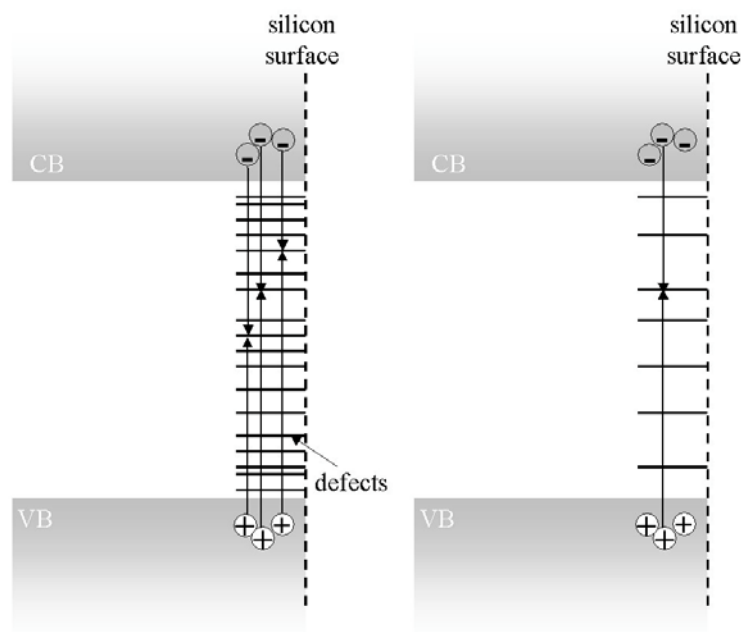


Figure 8.1: Scheme of a simple model for the recombination effect with unpassivated (left) and passivation through saturated defects (right) on the silicon solar cell's rear-side.

In this case the aim is to directly decrease the fundamental recombination velocities of electrons and holes. Since v_{th} is a constant of the semiconductor material and σ_n (σ_p) are parameters intrinsically related to the defect type, the strategy has to focus on a reduction of N_{st} . The cleaning of the surface before depositing a passivation layer is therefore of enormous importance. When additional atomic hydrogen can be supplied to saturate dangling bonds, the density of defects can be reduced significantly. Passivation layers like amorphous silicon and thermal oxide work with a bond saturation effect.

The schematic sketch in Figure 8.1 shows a reduced amount of active impurities (horizontal lines) on the rear-side of the wafer. For the passivation procedure used in this work we tried to achieve this status by cleaning the surface with plasma and passivating with hydrogen in one process step. The subsequently deposited $\text{Si}_x\text{C}_{1-x}$ saturated further free bonds on the surface.

Surface depletion for one carrier type:

To make a recombination process effective, much more holes than electrons are necessary. The reason therefore is the difference in capture cross sections of electrons and holes [121]. When decreasing the hole concentration a significant decrease of recombination can be achieved. This effect can be achieved through an electric field which affects the charged carriers. It is therefore called a field effect passivation: fixed charges which act as a passivation field realised through fixed charges in the passivation layer itself.

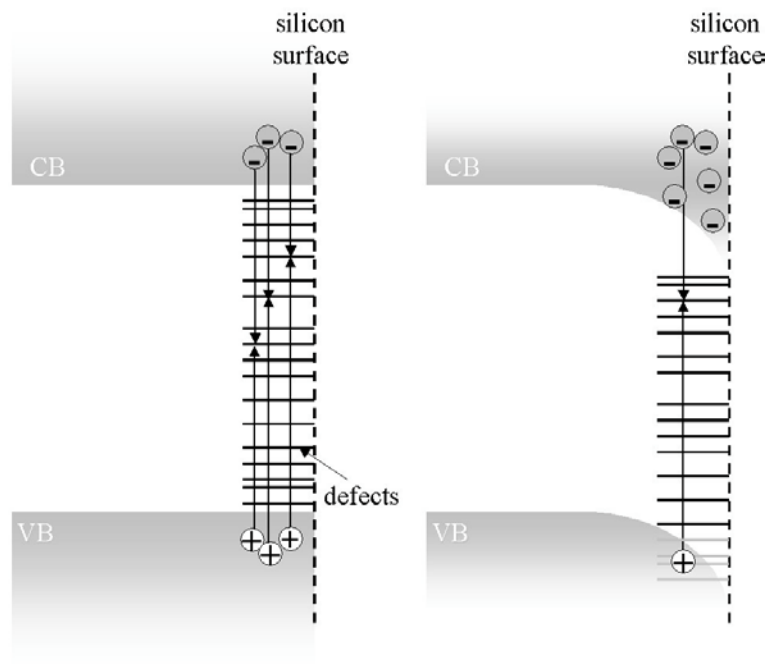


Figure 8.2 Scheme of a simple model for the recombination effect with no passivation (left) and passivation through a field effect (right) on the silicon solar cell's rear side.

In Figure 8.2 the field effect is displayed by a bending of the conduction and valence band. The amount of holes and by that the recombination itself decreases. This effect

also appears in the Si_xC_{1-x} passivation layer used in this work. In order to achieve a field passivation effect a second layer of undoped stoichiometric SiC was deposited. In these layers (similar to SiN_x layers) fixed charges are incorporated and generate the described field.

8.1.3 State of the art passivation layers for c-Si surfaces

8.1.3.1 Thermally grown oxide

The best known and still most effective method to passivate crystalline silicon surfaces is thermally grown oxide. It allows effective surface recombination velocities (S_{eff}) below 10 cm s⁻¹ on both, n- and p-type Si. One disadvantage of this method is the high temperature (≈1000°C) which is necessary to grow the oxide at reasonable times. Especially for multi-crystalline Si Schultz *et al.* [122] showed that wet oxidation, which can be performed at <850°C, is a good alternative.

8.1.3.2 Plasma deposited layers

Passivation layers deposited with plasma enhanced chemical vapour deposition (PECVD) like SiO₂, SiN_x and amorphous Si can be deposited at temperatures around 200 to 400°C. To achieve a really good performance, an additional annealing step is necessary for SiO₂ and SiN_x. Especially SiN_x is nowadays a standard passivation layer in industrial solar cell processing. Alternative deposition methods like reactive sputtering which promise a much higher throughput than PECVD are actually under investigation [92]. Amorphous Si leads to the best passivation results so far known for plasma deposited layers [123]. One reason for not being used more frequently is its poor temperature stability.

Latest developments [124-128] focussed on amorphous silicon carbide layers (Si_xC_{1-x}) also deposited by PECVD. As this material was already strongly under investigation, I also started to investigate its passivation behaviour. As it has a widely tuneable bandgap (see chapter 4), a p- or n-dopability, a high hydrogen content (see chapter 6) and an excellent thermal and mechanical stability (see chapter 5) I thought it could be a well suited material for a temperature stable surface passivation.

8.1.4 In-situ plasma cleaning

As mentioned above cleaning of the surface before deposition of the passivation layer is of crucial importance to reduce N_{st} . Other groups use RCA, HNF or just HF wet chemical cleaning for this purpose. The deposition of the passivation layer immediately after cleaning or waiting for some hours under clean conditions can be preferable. In the first case even rinsing, which is for security reasons normally done after wet chemical cleaning, is sometimes left away to saturate the wafer's surface with more hydrogen (hydrofluoric acid). On the other hand the waiting procedure can be necessary to grow some nanometers of native oxide which leads to good passivation results in combination with SiN_x layers.

A procedure developed during this work was an in-situ plasma cleaning which was done directly before deposition and in the same reactor which is also used for deposition. The wafer were taken "out-of-box", with around 3 nm of native oxide, and introduced directly into the plasma reactor. The thin oxide was removed with a Ar/H₂ gas mixture at pressures of around 30 Pa. The additional effect was, that the surface defects were passivated with hydrogen. Comparisons with HF and HNF cleaning procedures did not show as good results. Although the results were really satisfying comprehensive investigation comparing all possible cleaning procedures are still missing.

8.1.5 Si_xC_{1-x} deposition conditions

The Si_xC_{1-x} layer deposition was done directly after the cleaning procedure at $T = 350^\circ\text{C}$ and an energy density generated by the rf-generator of around 0.03 W/cm^2 (see chapter 1). The power for the microwave source was also tuned very low. In addition to the deposition gases methane and silane some layers were doped with phosphorus (PH₃). For low surface damage a relatively high pressure of 30 Pa was used which led to problems with homogeneity compared to other deposition regimes. Nevertheless an area of $200 \times 100 \text{ mm}^2$ could be used for comparable results. The process was not optimised yet according to growth rate (5 nm/min) because we focused exclusively on the passivation performance of our layers.

8.1.6 Physical mechanism of $\text{Si}_x\text{C}_{1-x}$ passivation

As the development of $\text{Si}_x\text{C}_{1-x}$ as a surface passivation layer is still a relatively new field of interest at our institute, comprehensive physical investigations concerning the passivation mechanism have not been realised yet. From optical measurements we know, that the layers are closely related to amorphous silicon (see chapter 3). The striking difference are the carbon atoms incorporated in the network which seem to stabilise it. Charging experiments of the layers indicated electrical conductivity because no charging was possible. The effect of the phosphorus atoms in the layers is still unclear. Although our knowledge about the passivation mechanism is still poor, a saturation of free bonds with $\text{Si}_x\text{C}_{1-x}$ and hydrogen seems to be the dominating effect. Stoichiometric SiC layers did not show as good passivation performances yet. The close relation to SiN_x would propose a field effect passivation. We think that in a deposition regime with lower surface damage (induced by the process) this stoichiometric SiC layers could also be used as good passivation layers. Up to now these SiC layers were only used in stack systems as a kind of capping layer on top of a unstable $\text{Si}_x\text{C}_{1-x}$ layer. Due to its excellent stability and a much lower refraction index this application could be favourable for a solar cell process (see chapter 9).

8.2 Lifetime Samples

First characterisation steps will be presented which were realised by depositing the passivation layers on both sides of a float zone wafer and measuring the minority carrier lifetime. Furthermore, investigations concerning deposition homogeneity, blistering effects and thermal stability of the $\text{Si}_x\text{C}_{1-x}$ layers will be discussed.

8.2.1 Quasi Steady-State Photo Conductance (QSSPC) method

Effective minority carrier lifetimes were measured by means of the Quasi Steady-State Photo Conductance (QSSPC) method. This method was developed by R. A. Sinton and A. Cuevas [129] (see Appendix A). These measurements require the knowledge of the amount of light being absorbed by the silicon. Experimentally this can be achieved by use of the photo conductance measurements in quasi steady-state and transient mode and by comparison of the results [130].

In Equation 8.5 and 8.6 the effective minority carrier lifetimes τ_{eff} are calculated from the excess carrier density Δn , the generation rate $G(t)$ and the change of the injection level over time $\partial(\Delta n)/\partial t$ using the quasi steady-state or the transient mode, respectively:

$$\tau_{eff, QSS}(\Delta n) = \frac{\Delta n}{G} \quad 8.5$$

$$\tau_{eff, trans}(\Delta n) = -\frac{\Delta n}{\frac{\partial \Delta n(t)}{\partial t}}. \quad 8.6$$

Whereas Equation 8.5 shows a dependence on the amount of photons absorbed in the silicon in the generation G , Formula 8.6 is independent of that. By comparing the lifetime results of both modes, the amount of absorbed light and thus an effective optical transmission factor could be extracted. This factor was approximated to 0.5 for the deposited $\text{Si}_x\text{C}_{1-x}$ layer and a wafer of 250 μm thickness.

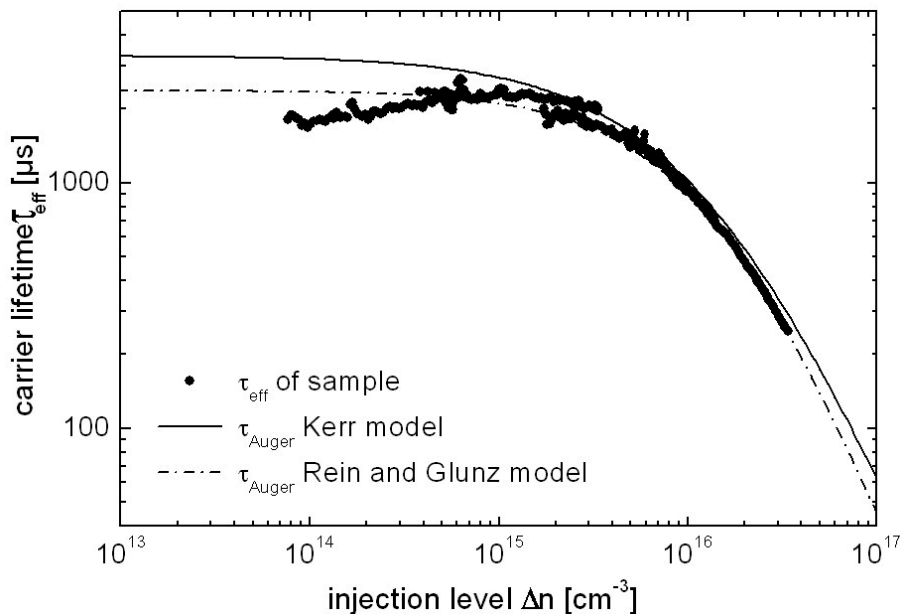


Figure 8.3: Injection dependent effective lifetime measured by QSSPC of a phosphorus doped $\text{a-Si}_x\text{C}_{1-x}$ passivation layer on a 1 Ωcm FZ Si wafer. Especially in the higher injection levels the lifetime is limited by Auger recombination.

For QSSPC measurements the 4" silicon FZ wafers were cleaned and coated on both sides as it is described in chapter 8.1.3.2. The measurements showed a very high level of effective lifetime. Looking at Figure 8.3, the injection dependent lifetime exhibited

a moderate increase in the mid injection regime. The decrease of effective lifetime for injection levels Δn higher than $1 \times 10^{15} \text{ cm}^{-3}$ is in good agreement with the Auger recombination expected for a background doping of $1.6 \times 10^{16} \text{ cm}^{-3}$. Also displayed in Figure 8.3 are the Auger recombination models by Kerr *et al.* [131], and Rein and Glunz [121]. Comparing these models with the measured lifetimes showed that the effective lifetime is fully dominated by intrinsic recombination for Δn greater than $1 \times 10^{15} \text{ cm}^{-3}$. Thus, the developed Si_xC_{1-x} layer suppressed surface recombination to a very high degree. Extracting the effective surface recombination velocity S_{eff} results in a big uncertainty, due to a high sensitivity to small variations in the Auger model used. Nevertheless, a S_{eff} value below 1 cm/s for Δn greater than $1 \times 10^{15} \text{ cm}^{-3}$ and below 5 cm/s for Δn between $1 \times 10^{14} \text{ cm}^{-3}$ and $1 \times 10^{15} \text{ cm}^{-3}$ is a conservative upper boundary.

Repeated measurements did not show deterioration of the passivation quality after additional illumination or longer storage (more than one month). Additional measurements with microwave detected photo conductance decay MW-PCD [132] yield an effective lifetime of around 1650 μs at an injection level of $1 \times 10^{15} \text{ cm}^{-3}$ confirming the very high lifetime level. This was the best value achieved. But all 8 samples of which 2 were processed together in one run were measured in the region of more than 1 ms effective lifetime at a Δn of $1 \times 10^{15} \text{ cm}^{-3}$.

8.2.2 Homogeneity and blistering

The homogeneity of the passivating SiC coating has been verified by measurements of the effective lifetime by the carrier density imaging technique (CDI). A description of this method can be found in Isenberg *et al.* [111]. The effective lifetime distribution was determined at an irradiation intensity equivalent to 1.2 suns yielding a mean injection level of $9.1 \times 10^{15} \text{ cm}^{-3}$. Since the bulk lifetime of the material is assumed to be constant throughout the whole wafer, the lifetime topography represent the variation in the quality of the surface passivation. Due to the measurement principle a separation of the influence of front or back surface passivation is not possible.

Figure 8.4 shows the histogram of the lifetime topography of a sample wafer with phosphorus doped Si_xC_{1-x}. Most of the wafer exhibits a high lifetime level leading to a narrow main peak in the histogram. A Gaussian distribution fitted to the histogram

shows the peak centre at $\tau_{\text{peak}} = 953 \mu\text{s}$ effective lifetime with a standard deviation of $\sigma = 83 \mu\text{s}$. The steep slope towards higher lifetime resembles the Gaussian distribution very well. Smaller areas with lower lifetimes at the border and in the middle of the wafer, which are most probably due to surface contamination (e.g. tweezers prints) or scratched layers by handling, contribute to increased counts at lower lifetimes. Smaller spot-like areas with relatively low lifetimes can be explained with occasionally occurring blistering effects (see chapter 5). This blistering becomes more likely with lower power densities of the RF-source and seems to go hand in hand with charging effects at the wafer surface. Variations in hydrogen flow during deposition showed no significant influence on this behaviour.

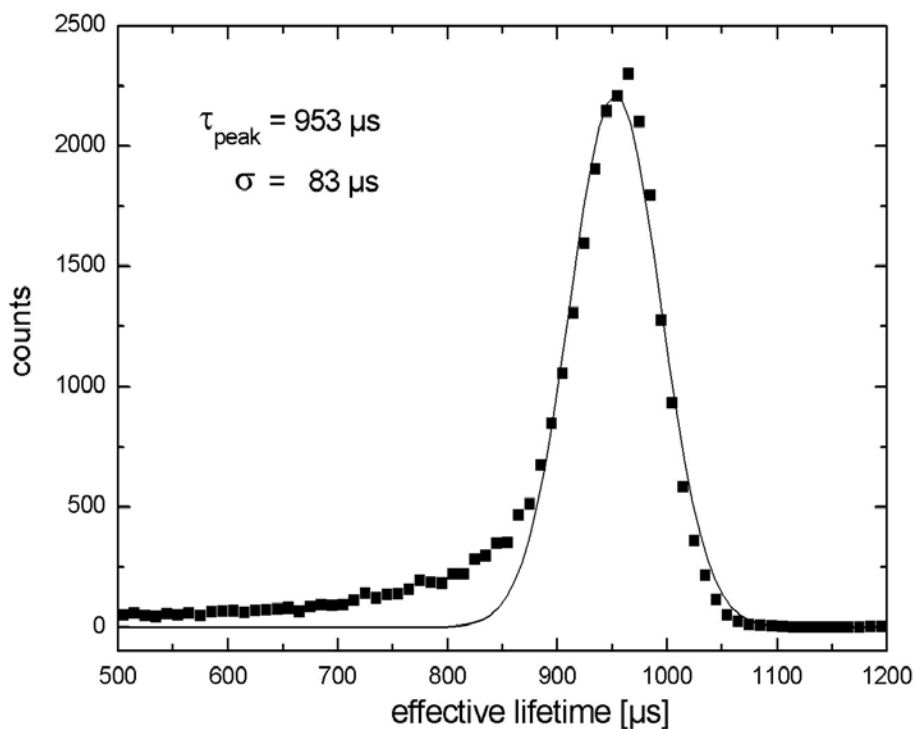


Figure 8.4: Histogram of effective lifetime distribution on a 4" silicon wafer passivated with Si_xC_{1-x} with Gaussian distribution fitted to the data.

To find out about process homogeneity (etching and deposition) we cleaned and coated two 4" silicon wafers in one run. This meant a deposition area of around 100 x 200 mm². The carrier density imaging graphs in Figure 8.5 show, that beside the lifetime decreasing effects described above, the deposition and in-situ cleaning homogeneity seems to be excellent over the whole deposition area. The expected

problems coming from the very high process pressure seem to be controllable which is a further encouraging result.

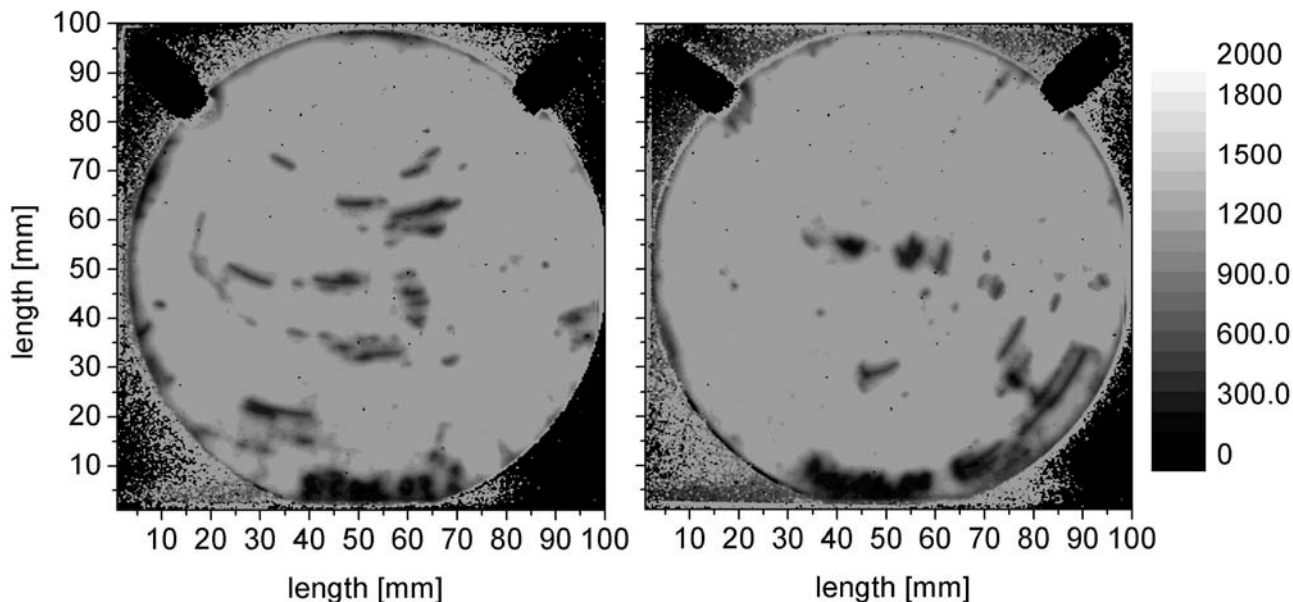


Figure 8.5: Two CDI measurements to show the homogeneity of the layer quality and some minor surface problems coming from tweezers prints, surface contamination or blistering effects.

8.2.3 Thermal annealing of lifetime samples

As described above the thermal stability of a passivation layer is one crucial point for its applicability as a rear side passivation layer. The combination of a low deposition temperature with good temperature stability is extremely desirable. As the layer deposition, independently from the method, will always take some minutes, the low deposition temperature causes no degradation effects of the silicon bulk. To withstand at least some seconds at temperatures above 800°C , which are the standard parameters for contact firing, would be the challenge for temperature stability of the $\text{Si}_x\text{C}_{1-x}$ layers.

The lifetime samples were annealed at 880°C for around 3 s in the furnace usually used for contact firing. Unfortunately many of the $\text{Si}_x\text{C}_{1-x}$ single layers show blistering effects. Additional discolouring complicated the QSSPC measurements. Nevertheless some layers show still a good passivation effect after the extreme thermal treatment. In Table 8.1 the comparison of three different layers is presented.

The layers differ in principle in the carbon content from 1 (high) to 3 (low). It can be seen that the carbon content is one striking factor in the stability of the layer network and by that also for the passivation effect. Another important factor is the dopant concentration and activation. As this electrical activation of the phosphorus during firing has an extreme impact on the contacting problem, all further firing experiments were done on a solar cell test structure.

Table 8.1: Lifetime measured with QSSPC at a minority-carrier density of $5 \times 10^{14} \text{ cm}^{-3}$ of different Si_xC_{1-x} passivation layers.

Si _x C _{1-x} layer	τ_{eff}	τ_{eff}
	before firing	after firing
	[μs]	[μs]
1	341	250
2	381	52
3	1126	18

This first high temperature annealing experiments show the necessity of protecting the Si_xC_{1-x} passivation layer during firing. As already discussed in chapter 5, this protective layer reduces blistering effects and possible cross contamination coming from the firing furnace. For the following experiments plasma deposited SiO_x capping layers were applied for this purpose.

8.3 Solar Cell Application

With the promising lifetime measurements achieved on float zone wafers we started to investigate the applicability of Si_xC_{1-x} passivation layers on high efficiency solar cell structures. Occurring problems in connection with the rear-side contacting will also be discussed. At the end of this section the optical performance of our passivation layers with respect to the internal reflection will be discussed.

8.3.1 First solar cell applications

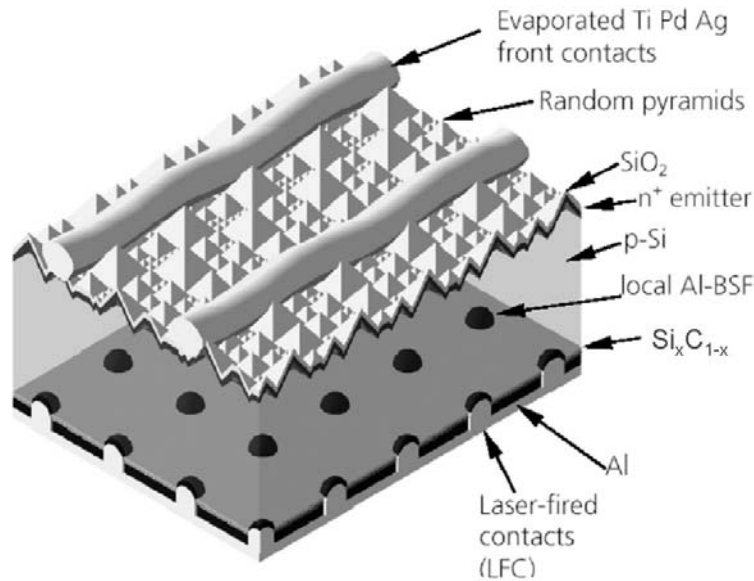


Figure 8.6: Scheme of the so called PERC/LFC structure with a $\text{Si}_x\text{C}_{1-x}$ passivation layer on the rear-side.

Different $\text{Si}_x\text{C}_{1-x}$ layers were now applied to the rear-side of solar cells with a high-efficiency front structure (FZ, $0.5 \Omega\text{cm}$, oxide-passivated $120 \Omega/\text{sq}$ emitter and evaporated contacts). Again not only the deposition but also the surface conditioning and cleaning was performed in the PECVD reactor. E-gun evaporation was used for the deposition of the $2 \mu\text{m}$ thick Al layer and the laser-fired contacts (LFC) [133] process was applied (see Figure 8.6).

Table 8.2: Solar cell results with $\text{Si}_x\text{C}_{1-x}$ rear-side passivation.

$\text{Si}_x\text{C}_{1-x}$ layer	τ_{eff} [μs]	V_{oc} [mV]	J_{sc} [mA/cm^2]	FF [%]	η [%]
(doped)	1126	632	36.8	81.6	19.0
(undoped)	341	662	37.9	81.0	20.3

First solar cell results with single passivation layers show, that not necessarily the best $\text{Si}_x\text{C}_{1-x}$ layers for high lifetimes (phosphorus doped) resulted in the best solar cell parameters (see Table 8.2). One possible explanation is a shunting effect of the aluminium contacts between passivation layer and silicon bulk. For further

explanations see chapter 8.3.3. Nevertheless, although the solar cells have not been annealed after e-gun evaporation and LFC formation, efficiencies exceeding 20% can be achieved.

It has to be considered that these were the very first solar cells with $\text{Si}_x\text{C}_{1-x}$ rear-side passivation layers realised at Fraunhofer ISE. Without any optimisation or adaptation on optical performance, aluminium contacts or laser firing parameters the 20% efficiency limit could be overcome. After these first attempts the efforts to reach still higher efficiencies were paused but will be continued in future works.

8.3.2 Thermal annealing of cell structures

In order to investigate the development of passivation behaviour in dependence of thermal annealing we had to adapt our solar cell structure. As a firing step had to be introduced, two important factors had to be considered. During firing (1) we could not accept any metal on our cell structure and (2) the front-side had to be untextured. The metal would contaminate the bulk material and cause massive recombination. A deterioration of the front-side passivating thermal oxide at the silicon pyramids (hot peaks) was the reason for leaving out the texturisation (see Figure 8.7).

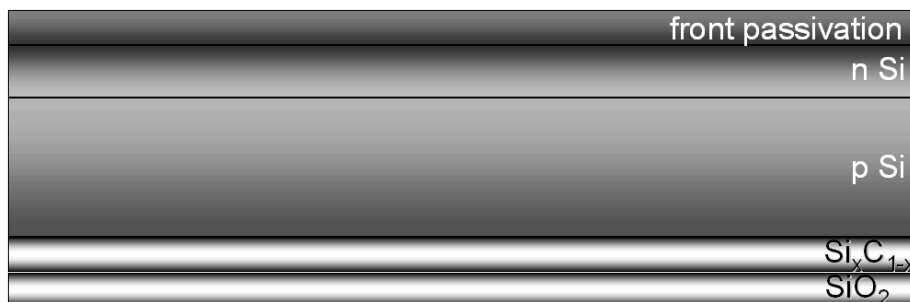


Figure 8.7: Schematic sketch of the solar cell test structure (without front-side texturisation and contacts) used for the firing experiments.

Without any grid we could not use standard characterisation methods to measure V_{oc} before and after firing. To solve this problem we measured the QSSPC and calculated V_{oc} from this data [134]. The front side passivation (thermal oxide) was assumed to be the better passivation layer than the rear side one. Therefore the measured V_{oc} values should be limited by the passivation performance of the $\text{Si}_x\text{C}_{1-x}$ layer. Because

we worried about blistering effects the Si_xC_{1-x} layer was capped with a plasma deposited SiO_x layer.

The Si_xC_{1-x} layers used for this experiment based on the excellent phosphorus doped passivation layers presented above. From our lifetime measurements on FZ wafers, a lot about the influence of phosphorus doping on passivation performance has been learned. These adapted Si_xC_{1-x} layers were applied. The carbon content of these layers was slightly varied to check if the temperature stability of the passivation performance could be further improved compared to the lifetime samples. The annealing of the solar cell structures was again done in the furnace usually used for contact firing. As the optical absorption was much higher on our samples compared to a standard cell structure covered with aluminium we reduced the temperature to 800°C.

Table 8.3: V_{oc} values of Si_xC_{1-x} layers with different carbon contents calculated from QSSPC measurements.

carbon content	V_{oc}	V_{oc}
	before firing [mV]	after firing [mV]
low	643	676
middle	652	682
high	623	667

In general it was striking that all passivation layers improve in performance with the firing step. As the cell structure had already been sintered before the firing that effect has to be explained in connection with the Si_xC_{1-x} passivation layer. One possible reason could be an enhancement of the saturation effect due to lattice adaptation. Additional hydrogen effusing from the Si_xC_{1-x} bulk to the interface would be a second one. A third possible explanation could be the enhanced activation of the phosphorus atoms in the layer which would result in a stronger field effect. Nevertheless there seems to be an optimum carbon content where the network is stabilised during annealing and where a good match between silicon crystal and Si_xC_{1-x} network is possible.

The fired cell structures were processed to solar cells subsequently. To finish the structure, front- and rear-side metallisation was necessary. Before that the passivation layer on the rear-side had to be opened at some points with plasma etching (SF₆). A subsequent sintering of the contacts at 420°C led to the solar cell results presented in Table 8.4.

Table 8.4: Solar cell results with Si_xC_{1-x} rear passivation after a firing step at 800°C.

carbon content	V_{oc} [mV]	J_{sc} [mA/cm²]	FF [%]	η [%]
low	663	31.9	80.4	17.0
middle	674	33.1	80.6	18.0
high	663	32.6	80.9	17.5

Considering the untextured front-side and ineffective 105 nm SiO₂ ARC of the solar cell which leads to a relatively low J_{sc} , these are excellent results. Although two high temperature steps (800°C firing and 425°C annealing) were done with the solar cells, the V_{oc} values of 674 mV is extremely high still. The measured V_{oc} on the solar cell is furthermore in good correlation with the calculated values.

8.3.3 Laser-fired versus lithographic defined contacts

The industrial application of Si_xC_{1-x} as a rear-side passivation layer is extremely dependent on its feasibility on standard contacting methods. The most promising method is laser firing contacting (LFC) which has been developed at Fraunhofer ISE. First solar cell results presented above show that phosphorus doping of Si_xC_{1-x} layers can lead to some problems in connection with LFC. As we did not want to lose the benefit of the passivation enhancement with phosphorus doping the carbon content of the Si_xC_{1-x} was slightly varied. This should not just stabilise the layer's network, but should also have an influence on doping activation and thereby on the electrical behaviour of our layers.

In

Table 8.5 two solar cells which saw exactly the same process steps except the rear-side contacting are presented. In Figure 8.8 one can find the appropriate schematic

sketch of these two contact methods. When looking closer on the contacts themselves the crucial difference of the contacting methods is obvious. The electrical contact realised with LFC shunts the phosphorus doped Si_xC_{1-x} layer and deteriorates its passivation performance [135]. The contact realised with plasma etching and a subsequent aluminium deposition has no direct electrical contact to the doped passivation layer. Therefore the passivation performance is almost unchanged in comparison to V_{oc} values calculated from QSSPC measurements (682 mV).

Table 8.5: Solar cell results with Si_xC_{1-x} rear-side passivation contacted with laser fired (LFC) or etched contacts.

contact scheme	V_{oc} [mV]	J_{sc} [mA/cm ²]	FF [%]	η [%]
LFC	645	32.6	81.0	17.0
etched	674	33.1	80.6	18.0

Although the LFC method leads to lower V_{oc} values, the optimised carbon content of the Si_xC_{1-x} layer enhanced the values in comparison with earlier results by more than 10 mV (see chapter 8.3.1). When going to still higher carbon contents, which could further enhance the performance with LFC contacts, unfortunately the passivation performance itself is decreased.

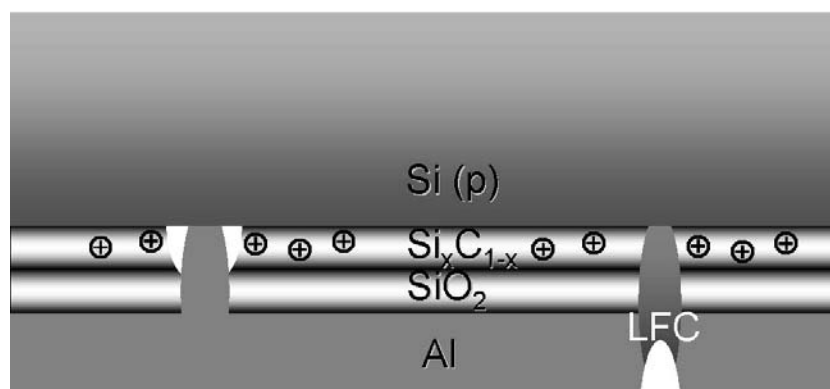


Figure 8.8: Rear-side of a PERC solar cell structure with a evaporated contact (left) and a laser fired contact (right).

One possible solution for this LFC contacting problem could be a Si_xC_{1-x} layer stack where the layer directly deposited on the cell surface is undoped. The subsequent

layer would then be phosphorus doped. This would create the wanted field effect but a direct shunting of passivation layer and cell bulk could possibly be prevented. Investigation approaching this subject could not be finished until the end of this work.

8.3.4 Optical performance of the Si_xC_{1-x} passivated solar cells

Another major issue of a rear-side passivation layer is its influence on the internal reflection of the solar cell (optical confinement). For details concerning the optical behaviour of our layers see chapter 3. As the Si_xC_{1-x} passivation layers are closely related to amorphous silicon a slightly lower refractive index of around 3.5 is expected. With increasing carbon content this refractive index can be further decreased which can slightly enhance internal reflection. In order to increase the internal reflection significantly the deposition of a second Si_xC_{1-x} layer with a much lower refractive index (≈ 2.5) should be done. For lack of time and because of its excellent optical performance ($n \approx 1.46$), we used PECVD deposited SiO₂ layer as an alternative. With a spectrophotometer (see chapter 3) we measured the solar cell's reflectivity in dependence of wavelength. By comparing the values in the long wavelength region conclusions about the optical performance of different passivation layers were expected.

Comparing the different data was quite complicated because just some of the solar cells were textured and because there were numerous layer stack combinations. Therefore a comprehensive comparison of different single passivation layers was impossible.

On textured cell structures, Si_xC_{1-x} layers with a small variation in carbon content were available. Although the overall passivation performance is extremely sensitive on carbon content, the reflectivities at 1200 nm wavelength just varied between 43 and 45%. Nevertheless, a significant difference in reflectivity between Si_xC_{1-x} single layers and SiO₂ single layers (40% at 1200 nm) on textured cells can be observed.

The solar cells with the untextured front-sides had several layer stacks on their rear-side. The additional SiO₂ layer, which acted as a protection layer during the firing process, significantly enhanced the reflectivity at 1200 nm. Therefore the variation of carbon content in the Si_xC_{1-x}, having already a small influence on the optical behaviour in single layer applications, shows no effect at all. The reflectivities at

1200 nm wavelength were 93% for all layers. This was just slightly below the reflectivity of an optimised SiO₂/SiN_x layer stack which achieved 94% at 1200 nm. The results show clearly that a plasma deposited Si_xC_{1-x}/SiO₂ layer stack already leads to an excellent internal reflection in the solar cells.

8.4 Conclusions

Si_xC_{1-x} is probably the best PECVD deposited passivation layer on lifetime samples. First applications as a rear-side passivation layer on high efficiency solar cells with PERC/LFC structure reach 20.3% efficiency. Furthermore, the excellent firing stability of our Si_xC_{1-x} layers could be proofed. After firing at 800°C for 3 s and additional annealing at 425°C maximum V_{oc} = 682 mV measured with QSSPC and V_{oc} = 674 mV on the completely processed solar cell could be achieved. As far as I know this is the best V_{oc} ever reached with a low temperature deposited and subsequently fired passivation layer. Comparing these results with thermally grown oxide, which can be seen as a reference passivation layer, the Si_xC_{1-x} performance lies just slightly below (around 10 to 15 mV). This means that our in-situ cleaning and low-temperature deposition process leads to almost as good V_{oc} after firing as a wet chemical cleaned and SiO₂ (thermally grown) passivation process.

9 FURTHER APPLICATIONS FOR PHOTOVOLTAICS

Two major applications of SiC for photovoltaics have already been presented and comprehensively discussed in this work. In this chapter I will furthermore present some applications which I just started to investigate or which are still in the planning stage. In the first part I will introduce some single layer applications such as etch-stop layers, emitter diffusion barrier layers, anti-reflection coatings for photovoltaic modules and tribologic coatings with tuneable optical performances. Silicon quantum dots embedded in a SiC matrix will be presented and the advantages of SiC over other possible matrices will be discussed. At the end I will motivate some multilayer applications where SiC layers with different physical properties are combined for still more advanced performances.

9.1 Etch-stop Layer

As we could learn in chapter 2 it can be very demanding to etch stoichiometric SiC layers, especially after annealing. This offers the possibility to use these layers as etch-stop layers for wet chemical etching solutions in a solar cell process. We focused our investigations on the field of wet chemical etchant solutions which are frequently used for photovoltaic standard processes.

Hydrofluoric acid etching

Hydrofluoric acid (HF) is normally used for SiO₂ removal. We exposed a stoichiometric SiC layer (deposited at 350°C on FZ silicon) for 6 min to highly concentrated (50%) HF. We expected no etching effect on the silicon substrate.

In Figure 9.1 one can see two micrographs of the SiC layer before and after etching in HF. The dominating area of the SiC seems to be completely unaffected by the etching procedure. The small crack in the layer shows also no change after the wet chemical

treatment. Only the contaminated areas (black dots) seem to be more pronounced after the HF treatment.

These results clearly show that stoichiometric SiC cannot be etched with HF (50%).

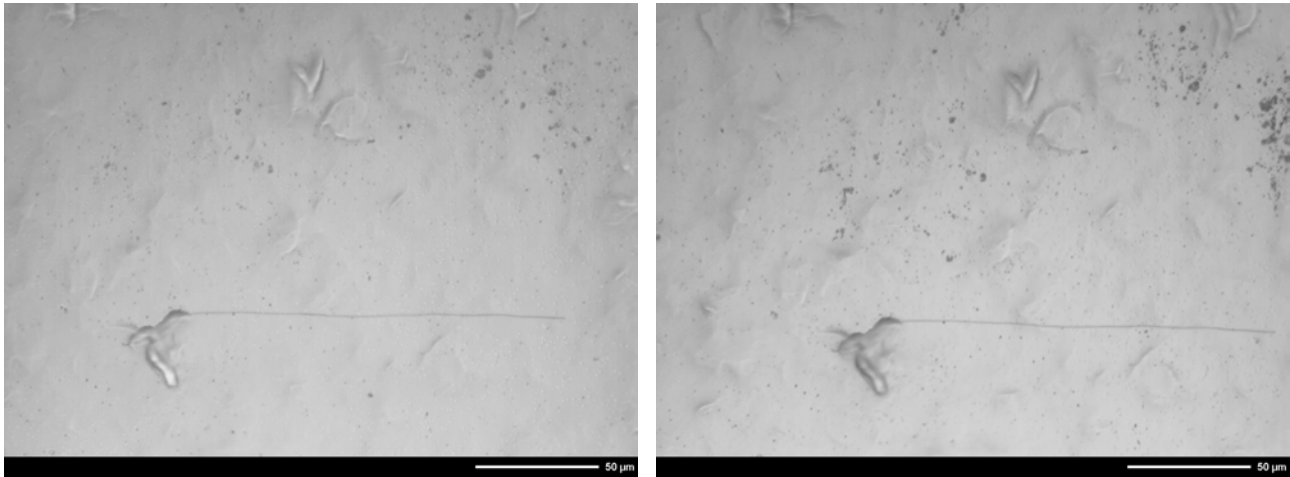


Figure 9.1: Micrographs of a stoichiometric SiC layer on a FZ silicon before (left) and after (right) exposure to 50% concentrated HF.

KOH etching

KOH is a frequently used etching solution to texture silicon wafers. As wet-chemical etching on just one side of a silicon wafer is not that simple (special etching apparatus necessary) a SiC layer could be used as a cover layer for the side to keep unetched. To enhance the etching process KOH is usually heated up to 85°C. In our investigations we used several KOH concentrations.

The stoichiometric SiC layer was again deposited at 350°C on a FZ wafer. An exposure to KOH (>3%, 90°C) for >10 min leads to no etching effect at all. After exposure for 6 min to 50% concentrated KOH (85°C) a slightly changing colour of the SiC layer indicates an etching effect. As the colour of SiC changes just on some positions on the surface a small etching rate can be presumed.

After annealing comparable SiC layers at 950°C (10 min) the 300 nm thick layer can even resist 85°C hot KOH (50%) for 30 min with almost no etching effect.

CP133 etching

Furthermore SiC was investigated as an etch-stop layer against CP133. This etching solution is e.g. used to remove the saw damage of an as-cut silicon wafer (“shiny etching”). As the etching rate of CP133 is very high ($\approx 7 \mu\text{m}/\text{min}$), it can be useful in some cases to cover surfaces which are e.g. already structured and would be removed otherwise.

A 1000 nm thick stoichiometric SiC layer was deposited on RBSiC ceramic at 350°C and covered with $15 \mu\text{m}$ of highly doped silicon (15 min at 950°C). Subsequently, the silicon layer was recrystallised (see chapter 7). After etching the whole sample in CP133 for one hour the silicon layer is completely dissolved. The remaining thickness of the SiC layer cannot be measured on the ceramic. Nevertheless, the whole surface is still completely covered with SiC which can be seen in scanning electron micrographs.

All these results show that stoichiometric SiC can be used as an excellent etch-stop layer against HF and KOH. Especially after additional thermal treatment the SiC layer is extremely stable and can even resist CP133 etching for 1 h.

9.2 Emitter Diffusion Barrier Layer

In chapter 6 a comprehensive study of the diffusion barrier performance of stoichiometric SiC layers was presented. One crucial point for solar cell processing is the emitter diffusion. For many cell concepts this emitter formation is realised with gas phase diffusion. For an n-type emitter POCl_3 gas is introduced into a quartz tube furnace at temperatures above 800°C . During this process a phosphorus doped glass is deposited on both sides of the wafer. This glass acts as an infinite source for phosphorus dopants.

If the wafer is covered with SiC ($\approx 100\text{-}300 \text{ nm}$) on one side the emitter diffusion can be prevented. This is also valid for p-type emitters with BBr_3 . A following removal of the emitter on the rear-side, which has to be done again with wet chemistry, could be omitted.

9.3 Anti-reflection Coating for Module Glasses

Moisture and corrosion resistance [10] is another SiC characteristic which could be used for photovoltaic applications. Its radiation hardness and optical properties (see chapter 3) in addition make an outdoor application possible.

Some module manufacturers already work on an optical confinement of their photovoltaic modules. Beside texturisation of the module's glass, anti-reflection coatings are investigated [136,137]. One major challenge for these anti-reflection coatings is the resistance against weather conditions. Frequently used amorphous SiN_x and SiO_2 layer stacks fulfil these demands. SiC as an alternative layer would in my opinion exceed their performance due to the numerous advantages mentioned above. Especially the extreme resistance against acid surrounding and high-energy radiation in the ultra-violet-wavelength-region would be an enormous advantage. Furthermore a layer stack with two different materials would be unnecessary. A just some nanometers thin stoichiometric SiC layer could be deposited on areas above 1 m^2 at 350°C in a high throughput plasma reactor in maybe one minute. This process should be economically competitive to the $\text{SiO}_2/\text{SiN}_x$ deposition and would probably exceed the module's lifespan significantly.

9.4 Tribologic Coatings with Good Optical Transmission

We tried to use the mechanical hardness of our stoichiometric layers, in connection with its excellent optical behaviour (see chapter 3) as a coating for an aluminium mirror. This mirror was used in a carrier density imaging apparatus (CDI) [111] as a back reflector for the infrared light. As the sample was put directly on the relatively soft aluminium, scratches, which deteriorated the reflectivity the longer it was used, could not be prevented. With a some nanometres thin SiC layer on it the scratching can be reduced significantly. Although the reflectivity of the mirror is reduced the lifetime of the mirror can be extended.

9.5 Quantum Dot Super Lattices

One novel approach to tandem cell design involves the use of bandgap engineered materials. These effective bandgaps could e.g. be controlled by their

respective quantum dot sizes and the distances between the quantum dots via quantum confinement [138]. A brief introduction into the physics behind this quantum dots will be given in this section. Furthermore, I will show how this theory could be applied on silicon quantum dots in a SiC matrix. The way to realise such a structure and the advantages over other possible matrices for silicon quantum dots will be discussed at the end of this section.

9.5.1 Theory

In indirect semiconductors the absorption of electromagnetic waves is, compared to direct semiconductors, more improbable because two in spite of one premises have to be fulfilled: the conservation of energy and momentum. As the minimum of the conduction band and the maximum of the valence band are at different momentum values k an absorption process needs a photon and a phonon. This behaviour on indirect semiconductors changes when the electronic wavefunction in the crystal is limited by the dimension. Such a system is called a quantum well. The changed conditions for a quantum well will be explained by a simple approximation for the conduction band [139]:

The electronic wavefunction ψ has to be a solution of the Schrödinger equation. For a one-dimensional movement (in direction x) and in time independent form the equation can be written as

$$\frac{\partial^2 \Psi}{\partial x^2} = -\frac{2m^*}{\hbar^2}(E-U)\Psi, \quad 9.1$$

where E is the total energy, U is the potential energy and m^* is the effective mass of the electron. When knowing U this simple form of the equation can be solved and the wavefunction (energy levels) can be calculated. For the one-dimensional quantum well with width L and infinite barrier height ($U=\infty$ outside, $U=0$ inside the well) the solution for the equation inside the well ($0 < x < L$) can be solved as

$$\frac{\partial^2 \Psi}{\partial x^2} = -\frac{2m^* E}{\hbar^2} \Psi = -k^2 \Psi; k = \frac{\sqrt{2m^* E}}{\hbar}. \quad 9.2$$

As $U=\infty$ outside the well

$$\psi(x) = 0 \text{ for } x \leq 0 \text{ or } x \geq L. \quad 9.3$$

When considering the boundary conditions the solution inside the well can be written as

$$\Psi(x) = A \sin(kx); kL = \frac{\sqrt{2m^*E}}{\hbar}; L = n\pi \quad 9.4$$

and the permitted energy levels therefore are

$$E_n = \left(\frac{\hbar^2}{8m^*L^2} \right) n^2; n=1, 2, 3, 4. \quad 9.5$$

The consequence is a discrete splitting of the energy levels (quantisation) which increases with n^2 and is dependent on the width L .

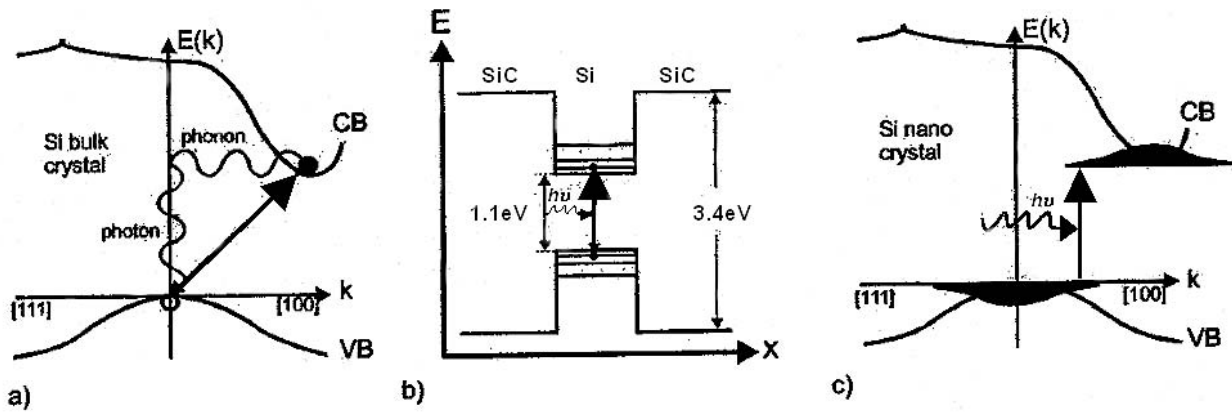


Figure 9.2: Schematic sketch of the band structure of crystalline silicon (a) and a silicon quantum dot (b: quantum well and c: direct absorption).

Similar behaviour can be found in a silicon crystallite which is embedded in a SiC matrix (see Figure 9.2). New quantised states are generated above the bandgap of the bulk silicon. As the confinement affects the conduction band and the valence band in all three dimensions, the photon energy can be written as

$$E_{\text{photon}} = E_g + 3 \cdot E_{h,VB} + 3 \cdot E_{n,CB}, \quad 9.6$$

where E_{photon} is the energy of the absorbed photon, $E_{h,VB}$ the confinement-energy of the hole in the valence band and $E_{n,CB}$ the confinement-energy of the electron in the conduction band. Parallel to the dimensional confinement a blurring in the momentum room takes place (due to “Heisenbergs Unschärferelation”). A transition of silicon from an indirect to a direct semiconductor is therefore possible.

9.5.2 Preparation of Si quantum dots in a matrix

The realisation of silicon quantum dots in a foreign matrix usually starts with numerous layer stacks with stoichiometric and silicon rich composition [140]. Substrates used for this approach have to be high temperature stable because of a necessary annealing procedure. During this annealing usually done at temperatures above 900°C [141], depending on the layer material, a segregation and crystallisation leads to crystalline silicon quantum dots in a foreign matrix. Through layer thickness and annealing procedure, size and distance of the QDs, which are directly connected to quantum confinement, can be affected.

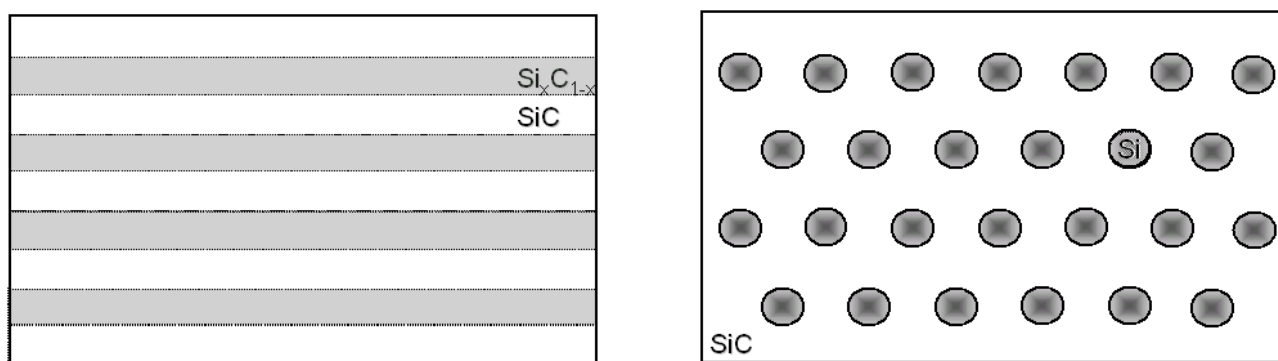


Figure 9.3: Silicon rich $\text{Si}_x\text{C}_{1-x}$ and stoichiometric layer stacks (left) form Si quantum dots in a stoichiometric matrix (right) after thermal annealing.

Kurokawa *et al.* [142] reported the preparation of silicon quantum dot super lattices (Si-QDSL) in a SiC matrix by depositing subsequently silicon rich hydrogenated $\text{Si}_x\text{C}_{1-x}$ and stoichiometric SiC, each layer some nm thick, as it can be seen in Figure 9.3 (left). With plasma enhanced chemical vapour deposition (PECVD) they deposited 30 super lattices on quartz substrates, and on silicon substrates capped with amorphous SiO_2 layers. After the deposition an annealing procedure in N_2 atmosphere at 900°C (20 min) was applied (see Figure 9.3, right). The generation of Si QDs in the SiC matrix could be proofed through Raman measurements. Suendo *et al.* [143] could even directly prepare silicon quantum dots at 250°C just by applying appropriate deposition conditions for the PECVD process.

First attempts to realise QDSLs in our plasma reactor show that SiC/ $\text{Si}_x\text{C}_{1-x}$ layer stacks (20 double layers) can be deposited in just a few minutes. The carbon concentration in the layers, determined with ToF SIMS, is varying between 45 and

50%. Subsequent annealing tests lead to no crack formation or blistering effects. The preparation of cross sections for Transmission Electron Microscopy could not be finished until the end of this work.

With our reactor a still more complicated layer stack system with floating carbon concentration could possibly lead to an even wider range of influence on silicon quantum dot size and annealing behaviour.

9.5.3 Potentials of the SiC quantum dot layers

The usage of SiC as the matrix material for silicon quantum dots would have two striking advantages: (1) The quantum well is relatively shallow compared to e.g. SiO₂ (9 eV, [139]) which together with (2) the dopability of the SiC matrix (see chapter 4) could make electrical conductivity possible. This would enable us to transport the generated minority carriers out of the quantum dot array.

As I could show in this work, the crystallisation behaviour does not seem to be affected by additional doping (see chapter 5). As comprehensive investigation using X-ray diffraction and Raman spectroscopy to understand crystallisation and segregation behaviour of doped and undoped SiC layers were realised, this knowledge should be precious for realising Si QDs. Furthermore I could already show that doped SiC matrices can be electrically activated (see chapter 4) through thermal annealing.

9.6 Layer Stacks for “Multi-performance” Applications

For many applications SiC layers with different physical properties would be preferable. In many cases this can be a contradiction. Therefore I will present layer stack systems which combine SiC layers with different physical properties to a “multi-performance” layer stack.

9.6.1 SiC stack systems for solar cell processing

One very interesting application of a SiC/Si_xC_{1-x} multi-layer stack would be a combination of a diffusion barrier and an etch-resist layer with a temperature stable passivation layer. In Figure 9.4 one can see the standard process chain most

frequently used in industrial production (left side) of multi crystalline silicon solar cells.

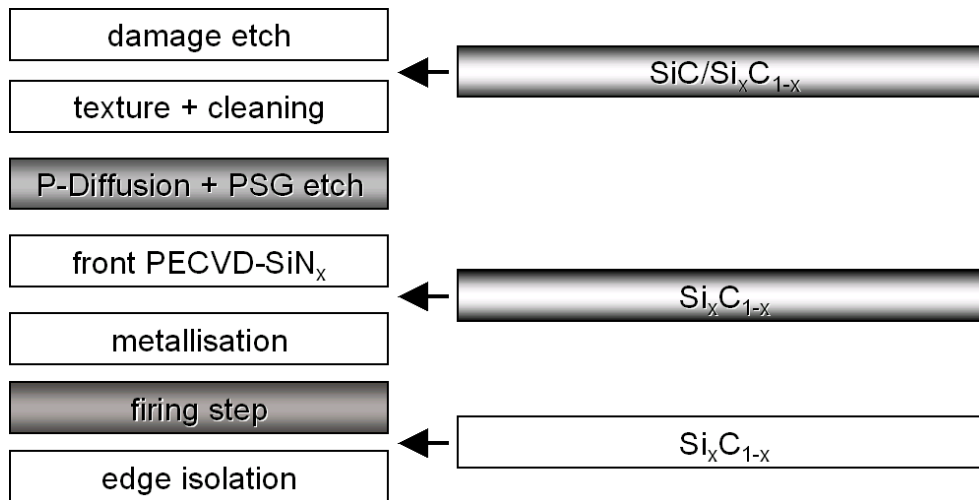


Figure 9.4: Process chain frequently used for industrial silicon solar cells.

A standard passivation layer with no thermal stability would be introduced almost at the end of the process chain after the contact firing step (right bottom). On this layer aluminium would be deposited and after LFC (see chapter 8) an annealing step at 350°C for some minutes would be sufficient. The requirements for such a layer would not be too challenging. However the cleaning of the surface is of enormous importance due to the high amount of contamination originating from former process steps.

The second possible moment for introducing the passivation layer would be directly after SiN_x deposition (right middle). This rear-side passivation layer should be able to withstand the contact firing process. Such a layer would be our Si_xC_{1-x} passivation layer already presented in chapter 8.

A real progress for solar cell processing would be a rear-side passivation almost at the beginning of the process chain. Directly after damage etching the Si_xC_{1-x} passivation layer could be deposited. As the plasma process includes a surface cleaning, no additional wet-chemical cleaning would be necessary. To enhance etch resistivity, a second stoichiometric SiC layer could be deposited on top of the first layer. This second layer would also act as a diffusion barrier during phosphorus

diffusion and would provide additional hydrogen for interface passivation (see chapter 6).

9.6.2 Rugate filters

A Rugate filter is an optical coating in which the refractive index varies sinusoidal throughout its thickness [144]. It reflects light over a certain band of wavelengths and is considered to be one of the more complex applications of inhomogeneous optical coatings.

9.6.2.1 Theory

The index variation can be written as

$$n(z) = n_0 + n_1 \sin\left(\frac{2\pi}{\Lambda} z\right), \quad 9.7$$

where n_0 and n_1 are the average index and the amplitude of the index variation, respectively, and Λ is the thickness of a single sinusoidal period. These three parameters determine the spectral characteristics of the filter.

In order to calculate the spectral response, Maxwell's equations must be solved with appropriate boundary conditions. By assuming $n_1 \ll n_0$, it is possible to neglect the second order term in the wave equation so that the one dimensional wave equation reduces to

$$\frac{d^2 E(z)}{dz^2} + \frac{\omega^2}{c^2} (n_0^2 + 2n_0 n_1 \sin Kz) E(z) = 0, \quad 9.8$$

where ω is the angular frequency of light, c is the speed of light and

$$K = \frac{2\pi}{\Lambda}. \quad 9.9$$

Lim *et al.* [144] reported about a derivation in closed form of equation 9.8 using the coupled mode theory. The resulting reflectance R of a film with a sinusoidal refractive index is given by

$$R = \frac{\kappa^2 \sinh^2 sL}{s^2 \cosh^2 L + \left(\frac{\Delta k}{2}\right)^2 \sinh^2 sL}, \quad 9.10$$

where

$$s^2 = \kappa^2 - \left(\frac{\Delta\kappa}{2}\right)^2 \quad 9.11$$

$$\kappa = \frac{\pi n_1}{\lambda_0} \quad 9.12$$

$$\Delta k = 2 \frac{\omega}{c} n_0 - K, \quad 9.13$$

with λ_0 as the central wavelength and L as the total thickness of the Rugate filter. The resulting maximum reflectance occurs at $\Delta k=0$ and from this condition the relationship between Λ and n_0 is given by

$$\Lambda = \frac{\lambda_0}{2n_0}. \quad 9.14$$

The bandwidth $\Delta\lambda$ for which the reflectance is a maximum, is given by

$$\Delta\lambda = 2\lambda_0 \left| \frac{n_1}{n_0} \right|. \quad 9.15$$

The reflectance or transmittance of the filters can be more accurately calculated by a computer simulation using the matrix method. In this method it is assumed that an inhomogeneous layer is composed of very thin homogeneous multiple layers.

9.6.2.2 SiC as a Rugate filter material

When using plasma enhanced chemical vapour deposited films for the Rugate filter layer stack, SiO₂ and SiN_x films are frequently used [144]. Young *et al.* [145] already reported about Rugate filters realised by using amorphous SiC layers.

Simulations done at our institute by M. Peters [unpublished] showed that our SiC layers could also be used to realise a Rugate filter. Details on this simulation will be presented in the following.

The parameters for the simulation were set as follows: $n_0=2.6$, $n_1=0.7$, $\Lambda=220$ nm and 10 layer stacks with a sinusoidal refractive index characteristic (from 1.9 to 3.3). The assumed refractive index curve can be found in Figure 9.5. There we can find, that an optimum thickness of around 1 to 2 nm of a single SiC layers should be achieved. To realise this refractive index characteristic in an appropriate time, a process which changes refractive index just by changing the gas flow has to be used. A suitable process was already presented in chapter 3. An additional advantage of our reactor

system could be the realisation of a smooth refractive index gradient without any steps. This could be done by depositing the layers without any plasma interruptions and very small changes in the gas flows. For the first simulations a discrete changing of the refractive index in small steps was assumed.

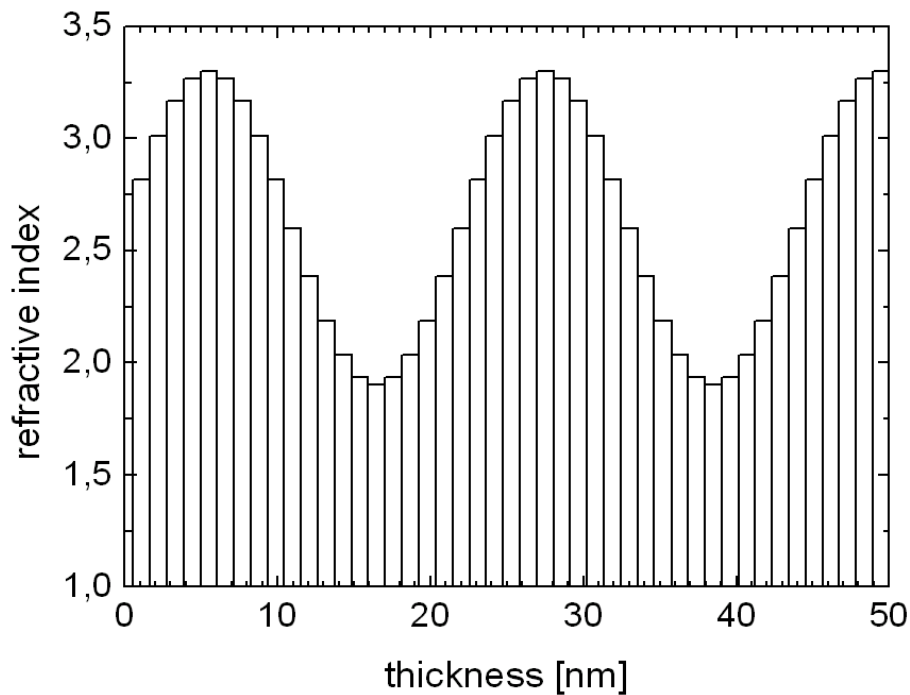


Figure 9.5: Discrete refractive indices characteristic as it was assumed for first simulations.

Assuming a refractive index curve similar to that in Figure 9.5, the simulated transmission behaviour as shown in Figure 9.6 can be expected. A relatively broad transmission minimum can be seen at 560 nm. Although this minimum is just some nm wide and does not reach zero transmission the result is encouraging. With an optimised deposition procedure (no steps in the refractive index) and a much higher amount of stack periods (30-50 instead of 10 periods) the filter performance could be enhanced significantly.

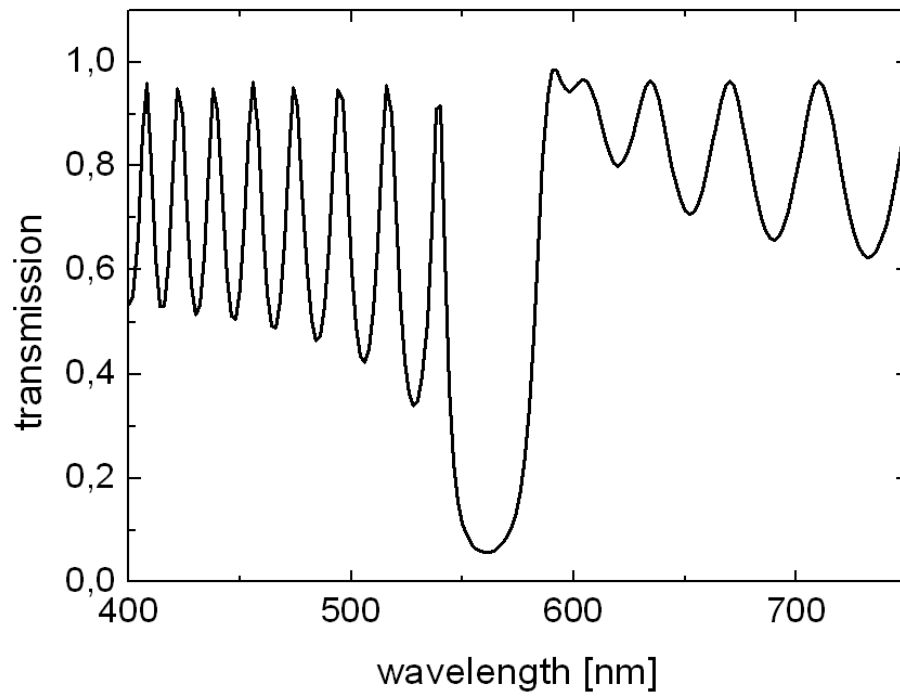


Figure 9.6: Simulated transmission behaviour of 10 SiC layer stacks with a sinusoidal refractive index.

10 SUMMARY

Within this work amorphous Silicon Carbide is investigated for its applicability in photovoltaic devices. The temperature stability and dopability of SiC makes this material very attractive for applications in this area. During this work several deposition processes in different plasma regimes could be established and the resulting layers were comprehensively investigated.

Physical basics of amorphous SiC networks and plasma processes are discussed and first measurements with FTIR of the different layer types show the complexity of the network. The special features of the plasma reactor such as high temperature deposition and two-source excitation are also discussed and the two main deposition regimes are introduced. Beside plasma etching I furthermore tested the etching behaviour of stoichiometric SiC in different wet chemical etching solutions. The results show that etching of SiC, especially when it is already annealed, is very difficult for both etching processes. Furthermore, stress measurements of our layers deposited and annealed at different temperatures show the change of stress from compressive (<600°C) to tensile with temperature. The widely tuneable optical behaviour of our SiC layers with Si/C ratio and deposition parameters is investigated. I show experiments where the refractive index can be varied from 2.3 to 3.7 just by changing one deposition parameter and at the same time varying the bandgap from 2.4 to 2.0. Photothermal deflection spectroscopy, a method to measure the bandgap of the different layers, proves that the defect density in the layers is small. Furthermore, I introduce physical basics of the electrical behaviour of amorphous semiconductors and show that our SiC layers can be successfully doped with boron, phosphorus or nitrogen. After an annealing of the stoichiometric and boron doped SiC layer at 650°C for 2 h a lateral conductivity of 10^{-3} Scm^{-1} can be measured. With temperature dependent measurements of the conductivity the activation energies of differently doped layers is calculated and plotted in the Meyer-Neldel plot. A lasting “activation” of the dopants with annealing can be found. Furthermore I present measurements of the SiC layer’s resistivity inside the Recrystallised Wafer Equivalent with the

especially developed “contow” access. The results show a resistivity of the SiC layers of $10^1 \Omega\text{cm}$. The high temperature processing obviously leads to further reduction of the resistivity which is then low enough to have no disturbing influence on the solar cells series resistivity. Other annealing effects in SiC at temperatures up to 1400°C are investigated. I discuss changes in the amorphous network and present comprehensive studies about starting crystallisation. With XRD and Raman measurements the appearance of different crystalline phases (3C, 4H, 6H) and small amounts of carbon and silicon clusters can be found. The results show that stoichiometric amorphous SiC layers crystallise to stoichiometric crystalline layers and that dopants in the matrix have no influence on this behaviour. Sometimes occurring cracking of the SiC layers at this high temperatures and reasons for that behaviour, like blistering, difference in expansion coefficients, contamination and so on, are discussed. The results show, that adapting the SiC layer’s thickness to the substrate’s surface conditions can prevent cracking up to annealing temperatures of 1400°C . I also present investigations concerning diffusion in and out of the SiC layers at this temperatures. The diffusion barrier performance of SiC layer against transition metals is discussed. Diffusion experiments focusing on iron show that SiC is an excellent barrier layer when cracking of the layers at the high temperature applied can be prevented ($D=10^{-15} \text{ cm}^2/\text{s}$ at 1200°C). Furthermore the out-diffusion of boron which dopes a neighbouring silicon layer is discussed and shows that a controllable doping of the silicon layer out of the SiC with boron is possible. Hydrogen effusion from the SiC layers is also investigated and shows that different effects, especially dependent on the diffusion temperature, influence this behaviour. Several measurements with FTIR and SIMS prove that SiC contains high amounts of hydrogen which lead to a significant bulk passivation effect in mc silicon.

The application of SiC in the Recrystallised Wafer Equivalent (RexWE) is presented and shows that SiC is a sufficiently conductive diffusion barrier layer. The crystalline silicon thin-film solar cell is introduced and special processing steps developed during this work are introduced. I furthermore present first solar cell results (7.2% on 1 cm^2 solar cell) and discuss potentials for an industrial realisation. In this connection comparisons to other thin-film technologies show that our technology has some outstanding cost advantages such as: (1) almost unlimited resources and (2) the possible benefit of all wafer technology developments in the future. As future photovoltaics industry has to produce modules in the Terrawatt scale and the

crystalline silicon wafer is the most intensively investigated solar cell concept, these cost advantages are unbeatable in my opinion.

One further focus is the surface passivation performance of $\text{Si}_x\text{C}_{1-x}$ layers on crystalline silicon. During this work a special homogeneous in-situ cleaning and deposition process could be developed which leads to excellent minority carrier lifetimes of up to 2 ms in FZ silicon ($0.5 \Omega\text{cm}$). The best solar cell result achieved with a PERC/LFC structure was 20.3% efficiency. I present investigations of the temperature stability of $\text{Si}_x\text{C}_{1-x}$ on untextured cell structures where a V_{oc} of 672 mV could be achieved. This temperature stable passivation layer makes alternative solar cell processing possible which can lead to cost reduction by increased solar cell efficiency.

I present some further applications of SiC layers for photovoltaics which are already under investigation or are still in the planning phase at our institute. These are etch-stop layers, emitter diffusion barrier layers, anti-reflection coatings for module glasses, tribologic coatings or silicon quantum dots in a SiC matrix. At the end layer stack combinations of SiC layers with different behaviours for even more advanced applications like e.g. Rugate filters are presented.

This work should help to increase the basic understanding of amorphous SiC layers. I want to show that the material has in fact the potential to combine several features like: diffusion barrier performance, tunable bandgap, p- and n-doping, conductivity, source for hydrogen and dopants, surface passivation, thermal stability, stress tuning and others. Therefore amorphous SiC seems to be most suitable for these and other applications in silicon semiconductor devices.

11 DEUTSCHE ZUSAMMENFASSUNG

Im Rahmen dieser Arbeit wurde amorphes Siliciumkarbid auf seine Anwendbarkeit in der Photovoltaik untersucht. Dazu wurde der Plasmareaktor AK400M, gebaut von Roth&Rau (Deutschland), auch für Hochtemperaturabscheidungen von uns weiterentwickelt und verschiedene Parameterräume für die Abscheidung eingeführt. Die abgeschiedenen Schichten wurden, wie in den ersten 6 Kapiteln dargestellt, umfassend untersucht.

In Kapitel 1 werden die Grundlagen eines amorphen Netzwerkes eingeführt und speziell auf SiC erweitert. Erste FTIR Messungen zeigen die Komplexität des vorhandenen Netzwerkes. Weiters wird die plasma enhanced chemical vapour deposition (PECVD) eingeführt. Die besonderen Möglichkeiten der AK400M werden erklärt und zwei Parameterräume für die Abscheidung eingeführt. In Kapitel 2 wird auf das Ätzverhalten und hier besonders auf das von stöchiometrischem SiC eingegangen. Neben im Plasmareaktor entwickelten Ätzprozessen wird auch auf nasschemisches Ätzen eingegangen. Die Ergebnisse zeigen, dass SiC - und hier besonders bereits getempertes SiC - sehr schwer zu ätzen ist. Weiter werden Stressmessungen von bei verschiedenen Temperaturen abgeschiedenen und/oder getemperten SiC Schichten diskutiert. Es zeigt sich ein Wechsel von Zug- (<600°C) zu Dehnstress mit steigender Temperatur. In Kapitel 3 wird das optische Verhalten von SiC diskutiert. Nach einer Einführung in die physikalischen Grundlagen wird die Einstellbarkeit des Brechungsindizes gezeigt. Ich stelle Experimente vor, in denen der Brechungsindex nur durch Änderung eines Prozessparameters während der Abscheidung von 2.3 bis 3.7 geändert wird. Parallel dazu ändert sich die Bandlücke von 2.4 bis 2.0. Transmissionmessungen werden präsentiert, die es uns ermöglichen, mit Hilfe der Theorie von Tauc die Bandlücke zu berechnen. PDS wird als weitere Methode zur Bestimmung der Bandlücke eingeführt und zeigt die geringe Defektdichte in den SiC Schichten. In Kapitel 4 werden die physikalischen Grundlagen zum elektrischen Verhalten von amorphen Halbleitern besprochen. Ich zeige, dass die SiC Schichten erfolgreich mit Bor, Phosphor und Stickstoff dotiert

werden können und beschäftige mich auch mit dem Einfluss von Dotiergasen auf den Abscheideprozess. Nach einem Temperprozess bei 650°C für 2 h wird eine laterale Leitfähigkeit von 10^{-3} scm^{-1} gemessen. Mit Hilfe von temperaturabhängigen Leitfähigkeitsmessungen wird die Aktivierungsenergie bestimmt und im Meyer-Neldel Diagramm dargestellt. Am Ende dieses Kapitels stelle ich Leitfähigkeitsmessungen an der SiC Schicht mit Hilfe des neu entwickelten „contow“ Konzepts vor. In Kapitel 5 wird das Temperverhalten von SiC bei Temperaturen bis zu 1400°C diskutiert. Ich präsentiere Untersuchungen im Zusammenhang mit den Veränderungen im Netzwerk und gehe auf die beginnende Kristallisation der Schichten ein. Mittels XRD- und Raman-Messungen werden die auftretenden kristallinen Phasen untersucht. Das manchmal auftretende Problem von Sprüngen in der Schicht während der Temperversuche wird ausführlich besprochen. Kapitel 6 beschäftigt sich mit der Diffusion durch und aus SiC Schichten. Nach einer Einführung in die Grundlagen der Diffusion wird die Diffusion von Metallen und hier im Speziellen Eisen umfassend untersucht. SiC zeigt dabei eine exzellente Barrierewirkung unter der Voraussetzung, dass die Schicht keine Sprünge aufweist. Weiter beschäftigt sich ein umfassender Teil des Kapitels mit der Ausdiffusion von Bor in eine benachbarte Siliciumschicht. Am Ende des Kapitels wird SiC als Quellschicht für Wasserstoff vorgestellt. Verschiedene Untersuchungen zu den dabei auftretenden Prozessen werden vorgestellt und der Einsatz von SiC als exzellente Wasserstoff-Quellschicht für die Defektpassivierung in Silicium wird gezeigt.

Im Kapitel 7 wird der Einsatz von SiC als leitfähige Diffusionsbarriere im Rekristallisierten Wafer Äquivalent (RexWE) vorgestellt. Es wird der Beweis erbracht, dass SiC für diese Aufgabe ausgezeichnet geeignet ist. Die spezielle Prozessierung von Solarzellen mit den hergestellten RexWEs wird vorgestellt und Anforderungen an die kristalline Silizium Dünnschichtzelle generell diskutiert. Erste Solarzellenergebnisse auf 1 cm^2 Zellen mit einem Wirkungsgrad von 7.2% werden vorgestellt. In Kapitel 8 wird die Anwendung von $\text{Si}_x\text{C}_{1-x}$ Schichten für die Oberflächenpassivierung präsentiert. Nach einer Einführung in die physikalischen Grundlagen wird der im Rahmen dieser Arbeit entwickelte in-situ Ätz- und Passivierungsprozess vorgestellt. Mit diesem homogenen Prozess können in FZ Silicium Minoritätsladungsträger-Lebensdauern von bis zu 2 ms gemessen werden. Solarzellen mit $\text{Si}_x\text{C}_{1-x}$ Rückseitenpassivierungsschichten erreichen Wirkungsgrade bis zu 20.3%. In weiteren Untersuchungen wird die exzellente Temperaturstabilität

der Schichten gezeigt. Selbst nach einem Feuerschritt bei 800°C können auf nicht texturierten Zellen noch Leerlaufspannungen mit bis zu 672 mV gemessen werden. In Kapitel 9 werden weitere mögliche oder bereits untersuchte Anwendungen von SiC - wie z.B. Ätzstoppschichten, Emitterdiffusions-Barrierschichten, Antireflexbeschichtungen für Modulgläser, mechanische Schutzschichten oder Silicium Quantenpunkte in einer SiC Matrix - für die Photovoltaik vorgestellt. Am Ende werden Schichtkombinationen mit SiC Schichten mit verschiedenen Eigenschaften wie z.B. Rugatefilter vorgestellt.

Appendix A Characterisation Methods

A.1 Ellipsometry

Ellipsometry is a method to get information about optical properties of thin layers [146]. Depending on the complexity of the apparatus the measured data can contain information about layer thickness and refractive index of one single layer or can contain the refractive index in dependence of the wavelength of a multi-layer stack. The ellipsometry bases on the difference in reflection behaviour of the normal and parallel to plane of incidence. Figure A.1 below illustrates this basic principle behind ellipsometry.

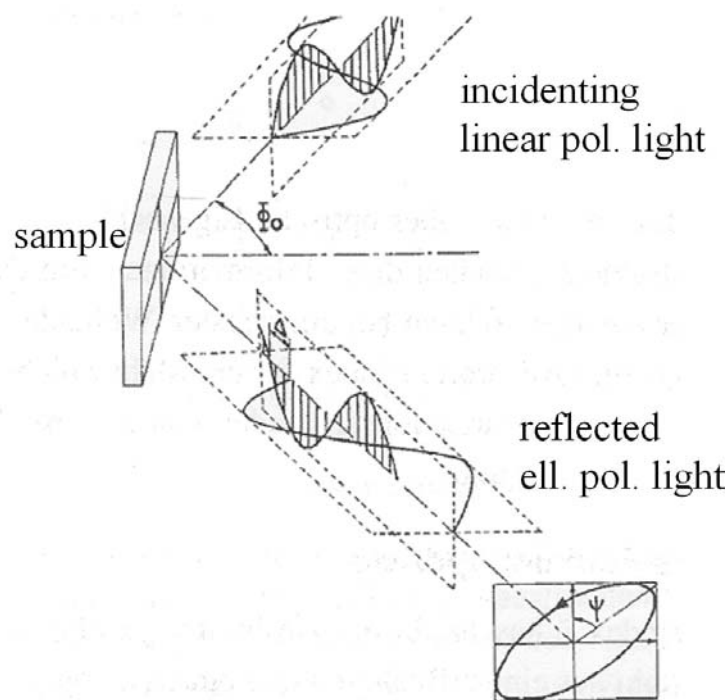


Figure A.1: Scheme of the ellipsometric parameters ψ and Δ and angle of incident Φ_0 .

First, the polarisation state of incoming light is known. This incident light interacts with the sample and is reflected by it. The interaction of the light with the sample causes a polarisation change in the light, from linear to elliptical polarisation. The polarisation change, or a change in the shape of the polarisation, is then measured by analysing the light reflected from the sample. Ellipsometry measures two values, ψ

and Δ , that describe this polarisation change. These values are related to the ratio of Fresnel reflection coefficients, R_p and R_s for p - and s - polarised light which is expressed by

$$\Phi = \tan(\Psi) \cdot e^{-i\Delta} = \frac{\tilde{R}_p}{\tilde{R}_s}. \quad 1$$

As ellipsometry measures the ratio of two values, it can be highly accurate and very reproducible. The ratio is a complex number, thus it contains “phase” information, Δ , which makes the measurement very sensitive.

A.2 Fourier Transformed Infrared Spectrometry (FTIR)

Fourier Transformed Infrared Spectroscopy (FTIR) is especially useful for identifying organic (carbon-containing) molecules [147]. FTIR is cost-effective in terms of labour and instrumentation, easy to perform, rapid, and provides fairly definitive or good circumstantial identification of contaminants. The FTIR tool we are using at Fraunhofer ISE is a Bruker IFS113V spectrometer (resolution 6 cm^{-1}) working at wavenumbers of 4000 to 500 cm^{-1} .

Spectroscopy is the study of chemical composition by observation of the interaction of molecules with electromagnetic radiation. Infrared (IR) spectroscopy uses light of about $2.5 \text{ }\mu\text{m}$ to $16 \text{ }\mu\text{m}$, which is beyond the visible range. Infrared spectroscopy is an absorption technique. FTIR is useful for identifying organic contamination because organic molecules are held together by covalent bonds. In contrast to ionic bonds (as in salts), covalent bonds are not rigid. Instead, they move or vibrate in a characteristic manner such as stretching or twisting. Particular portions of molecules absorb infrared radiation at specific frequencies. The specific pattern of absorption can be related to the molecular structure. The complex chemical IR fingerprint is interpreted by comparison with an infrared library of patterns of specific molecules. The popularity of FTIR is based not only on the physical measurement but on efficient data management. Specifically, fourier transform (FT) and computerised evaluation relative to standard IR libraries allow reliable and routine analysis. Fourier transform, a mathematical technique for converting a signal in the time domain into the frequency domain, enhances IR measurements by providing light speed and high sensitivity. A short pulse of broad-spectrum IR radiation is applied to the sample; the FT analysis breaks the response down to individual frequencies. Computerised IR libraries eliminate much of the analytical variability in compound identification.

A.3 Raman Spectroscopy

When measuring with Raman spectroscopy the sample is illuminated with monochromatic light of the frequency ν_0 . The scattered light is detected spectrally resolved [148]. When the frequency of the scattered radiation is analysed, not only the incident radiation wavelength observed via elastic scattering (Rayleigh scattering) is analysed, but also a relatively small amount of radiation which is scattered inelastically referring to as the Stokes and anti-Stokes Raman scattering.

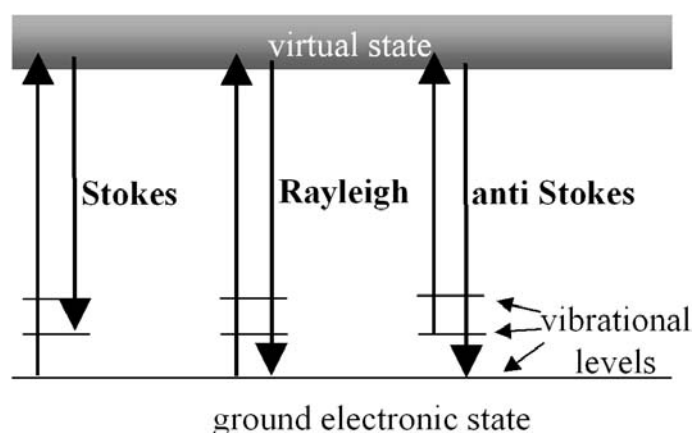


Figure A.2: Simplified energy diagram of the different scattering process used for Raman spectroscopy.

The scattered radiation occurs in all directions and may also have observable changes in its polarisation along with its wavelength. The shift in wavelength coming from the in-elastically scattered radiation provides the chemical and structural information. Raman shifted photons can be of either higher or lower energy, depending on the vibrational state of the investigated molecule. A simplified energy diagram that illustrates these Procedures can be found in Figure A.2. Stokes radiation occurs at lower energies and anti-Stokes at higher energies than the Rayleigh radiation. This energy decrease or increase is related to the vibrational energy levels in the ground electronic state of the molecules. The intensity of the scattered light is proportional to the product of the proportion in the volume and the Raman-scattering cross section. When the scattering cross sections of the involved phases are known, the composition can be extracted from the intensity of the occurring Raman band. In the spectrum of microcrystalline silicon for example a typical mode at 520 cm^{-1} and for monocrystalline one at 480 cm^{-1} can be observed.

A.4 Secondary Ion Mass Spectrometry (SIMS)

Secondary Ion Mass Spectrometry (SIMS) is a highly specialised analytic tool which combines high spatial resolution and high sensitivity [21]. This technique uses a highly focused ion beam (e.g. of caesium ions, Cs^+) which sputters material from a selected domain on a sample surface (see Figure A.3). The secondary ions which are ejected from the sample are focused into a mass spectrometer which separates the ion according to their mass/charge ratio. An advanced method is to combine the detector with a quadrupole filter which enables to separate mass and energy information of the charged particles because of different flight times (time of flight ToF).

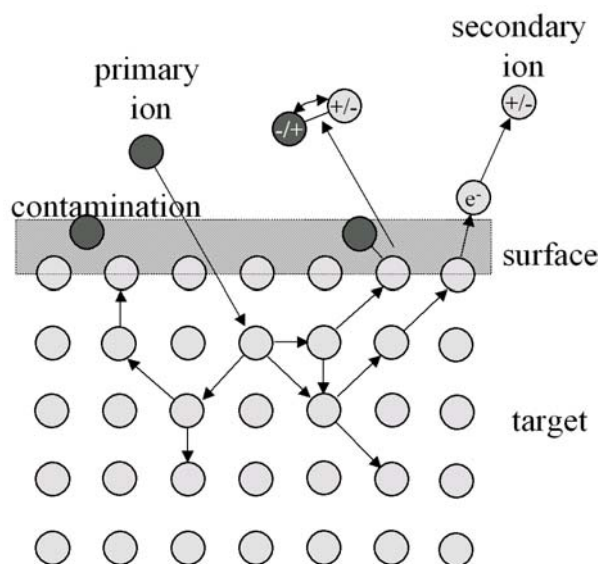


Figure A.3: Schematic picture of energy transfer and the emission process at the sputtering of a solid's surface with primary ions in the keV-region.

Most of our measurements were done at RTG Microanalyse GmbH in Berlin (Germany). The sputter source used caesium ions (Cs^+) with an energy of 14.5 eV. As caesium has a very low electronegativity (0.7) it tends to release light electrons after collision which ionise the sputtered particle negatively. The resulting secondary ion beam is passed through a sector magnet for mass separation. Signal detection uses either an electron multiplier operated in ion counting mode or, for intense secondary ion signals, a Faraday Cup is used to directly measure the secondary beam current. By repeatedly stepping the magnet through a sequence of mass stations it is possible to determine the concentration of each of the selected elements. In general, all

analytical sessions should both begin and end with an analysis of a calibration standard. Ion yields, the efficiency with which the sputtering process produces ions, is a function of both element and the matrix which are being studied. A very important aspect of SIMS technology is its capacity to provide information on the distribution of trace elements as a function of depth. This feature is of particular importance in the fields of semiconductor research and material design. SIMS depth profiling can provide important information for ion implant dosimetry, for thermal or chemical diffusion studies and for research projects evaluating chemical modification at thin film interfaces. The absolute abundance of a target element as a function of depth is generally calibrated by running an implant standard of identical matrix and of known total implant dosage.

A.5 Quasi-Steady-State Photoconductance Technique (QSSPC)

The experimental apparatus used in the present work for QSSPC measurements was fabricated by Sinton Consulting [129]. A photographic flash-lamp is used as the generation source. The sample is inductively coupled by a coil to an RF-bridge, which senses changes in the permeability of the sample and therefore its conductance. A reference solar cell and an oscilloscope are used to determine the time dependence of both, the excess photoconductance of the test sample $\Delta\sigma(t)$ and its illumination $I(t)$ by using appropriate calibration functions. The average excess carrier density $\Delta n_{av} = \Delta p_{av}$ in the test sample can be determined by

$$\Delta n_{av}(t) = \frac{\Delta\sigma(t)}{q(\mu_n + \mu_p)W}, \quad 2$$

where W is the sample thickness and μ_n and μ_p are the electron and the hole mobilities. As μ_n and μ_p themselves are functions of the carrier density, the determination of Δn_{av} requires an iterative procedure on the basis of a carrier-density-dependent mobility model.

The illumination intensity I_{av} , measured by the calibrated reference solar cell and normally quoted in suns ($1 \text{ sun} = 1000 \text{ W/m}^2$), is a measurement of the number of photon incidents on the sample's surface. As any real sample will only absorb a fraction f_{abs} of these available photons, the remainder being lost by reflection and transmission, the generation rate within the sample can be determined as

$$G_{av}(t) = \frac{I_{av}(t) f_{abs} N_{ph}^{1sun}}{W}, \quad 3$$

where N_{ph}^{1sun} is the density of photons in solar light with an irradiance of 1 sun, which generate electron-hole pairs in the sample. As the required quantities in

$$\tau_{eff} = \frac{\Delta n_{av}}{G_{av}(t) - \frac{\partial \Delta n_{av}(t)}{\partial t}} \quad 4$$

can thus be measured, a determination of the effective lifetime is possible.

As the decay time of the flash-lamp may be varied by two orders of magnitude, the QSSPC setup allows measurements in the transient mode (PCD) and in the quasi-steady-state mode (QSSPC). In conjunction with the simplified analyses

$$\tau_{eff} = \frac{\Delta n_{av}}{\frac{\partial \Delta n_{av}(t)}{\partial t}}, \quad 5$$

$$\tau_{eff} = \frac{\Delta n_{av}}{G_{av}(t)}. \quad 6$$

Both modes are restricted to certain lifetime ranges. However, using the QSSPC mode in conjunction with the generalised analysis given in equation 3, it constitutes an excellent method for measuring a large range of carrier lifetimes (from 0.1 μ s to several ms) over a large range of carrier densities (10^{12} - 10^{17} cm^{-3} , depending on the lifetime level). Thus this technique is ideally suited for injection-dependent lifetime measurements and has been used throughout this work.

A.6 X-Ray Diffraction (XRD)

X-ray Diffraction can deliver information on the crystalline state of a thin film. The basis of XRD is the constructive interference of X-ray reflections from regularly spaced atomic planes [21]. Elastically scattered X-ray waves can only propagate in directions for which there is constructive interference. Thus an X-ray photon elastically scattered by a single plane of waves must have an exit angle equal to the entry angle (relative to the plane) as shown in Figure A.4. The path length difference between reflections from adjacent planes must have a path length difference (PLD) equal to an integer number of wavelengths in order to obtain constructive interference, thus leading to Bragg's law

$$PLD = n\lambda = 2d_{hkl} \sin \Theta, \quad 7$$

which relates the scattering angle 2θ to the hkl plane spacing d_{hkl} , the X-ray wavelength λ and the order of the reflection n .

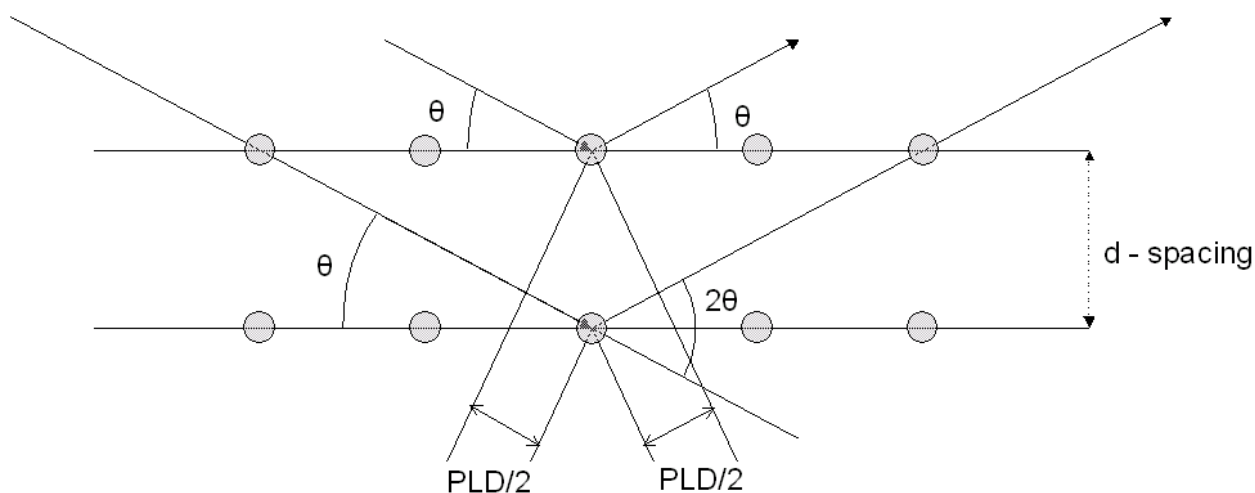


Figure A.4: Schematic picture of Bragg's reflection condition on a lattice plane.

The difficulty in recording diffraction from thin films arises from the restricted path length in the layer. One has to consider that the attenuation of an X-ray beam follows a standard exponential decay law. The used source, 1.54Å CuK α X-ray, has a skin depth d_s in SiC of 66.3 μm . When using the conventional Bragg-Brentano powder geometry (angle of incidence $\omega = \theta = 2\theta/2$) for the largest peak in 3C SiC (the 111 plane, $2\theta = 35.67^\circ$) the beam penetrates a depth $d = d_s \sin \omega = 20.3 \mu\text{m}$. This is no problem for a semi-infinite bulk sample (several hundred μm thick) but the thin films deposited are much thinner and thus only absorb $\approx 1.5\text{-}3\%$ of the incident intensity. The intensity of the diffracted beam is only 5.7% of the total diffracted power that would be obtained from a semi-infinite sample. Therefore many groups perform what is known as „grazing incidence“ XRD in order to overcome the low diffracted powers from thin films. This thin film geometry has ω fixed at a very small angle (usually 2°) to maintain a long pathlength in the film and scans only around 2θ . This is also necessary for our films, giving large increases in peak height when compared to Bragg-Brentano geometry. Still, very long count times are required to average out noise from the pattern and at low diffracted beam intensities, these fluctuations could

hide other features of the pattern. Scanning speeds of 8 min per ° of 2θ are adequate to separate peaks from noise. For the 2 μm thin film, an incident angle of $\omega=3^\circ$ is used.

Orientation also affects the ability to measure diffraction. For single crystals, the incident beam must simultaneously be oriented at the correct angle relative to the normal from the plane, and also satisfy the Bragg law for that plane. For polycrystalline samples with randomly oriented grains, the normal vectors for any set of hkl planes are pointing in all directions, thus removing the restriction on the sample orientation. This means that, when the detector is scanned through 2θ , all allowed reflections should be present in the diffraction pattern.

PUBLICATIONS

- [1] S. Janz, S. Bau, F. Lutz, C. Schetter, S. Reber, „PECVD-SiC as Intermediate Layer for Crystalline Silicon Thin-Film Solar Cells on Ceramic Substrates“, Proceedings of the 19th EUPVSEC, Paris (2004), p. 1217.
- [2] S. Janz, S. Reber, F. Lutz, C. Schetter, „SiC as an Intermediate Layer for CSiTF Solar Cells on Various Substrates“, Proceedings of the 20th EUPVSEC, Barcelona (2005), p. 1016.
- [3] S. Janz, S. Reber, H. Habenicht, „C-Si Thin-Film Solar Cells on Ceramic Substrates with SiC Intermediate Layers“, Technical Digest of the 15th PVSEC, Shanghai (2005), p. 873.
- [4] S. Janz, S. Reber, H. Habenicht, H. Lautenschlager, C. Schetter, „Processing of C-Si Thin-Film Solar Cells on Ceramic Substrates with Conductive SiC Diffusion Barrier Layer“, Proceedings of the 4th WCPEC, Hawaii (2006), p. 1403.
- [5] S. Janz, S. Riepe, M. Hofmann, S. Reber, S. Glunz, „Phosphorus-doped SiC as an excellent p-type Si surface passivation layer“, Appl. Phys. Letters **88**, 1333516 (2006).
- [6] S. Janz, S. Reber, F. Lutz, C. Schetter, „Conductive SiC as an intermediate layer for CSiTF solar cells“, Thin Solid Films 511-512 (2006), p. 271.
- [7] S. Janz, S. Reber, H. Habenicht, S. Lindekugel, H. Lautenschlager, C. Schetter, F. Lutz, „Solar Cell processing of Recrystallized Wafer Equivalents on Low-Cost Ceramics“, Proceedings of the 21st EUPVSEC, Dresden (2006), p. 996.
- [8] S. Janz, S. Reber, S. W. Glunz, „Amorphous SiC: Applications for Silicon Solar Cells“, Proceedings of the 21st EUPVSEC, Dresden (2006), p. 660.
- [9] S. Bau, S. Janz, T. Kieliba, C. Schetter, S. Reber, F. Lutz, „Application of PECVD-SiC as an Intermediate Layer in Crystalline Silicon Thin-Film Solar Cells““ Proceedings of the 3rd WCPEC, Osaka (2003), p. 1178.

-
- [10] S. Reber, A. Eyer, F. Haas, N. Schillinger, S. Janz, E. Schmich, „Progress in Crystalline Silicon Thin-Film Solar Cell Work at Fraunhofer ISE“, Proceedings of the 20th EUPVSEC, Barcelona (2005), p. 694.
- [11] S. W. Glunz, A. Grohe, M. Hermle, M. Hofmann, S. Janz T. Roth, O. Schultz, M. Vetter, I. Martin, R. Ferré, A. Bermejo, W. Wolke, W. Warta, R. Preu, G. Willeke, „Comparison of Different Dielectric Passivation Layers for Application in Industrial Feasible High-Efficiency Crystalline Silicon Solar Cells“, Proceedings of the 20th EUPVSEC, Barcelona (2005), p. 572.
- [12] A. Eyer, F. Haas, S. Janz, F. Lutz, H. Hurre, N. Schillinger, S. Reber, „High Throughput CVD and ZMR for Crystalline Silicon Thin-Film Solar Cells“, Technical Digest of the 15th PVSEC, Shanghai (2005), p. 318.
- [13] S. W. Glunz, S. Janz, M. Hofmann, T. Roth, G. Willeke, „Surface Passivation of Silicon Solar Cells Using Amorphous Silicon Carbide Layers“, Proceedings of the 4th WCPEC, Hawaii (2006), p. 1016.

REFERENCES

- [1] P. Raback, "*Modelling of the Sublimation Growth of Silicon Carbide Crystals*" (Helsinki University of Technology, Helsinki, Finland, 1999).
- [2] S. Adenwalla, et. al., "*Boron carbide/ n-silicon carbide heterojunction diodes*", Appl. Phys. Lett. **79** (2001), p. 4357-4359.
- [3] T. Itoh, et. al., "*Wide gap and low resistive hetero-structured SiCx films for wide gap window of heterojunction solar cells*", Proc. of the 3rd World Conference on Photovoltaic Energy Conversion (2003), p. 1706-1709.
- [4] R. Schwarz, et. al., "*Effect of interface defects on the response time of a-Si:H / a-SiC:H superlattices*", Superlattices and Microstructures **10** (1991), p. 147-152.
- [5] N. I. Klyui, et. al., "*Silicon solar cells with antireflection diamond-like carbon and silicon carbide films*", Solar Energy Materials and Solar Cells **72** (2002), p. 597-603.
- [6] M. A. E. Khakani, et. al., "*Hardness and Young`s modulus of amorphous a-SiC thin films determined by nanoindentation and bulge tests*", J. Mater. Res. **9** (1994), p. 96-103.
- [7] H. T. M. Pham, et. al., "*Evaluation of in-situ doped PECVD SiC thin films for surface micromachining*", Proc. of the SESENS (2001), p. 856-860.
- [8] P. M. Sarro, "*Silicon carbide as a new MEMS technology*", Sensors and Actuators **82** (2000), p. 210-218.
- [9] P. Misaelides, et. al., "*Surface characterisation and corrosion behaviour of SiC-coated AISI 321 stainless steel*", Nuclear Instruments and Methods in Physics Research **B 129** (1997), p. 221-227.
- [10] L. Jiang, et. al., "*a-SiCx:H films deposited by plasma-enhanced chemical vapor deposition at low temperature used for moisture and corrosion resistant applications*", Thin Solid Films **352** (1999), p. 97-101.

- [11] A. F. Flannery, et. al., "*PECVD silicon carbide as a chemically resistant material for micromachined transducers*", *Sensors and Actuators A* **70** (1998), p. 48-55.
- [12] T. Blum, et. al., "*Wear-resistant amorphous SiC coatings produced by plasma-enhanced CVD*", *Surface and Coatings Technology* **116-119** (1999), p. 1024-1028.
- [13] A. Auditore, et. al., "*Human serum albumin adsorption onto a-SiC:H and a-C:H thin films deposited by plasma enhanced chemical vapor deposition*", *Biomolecular Engineering* **19** (2002), p. 85-90.
- [14] M. Amon, et. al., "*Coating of cardiovascular stents with amorphous silicon carbide to reduce thrombogenicity*", *Proc. of the IEEE* (1994), p. 838-839.
- [15] J. Bullo, et. al., "*Physics of Amorphous Silicon-Carbon Alloys*", *Phys. Stat. Sol B* **143** (1987), p. 345.
- [16] V. I. Ivashchenko, et. al., "*Tight-binding-molecular-dynamics investigation of the atomic and electronic structure properties of a-C, a-Si, and a-SiC*", *Diamond and Related Materials* **12** (2003), p. 993-997.
- [17] D. G. McCulloch, et. al., "*Wannier function analysis of tetrahedral amorphous networks*", *Diamond and Related Materials* **12** (2003), p. 2026-2031.
- [18] F. Demichelis, et. al., "*Bonding structure and defects in wide band gap a-Si_{1-x}C_x:H films deposited in H₂ diluted SiH₄ + CH₄ gas mixtures*", *Philosophical Magazine B* **71** (1995), p. 1015-1033.
- [19] M. L. d. Oliveira, et. al., "*On the carbon incorporation into a-SiC:H films with low carbon content*", *J. Appl. Phys.* **71** (1992), p. 1531-1533.
- [20] T. Stapinski, et. al., "*Defect characterization of SiC:H and SiN:H alloys produced by ultrahigh vacuum plasma chemical vapor deposition in different plasma conditions*", *Physica B* **254** (1998), p. 99-106.
- [21] O. Brümmer, et. al., "*Handbuch Festkörperanalyse mit Elektronen, Ionen und Röntgenstrahlen*" (F. Viewag & Sohn, Braunschweig, Wiesbaden, 1980).
- [22] T. Kunz, et. al., "*Silicon carbide barrier layer on ceramic substrates for crystalline silicon thin-film modules with an integrated series connection*", *Proc. of the 3rd World Conference on Photovoltaic Energy Conversion* (2003), p. 1255-1258.

- [23] W. H. Lee, et. al., "*Effects of CH₄/SiH₄ flow ratio and microwave power on the growth of β -SiC on Si by ECR-CVD using CH₄/SiH₄/Ar at 200 °C*", Thin Solid Films **405** (2002), p. 17-22.
- [24] A. Matsuda, et. al., "*Preparation of highly photosensitive hydrogenated amorphous Si-C alloys from a glow-discharge plasma*", J. Appl. Phys. **60** (1986), p. 4025-4027.
- [25] P. R. McCurdy, et. al., "*Pulsed and continuous wave plasma deposition of amorphous, hydrogenated silicon carbide from SiH₄/CH₄ plasmas*", Journal of Vacuum Science & Technology A: Vacuum, Surfaces, and Films **17** (1999), p. 2475-2484.
- [26] W. A. Nevin, et. al., "*Wide band-gap hydrogenated amorphous silicon carbide prepared from a liquid aromatic carbon source*", J. Appl. Phys. **72** (1992), p. 4989-4991.
- [27] X. Redondas, et. al., "*Dependence on the C₂H₄ and SiH₄ gas mixture of the Si-C film properties obtained by excimer lamp chemical vapour deposition*", Surface and Coatings Technology **100-101** (1998), p. 160-163.
- [28] M. D. Stamate, "*Strong dependence on IR absorption in a-SiC:H dc magnetron sputtered thin films on H₂ partial pressure*", Applied Surface Science **172** (2001), p. 47-50.
- [29] B. P. Swain, et. al., "*Revisiting the B-factor variation in a-SiC:H deposited by HWCVD*", Thin Solid Films **430** (2003), p. 186-188.
- [30] L. Thomas, et. al., "*Microwave plasma chemical vapour deposition of tetramethylsilane: correlations between optical emission spectroscopy and film characteristics*", Surface and Coatings Technology **142-144** (2001), p. 314-320.
- [31] M. A. Lieberman, et. al., "*Principles of Plasma Discharges and Materials Processing*" (John Wiley & Sons, Inc., 1994).
- [32] P. Kae-Nune, et. al., "*Mass spectrometry detection of radicals in SiH₄-CH₄-H₂ glow discharge plasmas*", (1994), p. 250-259.
- [33] J. Perrin, "*Deposition of amorphous silicon alloys*", Pure & Appl. Chem. **62** (1990), p. 1681-1688.

- [34] H. T. M. Pham, et. al., "*Influence of deposition parameters and temperature on stress and strain of in situ doped PECVD silicon carbide*", Materials Science Forum **389-393** (2002), p. 759-762.
- [35] J. W. Coburn, "*Plasma etching and reactive ion etching*".
- [36] L. Jiang, et. al., "*Surface characterization of inductively coupled plasma etched SiC in SF₆/O₂*", Microelectronic Engineering **1** (2003), p. 1-7.
- [37] A. Tasaka, et. al., "*Plasma etching of SiC surface using NF₃*", J. Vac. Sci. Technol. **A 20** (2002), p. 1254-1260.
- [38] P. Leerungnawarat, et. al., "*Comparison of F₂ Plasma Chemistries for Deep Etching of SiC*", Journal of Electronic Materials **30** (2001), p. 202-206.
- [39] U. Schmid, et. al., "*Etching characteristics and mechanical properties of a-SiC:H thin films*", Sensors and Actuators **A 94** (2001), p. 87-94.
- [40] D. Zhuang, et. al., "*Wet etching of GaN, ACN and SiC: a review*", Materials Science and Engineering **R 48** (2005), p. 1-46.
- [41] T. Y. Lin, et. al., "*Fabrication of Low-Stress Plasma Enhanced Chemical Vapor Deposition Silicon Carbide Films*", Jpn. J. Appl. Phys. **39** (2000), p. 6663-6671.
- [42] V. J. Minkiewicz, et. al., "*Some mechanical and thermal properties of PECVD a-Si_{1-x}Cl_x : H and a-Si_{1-x}N_x : H films prepared by mixed frequency plasma processes*", Surface and Coatings Technology **68/69** (1994), p. 229-233.
- [43] M. P. Hughey, et. al., "*Massive stress changes in plasma enhanced chemical vapor deposited silicon nitride films on thermal cycling*", Thin Solid Films **460** (2004), p. 7-16.
- [44] R. A. Street, "*Hydrogenated Amorphous Silicon*" (Cambridge University Press, 1991).
- [45] S. H. Rejeb, et. al., "*Light induced defects in amorphous silicon - carbon alloys a-SiC:H*", Optical Materials **6** (1996), p. 13-16.
- [46] T. Stapinski, et. al., "*Optical and structural properties of amorphous silicon-carbon films for optoelectronic applications*", Applied Surface Science **238** (2004), p. 367-374.

- [47] F. Demichelis, et. al., "*Density of gap states in a-SiC:H films by means of photoconductive and photothermal spectroscopies*", *Physica B* **205** (1995), p. 169-174.
- [48] B. G. Budaguan, et. al., "*The development of a high-rate technology for wide-bandgap photosensitive a-SiC:H alloys*", *Journal of Alloys and Compounds* **327** (2001), p. 146-150.
- [49] K. B. K. Teo, et. al., "*Highest optical gap tetrahedral amorphous carbon*", *Diamond and Related Materials* **11** (2002), p. 1086-1090.
- [50] J. P. Xanthakis, "*Effects of short-range order on the electronic structure and optical properties of amorphous carbon*", *Diamond and Related Materials* **9** (1999), p. 1369-1373.
- [51] R. Swanepoel, "*Determination of the thickness and optical constants of amorphous silicon*", *J. Phys. E: Sci. Instrum.* **16** (1983), p. 1214-1222.
- [52] J. Tauc, et. al., "*States in the Gap*", *Journal of Non-Crystalline Solids* **8** (1972), p. 569-585.
- [53] Y. Hishikawa, et. al., "*Interference-Free Determination of the Optical Absorption Coefficient and the Optical Gap of Amorphous Silicon Thin Films*", *Japanese Journal of Applied Physics* **30** (1991), p. 1008-1014.
- [54] W. B. Jackson, et. al., "*Direct measurement of gap-state absorption in hydrogenated amorphous silicon by photothermal deflection spectroscopy*", *Physical Review B* **25** (1982), p. 5559-5561.
- [55] J. Singh, "*Electronic process in amorphous semiconductors*", *J. Mat. Sci: Materials in Electronics* **14** (2003), p. 171-186.
- [56] M. N. P. Carreno, et. al., "*p-Type doping in a-Si_{1-x}C_x:H obtained by PECVD*", *Journal of Non-Crystalline Solids* **266-269** (2000), p. 699-703.
- [57] F. Demichelis, et. al., "*Boron and phosphorus doping of a-SiC:H thin films by means of ion implantation*", *Thin Solid Films* **265** (1995), p. 113-118.
- [58] F. Demichelis, et. al., "*Influence of doping on the structural and optoelectronic properties of amorphous and microcrystalline silicon carbide*", *J. Appl. Phys.* **72** (1992), p. 1327-1333.

- [59] M. N. P. Carreno, et. al., "*N-type doping in PECVD a-Si_{1-x}C_x:H obtained under 'starving plasma' condition*", Journal of Non-Crystalline Solids **227-230** (1998), p. 483-487.
- [60] J. Huran, et. al., "*Influence of nitrogen concentration on conductivity of N-doped a-SiC:H films deposited by PECVD*", Vacuum **67** (2002), p. 567-570.
- [61] A. Madan, et. al., in *The Physics and Applications of Amorphous Semiconductors* (Academic Press, New York, 1988)
- [62] P. Deac, et. al., "*'Some like it shallower' - p-type doping in SiC*", phys. stat. sol. **235 (b)** (2002), p. 139-145.
- [63] P. P. Altermatt, et. al., "*Impact of incomplete ionisation on measurements of sheet resistivity and of carrier mobility in c-Si solar cells at room temperature*", Proc. of the 20th EU-PVSEC (2005), p. 1267-1270.
- [64] M. Hofmann, "*Entwicklung und Charakterisierung von Schichtsystemen zur Passivierung von kristallinen Siliziumscheiben*", Diploma Thesis, Fachhochschule Koblenz (2003).
- [65] Y. C. Chou, et. al., "*Doping and electrical properties of amorphous silicon carbon nitride films*", Diamond and Related Materials **12** (2003), p. 1213-1219.
- [66] J. S. Chen, et. al., "*Contact resistivity of Re, Pt and Ta films on n-type b-SiC: preliminary results*", Materials Science and Engineering **B29** (1995), p. 185-189.
- [67] I. Pereyra, et. al., "*Highly ordered amorphous silicon-carbon alloys obtained by RF PECVD*", Brazilian Journal of Physics **30** (2000), p. 533-540.
- [68] S. Fernandez-Robledo, "*PECVD-SiC barrier layer for crystalline thin film solar cells*", Report on Practicum Work, Freiburg (2004).
- [69] J. M. Eldridge, et. al., "*Oxidation of plasma-deposited a-Si_xC_{1-x}:H films*", J. Electrochem. Soc. **137** (1990), p. 2266-2271.
- [70] T. Friessnegg, et. al., "*Defect structure of carbon rich a-SiC:H films and the influence of gas and heat treatments*", Journal of Applied Physics **84** (1998), p. 786-795.
- [71] R. J. Prado, et. al., "*Annealing effects of highly homogeneous a-Si_{1-x}C_x:H*", Journal of Non-Crystalline Solids **330** (2003), p. 196-215.

- [72] D. K. Basa, et. al., "*Infrared study of amorphous-crystalline phase transition in an annealed amorphous hydrogenated silicon-carbon alloy film*", *Mat. Res. Soc. Symp. Proc.* **162** (1990), p. 439-444.
- [73] L. Calcagno, et. al., "*Crystallisation mechanism of amorphous silicon carbide*", *Applied Surface Science* **184** (2001), p. 123-127.
- [74] E. Ermer, et. al., "*FTIR studies of structural effects due to boron addition in sintered silicon carbide*", *Vibrational Spectroscopy* **29** (2002), p. 211-215.
- [75] E. Gat, et. al., "*A study of the effect of composition on the microstructural evolution of a-Si_{1-x}C_{1-x}:H PECVD films: IR absorption and XPS characterizations*", *J. Mater. Res.* **7** (1992), p. 2478-2487.
- [76] N. Laidani, et. al., "*Spectroscopic characterization of thermally treated carbon-rich Si_{1-x}C_x films*", *Thin Solid Films* **223** (1993), p. 114-121.
- [77] W.-L. Lin, et. al., "*Identification of infrared absorption peaks of amorphous silicon-carbon alloy by thermal annealing*", *Appl. Phys. Lett.* **51** (1987), p. 2112-2113.
- [78] F. Demichelis, et. al., "*Microcrystallization formation in silicon carbide thin films*", *Philosophical Magazine B* **66** (1992), p. 135-146.
- [79] F. Sanchez-Bajo, et. al., "*Accuracy of X-ray diffraction SiC polytype-composition analyses performed by a polymorphic method*", *Journal of Materials Science Letters* **20** (2001), p. 297-299.
- [80] A. R. Oliveira, et. al., "*Post thermal annealing crystallization and reactive ion etching of SiC films produced by PECVD*", *Journal of Non-Crystalline Solids* **352** (2006), p. 1392-1397.
- [81] J. C. Burton, et. al., "*Characterization of Silicon Carbide using Raman Spectroscopy*", *Materials Science Forum Vols.* **338-342** (2000), p. 615-618.
- [82] A. Chehaidar, et. al., "*Chemical bonding analysis of a-SiC:H films by Raman spectroscopy*", *Journal of Non-Crystalline Solids* **169** (1994), p. 37-46.
- [83] Y. Inoue, et. al., "*Raman Spectra of Amorphous SiC*", *Solid State Communications* **48** (1983), p. 1071-1075.
- [84] A. L. Baia Neto, et. al., "*Annealing effects on near stoichiometric a-SiC:H films*", *Surface and Coatings Technology* **120-121** (1999), p. 395-400.

- [85] G. Compagnini, et. al., "*Vibrational analysis of compositional disorder in amorphous silicon carbon alloys*", *Europhysics Letter* **41** (1998), p. 225-230.
- [86] A. Morimoto, et. al., "*Annealing and crystallization processes in tetrahedrally bonded binary amorphous semiconductors*", *Philosophical Magazine B* **50** (1984), p. 517-537.
- [87] M. Huang, et. al., "*Thin film cracking and ratcheting caused by temperature cycling*", *J. Mater. Res.* **15** (1999), p. 1239-1242.
- [88] G. L. Harris, "*Properties of Silicon Carbide*", Harris, G.L. ed. (Institution of Engineering and Technology, 2005).
- [89] R. G. Munro, "*Material Properties of a Sintered alpha-SiC*", *Chemical Reference Data* **26** (1997), p. 1195-1203.
- [90] R. Hull, "*Properties of Crystalline Silicon*", INSPEC, London (1999).
- [91] G. F. Cerofolini, et. al., "*Hydrogen and Helium bubbles in Silicon*", *Materials Science and Engineering* **27** (2000), p. 1-52.
- [92] W. Wolke, "*Kathodenzerstäubung zur Beschichtung von kristallinen Silizium-Solarzellen*", PhD, Albert-Ludwigs-Universität Freiburg (2005).
- [93] S. S. J. Camargo, et. al., "*Hydrogen effusion from highly-ordered near-stoichiometric a-SiC:H*", *Journal of Non-Crystalline Solids* **338-340** (2004), p. 70-75.
- [94] G. DellaMea, et. al., "*Influence of hydrogen on the evolution of structural properties of amorphous silicon carbide*", *Journal of Non-Crystalline Solids* **137&138** (1991), p. 95-98.
- [95] Y. Suzuki, et. al., "*Concentration and thermal release of hydrogen in amorphous silicon carbide films prepared by rf sputtering*", *Thin Solid Films* **311** (1997), p. 207-211.
- [96] S. N. Rashkeev, et. al., "*Defect Generation by Hydrogen at Si-SiO₂ Interface*", *Physical Review Letters* **87** (2001), p. 165506-1.
- [97] R. Jansen, et. al., "*Metalle schneller auflösen - Ein neuer Wasserstoffkatalysator*", *Galvanotechnik - MO Jahrg.* **53** (1999), p. 37-39.
- [98] S. Reber, "*Electrical Confinement for the Crystalline Silicon Thin-Film Solar Cell on Foreign Substrate*" (ibidem-Verlag, Stuttgart, Mainz, Germany, 2000).

-
- [99] T. Kieliba, "*Zonemelting Recrystallization for Crystalline Silicon Thin-Film Solar Cells*", PhD, Universität Konstanz (2006).
- [100] H. Habenicht, "*SiC-Schichten als Diffusionsbarriere für kristalline Silizium-Dünnschicht-Solarzellen auf Keramiksustrat*", Diploma Thesis, Universität Konstanz (2006).
- [101] T. Buonassisi, et. al., "*Distinguishing the impacts of individual metal species on multicrystalline silicon performance in a multiple-metal environment*", Proc. of the 20th EU-PVSEC (2005), p. 569-571.
- [102] J. R. Davis, et. al., "*Characterization of the effects of metallic impurities on silicon solar cell performance*", Proc. of the 13th IEEE Photovoltaic Specialists Conference (1978).
- [103] J. F. Ziegler, et. al., "*The Stopping and Range of Ions in Solids*", Pergamon Press, New York (1985).
- [104] D. Suwito, "*Dünnschichtsolarzellen aus zonengeschmolzenen Siliziumschichten mit in-situ Back Surface Field*", Diploma Thesis, Albert-Ludwigs-Universität Freiburg (2006).
- [105] S. Bau, "*High-Temperature CVD silicon films for crystalline silicon thin-film solar cells*", PhD, Universität Konstanz (2003).
- [106] L. Calcagno, et. al., "*Ion-beam processing of hydrogenated amorphous silicon carbide grown by plasma-enhanced chemical vapour deposition*", Philosophical Magazine B **80** (2000), p. 539-546.
- [107] D. S. Kim, "*Annealing effects on a-SiC:H and a-SiC:H(F) thin films deposited by PECVD at room temperature*", Thin Solid Films **261** (1995), p. 192-201.
- [108] W. Beyer, "*Diffusion and evolution of hydrogen in hydrogenated amorphous and microcrystalline silicon*", Solar Energy Materials & Solar Cells **78** (2003), p. 235-267.
- [109] W. B. Jackson, et. al., "*Hydrogen Transport in Amorphous Silicon*", Phys. Rev. B **45** (1992), p. 6564-6580.
- [110] W. B. Jackson, et. al., "*Role of clustering in hydrogen transport in silicon*", Physikal Review B **47** (1993), p. 9993-9996.

- [111] J. Isenberg, et. al., "*Imaging method for laterally resolved measurement of minority carrier densities and lifetimes: measurement principle and first applications*", Journal of Applied Physics **93** (2003), p. 4268-75.
- [112] "*Thin Film Solar Cells*", Jef Poortmans, Vladimir Arkhipov ed. (John Wiley & Sons, Ltd, 2006).
- [113] J. Bloem, et. al., (North Holland Publishing Company, 1978), p. 147-342.
- [114] J. Isenberg, et. al., "*Fast, contactless and spatially resolved measurement of sheet resistance by an infrared method*", Progress in Photovoltaics **12** (2004), p. 539-552.
- [115] A. Basore, "*Numerical Modeling of Textured Silicon Solar Cells Using PC-ID*", IEEE Transactions on Electron Devices **37** (1990), p. 337-343.
- [116] A. Goetzberger, et. al., "*Sonnenenergie: Photovoltaik*" (B. G. Teubner Stuttgart, Freiburg, Germany, 1997).
- [117] S. Janz, "*Aufbau einer Apparatur zur spektral aufgelösten Kurzschlussstopographie mit besonderer Berücksichtigung der Reflexion an der Probenoberfläche*", Diploma Thesis, TU Graz (2003).
- [118] I. Martín, "*Silicon surface passivation by Plasma Enhanced Chemical Vapor Deposited amorphous silicon carbide films*", PhD, Universitat Politecnica de Catalunya (2003).
- [119] W. Shockley, et. al., "*Statistics of the recombinations of holes and electrons*", Physical Review **87** (1952), p. 835-42.
- [120] R. N. Hall, "*Electron-hole recombination in germanium*", Physical Review **87** (1952), p. 387.
- [121] S. W. Glunz, et. al., "*Field-effect passivation of the SiO₂-Si interface*", Journal of Applied Physics **86** (1999), p. 683.
- [122] O. Schultz, "*High-Efficiency Multicrystalline Silicon Solar Cells*" (Verlag Dr. Hut, München, Freiburg, 2005).
- [123] M. Hofmann, et. al., "*21%-Efficient Silicon Solar Cells using amorphous Silicon Rear Side Passivation*", Proc. of the 21st EU-PVSEC (2006), p. 609.
- [124] I. Martin, et. al., "*Surface passivation of p-type crystalline Si by plasma enhanced chemical vapor deposited amorphous SiC_x:H films*", Appl. Phys. Lett. **79** (2001), p. 2199-2201.

-
- [125] I. Martin, et. al., "*Characterization and application of a-SiCx:H films for the passivation of the c-Si surface*", *Thin Solid Films* **403-404** (2002), p. 476-479.
- [126] M. Vetter, et. al., "*Comparison of the surface passivation quality of SiCx and SiNx films on p-type and n-type multicrystallien silicon*", *Proc. of the 20th EU-PVSEC* (2005), p. 1454-1456.
- [127] M. Vetter, et. al., "*Investigatin of the surface passivation of p+-type Si emitters by pecvd silicon carbide films*", *Proc. of the 4th World PVSEC* (2006), p. 1271.
- [128] M. Vetter, et. al., "*Electronic properties of intrinsic and doped amorphous silicon carbide films*", *Thin Solid Films* **511-512** (2006), p. 290-294.
- [129] R. A. Sinton, et. al., "*Quasi-steady-state photoconductance, a new method for solar cell material and device characterization*", *Proc. of the 25th IEEE Photovoltaic Specialists Conference* (1996), p. 457-60.
- [130] S. Janz, et. al., "*Phosphorous-doped SiC as an excellant p-type Si surface passivation layer*", *Applied Physics Letter* **88**, 133516 (2006).
- [131] M. J. Kerr, et. al., "*General parameterization of Auger recombination in crystalline Silicon*", *Journal of Applied Physics* **91** (2002), p. 2473-2480.
- [132] S. W. Glunz, et. al., "*Solar Cells with Meshstructured Emitter*", *Progress in Photovoltaics: Research and Applications* **4** (1996), p. 415-424.
- [133] S. W. Glunz, et. al., "*Laser-fired contact silicon solar cells on p- and n-substrates*", *Proc. of the 19th EU-PVSEC* (2004), p. 408-411.
- [134] R. A. Sinton, et. al., "*A quasi-steady-state open-circuit voltage method for solar cell characterization*", *Proc. of the Proceedings of the 16th European Photovoltaic Solar Energy Conference* (2000), p. 1152.
- [135] S. Dauwe, "*Low-Temperature Surface Passivation of Crystalline Silicon and its Application to the Rear Side of Solar Cells*", PhD, Universität Hannover (2004).
- [136] P. Grunow, et. al., "*Modelling of the encapsulation factors for photovoltaic modules*", *Proc. of the 4th World PVSEC* (2006), p. 2152.
- [137] M. Neander, et. al., "*Anti-reflective-coating tuned for higher solar module voltage*", *Proc. of the 4th World PVSEC* (2006), p. 2070.

-
- [138] G. Scardera, et. al., "*Investigating large area fabrication of silicon quantum dots in a nitride matrix for photovoltaic applications*", Proc. of the 4th World PVSEC (2006), p. 122.
- [139] U. Kahler, "*Darstellung, Charakterisierung und Oberflächenmodifizierung von Siliziumnanopartikeln in SiO₂*", PhD, Universität Halle (2000).
- [140] M. A. Green, "*Third Generation Photovoltaics: Theoretical and Experimental progress*", Proc. of the 19th European PVSEC (2004), p. 3-8.
- [141] Y. Takeda, et. al., "*A novel method based on oblique deposition to fabricate quantum dot arrays*", Proc. of the 4th World PVSEC (2006), p. 1-4.
- [142] Y. Kurokawa, et. al., "*Nanocrystalline silicon in amorphous silicon carbide matrix for si quantum dots superlattice*", Proc. of the 4th World PVSEC (2006), p. 138.
- [143] V. Suendo, et. al., "*Luminescence of polymorphous silicon carbon alloys*", Optical Materials **27** (2004), p. 953-957.
- [144] S. Lim, et. al., "*Rugate filters grown by plasma-enhanced chemical vapor deposition*", Thin Solid Films **245** (1994), p. 141-145.
- [145] R. M. Young, et. al., "*Amorphous silicon, amorphous carbon and amorphous silicon carbide deposited by remote plasma chemical vapor deposition*", Thin Solid Films **213** (1991), p. 170-175.
- [146] H. G. Tompkins, "*A Users Guide to Ellipsometry*" (Academic Press, 1993).
- [147] R. J. Bell, "*Introductory Fourier Transform Spectroscopy*" (Academic Press, 1972).
- [148] I. R. Lewis, et. al., "*Handbook of Raman Spectroscopy*" (New York, 2001).

ACKNOWLEDGEMENTS

At the end of this work, I would like to express my gratitude to all people who supported me.

First of all I want to thank the head of our department Gerhard Willeke who advised me during my PhD time. Thank you to the colleagues who worked with me directly on the SiC topic: Suzanna Fernandez-Robledo (University of Northumbria, England), Ed Pink (UNSW, Australia) who worked on the annealing topic and Holger Habenicht (Universität Konstanz) and Dominik Suwito (Universität Freiburg) who worked on the diffusion behaviour of SiC. Furthermore I want to thank my PhD colleagues Sandra Bau and Thomas Kieliba who conducted me during the starting period of my work and Evelyn Schmich and Stefan Lindekugel who joined me and our group later on. For processing my samples I want to thank Harald Lautenschlager, Mira Kwiatkowska, Antonio Leimenstoll, Sonja Seitz and Anke Herbolzheimer. For technical support I have to thank Christian Schetter who kept the AK400M running. Many thanks to the all the other crystalline silicon thin-film group members. Especially Stefan Reber who taught me how to write a paper and a project sketch and who supplied me with the appropriate pressure during all these years.

Other colleagues at Fraunhofer ISE were always helpful when I had questions concerning photovoltaic problems or when I did not know how to handle an apparatus. Thank you to Elisabeth Schäffer, Thomas Roth, Stephan Riepe, Stephan Diez and Marc Hofmann. Furthermore I have to thank Stefan Glunz who helped me to exceed the magic 20% solar cell efficiency. I want to thank Michael Vetter and his team at Universitat Politecnica de Catalunya for introducing me into the fascinating world of surface passivation.

For making me feel something like home (although it's geographically far away) I want to thank my friends here in Freiburg who were there and let me have an excellent time. A lot of thanks to my family and my friends back home in Austria who are supporting me now for more than 3 decades without any sign of fatigue. You give me an idea of what life is all about. And at the end I want to thank my former

girlfriend for spending some brilliant years together while I tried to figure out (amongst others) that SiC thing.

CURRICULUM VITAE

Name	Stefan Janz
Date of Birth	February 9 th , 1974
Place of Birth	Leoben, Austria
Marital Status	single
Nationality	Austria
Education	1980 – 1984: Elementary School, Kindberg 1985 – 1988: Bundes Realgymnasium, Mürzzuschlag 1988 - 1993: Höhere Technische Bundeslehranstalt, Kapfenberg
Service	1995 – 1996: Civil Service as carer for the elderly, LAPH Kindberg
Higher Education	10/1993 – 03/2003: Technical University of Graz, Department of Physics March 2003: Diploma Exam (equivalent of M.Sc.) Diploma Thesis: “Aufbau einer Apparatur zur spektral aufgelösten Kurzschlussstopografie mit besonderer Berücksichtigung der Reflexionen an der Probenoberfläche”
Experience	04/2003-12/2006: PhD at Fraunhofer ISE in association with the University of Konstanz, Department of Physics